# CHALMERS



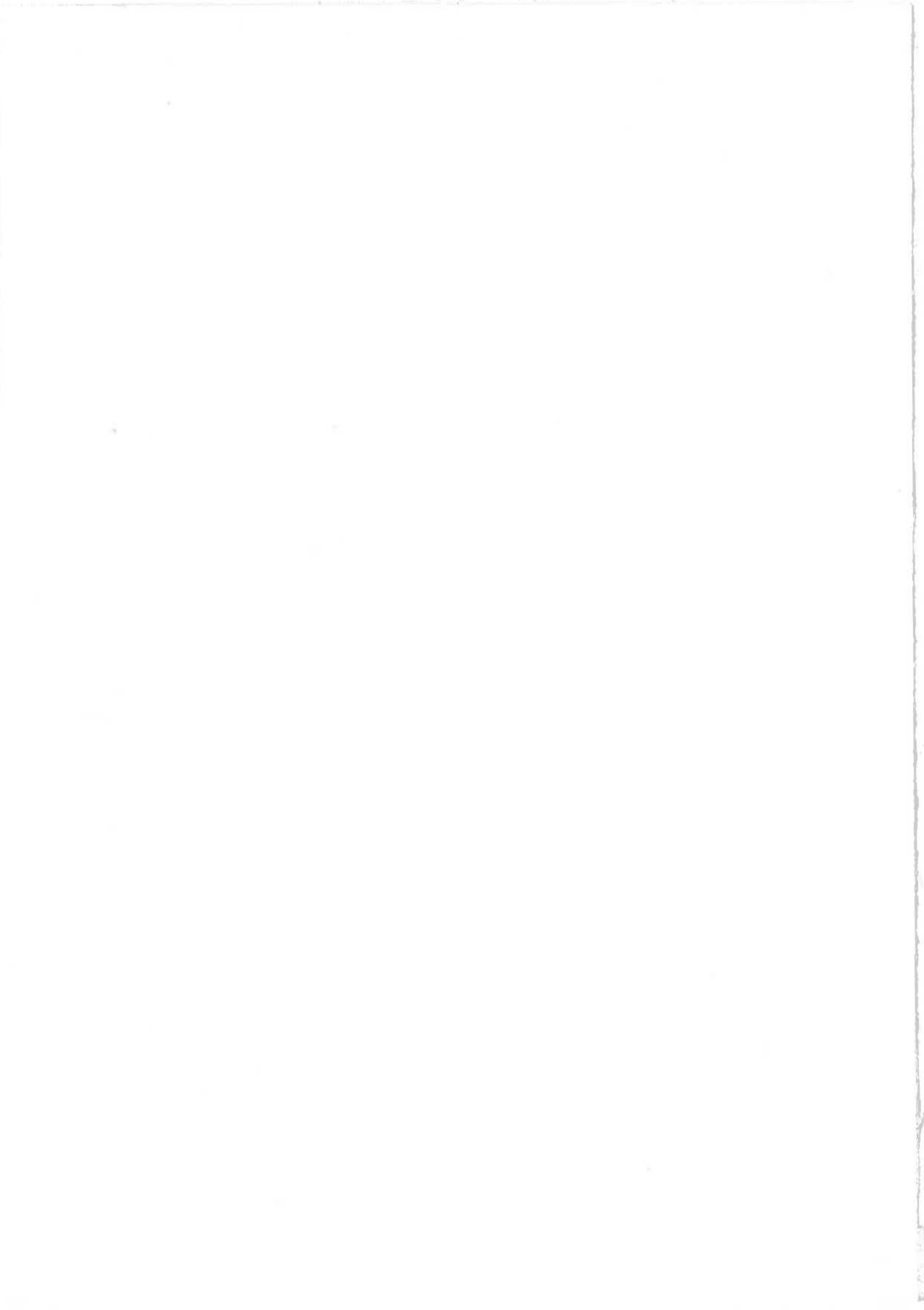## Splicing of Reinforcement Loops in Beams

Experiments and Non-linear Finite Element Analyses

Peter Grassl

# CHALMERS

# Splicing of Reinforcement Loops in Beams

## Experiments and Non-linear Finite Element Analyses

Peter Grassl

Göteborg December 1999

Cover:

The crack patterns of the test and a non-linear finite element analysis of specimen RV12 are shown. The grey marked elements indicate cracks. For more information see Section 4.

# Abstract

Loop splices are practicable in connections of concrete members taking advantage of the high anchorage capacity of the bend part of the loops. Nevertheless, the radial pressure due to the bend can cause spalling of the side concrete cover. The aim of the study was to investigate the behaviour of reinforcement loop splices without a transverse reinforcement in the splice zone. Hereby, it was focused on the flow of forces and the different failure modes. Furthermore, the influence of varying splice length and beam width was investigated.

Four full-scale tests of beams using a three-point test set-up were carried out. Hereby, the splice length and the beam width were varied. Additionally, non-linear finite element analyses were performed, where the influence of a varied splice length was further investigated by means of two-dimensional models.

With an increased splice length designed according to the Swedish Shelter Regulation spalling of the concrete cover could be prevented and the load capacity of a similar specimen with continuous reinforcement was obtained. Most of the anchorage capacity was provided by the straight part. With a splice length composed by two semi-circles spalling of the side concrete cover occurred. Hereby, an increased width of the specimen had a favourable influence on the load capacity.

Keywords: Concrete, Splicing of reinforcement, reinforcement loops, bond, anchorage, beam tests, finite element analysis.

I

# Contents

**Appendixes**

# Preface

In this Master's thesis splicing of reinforcement loops in beams were studied by means of experiments and non-linear finite element analyses. The project was carried out from June to December 1999 at the Division of Concrete Structures at Chalmers University of Technology. The study was part of a research project concerning reinforcement detailing of frame corners, which is financed by the Swedish Rescue Services Agency.

I would like to thank my supervisor Morgan Johansson for his help and advice. I also wish to thank everybody at the Division of Concrete Structures for their support. Thanks to Detlef Schulz, Lars Wahlström, Hans Coster and Nils Nilsson from the Structural Engineering Laboratory for their help to construct and test the beams. The photos were taken by Lars Wahlström. The examiner was Professor Kent Gylltoft.

Göteborg, December 1999

Peter Grassl

# Notations

## Roman upper case letters

$A_s$          cross-section area of reinforcement

$A_{st}$         transverse reinforcement

$E_c$          Young's modulus for concrete

$E_s$          Young's modulus for steel

$F$           load

$F_s$          force carried by reinforcement

$G_f$          fracture energy

$M$          bending moment [kNm]

$P$           radial pressure [N/m]

$P^*$          radial pressure [N/m$^2$]

$S_b$          final anchorage capacity (BBK 94) [N/m]

$V$           shear force [kN]

## Roman lower case letters

$c$           side concrete cover

$f_c$          compressive strength of concrete

$f_{c,cube}$      compressive cube strength of concrete

$f_{c,cyl}$       compressive cylinder strength of concrete

$f_{su}$         ultimate strength of reinforcement

$f_{sy}$         yield strength of reinforcement

$f_t$           tensile strength of concrete

$f(w)$        softening function

$f_b$          bond strength

k           coefficient considering transverse bars (BBK 94)

$l_b$          basic anchorage length

$l_s$          splice length

$n$           number of bars

$p$           radial pressure [N/m$^2$]

$r$           radius of reinforcement loop

$s_{lp}$         spacing of the loop pairs

$s_l$          spacing of the loops

| | |
|---|---|
| $s$ | slip of the reinforcement relative to the surrounding concrete |
| $s_b$ | anchorage capacity (BBK 94) [N/m] |
| $s_{rm}$ | mean crack spacing |
| $u$ | displacement |
| $u$ | length of the final crack |
| $w$ | crack opening |
| $w_u$ | ultimate crack opening |

**Greek letters**

| | |
|---|---|
| $\delta$ | displacement |
| $\varepsilon_c$ | concrete strain |
| $\varepsilon_h$ | strain at steel hardening |
| $\varepsilon_s$ | steel strain |
| $\varepsilon_u$ | ultimate steel strain |
| $\phi$ | bar diameter |
| $\rho$ | reinforcement ratio |

# 1 Introduction

## 1.1 Background

At the Division of Concrete Structures at Chalmers University of Technology a research project is carried out concerning reinforcement detailing of concrete frame corners of civil defence shelters. Different types of reinforcement detailing were examined by means of full-scale frame corner tests. The specimens were subjected to closing and opening bending moments. Additionally to the tests, non-linear finite element analyses have been conducted to study the behaviour more thoroughly. One of the results of the project was that reinforcement loops are suitable for the detailing of frame corners and result in a satisfying behaviour. The financier of the project, the Swedish Rescue Services Agency, received these results very positively and initiated a change in the Swedish shelter regulations. Thus, the complicated, conventional reinforcement detailing was replaced by a practicable loop arrangement, as shown in Figure 1.1.



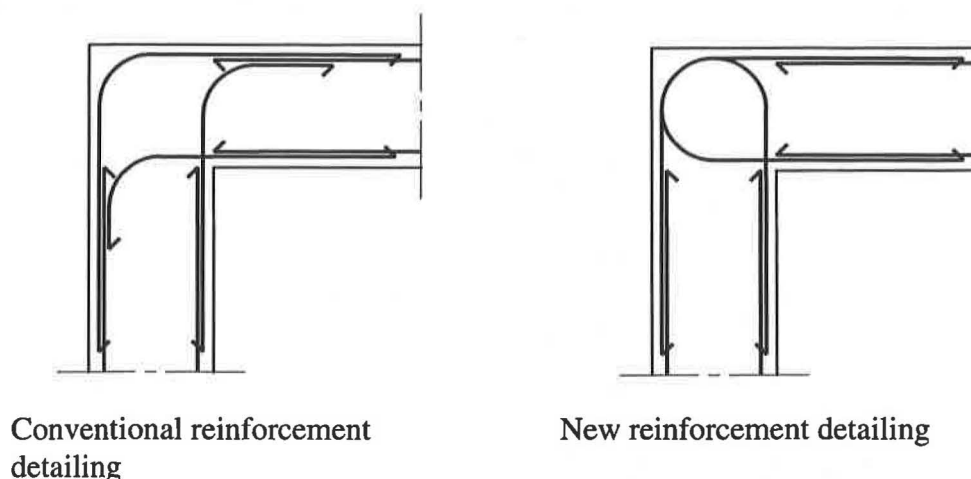Conventional reinforcement detailing                    New reinforcement detailing

Figure 1.1     Conventional and new reinforcement detailing in frame corners.

Additionally, the question was posed, whether it is possible to use the loop splicing at other places of the structure outside of frame corners taking advantage of the high anchorage capacity of the bend part of the loops.

- This may be practical in for example ground slab-wall connections. The wall could be easily connected to the already casted slab by means of reinforcement loops, as shown in Figure 1.2 a.

1

- Another useful application could be the ordinary straight splicing, as shown in Figure 1.2 b. By means of loops the splice length would be considerably reduced due to the increased anchorage capacity.
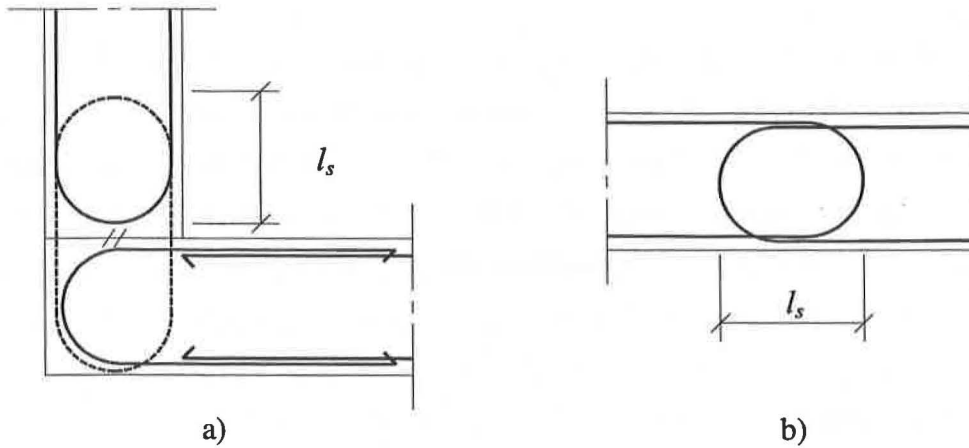


a)                          b)

Figure 1.2      Splicing of reinforcement outside the corner area using reinforcement loops.

However, one problem of reinforcement loop splices is the radial pressure due to the bend part. This forces the concrete to a lateral expansion, which can result in spalling of the side concrete cover, as shown in Figure 1.3. Consequently, the spalling phenomenon has to be carefully investigated. In the present version of the Swedish shelter regulation, Swedish Rescue Service Agencies (1998), the splice length is therefore elongated by an additional straight part.
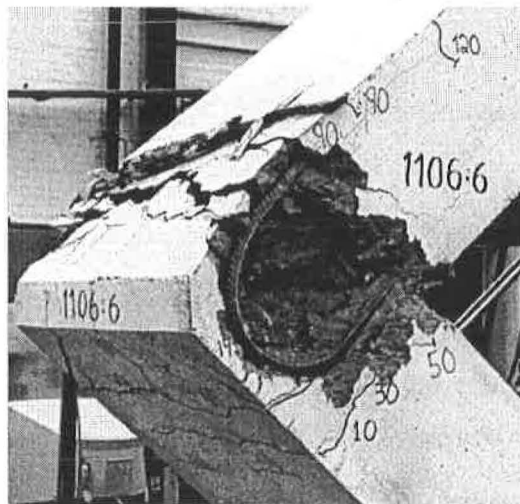


Figure 1.3      Spalling of the concrete cover using reinforcement loops. From Johansson (1996).

2

## 1.2 Aim of the Study

The aim of the study is to examine splicing of reinforcement loops in beams subjected to bending moments and shear forces. This research field shows a high complexity with various interacting influences. Consequently, it is necessary to focus on some aspects, which are to be elaborated:

- Examination of the behaviour of reinforcement loop splices in beams without a transverse reinforcement in the splice zone. Furthermore, the study is limited to the behaviour in the Ultimate Limit State.

- The flow of forces and the different failure modes when using loop splices. Therefore, a literature study of already conducted research work, a test series of four full-scale tests of beams with reinforcement loop splices and non-linear finite element analyses are carried out.

- The influence of varying splicing length and beam width. These influences are examined by means of the above-described full-scale tests and the former also by non-linear finite element analyses using two-dimensional models.

# 2 Loop splices in beams

## 2.1 Failure types

The advantage of loop splicing compared to straight splicing is the increased anchorage capacity due to the curved part of the loop. Knowing this, it is clear that there may exist failure modes different to those of a straight splice.

When bond and other mechanism for anchorage are acting, it is not correct to assume that the anchorage capacity can be calculated by adding the full capacities of the various mechanisms. Instead it is necessary to examine separately the different possible failure types.

Three different failure types can be distinguished when using spliced loops:

- Concrete tensile failure in form of splitting and bursting

- Bond failure due to slip between concrete and reinforcing bar

- Concrete crushing in virtue of pulverisation of the concrete surface that is in contact to the bend part of the bar.

The most dangerous failure type of loop splices in beams is the tensile failure in form of splitting and bursting. However, all failure types are caused or at least influenced by a radial pressure along the curved part, which balances the steel force that is turned round. Therefore, a theoretical consideration of the acting pressure is preceded.

If the steel stress along the half circle is known the magnitude of the pressure can be calculated by equation (2.1).

$$P = \frac{F_s}{r} \tag{2.1}$$

The geometry and the belonging notation are shown in Figure 2.1. The distribution of the steel stress along the bend can be seen in Figure 2.2.
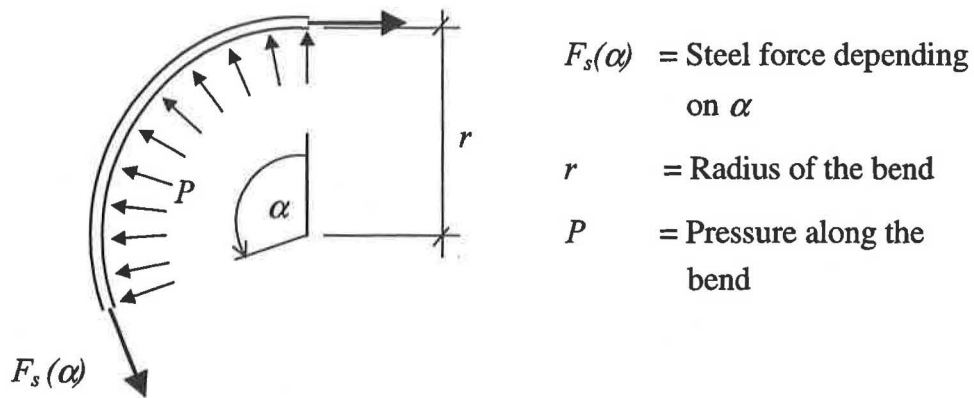
4

Figure 2.1    Geometry of the loop.

Thus, in the case of a splice that transfers mainly bending moments the radial pressure varies, as shown in Figure 2.2. Tests at hook splices by Franz and Timm (1972) resulted in steel stresses changing from tension at point B to compression at point C. Additionally, it was determined that such a stress distribution can be assured if the end of the hook is anchored in the compressive zone of the member.
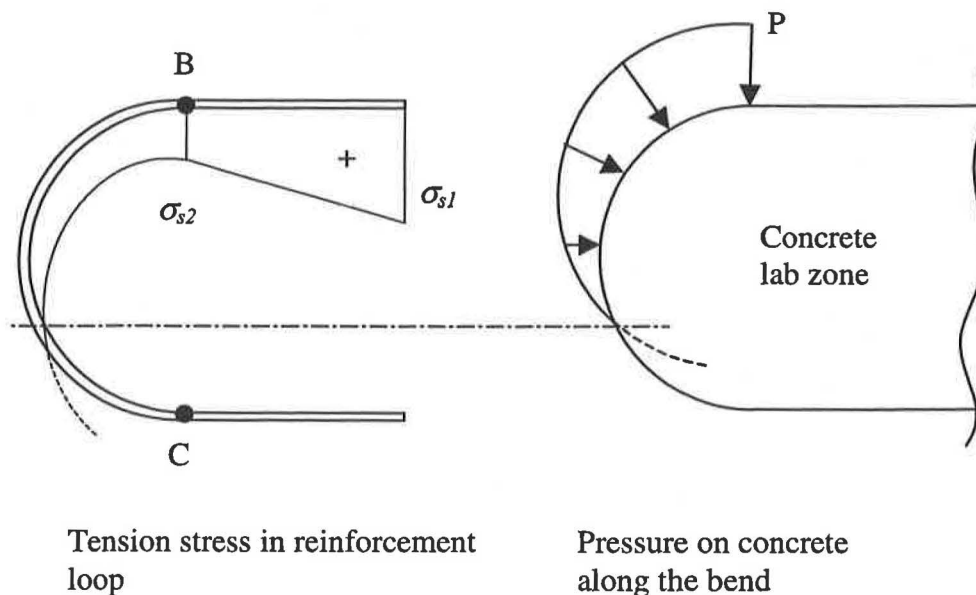


Tension stress in reinforcement         Pressure on concrete
loop                                     along the bend

Figure 2.2    Tensile stresses in the loop and resulting radial pressure along the bend
              for a member subjected to a negative bending moment.

5

## 2.1.1  Tensile failure

The most dangerous failure type is the tensile failure of the concrete in the splice zone. Different effects cause lateral tensile stresses in loop splices. However, tensile stresses out of the plane may cause spalling of the concrete cover, if the tensile strength of the concrete is exceeded and no lateral reinforcement provided.

The bend part of the loops introduces concentrated radial pressure, as shown in Figure 2.2. The pressures of one loop pair balance each other in longitudinal direction, as long as the steel stresses in the loops are equal, as shown in Figure 2.3. A tension field in the upper and a compressive stress field in the lower chord balance the acting moment due to the eccentricity of the pressures. Nevertheless, the magnitude of these stresses is small compared to the tensile stresses caused by the spread of the pressure.
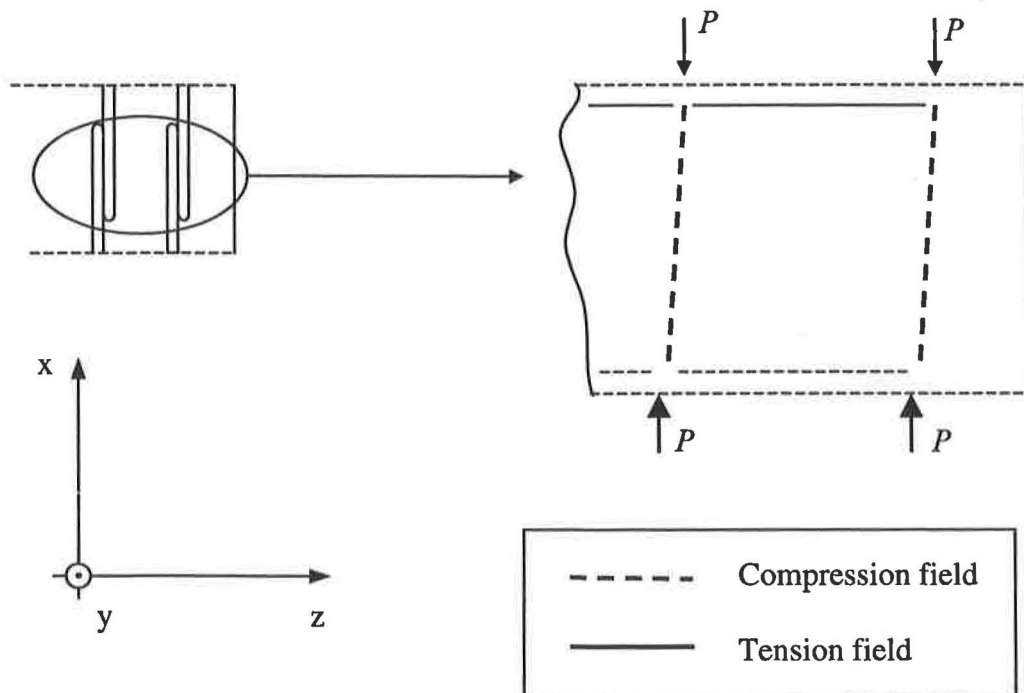


Figure 2.3     Balancing radial pressure on the concrete from the loop pairs. Top view.

The latter are shown in Figure 2.4. Hereby, two different regions can be distinguished. Nearby the acting pressure (region I) an tri-axial compressive stress state exists. This stress state may lead to a splitting failure of the concrete. In the other deeper region (region II) the distributed pressure leads to tensile stresses, which may cause bursting of the concrete. Hereby, the pressure is acting along the complete length of the bend with

6

varying magnitude. Therefore, the predominating stress state inside the loop consists of a superposition of the varying pressure distributions. However, if the splitting failure is considered to be the more dangerous tensile failure type, see Section 2.3.1, the effect of the superposition is negligible.
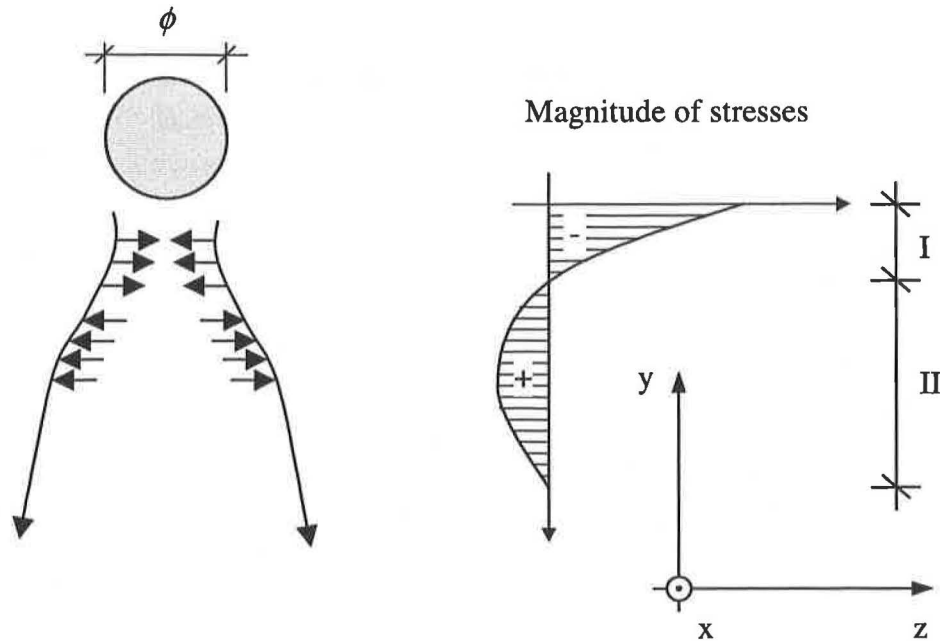


Figure 2.4    Stress field under concentrated load according to CEB-FIP Model Code, CEB (1993). The concentrated pressure spreads out in z-direction.

The tensile stresses acting out of the plane are a smaller problem at the inner parts of the structure where the confinement of the concrete is considerable larger.

However, a splitting failure between the loops of the edge-pair may cause spalling of the side concrete cover. This is the case if the tensile crack between the loops propagate outside the splice zone to the edge of the structure or is brought together with a flexure crack parallel to the splice zone. Both possibilities are illustrated in Figure 2.5. As a result, the anchorage capacity of the outer loops is lost.
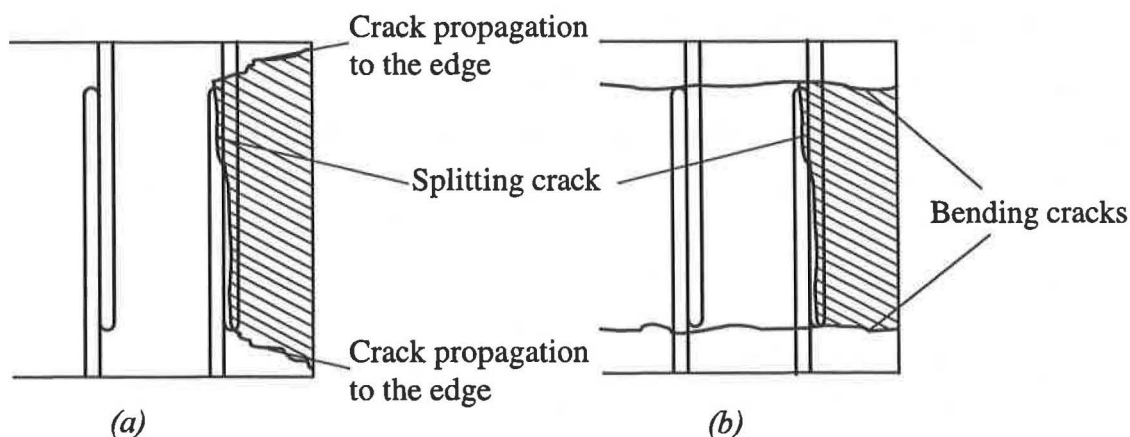
Figure 2.5      Possible crack patterns, which cause spalling of the concrete cover.

Hereby, the radial pressure due to the remaining loops is increased after the spalling failure. In other words, fewer loops have to transmit the same load. However, the confinement of the interior loops is larger and therefore a total splitting failure is delayed. Hence, the structural response close to the maximum load largely depends on the behaviour of the remaining loops.

Apart from the radial pressure, an additional effect may increase the acting tensile stresses. As mentioned, the steel stress varies along the curved part. Therefore, also the pressure along the bend varies. The sum of the pressure and the friction stresses caused by the pressure in vertical direction gives a resultant. This resultant has a lever arm to the centre line of the splice zone and can therefore be described as a torsional moment around the centre line of the splice zone, see Figure 2.6.

Apart from the concentrated radial pressure caused by the curved part, the bond forces between concrete and reinforcement along the complete length of the loop result in conical compressive shells, which are balanced by tensile stresses. Figure 2.7 shows a schematic diagram of the described phenomenon. These additional tensile stresses, which cause the splitting failure of a splice with straight bars, is in the case of loop splicing without a straight splice length of minor importance.
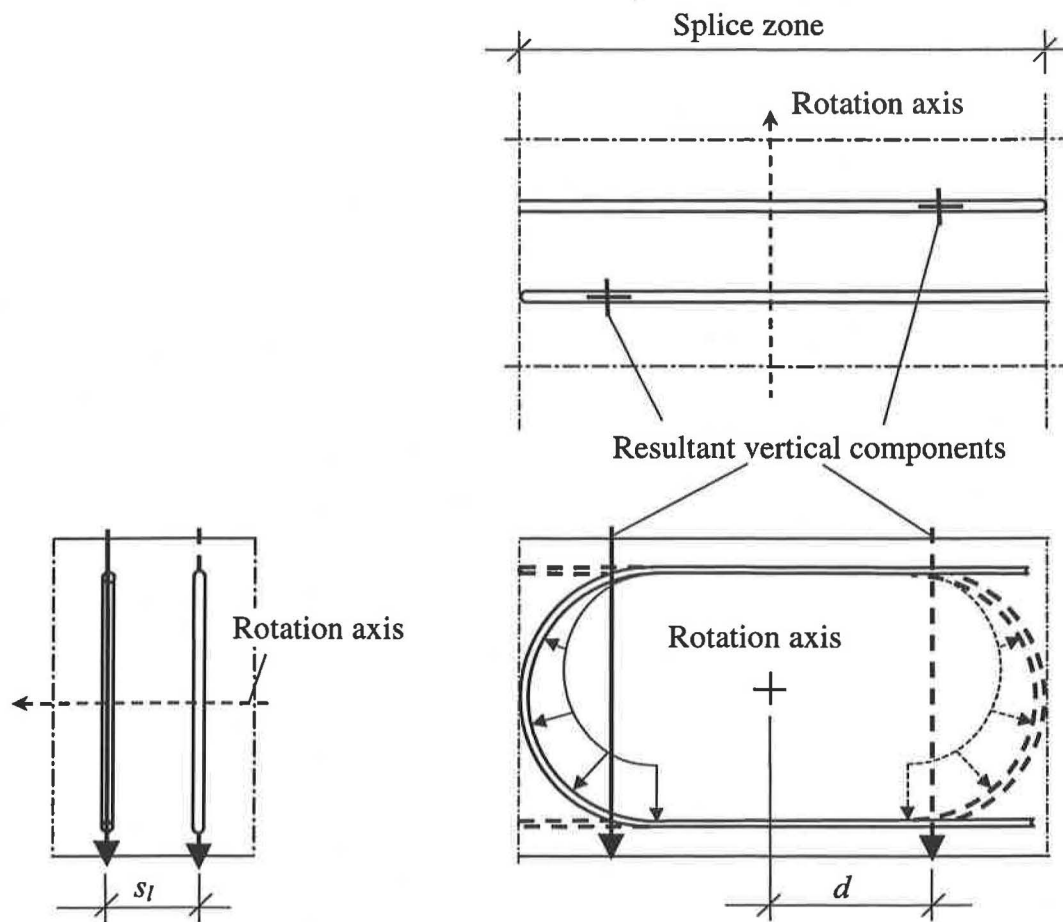
8

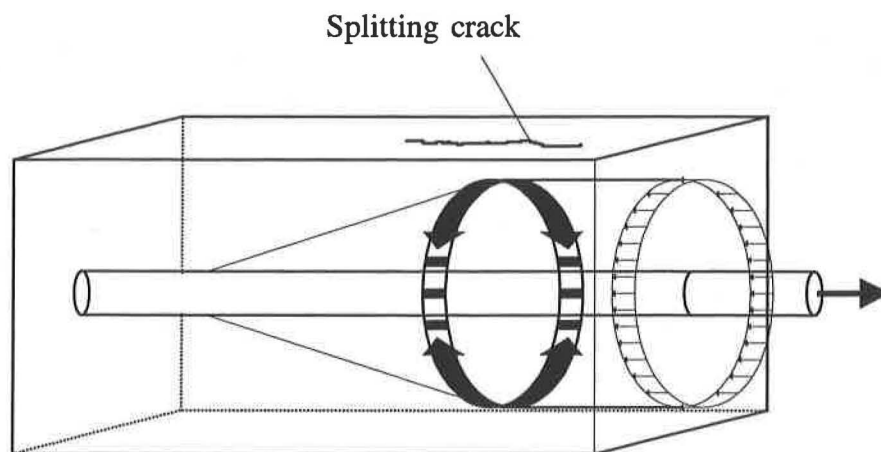Figure 2.6     Vertical resultants of the varying radial pressure



Figure 2.7     Three-dimensional model of inclined bond forces in space, which compose a conical compressive shell balanced by tensile stresses based on Tepfers (1973). From Magnusson (1997).

## 2.1.2 Bond failure

Another principal failure type is the bond failure between the reinforcement and the surrounding concrete. A bond failure occurs if the tensile force in the reinforcement exceeds the sum of the maximal bond stresses along the provided loop length and the friction stresses caused by the radial pressure along the curved part. The acting stresses are shown in Figure 2.8.

The bond stress is activated by a slip of the reinforcement bar in relation to the surrounding concrete. It can be distinguished in part due to the straight length, shown in equation (2.2) and a part due to the bend as seen in equation (2.3). A more thoroughly derivation of the expressions can be found in Appendix D.

$$\frac{d\sigma_s}{dx} = -\frac{\tau \cdot U_s}{A_s} \tag{2.2}$$

$$\frac{dF_s}{d\varphi} = -\left(\mu \cdot F_s + \tau \cdot U_s \cdot r\right) \tag{2.3}$$

where

$\mu$ = friction coefficient,
$U_s$ = bar perimeter,
$r$ = loop radius and
$\tau$ = bond stress

In case of a loop it is practically impossible to achieve a failure in form of a pull out, because the anchorage length of the bar is not limited.

However, a partly destruction of the bond can influence the load carrying behaviour in an unfavourable way. Especially, if the bond failure reaches into the compressive zone, the capacity of the section can be weakened. The positive effect of the compressive reinforcement may be lost and the concrete around the bar destroyed by inclined bond cracks. Furthermore, the bond behaviour influences directly the magnitude of the acting radial pressure.
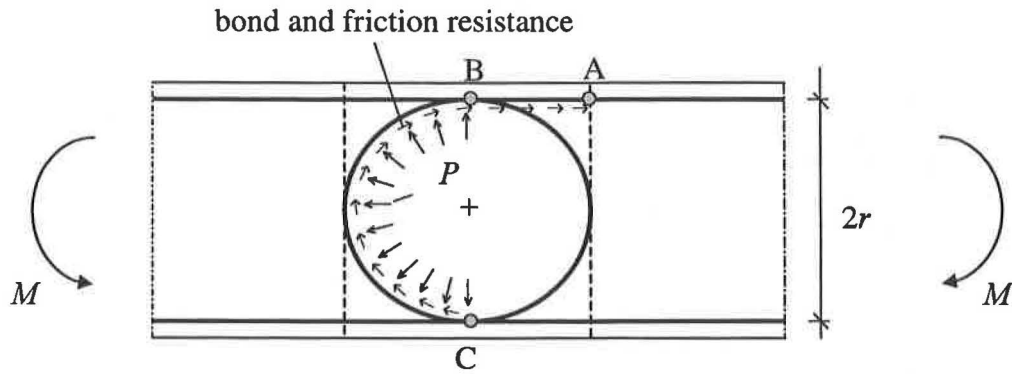
Figure 2.8    Bond and friction resistance of the loop

### 2.1.3  Surface crushing

If the loading area is very small compared to the surrounding unloaded region, the tri-axial stress under the loop may reach a magnitude at which pulverisation of the concrete may theoretically occur.

This pulverised concrete produces a hydrostatic stress state on the surrounded area that may cause wedging of the concrete surface, as shown in Figure 2.9. However, this failure type only occurs, if the loaded concrete region is almost completely confined, see Imran and Pantazopoulou (1996). Therefore, this type is less important in case of loop splices, where the confinement is usually weak.
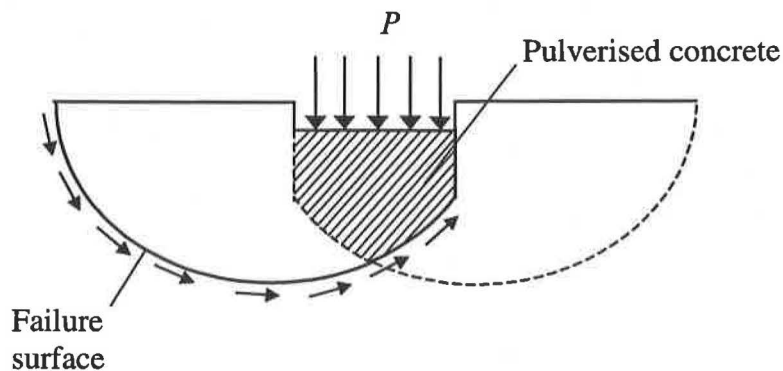


Figure 2.9    Surface crushing (Prandtl's wedge) according to CEB-FIP Model Code, CEB (1993).

## 2.2 Influencing parameters

The load capacity of a loop splice is influenced by several parameters concerning the arrangement of the reinforcement and the material properties. In the following list most of them are mentioned:

- Side concrete cover

- Splice length

- Width of the beam

- Spacing of the loops

- Loop radius

- Bar diameter

- Bond between reinforcement and concrete

- Type of loading in splicing zone

### 2.2.1 Side concrete cover

The side concrete cover $c$ is defined as the distance from the outer loop to the beam edge, see Figure 2.10. It contributes to the confinement of the concrete zone under radial pressure, which cause a lateral expansion of the concrete in the splice zone.

Three different test series carried out by Dragosavić *et al.* (1975), Franz and Timm (1972), and Kordina and Fuchs (1972), concerning loop and hook[1] splicing in slabs showed that an increased concrete cover has a favourable influence. The cracks between the loops of the outer pair, see Figure 2.5, are delayed by an increased concrete cover.

---

[1] The test series by Franz and Timm (1972) and Kordina and Fuchs (1972) examined splicing with large hooks. Their ends were anchored in the compressive zone of the member. Therefore, the behaviour of such hooks is similar to them of loops. Thus, the results of these tests are meaningful for the present study.
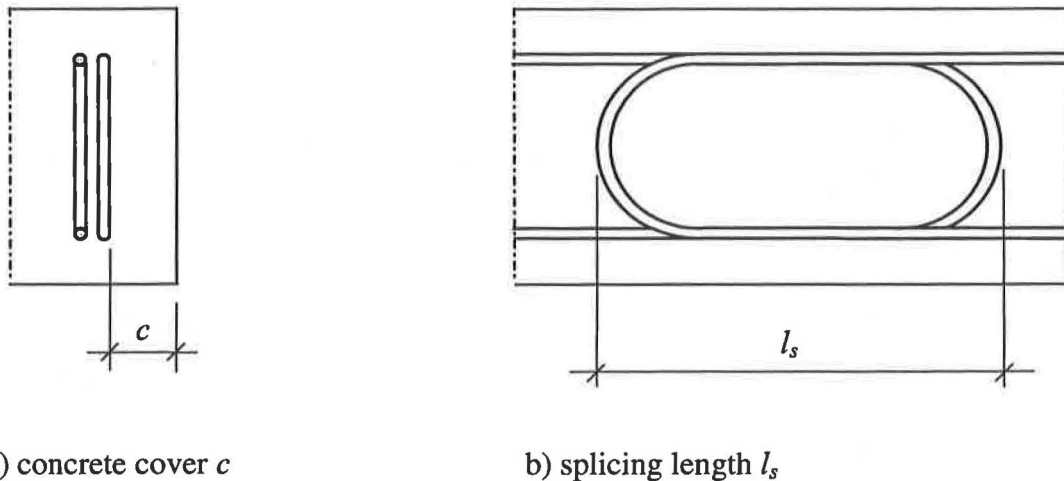
a) concrete cover $c$                          b) splicing length $l_s$

Figure 2.10    Definition of the concrete cover $c$ and splice length $l_s$

Without transverse reinforcement[2] the concrete cover spalls off and the anchorage of the outer reinforcement loops is lost. The presence of lateral reinforcement may resist the tensile stresses after cracking of the concrete between the loops and, thus prevent spalling of the outer loop. However, this lateral reinforcement has to be anchored in the concrete; something that might be difficult to achieve.

In the research work of Dragosavić *et al.* (1975) an empirical formula was proposed, see Section 2.3.4, in which the load capacity of a loop splicing can be estimated. In this formula the increasing edge distance has a favourable influence on the load capacity. However, the formula is mainly aimed for slabs. Therefore, it is difficult to estimate how far the results are compatible to beams.

## 2.2.2   Width of the beam

The width of the beam by constant reinforcement ratio has a considerable influence on the load capacity in case of spalling failure. After spalling of the outer loops the remaining have to bear the entire load. Consequently, the load capacity of a loop splicing increases with increased beam width.

---

[2] No lateral reinforcement is provided in the present test series.

13

### 2.2.3 Loop radius

The loop radius is one of the major factors whether spalling will occur or not. The pressure on the concrete in the splice zone is caused by the bend of the steel bar and depends directly on the radius of the loop, see Figure 2.1 and equation (2.1). The pressure can cause tensile failure or concrete crushing, as discussed in Section 2.1.1 and 2.1.3. Consequently, the risk of both failure types is decreased with increased loop radius. Moreover, the provided bond length is increased with increased radius.

### 2.2.4 Splice length

The splice length is defined as the distance between the vertexes of two overlapping loops in longitudinal direction, as shown in Figure 2.10. The minimum recommended length according to Franz and Timm (1972) and Kordina and Fuchs (1972) is the diameter of the loop. In this case two semi-circles compose the splice length. An increase of the splice length results in an additional straight part between the bends. Along the added part the stress in the reinforcement is decreased by the bond resistance, see Figure 2.8. Therefore, the steel stress where the bend begins is smaller than in the case of a minimum splicing length. Smaller steel stress results in smaller radial pressure on the concrete, as clarified in equation (1), which reduces the risk of a splitting failure.

Apart from the decrease in pressure, the splitting resistance is also increased by the increased angle between the loop axis and the compressive struts, see Figure 2.3. This means that more concrete is provided on which the tensile forces can be distributed, see Kordina and Fuchs (1972). However the larger concrete area has only an influence regarding bursting as further described in Section 2.11. The above-described decrease results also in a smaller friction resistance, which has a slightly unfavourable influence, see Appendix 11. However, the positive factor of the additional straight bond length is more decisive. The tensile stresses due to the torsional stresses, as shown in Figure 2.6, are both positive and negative affected by the splice length. On the one hand the increasing splice length enlarges the lever arm of the vertical forces and therewith also the torque. On the other hand the vertical forces are reduced by the pressure decrease. Furthermore, the concrete core, which has to resist the torque, is increased.

14

### 2.2.5  Bar diameter

An increased bar diameter can transmit larger forces, which result in a higher radial pressure along the bend. Both the risk of surface crushing and tensile failure increase, see Section 2.1. In addition, a large diameter has a smaller ratio of perimeter to cross-section, which results in a smaller bond resistance. However, the chosen diameter depends on the spacing of the loop pairs. With increasing loop spacing the bar has to be enlarged to provide the same load capacity.

### 2.2.6  Spacing of the loops

Two different types of spacing can be distinguished:

- Spacing of the loop pairs, $s_{lp}$

- Spacing of the loops in a pair, $s_l$

The spacing of the loop pairs $s_{lp}$ is defined as the distance between the axes of two neighbouring pairs, as shown in Figure 2.11. If not otherwise mentioned the term loop spacing refers to the spacing of the loop pairs $s_{lp}$.
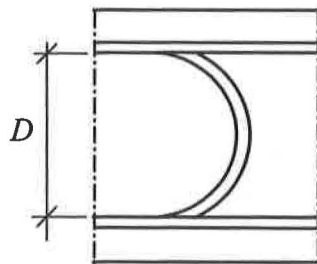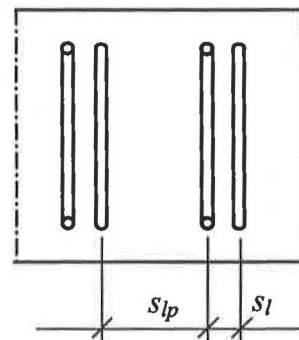


a) Mandrel diameter $d$                b) Spacings of loops $s_{lp}$ and $s_l$

Figure 2.11   Definition of mandrel diameter $D$, spacing of loop pairs $s_{lp}$ and spacing of loops $s_l$.

After spalling failure of the outer loop pair the spacing $s_{lp}$ is the new "side concrete cover", which contributes to resist the tensile failure, see Section 2.1.1. Thus, a small spacing of the loop pairs can increase the risk of a chain reaction of spalling failures.

The spacing of the loops of a pair is defined as the distance between the bar axes of the two overlapping loops, see Figure 2.11. An increased distance has both positive and negative effects. With increasing spacing the eccentricity of the concentrated radial pressure increases. Therefore, the angle between the loop axis and the compressive field decreases, see Figure 2.3. As a result, larger tensile forces have to be resisted and the risk of splitting failure rises. However, a contact of the loops may have a slight unfavourable influence on the bond strength, especially if the loop has a long straight splice length, which results in a long contact length of the loops. In the tests carried out by Kordina and Fuchs (1972) it was observed, that the spacing of the loops inside the pair has a hardly noticeable effect on the load capacity. However, a distance of $5\phi$ had a slightly unfavourable influence on the crack development[3] compared to a distance of $2\phi$.

## 2.2.7   Bond between reinforcement and concrete

The bond stress transfers the tensile stresses from the reinforcement to the surrounding concrete. It is an important factor as it compose the anchorage capacity of the loop. The bond stress is activated by a slip of the reinforcement bar in relation to the concrete. According to Magnusson (1997), the bond resistance is composed by three components:

- Adhesion,

- Friction and

- Mechanical interaction of the reinforcement ribs and the concrete, see Figure 2.12.

---

[3] The crack width concerning Serviceability requirements is in the present study of minor concern. Nevertheless, the crack development leads often to conclusions about the failure type.
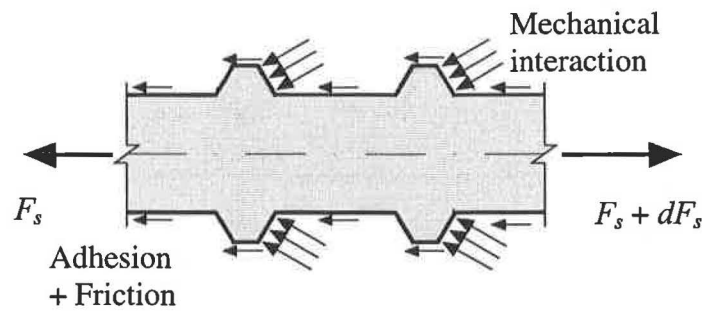
Figure 2.12    Contact stresses on a deformed bar embedded in concrete. Adhesion and friction are idealised by the longitudinal arrows and mechanical interaction of the reinforcement ribs and the concrete by the inclined arrows. Modified from Plos (1996).

With increasing slip the contribution of adhesion and friction is lost and the mechanical interaction represents the bond strength.

However, the bond stress is not only depending on the slip of the reinforcement, but on several properties of the structure, for instance the way of casting, the present confinement and the behaviour of the reinforcement, see Lundgren (1999).

For a loop splice in which the anchorage length may be composed by a straight and curved part a high bond strength increases the anchorage capacity since the tensile stress at the beginning of the loop is further reduced and a splitting crack due to the curved part is delayed.

## 2.2.8    Type of loading

Reinforcement splices in concrete structures are mostly subjected to a combination of bending moments and shear forces. Especially in frames it can be required to transmit large shear forces. However, the failure modes described in Section 2.1 are all related to splices subjected to moments. In test series by Dragosavić *et al.* (1975) and Kordina and Franz (1972) no influence of shear could be observed. Both studies analysed four- and three-point set-ups. However, the transmitted shear in the three-point set-ups used in the above described tests was relative small, so that these results can give only limited conclusion about the influence of shear forces, see Kordina and Franz (1972). Thus, it is not examined in what way a loop splice is influenced by a large shear transfer. In the test series presented in this report the influence of shear in the splice zone was further

investigated, see Section 3. Hence, the test set-up was designed so that the loop splices were subjected to a moment and a high shear force.



a) Three-point loading          b) Four-point loading
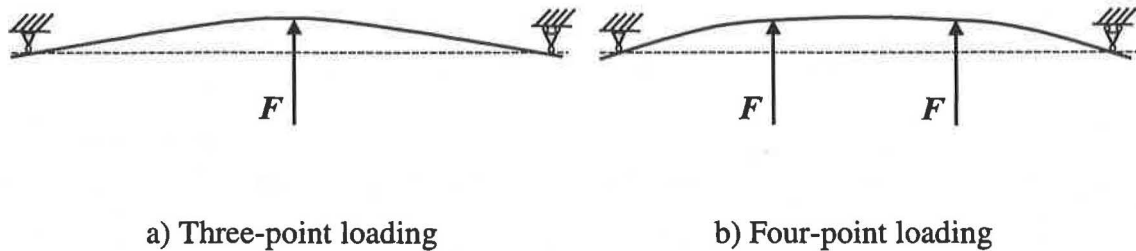
Figure 2.13    Two different loading arrangements: Three-point loading with varying moment and four-point loading with constant moment in the splice region.

## 2.3    Design approaches

There are several design approaches dealing with the design of reinforcement splicing. Four of them are described in the following sections. Except the Committee B7 formula, see Dragosavić *et al.* (1975), the design approaches are aimed on splicing of straight bars and deal with loop splices as a modification of a straight splice.

### 2.3.1    CEB-FIP Model Code 1990

Two main steps compose the design approach of the CEB-FIP Model Code, CEB (1993) concerning loop splices:

- Determination of the required splice length

- Limitation of the mandrel radius.

The former step assures the transfer of tensile stresses from one loop to the other and the latter that rupture of the reinforcement or spalling of the concrete cover is avoided.

The splice length depends on the basic anchorage length. The basic anchorage length is defined as the length of the reinforcement bar, which is needed to transfer the steel force of the bar to the surrounding concrete at yield strength. This stress transfer depends on

the activated bond strength. The design bond strength is calculated by means of the design tensile strength of the concrete as

$$f_{bd} = \eta_1 \cdot \eta_2 \cdot \eta_3 \cdot f_{ctd} \quad \text{with} \quad f_{ctd} = \frac{f_{ctk,\min}}{1.50} \tag{2.4}$$

where

$\eta_1$ considers the surface type of the reinforcement $\qquad \eta_1 = 2.25$ for ribbed bars

$\eta_2$ considers the bond conditions due to casting $\qquad \eta_2 = 1.0$ for good bond conditions,

$\qquad\qquad\qquad\qquad\qquad\qquad\qquad\qquad\qquad\qquad \eta_2 = 0.7$ in all other cases

$\eta_3$ considers the bar diameter $\qquad\qquad\qquad\qquad \eta_3 = 1.0$ for $\phi \le 32$ mm,

$$\eta_3 = \frac{132 - \phi}{100} \text{ for } \phi > 32 \text{ mm}$$

$f_{ctk,\min}$ $\qquad\qquad$ is the characteristic minimum tensile strength of concrete

The basic anchorage length $l_b$, which is required to transfer the yield force of a bar, is calculated by force equilibrium

$$l_b \cdot \phi \cdot \pi \cdot f_{bd} = \frac{\phi^2}{4} \cdot \pi \cdot f_{yd} \tag{2.5}$$

as

$$l_b = \frac{\phi}{4} \cdot \frac{f_{yd}}{f_{bd}} \tag{2.6}$$

where $\phi$ is the bar diameter and $f_{yd}$ the reinforcement yield strength.
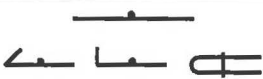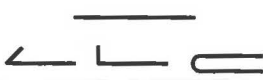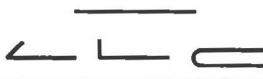
With the basic anchorage length the design splice length $l_s$ is calculated as

$$l_s = \alpha_1 \cdot \alpha_2 \cdot \alpha_3 \cdot \alpha_4 \cdot \alpha_5 \cdot \alpha_6 \cdot l_b \cdot \frac{A_{s,cal}}{A_{s,ef}} \ge l_{s,\min} \tag{2.7}$$

where

19

$\alpha_1$     considers the form of the splice;

$\alpha_2$     considers the influence of welded transverse bars along the anchorage length;

$\alpha_3$     considers the confinement due to the concrete cover;

$\alpha_4$     considers not welded transverse bars;

$\alpha_5$     considers the confinement due to a transverse pressure; and

$\alpha_6$     considers the percentage of the spliced reinforcement within $1.3 \cdot l_s$ from the centre of the splice length.

$A_{s,cal}$   calculated reinforcement amount

$A_{s,ef}$   chosen reinforcement amount

Table 2.1     Alfa coefficients for the calculation of the design splicing length.

| Influencing factor | Type of anchorage | Alfa coefficient |
|---|---|---|
| Form of bars | ——— | $\alpha_1 = 1.0$ |
| | (bent bars) | $\alpha_1 = 0.7$ |
| Welded transverse bars | (welded transverse bars) | $\alpha_2 = 0.7$ |
| Confinement by concrete [1] | ——— | $\alpha_3 = 1 - 0.15\dfrac{c_d - \phi}{\phi} \begin{cases} \geq 0.7 \\ \leq 1.0 \end{cases}$ |
| | (bent bars) | $\alpha_3 = 1 - 0.15\dfrac{c_d - \phi}{\phi} \begin{cases} \geq 0.7 \\ \leq 1.0 \end{cases}$ |
| Confinement by not welded transverse reinforcement [2] | (bent bars) | $\alpha_4 = 1 - k \cdot \lambda \begin{cases} \geq 0.7 \\ \leq 1.0 \end{cases}$ |
| Confinement by transverse pressure | (bent bars) | $\alpha_5 = 1 - 0.04 p \begin{cases} \geq 0.7 \\ \leq 1.0 \end{cases}$ |

[1] $c_d = \min(a/2, c)$.

[2] $\lambda = (\Sigma A_{st} - \Sigma A_{st,min})/A_s$, where

$\Sigma A_{st}$         is the cross-sectional area of the transverse reinforcement along the splice length $l_s$, and

$\Sigma A_{st,min}$     is the area of the minimum transverse reinforcement ($1.0\,A_s$) for splices in beams.

The notation for the definition of $c_d$ can be found in Figure 2.14 and the different values for $k$ in Figure 2.15.
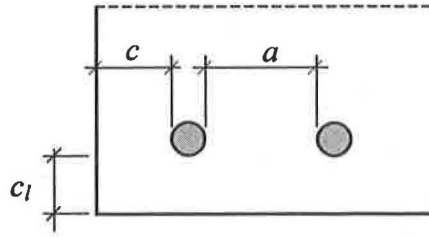
Figure 2.14    Notation for the definition of $c_d$.
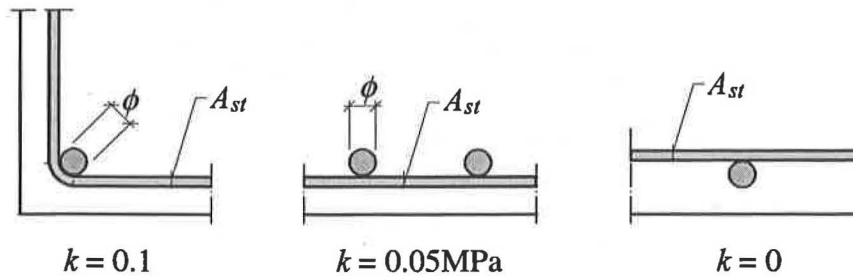


Figure 2.15    k-values for the calculation of $\alpha_4$.

The limitation of the mandrel diameter $D$ is not explicitly evaluated in the CEB-FIP Model Code. However, two conditions have to be kept. The steel bar shall not fail or crack due to bending. Therefore, the minimum mandrel diameter $D$ depends on the plastic uniform elongation under flexural conditions.

Furthermore, crushing or splitting of the concrete shall be avoided under Ultimate Limit State conditions. A calculation approach for this case is implied. Thereby, the minimum mandrel radius depends on the resistance of the splicing zone against splitting failure. The splitting failure may be caused by the triaxial compressive state under the radial pressure inside the bend. The varying radial pressure is simplified into a constant pressure in longitudinal direction along the half of the mandrel diameter, as shown in Figure 2.16.

21

$$A_c = \frac{D \cdot \phi}{4}$$

$$D + c + \frac{3}{2} \cdot \phi$$

$$A_c^{'} = \left( D + c + \frac{3}{2} \cdot \phi \right) \cdot \left( c + \frac{\phi}{2} \right)$$
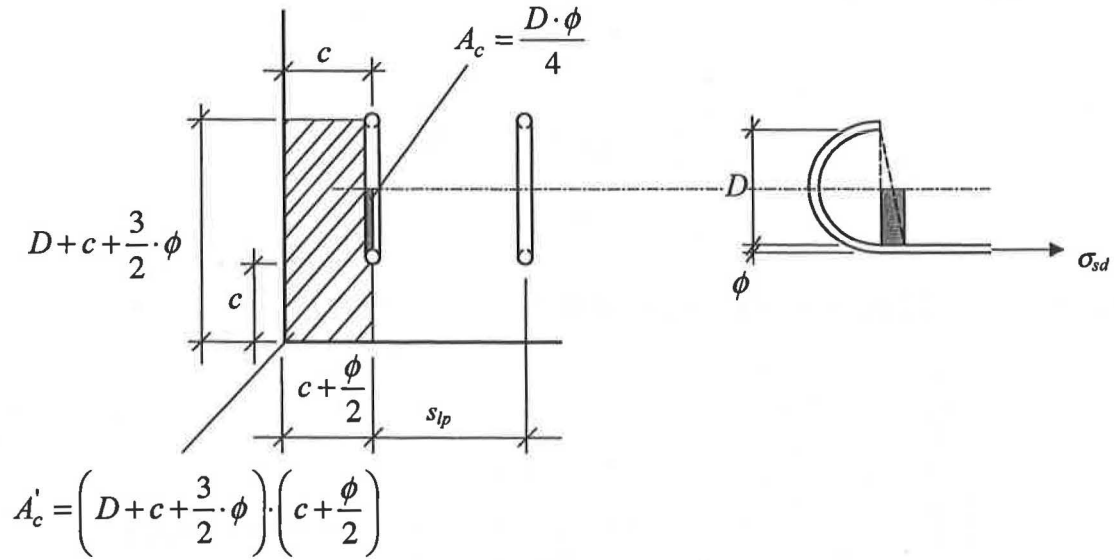
Figure 2.16   Simplified model of the acting forces along the bend. Based on the CEB-FIP Model Code, CEB (1993).

The maximum radial pressure without causing a splitting failure is estimated by equation (2.8).

$$f_{cd}^{*} = f_{cd} \cdot 0.7 \cdot \sqrt{\left( \frac{A_c^{'}}{A_c} \right)}$$  (2.8)

The force equilibrium in longitudinal direction in equation (2.9) determines the allowable mandrel diameter, which depends mainly on

- steel stress $\sigma_{sd}$,

- concrete strength $f_{cd}$,

- the bar diameter $\phi$, and

- relation of loaded area $A_c$ to unloaded area $A_c^{'}$.

$$0.5 \cdot D \cdot f_{cd}^{*} = \frac{\pi \cdot \phi^2}{4} \cdot \sigma_{sd}$$  (2.9)

Further simplifications lead to a practicable design formula:

$$\frac{D}{\phi} \approx \frac{\delta}{\sqrt{1+2 \cdot \dfrac{c}{\phi}}} \cdot \frac{\sigma_{sd}}{f_{cd}} \qquad (2.10)$$

The different values for $\delta$ are shown in Figure 2.17



(a) $\delta \cong 1.6$        (b) $\delta \cong 1.8$        (c) $\delta \cong 2.6$
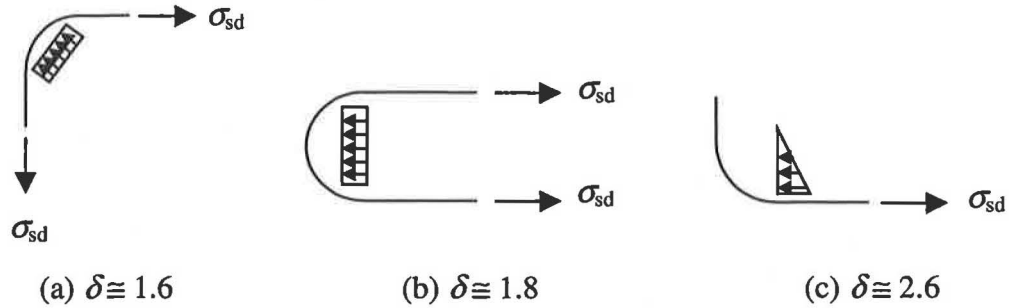
Figure 2.17    $\delta$-values for various anchorage schemes according to CEB-FIP Model Code, CEB (1993).

## 2.3.2   Eurocode 2

The design approach for loop splices in EC 2 is similar to the one in the CEB-FIP Model Code.

- Splice length and
- mandrel diameter

have to be checked. The calculation of the design bond strength $f_{bd}$ and the basic anchorage length $l_b$ is identical to the one in CEB-FIP Model Code.

The required splice length is calculated with equation (2.11)

$$l_s = l_b \cdot \alpha_a \cdot \alpha_1 \cdot \frac{A_{s,req}}{A_{s,prov}} \geq l_{s,min} \qquad (2.11)$$

with

$$l_{s,min} = 0.3 \cdot \alpha_a \cdot \alpha_1 \cdot \frac{A_{s,req}}{A_{s,prov}} \geq 15 \cdot \phi \geq 200 \, \text{mm} \qquad (2.12)$$

23

$\alpha_a$    considers the form of the bars          $\alpha_a = 0.7$ for curved bars in tension if the concrete cover perpendicular to the curved part is at least $3\phi$

$\alpha_a = 1.0$ for straight bars

$\alpha_l$    considers the percentage of spliced bars, which are lapped in the section and the provided confinement due to the concrete cover ($\alpha_1 = 2$ if more than 30 % of the loops are spliced in the section and the concrete cover is smaller than $5\phi$)[4].

Furthermore, it is required to provide a transverse reinforcement inside the splice zone. With this transverse reinforcement a spalling of the side concrete cover shall be avoided.
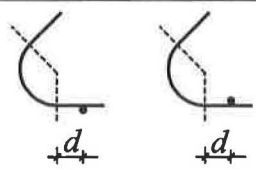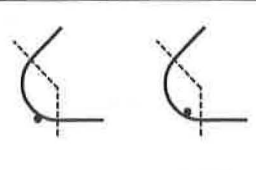
The mandrel diameter $D$ is limited to avoid cracking of the reinforcement bar due to bending and splitting or crushing of the concrete inside the bend of the bar. In Table 2.2 and 2.3 minimum mandrel diameters are given. The limitations consider the formability of the reinforcement bar (on the left side of Table 2.2) and the resistance of the concrete zone inside the bend against crushing and splitting (on the right side of Table 2.2).

Table 2.2    Minimum mandrel diameter.

| | Hooks, bends, loops | | Bent-up bars or other curved bars | | |
|---|---|---|---|---|---|
| | Bar diameter | | Value of the minimum concrete cover, perpendicular to plane of curvature | | |
| | $\phi < 20\,mm$ | $\phi \geq 20\,mm$ | $> 100\ mm$ and $> 3\cdot\phi$ | $> 50\,mm$ and $> 3\cdot\phi$ | $\leq 50\,mm$ and $\leq 3\cdot\phi$ |
| Plain bars S 200 | $2.5\cdot\phi$ | $5\cdot\phi$ | $10\cdot\phi$ | $10\cdot\phi$ | $15\cdot\phi$ |
| High bond bars S 400, S 500 | $4\cdot\phi$ | $7\cdot\phi$ | $10\cdot\phi$ | $15\cdot\phi$ | $20\cdot\phi$ |

---

[4] For detailed description of the values of $\alpha_1$ see EC2, 5.2.4.1.3.

Table 2.3    Minimum mandrel diameter in case of welds in the bend zone.

| Minimum diameter of the mandrel | |
| --- | --- |
| Welds outside bends | Welds inside bends |
|  |  |
| $d < 4 \cdot \phi$:  $20 \cdot \phi$ <br> $d \geq 4 \cdot \phi$:  Table 1 applies | $20 \cdot \phi$ |

### 2.3.3  Swedish Code (BBK 94)

The design concept in the Swedish Handbook for Concrete Structures BBK 94, Boverket (1994) concerning the splice length of deformed and bend bars is different to the former. The design method for straight part of the loop is based on the splitting method according to Tepfers (1973). Hereby, the splice capacity is limited by a splitting failure of the concrete cover, see Figure 2.7. Different possible crack patterns are shown in Figure 2.18, where primary and final cracks can be distinguished. It is assumed that the primary cracks reached the reinforcement bar and a new equilibrium can be established. The final splitting cracks cause the loss of anchorage capacity for the reinforcement bars. Therefore, the capacity is determined by the length of the final cracks, $u$, and the number of affected bars, $n$. The decisive crack pattern is the one with the smallest ratio, $u/n$. The anchorage capacity is calculated by

$$s_b = \eta \cdot 2.3 \cdot \frac{u}{n} \cdot f_{ct} \tag{2.13}$$

as the maximum transferable tensile force rate with an upper limit of

$$s_b < \eta \cdot 15 \cdot \phi \cdot f_{ct} \tag{2.14}$$

The coefficient, $\eta$, takes into account the position at casting and a possibly unfavourable multi-axial stress state.
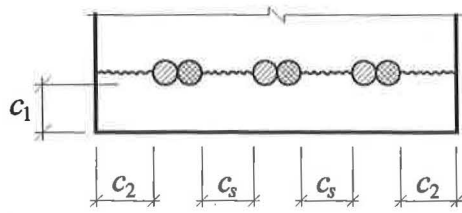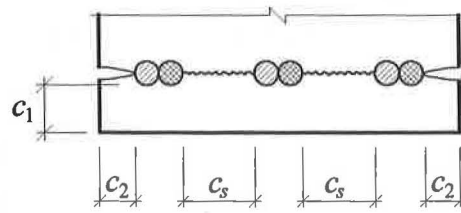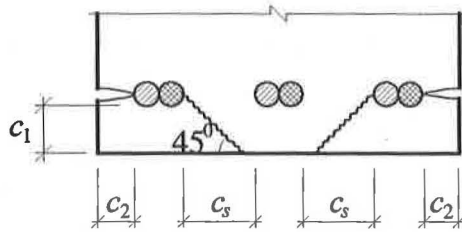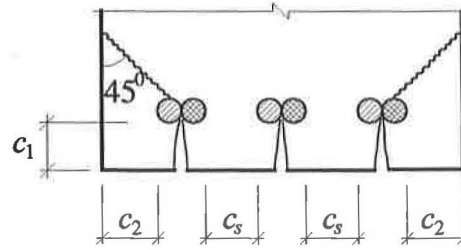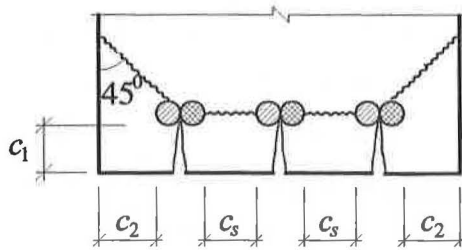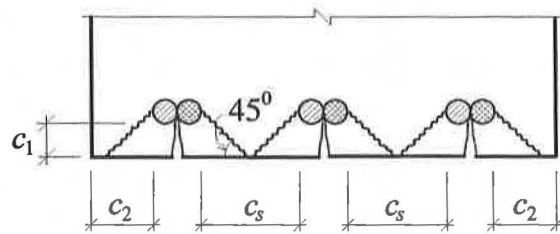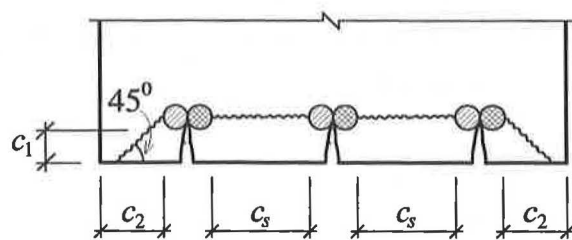
Figure 2.18    Splitting crack patterns, according to Tepfers (1973). From Magnusson (1997).

A lateral reinforcement in form of stirrups is considered by an additional part, which may be added to the splice capacity:

$$\Delta s_b = \frac{k \cdot \pi \cdot A_{st}}{s} \tag{2.15}$$

with a coefficient $k$ depending on the arrangement of the transverse bars as shown in Figure 2.19.



$$k = 40 \text{ MPa} \qquad k = 20 \text{ MPa} \qquad k = 0$$
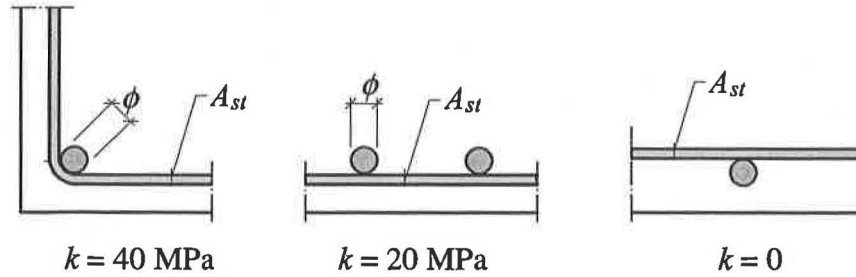
Figure 2.19  Factor $k$ depends on the arrangement of the transverse bars.

The final anchorage capacity can then be expressed as

$$S_b = s_b + \Delta s_b \tag{2.16}$$

with an upper limit of

$$s_b < \eta \cdot 15 \cdot \phi \cdot f_{ct} \tag{2.17}$$

The mandrel radius is limited by means of an empirical formula to avoid rupture of the reinforcement and spalling of the concrete cover

$$\frac{r}{\phi} \geq 0.028 \cdot \frac{f_{st}}{f_{ct}} - 0.5 - \frac{1}{\sin\left(\dfrac{\beta}{2}\right)} \cdot \left(\frac{c}{\phi} + 0.5\right) \tag{2.18}$$

with $\beta = \pi$ in case of a loop and an upper limit of

$$\frac{c}{\phi} \leq 3.5 \tag{2.19}$$

In frame corner tests carried out by Johansson (1996) the limitation of the mandrel radius according to BBK 94 was fullfilled and still resulted in spalling of the side concrete cover.

### 2.3.4 Committee B7 formula

Investigations concerning loop connections by Dragosavić *et al.* (1975) led to an empirical formula, which is presented in equation (2.20). The formula is aimed on loop connections of pre-cast slabs, which are subjected by flexural bending. The experiments for this research work were conducted by the Committee B7 of the Institute TNO for Building Materials and Building Structures (IBBC). Furthermore, earlier tests performed by Franz and Timm (1972) and Kordina and Fuchs (1972) were considered in the investigation.

$$\sigma_s = 230 \cdot f_{ct} \cdot \left( 0.7 + 0.03 \cdot \frac{l_s}{\phi} \right) \cdot \left( 1 + 0.25 \cdot \frac{A_{st}}{A_s} \right) \cdot \alpha \qquad (2.20)$$

with

$$\alpha = \left( 0.5 + 0.05 \cdot \frac{c}{\phi} \right) \leq 1.0$$

The loop moment can be calculated by means of Equation (2.21) or (2.22)[5]

$$M = n \cdot A_s \cdot z \cdot \sigma_s^* \qquad (2.21)$$

or

$$M = (n - 2) \cdot A_a \cdot z \cdot \sigma_{al}^* \quad^6 \qquad (2.22)$$

with

$$\sigma_s^* = 230 \cdot f_{ct} \cdot \left( 0.7 + 0.03 \cdot \frac{l_s}{\phi} \right) \cdot \left( 1 + 0.25 \cdot \frac{A_{st}}{A_s} \right) \qquad (2.23)$$

---

[5] Equation (2.21) and (2.22) are only valid if the additional conditions are met.

[6] Equation (2.22) is only valid if the distance between the loop pairs is greater than $20 \cdot \phi$.

Additional conditions :

$$l_s - 2 \cdot \phi \geq 10 \cdot \phi$$

$$l_s - 2 \cdot \phi \geq 2 \cdot R$$

$$D \geq 5 \cdot \phi$$

$$c \geq 5 \cdot \phi$$

$$s_l \leq \tfrac{1}{3} \cdot (l_s - 2 \cdot \phi)$$
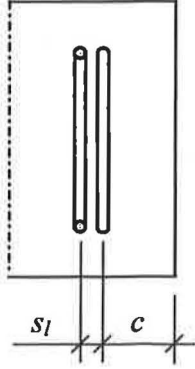


a) concrete cover $c$ and  
loop spacing $s_l$
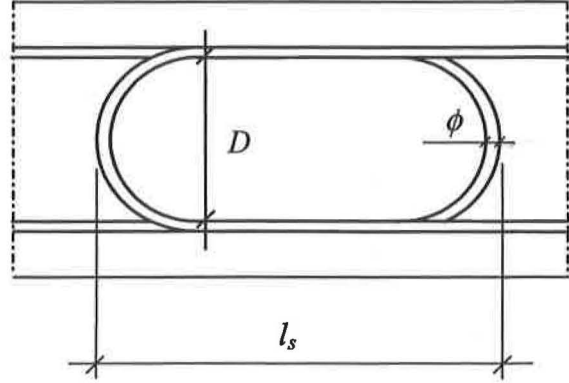
b) splice length $l_s$ and mandrel  
diameter $D$

Figure 2.20    Notation of the additional conditions of equation (2.22) and (2.23).

In a schematic way the formula (13) can be written as

$$\sigma_s = 230 \cdot a \cdot b \cdot c \cdot d \qquad (2.24)$$

The coefficient $a$ considers the influence of the edge concrete cover as confinement by

$$a = \left( 0.5 + 0.05 \cdot \frac{c}{\phi} \right) \leq 1.0 . \qquad (2.25)$$

Hence, according to this expression, an edge concrete cover larger than $10\phi$ has no further influence on the calculated strength of the loop splicing.

- The coefficient $b$ introduces the influence of the lab length by the factor

$$b = 0.7 + 0.03 \cdot \frac{l_s}{\phi} \qquad (2.26)$$

29

- The influence of the lateral reinforcement[7] is represented by the factor $c$ as

$$c = \left(1 + 0.25 \cdot \frac{A_{st}}{A_s}\right)$$ (2.27)

- The concrete strength is considered by means of the factor $d$

$$d = f_{ct}$$ (2.28)

---

[7] The interaction of the lateral reinforcement and the anchorage capacity of the concrete cover are not considered in this expression.

# 3 Experiments

The aim of the test series was to investigate the behaviour of reinforcement loop splicing in beams without a lateral reinforcement in the splice zone. Hereby, the influence of beam width and splice length was evaluated.

The present series included four reinforced concrete beams. In Specimen RV12 the spliced loops composed a circle. In specimen RV13 the splice length and in specimen RV14 the beam width was elongated. Specimen RV15 was provided with straight reinforcement bars without splicing. A detailed description of the specimens is given in Section 3.2 and Appendix A.

## 3.1    Material properties

### 3.1.1    Concrete

A concrete of a strength class of K35 according to Swedish standard with a mean cylinder compressive strength of $f_{cm}$ = 33 MPa was ordered. This strength is comparable with a strength class between C20/25 and C30/37 according to Eurocode 2, ENV (1992-1-1). However, the delivered concrete had a strength of $f_{cm}$ = 28 MPa, which was considerably smaller. The material properties cylinder compressive strength, cube compressive strength and Young's modulus in compression were determined in the laboratory of Structural Engineering at Chalmers University of Technology according to Swedish Standard, Byggstandardiseringen (1997). Additionally, the fracture energy was determined by SP, Swedish National Testing and Research Institute, according to RILEM's recommendations, see RILEM 50-FMC (1985). All test specimens were casted out of one batch. The concrete composition can be found in Table 3.1 and an evaluation of the grading of the aggregates in Appendix B.

The results of the material tests at an age of 28 days and testing day (36 days) are listed in Table 3.2. Further information about the material tests can be found in Appendix B.

Table 3.1     Composition of the concrete mixture used for the specimens.

| Constituents for RV12-15 | [kg/m$^3$] |
|---|---|
| Cement | 315 |
| Water | 198 |
| Sand | 907 |
| Crushed stones 8/16 | 941 |

Table 3.2     The properties of the concrete used in the test specimens (mean value of three specimens).

| Test specimen | 28 days | | | | Testing day (36 days) | | | | Fracture energy[1] [N/m] |
|---|---|---|---|---|---|---|---|---|---|
| | $f_{cc,cyl}$ [MPa] | $f_{cc,cube}$ [MPa] | $E_{c1}$ [GPa] | $E_{c2}$ [GPa] | $f_{cc,cyl}$ [MPa] | $f_{cc,cube}$ [MPa] | $E_{c1}$ [GPa] | $E_{c2}$ [GPa] | |
| RV12-RV15 | 27 | 36 | 24 | 25 | 28 | 38 | 25 | 26 | 113 |

[1]The fracture energy was determined after 28 days.

## 3.1.2  Reinforcement

The main reinforcement consisted of ribbed hot-rolled bars of type B500 BT, diameter 16 mm. Additionally, transverse reinforcement bars of the same type and a diameter of 10 mm were provided to facilitate the construction. The mechanical properties of the reinforcement, see Table 3.3, were determined by means of five tensile tests according to a standard procedure at Chalmers Structural Engineering Laboratory.

Table 3.3     Mechanical properties of the reinforcement, average of five tests.

| Specimen | $A_s$ [mm$^2$] | $f_{sy}$ [MPa] | $f_{su}$ [MPa] | $\varepsilon_{s1}$ [10$^{-3}$] | $\varepsilon_{sy}$ [10$^{-3}$] | $\varepsilon_{s2}$ [10$^{-3}$] | $\varepsilon_{su}$ [10$^{-3}$] | $E_s$ [GPa] |
|---|---|---|---|---|---|---|---|---|
| B500 BT | 201 | 543 | 649 | 2.6 | 3.3 | 27.3 | 120.4 | 199 |
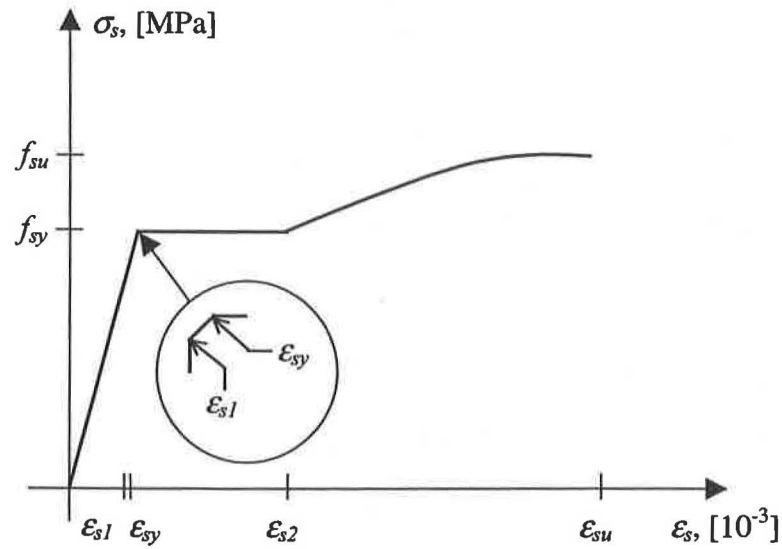
Figure 3.1    Notation for the reinforcement properties.

## 3.2    Test specimens

Four beams with different reinforcement arrangement were tested. In three of them loop splices were provided; the forth specimen was used as a reference and was reinforced with straight bars. The parameters varied were the splice length and the width of the beam. The overall dimensions are shown in Figure 3.2 and a comparison of the parameters in Table 3.4. A more detailed presentation of the dimensions can be found in Appendix A.
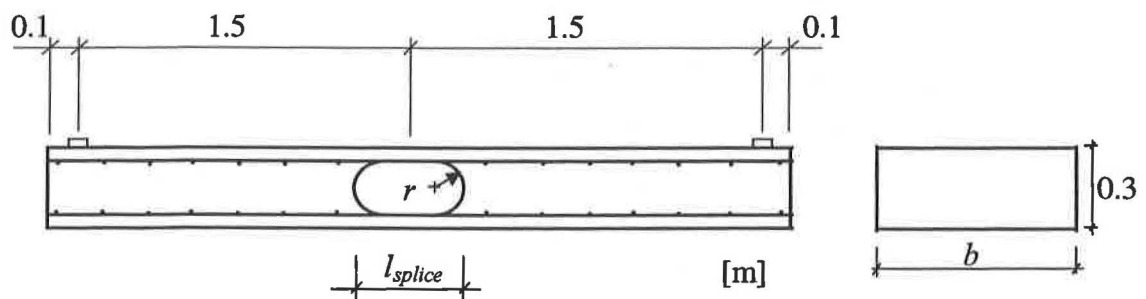


Figure 3.2    Overall dimensions of the test specimens. The belonging dimensions for the different variations are shown in Table 3.4.

Table 3.4    Parameters that were varied in the experiments.

| Specimen | $b$ [mm] | $l_{splice}$ [mm] | $r$ [mm] | $A_s$ | $\rho$ [%] |
|----------|----------|-------------------|----------|--------|------------|
| RV12 | 600 | 220 | 110 | 7$\phi$16 | 0.88 |
| RV13 | 600 | 600 | 110 | 7$\phi$16 | 0.88 |
| RV14 | 1200 | 220 | 110 | 14$\phi$16 | 0.88 |
| RV15 | 600 | --- | --- | 7$\phi$16 | 0.88 |

In specimen RV12 the loop splice was composed by two semi-circles, which were overlapped in the middle of the beam and showed the same detailing as used in the frame corner tests conducted by Johansson (1996).

In beam RV13 the splice length was elongated in accordance with the Swedish Shelter Regulations, Swedish Rescue Services Agency (1998), so that the influence of an additional straight splice length was investigated.
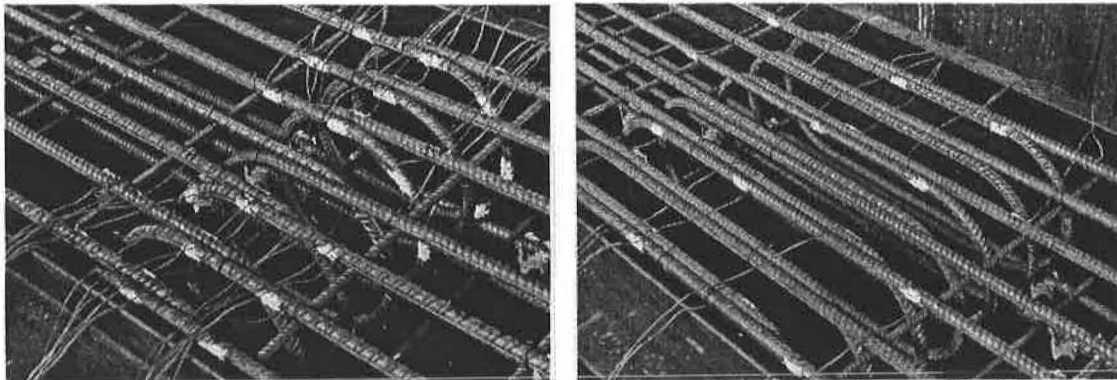


Figure 3.3    Loop arrangement in specimen RV12 and RV13.

Specimen RV14 had the same detailing as RV12, but its width was doubled from 600 mm to 1200 mm. Hereby, the influence of the spalling of the side concrete cover on the remaining loops was investigated.

Specimen RV15 was used to compare the results of the beam with splices to an ordinary reinforced specimen. Therefore, straight reinforcement bars without splicing were installed.
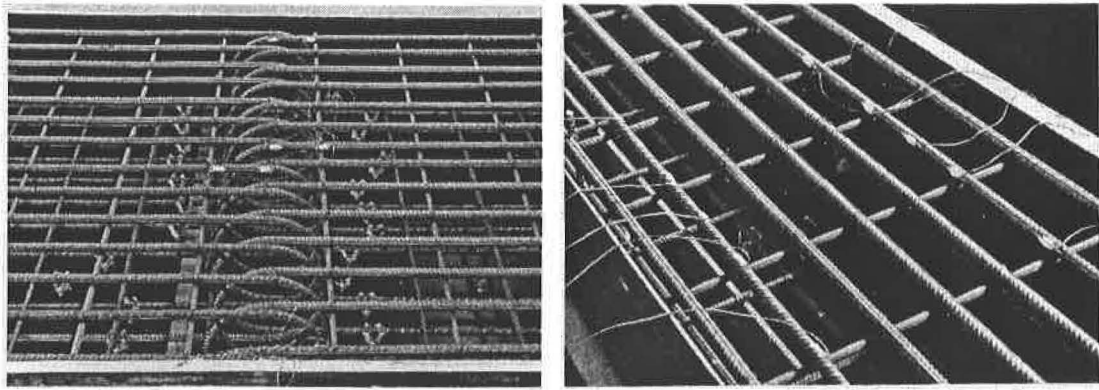
Figure 3.4    Reinforcement arrangement in specimen RV14 and RV15.

Strain gauges were provided to measure the strains in the reinforcement loops. They were glued on the side of the reinforcement bar. To assure a plain contact surface with the sensitive gauges the ribs of the bar were polished on a small area. Later on an epoxy compound was attached to achieve a waterproof cover. The positioning of the strain gauges is shown in Appendix A.

The transverse reinforcement was used to facilitate the construction of the beams. To minimise the influence on the response of the beams the transverse bars were positioned inside the main reinforcement. Furthermore, the splice zone was constructed without transverse bars.

## 3.3    Test set-up

A three-point test set-up was chosen, as shown in Figure 3.5 and Figure 3.6. The specimens were simply supported at both ends and a load transducer was acting in the middle. Hence, the splice zone located in the middle of the beam was subjected to both a bending moment and a large shear force. The load was applied from below; thus, enabling continues registration of the crack pattern on the top of the specimen. The reason for this was to be able to follow the propagation of expected longitudinal cracks in the spliced zone. Due to this particular set-up, the specimen had to be additionally supported in the unloaded stage. Steel girders positioned on the floor supported the beam. As soon as the beam-ends touched the supports the steel girders could be removed.

A displacement control was used. Hereby, a displacement was directly prescribed and the reaction force measured, see also Section 4.4.1. For all tests the loading started with a displacement velocity of 0.2 mm/min. After reaching maximum load the speed was increased, first with a factor two and after a while with a factor four and eight. The exception to this was specimen RV13 that failed before the rate of displacement was increased. The advantage with displacement controlled loading is that it is possible to register the post-peak behaviour of the specimens; thus enabling an examination of the ductility of the detailing.
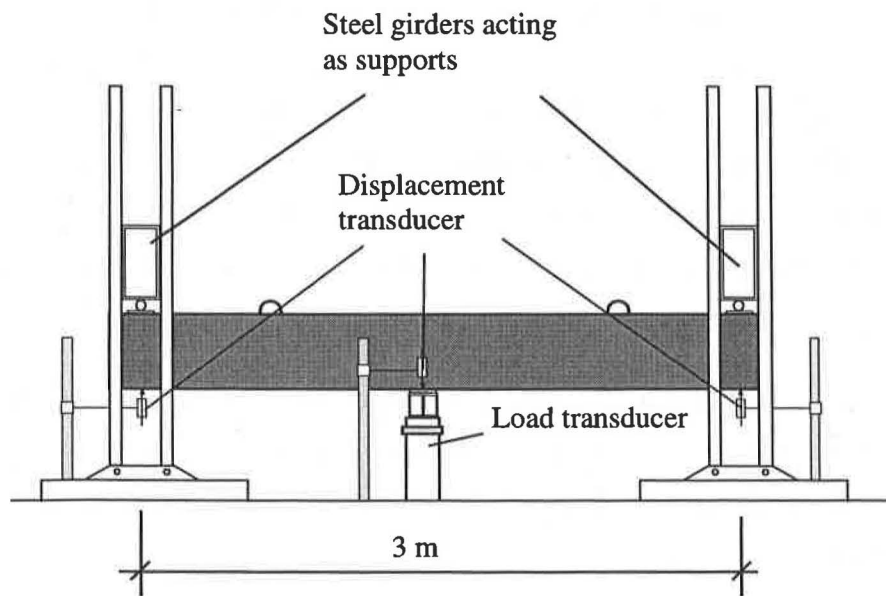


Figure 3.5    Schematic test set-up
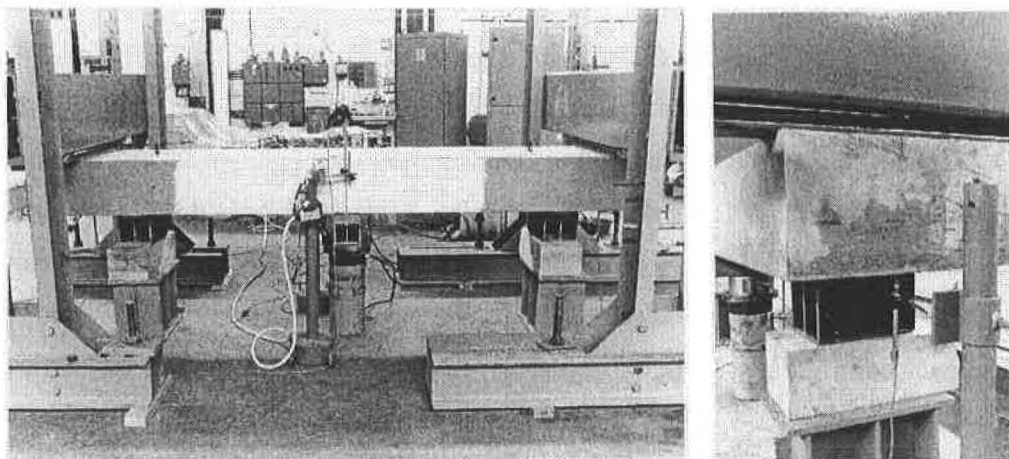


Figure 3.6    Test set-up with provisional support in unloaded state.

Four displacement transducers measured the acting displacements. Two of them (one on each side) were located in the middle of the beam to measure the deformation introduced by the hydraulic jack. The other two were positioned at the ends to register the rigid displacement of the specimen.

## 3.4 Test results

The load-displacement relations for all tests are compared in Figure 3.7. The specimens at the end of the tests are shown in Figure 3.8.
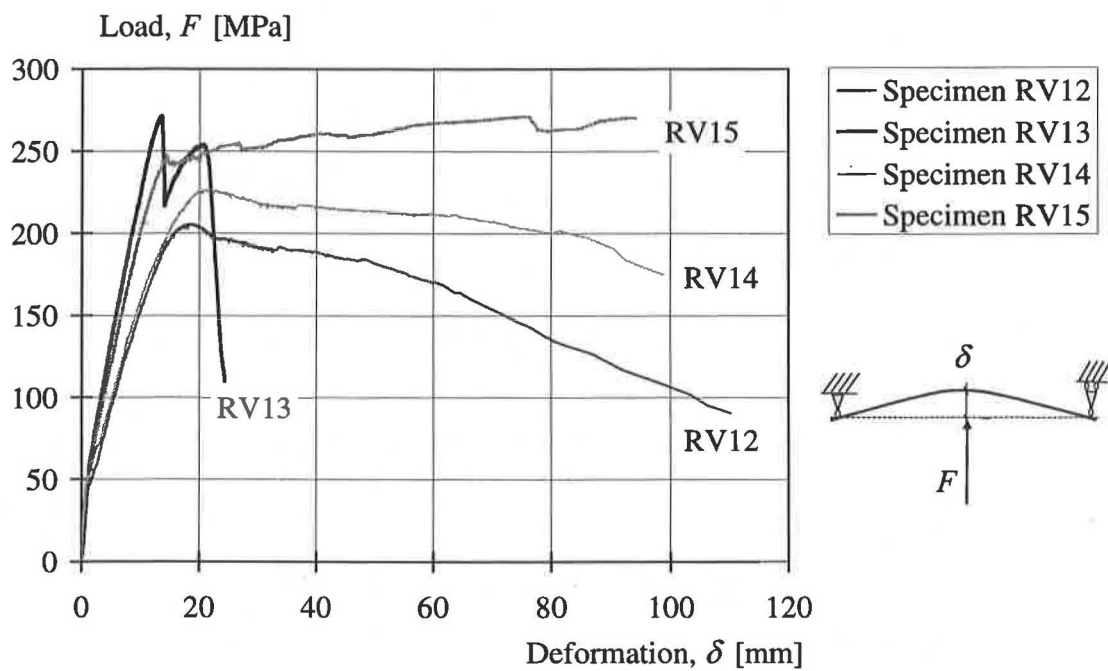


Figure 3.7 Load-deformation relations of all test specimens. The load of specimen RV14 was divided by two. The self-weight of the specimens was subtracted.
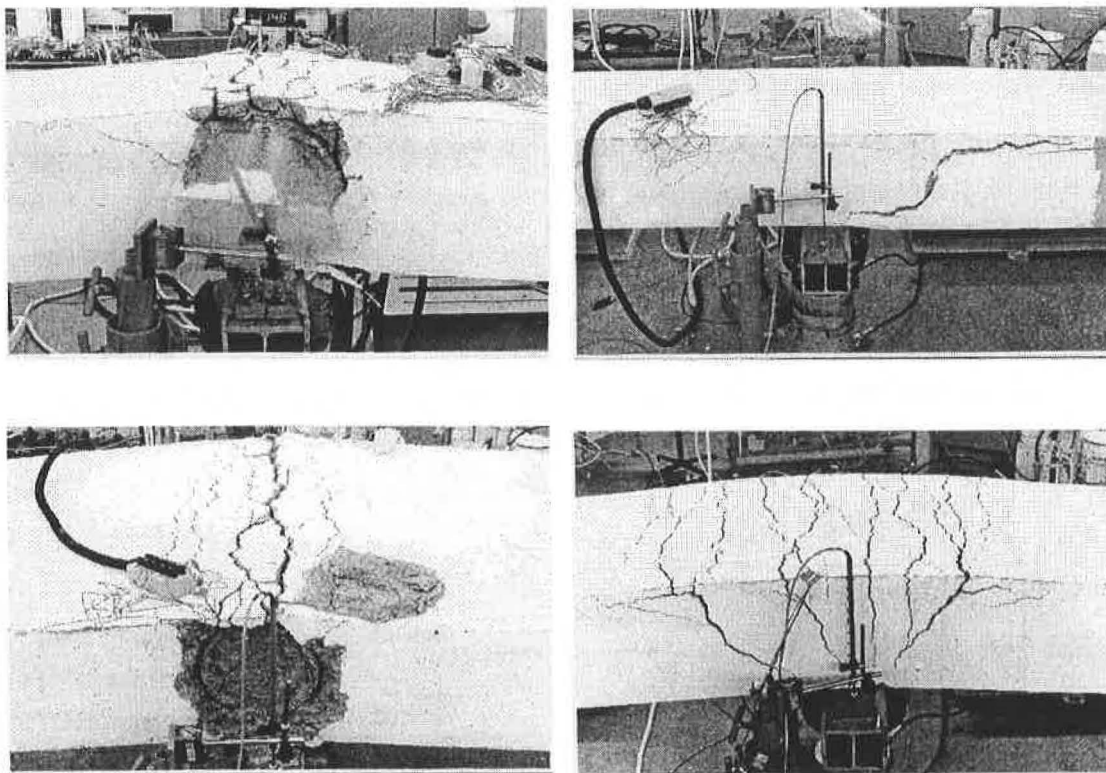
Figure 3.8    Specimen RV12, RV13, RV14 and RV15 at the end of the tests.

The failure development gives important conclusions about the behaviour of the loop splices. Therefore, the responds of the specimens are described in the following sections, before the results are evaluated in Section 3.5.

### 3.4.1    Specimen RV12

Specimen RV12 was provided with a short splice length. Hence a spalling failure was anticipated. The final crack pattern is shown in Figure 3.10 and Figure 3.11.

The first cracks were flexural bending cracks in the middle of the beam at a load of 27 kN. At a load of 81 kN cracks, which followed the bend of the loop were observed. Afterwards, first longitudinal cracks on the top of the beam could be observed at a load of 74 kN. They started in the middle of the splice zone. Longitudinal cracks at the side on the level of the tension reinforcement appeared. Similar cracks at the second loop pair were not observed until a load of 167 kN was reached. The maximum load capacity was 204 kN, a value far below that of the estimated theoretical capacity of 243 kN. With slightly decreasing load the concrete cover spalled off. Large longitudinal cracks about

15 cm from the outer edge were detected. The loop splice developed further and further to a hinge with decreasing resistance.
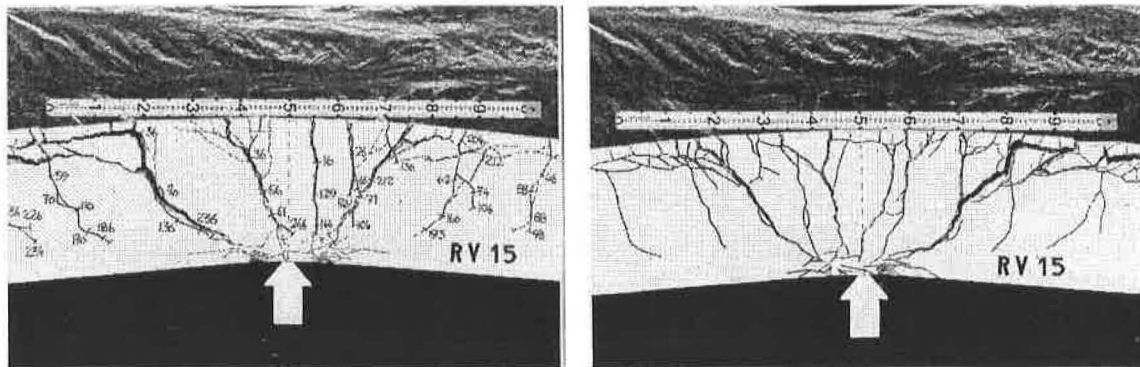


First crack observed
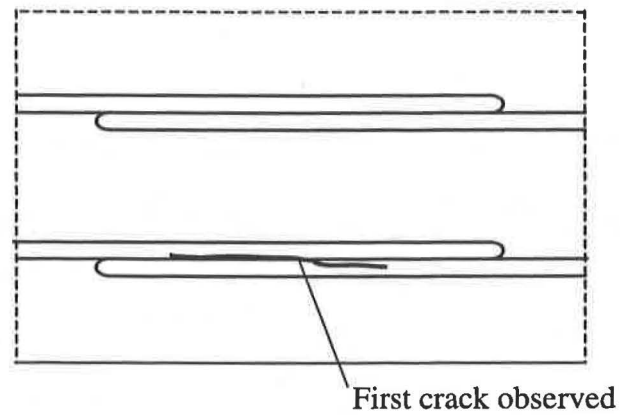
Figure 3.9    Location of crack initiation.
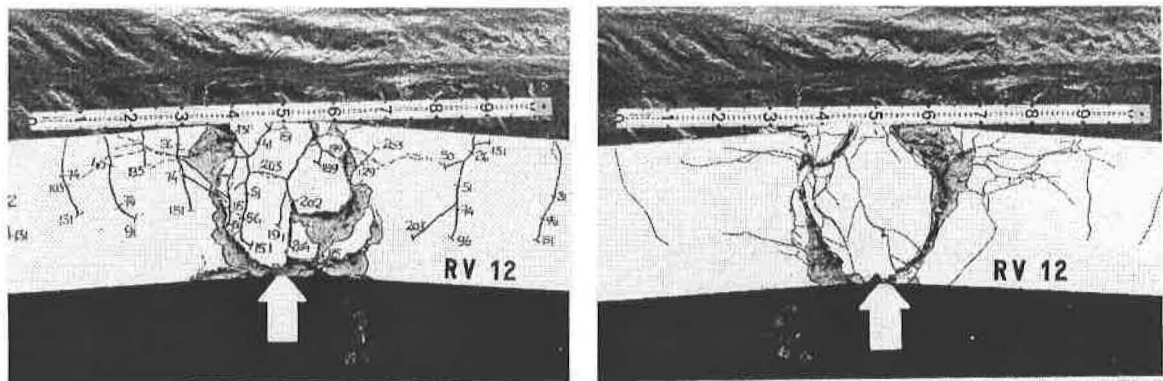


Figure 3.10    Final crack pattern of specimen RV12. Side elevation.
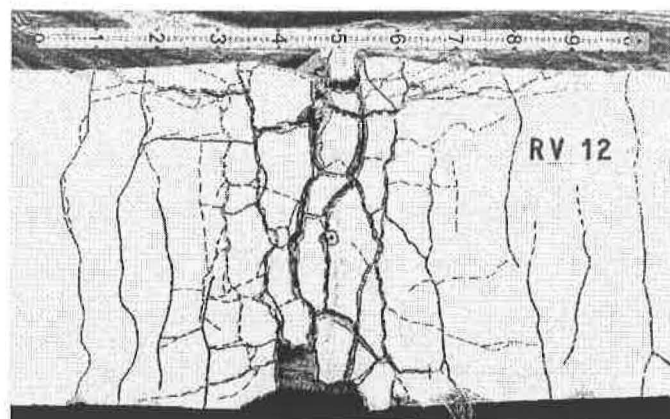


Figure 3.11    Final crack pattern of specimen RV12. Top view.

39

### 3.4.2 Specimen RV13

In specimen RV13 the splice length was elongated. It was expected that thereby spalling of the edge concrete cover could be prevented. The final crack pattern is shown in Figure 3.12 and Figure 3.13.
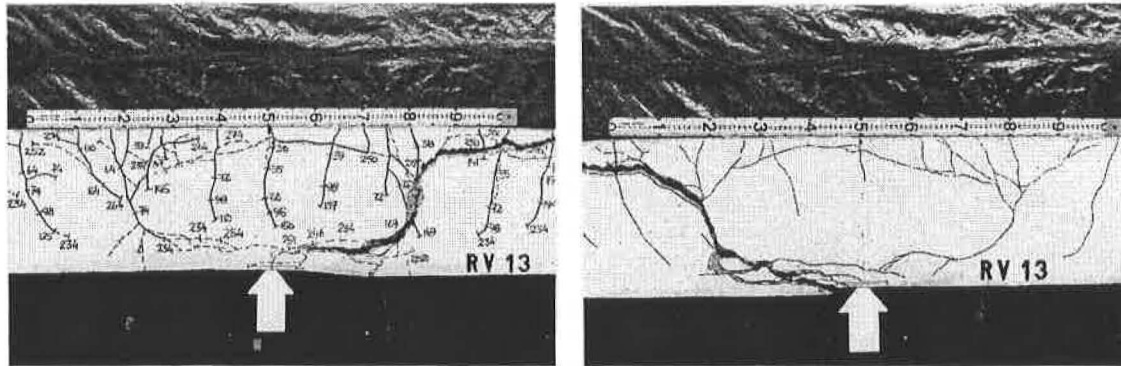


Figure 3.12    Final crack pattern of specimen RV13. Side elevation.
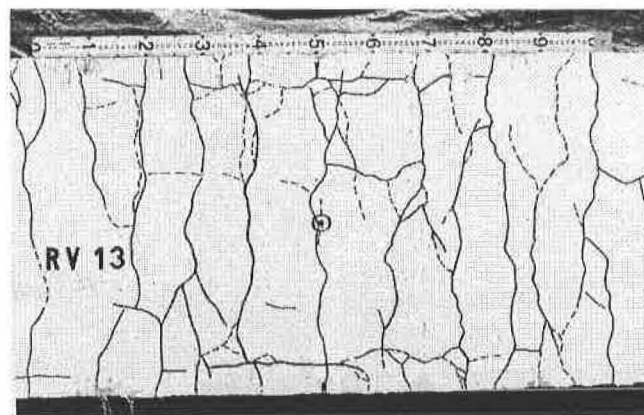


Figure 3.13    Final crack pattern of specimen RV13. Top view.

Flexural cracks were observed inside and outside of the splice zone at a load of 37 kN. With increasing deformation the initial flexural cracks developed to flexural shear cracks. The largest cracks eventually developed outside the splice zone and followed the bend in the lower half of the beam. At a load of 203 kN longitudinal cracks were visible at the top of the beam at the level of the outer loop pair. At a load of 260 kN longitudinal cracks at the level of the tensile reinforcement became visible within the splice zone on both sides of the beam. Shortly after this a sudden load drop of 50 kN took place. The load then increased again and a new crack distribution could be observed in form of cracks following the loop in the upper part of the beam. Finally, the

shear cracks followed the tensile reinforcement and a complete failure of the specimen took place at a load of 254 kN.

### 3.4.3 Specimen RV14

In specimen RV14 the beam width was doubled. Similar to specimen RV12 a short splice length was provided. Therefore, a spalling failure was expected. The final crack pattern is shown in Figure 3.14 and Figure 3.15.
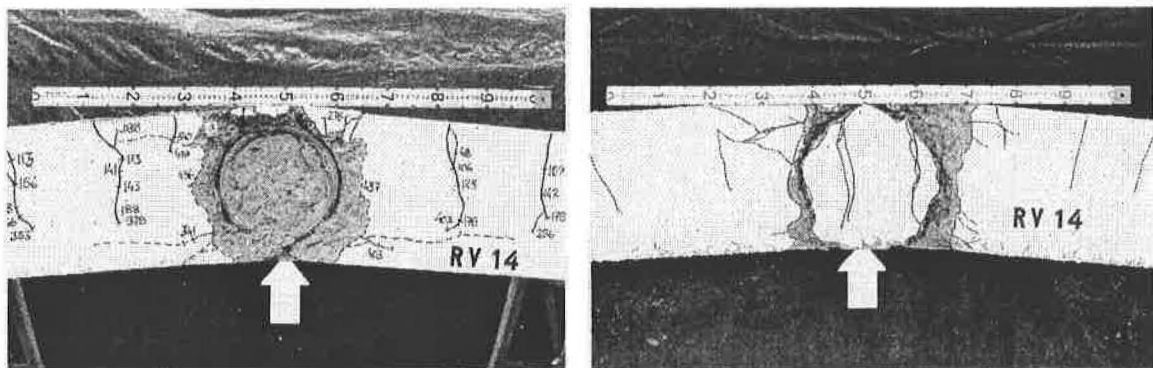


Figure 3.14    Final crack pattern of specimen RV14. Side elevation.
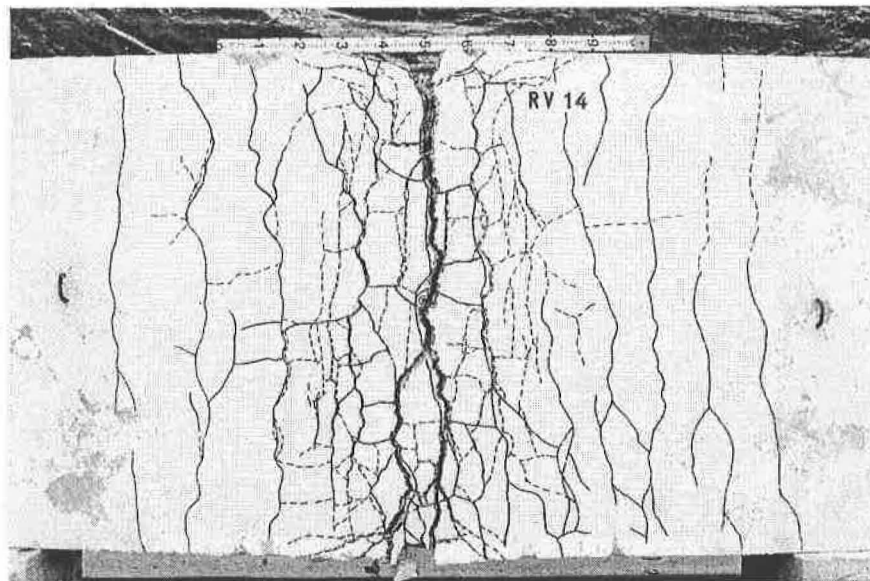


Figure 3.15    Final crack pattern of specimen RV14. Top view.

Several initial shrinkage cracks were observed. Some of them were located on the level of the tensile reinforcement in the splice zone. At a load of 124 kN cracks were detected, which followed the loop. Longitudinal cracks appeared at a load of 172 kN at the top of the beam at the level of the second loop pair. Due two the initial shrinkage cracks no longitudinal cracks were detected at the edge of the beam. When the maximum load of 448 kN was reached longitudinal cracks over the whole width were visible. With decreasing load the concrete cover spalled off.

### 3.4.4 Specimen RV15

Specimen RV15 was provided with straight reinforcement bars. The final crack pattern is shown in Figure 3.16 and Figure 3.17.



Figure 3.16    Final crack pattern of specimen RV15. Side elevation.
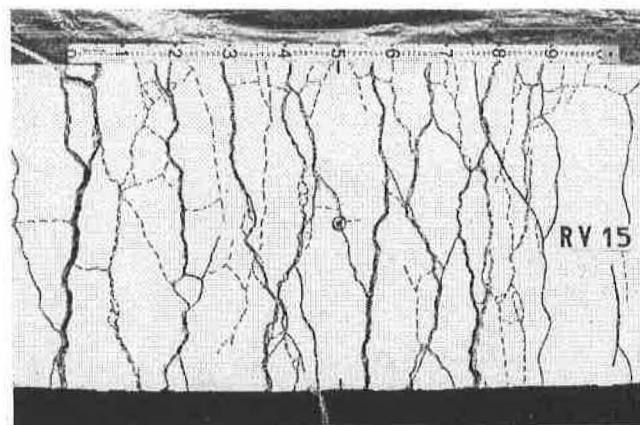


Figure 3.17    Final crack pattern of specimen RV15. Top view.

Flexural bending cracks could first be observed at a load of 33 kN. At a load of 135 kN the flexural bending cracks changed to flexural shear cracks pointing to the acting load.

Finally at a load of 270 kN, after substantial yielding of the reinforcement, the failure was caused by flexural shear cracks propagating along the tensile reinforcement.

## 3.5    Discussion of the test results

### 3.5.1    Specimen RV12

The load-displacement relation for specimen RV12 is shown in Figure 3.18. The behaviour was determined by spalling of the outer concrete covers. This process started soon after cracking and was continued until termination of testing. The comparison of the load-deformation relations in Figure 3.7 at the beginning of Section 3.4 shows that the stiffness of the specimen RV12 was considerably smaller than the stiffness of specimen RV15 and RV13. This supports the theory, that the anchorage capacity of the outer loops was affected, even when a spalling of the concrete cover was invisible.

Furthermore, it can be seen that after the achievement of the maximum load the behaviour of the specimen was ductile. This is contrary to the observations made by Franz and Timm (1972) and Kordina and Fuchs (1972). In their experiments the spalling of the concrete cover seemed to cause a sudden failure without a provided transverse reinforcement. An explanation for this difference can be found by comparison of the test control approaches. In the present study a displacement control was used, so that the behaviour of the specimen after maximum load could be studied. It is probable that for the experiments by Franz and Timm (1972) and Kordina and Fuchs (1972) only a load control testing was realisable. In case of load control the registration of the post-peak behaviour depends mainly on the skill of the laboratories personal and the provided instruments. On the other hand, the specimens had a smaller height, so that the compressive zones of the specimens were affected by spalling of the edge concrete cover. A partial loss of the compressive zone was observed, see Franz and Timm (1972).

43
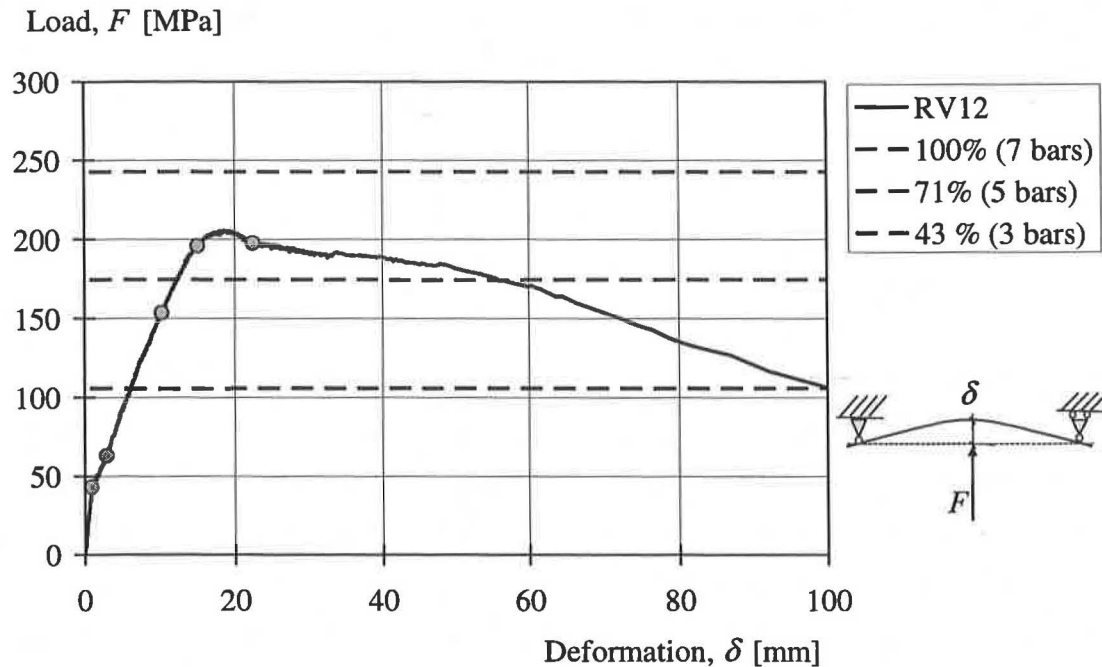
Figure 3.18    Load-deformation relation of specimen RV12.

Figure 3.18 shows the expected load capacity determined according to Eurocode 2, for beams with 7, 5, and 3 continuos reinforcement bars with the same general dimensions as specimen RV12. It can be seen that with increasing load the loops were more and more affected by the spalling. At a displacement of around 55 mm the bearable load was equal to the load capacity of a beam with five continuos bars. At a displacement of 99 mm the load was even reduced to the capacity of a beam with three continuos bars.

The average stress in the reinforcement loops is determined from the glued-on strain gauges shown in Figure 3.19 and Figure 3.20 separated into inner and outer loops. The stress distributions of the other loops are shown in Appendix E. The results coincide with the findings of the literature study in Section 2. In an early stage the stresses in the loops change from tension at point B to compression at point C, see Figure 3.21. With increasing deformation the tensile stress increases and reaches further into the compressive zone. Furthermore, the steel stress increases with increasing distance to the outer edge, as with increasing "concrete cover" the confinement increases and consequently also the anchorage capacity.

It is interesting to note that the anchorage length was reduced on the two overlapping half-circles, see Figure 3.21. The additional straight part between point A and A* just

outside the loop of the splice did not contribute to the anchorage capacity. This reduction was caused by the critical crack, which followed the loop.
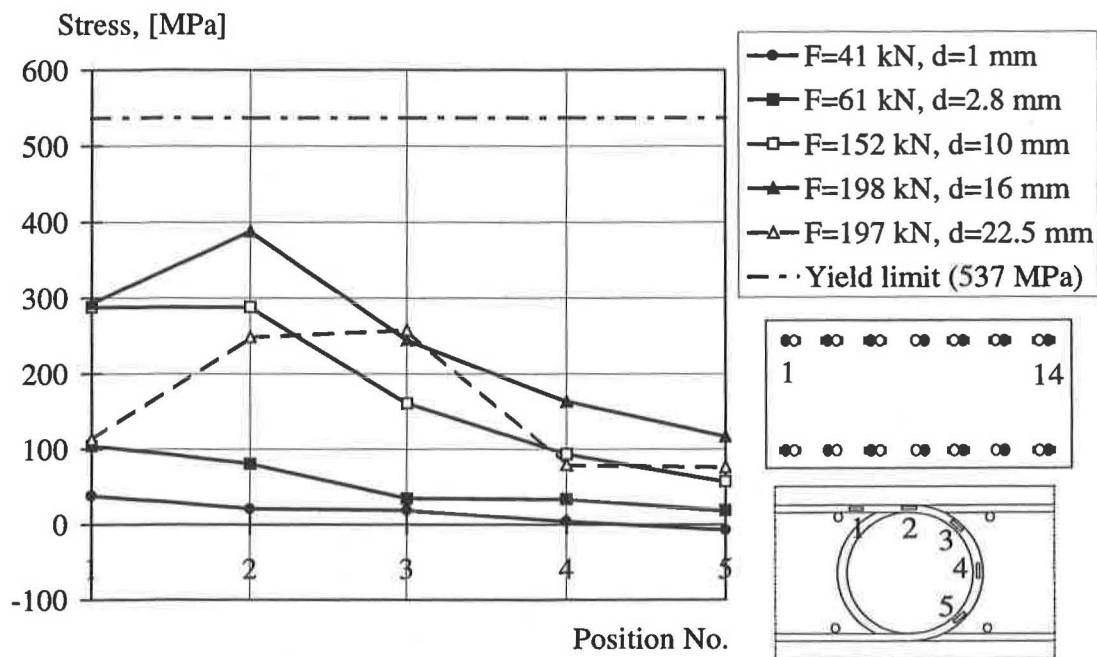


Figure 3.19    Average stress of loops 1 and 14 of specimen RV12.
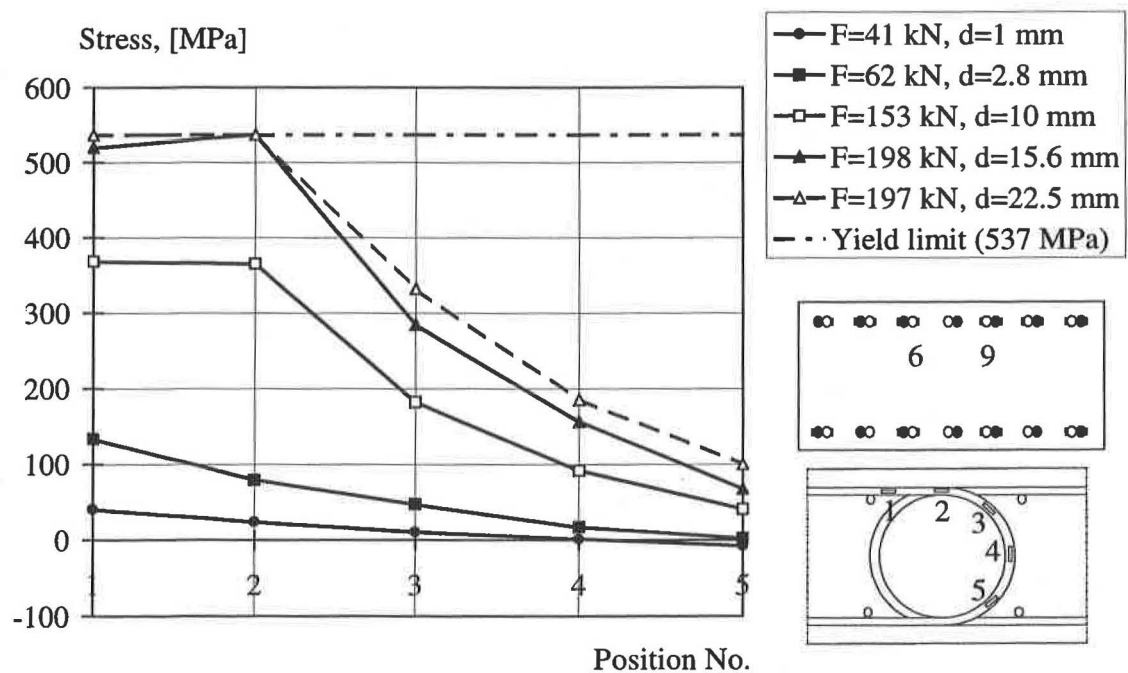


Figure 3.20    Average stress of loops 6 and 9 of specimen RV12.
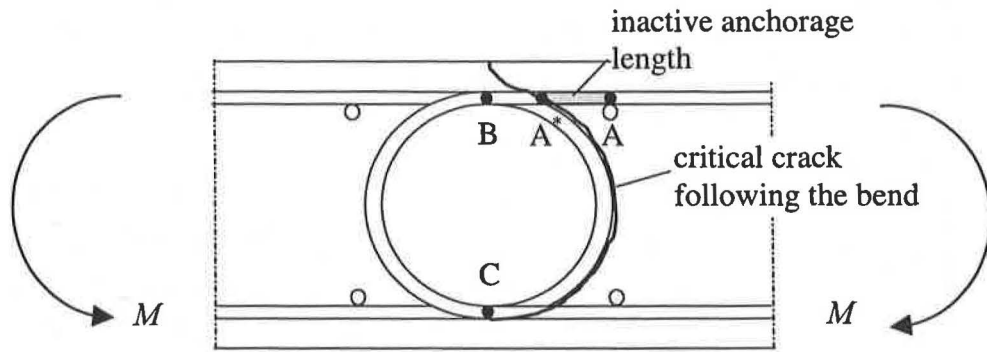
Figure 3.21    Reduction of the anchorage length due to cracks following the loop.

### 3.5.2   Specimen RV13

The load-deformation curve of specimen RV13 is shown in Figure 3.22. Spalling of the side concrete cover was prevented due to the additional straight splice length. The stiffness of specimen RV13 in cracked stage, is clearly higher than the one of the specimens RV12 and RV14, which were weakened by spalling of the side concrete cover, see Figure 3.7. The load capacity is higher than for specimen RV15, with continuous reinforcement. This high load could be resisted, due to the doubled reinforcement area in the splice zone.
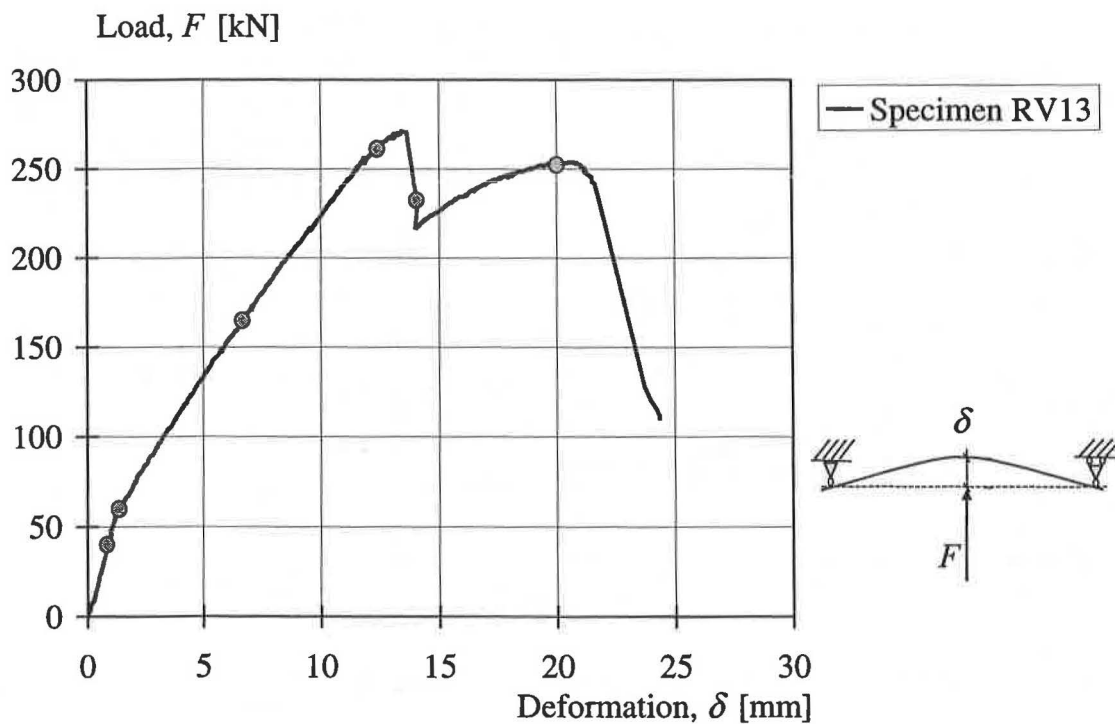


Figure 3.22    Load-deformation relation of specimen RV13.

46

Even though a higher load was obtained, the post-peak behaviour was brittle. The first load-drop occurred simultaneously with a strain redistribution in the tensile reinforcement, see Appendix E. This can also be seen in and Figure 3.23 and Figure 3.24 in which the steel stresses at the position of the strain gauges are shown.
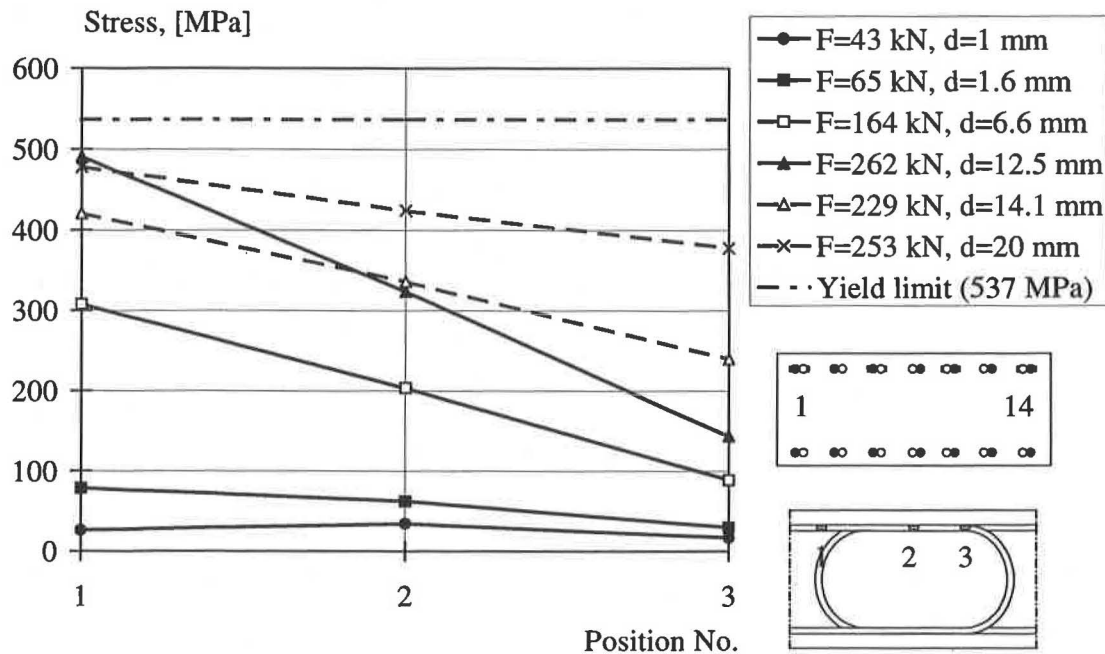


Figure 3.23    Average stress of loops 1 and 14 of specimen RV13.
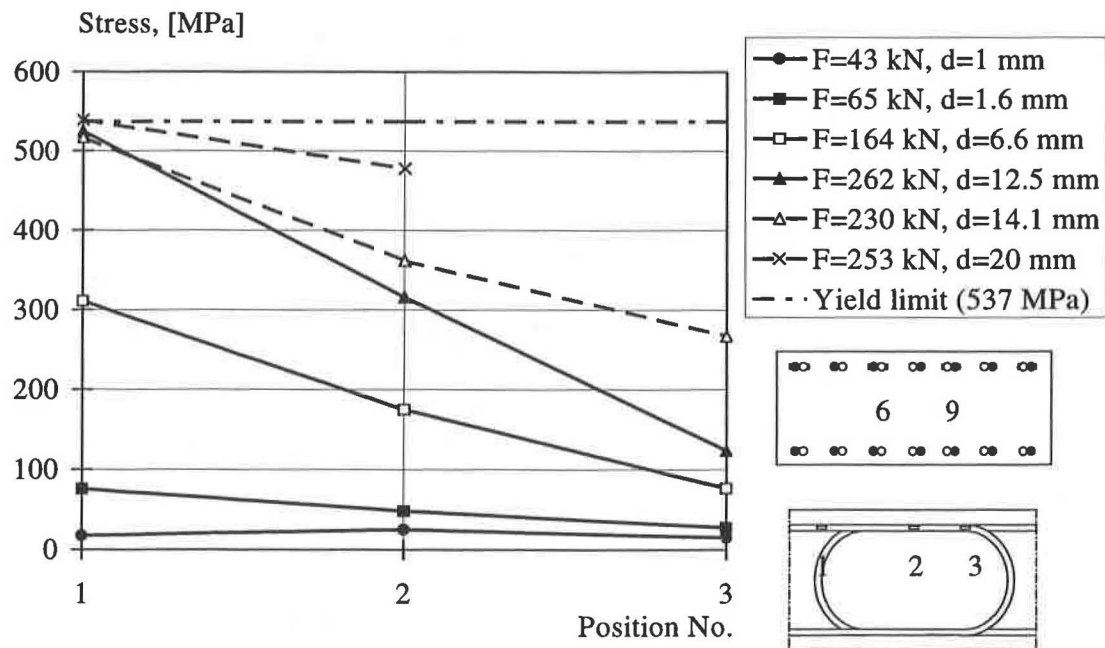


Figure 3.24    Average stress of loop 6 and 9 of specimen RV13.

47

After the load drops, the stress at the beginning of the splice was reduced. At the same time, a stress increase at the end of the straight splice length took place. All reinforcement loops were affected by this stress redistribution.

Considering the crack development described in Section 3.5.2 it is probable, that the load drop was caused by a splitting failure in the straight splice length. However, the anchorage capacity was not totally lost but only reduced. Instead, this slip activated the anchorage capacity of the bend part. Hereby, it can be concluded that the splitting failure of the straight part was brittle. Instead of a smooth redistribution from the straight part to the bend, the anchorage reduction occurred sudden and caused a considerable load drop. However, due to the bend part, the load could increase again, as a new anchorage mechanism was acting similar to the one in specimens RV12 and RV14, where the bend provides the anchorage capacity of the splice.

Finally, the shear failure occurred at a load of 253 kN, i.e. was slightly smaller than that of specimen RV15. This decreased shear capacity may be caused due to the new acting mechanism. The larger distance between the two bends prevented a localised hinge as in specimen RV12 and RV14.

### 3.5.3  Specimen RV14

The load-deformation relation of specimen RV14 is shown in Figure 3.25. The results of specimen RV14 are similar to those obtained in specimen RV12. As in specimen RV12, spalling limited the load capacity and the post-peak behaviour was ductile. Soon, the capacity of the outer loops was strongly reduced. Due to the initial cracks, see Section 3.4.3, the spalling process was initiated without longitudinal cracks at the edge. The increased width, though, had significantly influence on the result. The maximum load was higher than in specimen RV12 and the post-peak behaviour more ductile. This was due to the larger number of loops since more loops could carry the load after the spalling of the outer loops; i.e. a smaller percentage of the total number of bars were affected when the outer bars were lost.
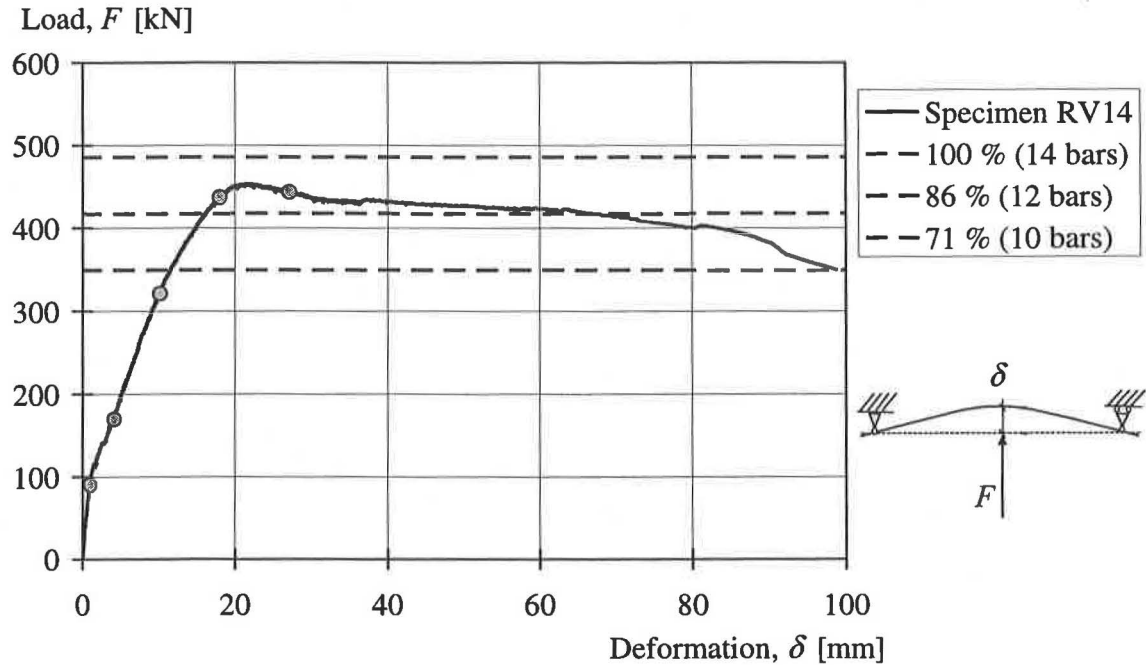
Figure 3.25    Load-deformation relation of specimen RV14.

Nevertheless, the stiffness of specimen RV14 in the cracked state is similar to the one of specimen RV12. This indicates that the bond conditions of the inner loops were affected by splitting cracks due to the radial pressure. Consequently, the stiffness was reduced compared to specimen RV13. However, due to the confinement provided by the surrounding loops and concrete yielding of the reinforcement was still obtained.

In Figure 3.25 the load capacity of a section with 14, 12, 10 and 6 continuos bars is shown. At maximum load the capacity of less than two reinforcement bars was lost since a part of the anchorage capacity of the outer loops still remained. In Figure 3.26 and Figure 3.27 the average stresses for outer and inner loops on the position of the strain gauges are presented. The inner loops reached yielding whereas the stress in the outer loops decreased with increasing deformation. In turn, the largest stresses in the loops were acting at the position of gauge 2, see also Figure 3.23.

49
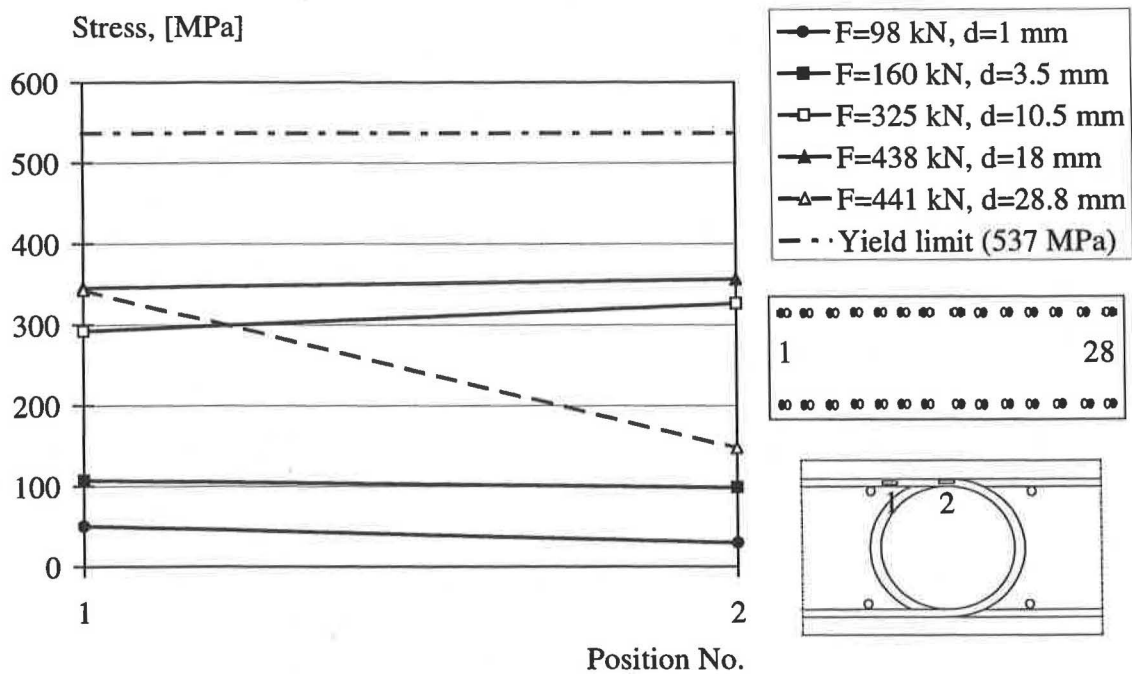
Figure 3.26    Average stress in loops 1 and 28 of specimen RV14.
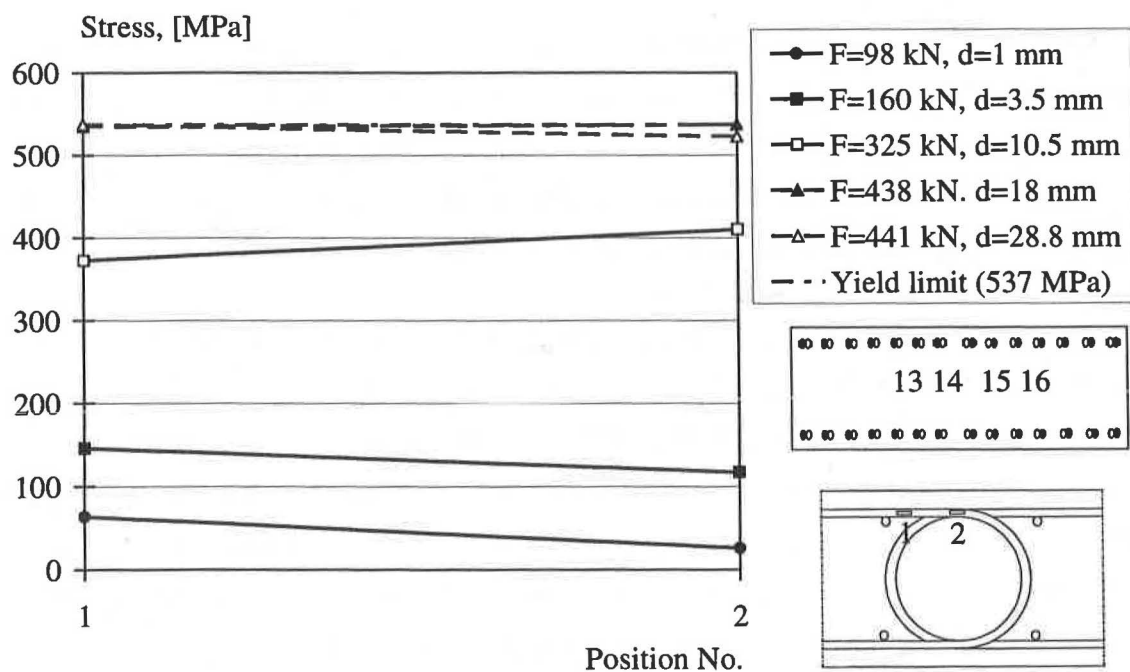


Figure 3.27    Average stress in loops 13, 14, 15 and 16 of specimen RV14. At the load
level F = 438 kN and F = 441 kN the yield limit was reached.

50

### 3.5.4 Specimen RV15

The specimen RV15 shows the typical behaviour of an under-reinforced beam with continuos reinforcement. The tensile reinforcement reaches its yield strength far before failure, see Appendix F. The load-deformation relation is shown in Figure 3.28. The stress-deformation relation on the position of the strain gauges is shown in Figure 3.29.
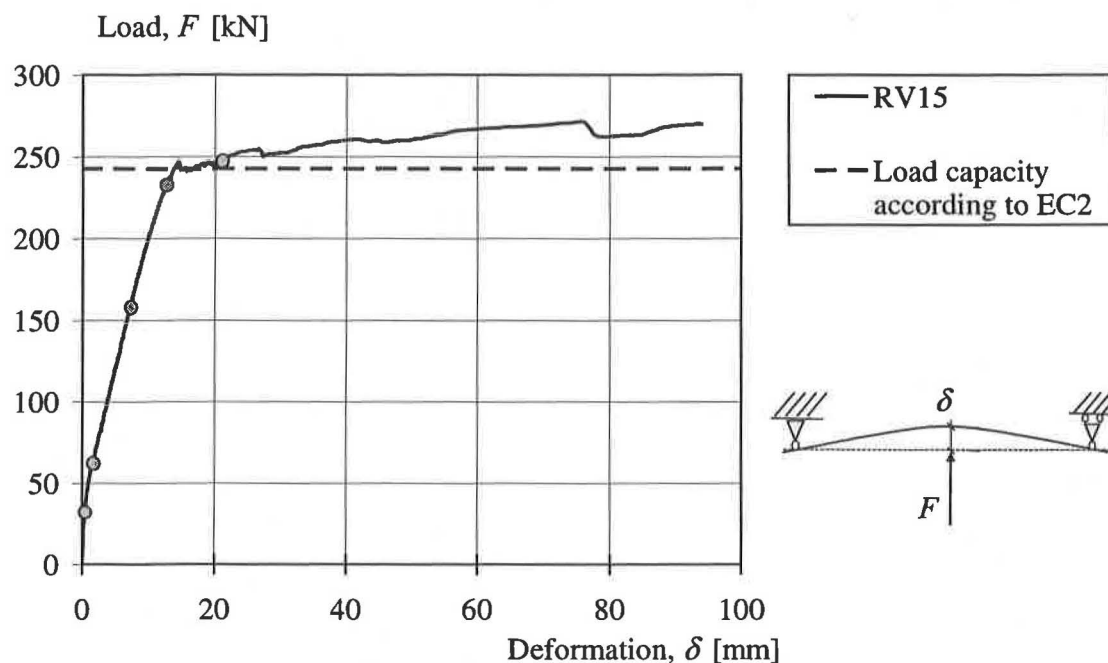


Figure 3.28    Load-deformation relation of specimen RV15.

Even with weaker concrete as planned, see Section 3.2, the shear capacity was sufficient enough, so that the shear failure occurred after hardening of the reinforcement. Nevertheless, the obtained crack pattern with strongly inclined cracks pointing to the acting force shows the large influence of the shear force.
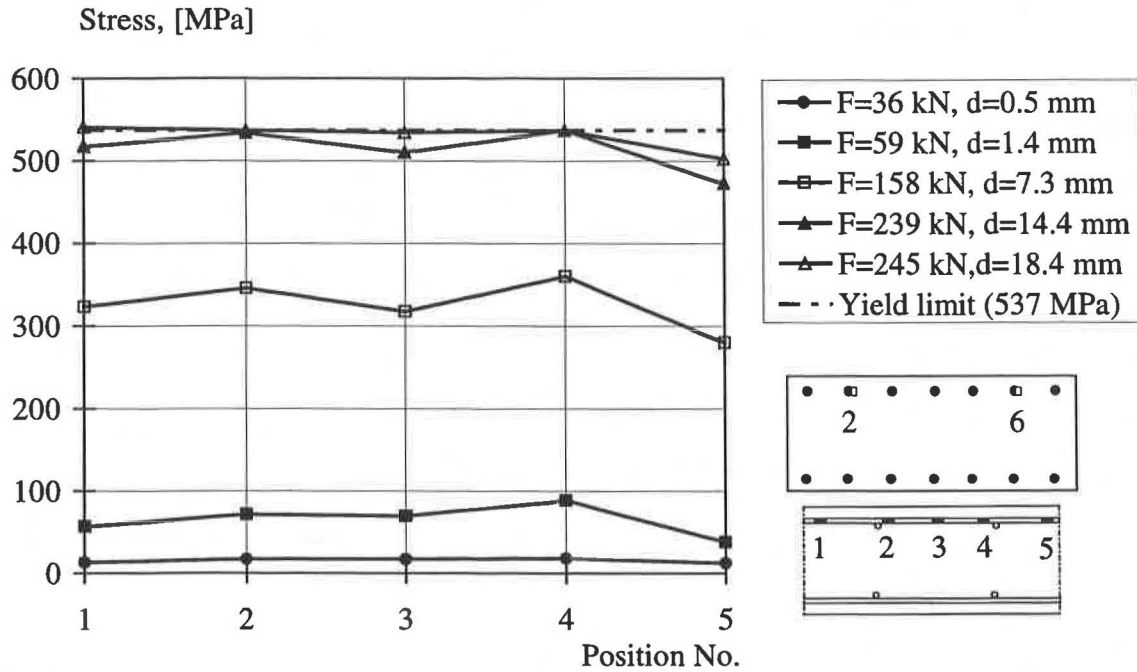
Figure 3.29    Average stress in bars 2 and 6 of specimen RV15.

## 3.6    Concluding comments concerning the experiments

With a splice length composed by two semi-circles, $l_s = 220$ mm, the concrete cover spalled off. Due to this, the anchorage capacity of the outer loops was lost to a large degree and hence, the maximum load capacity reduced. Nevertheless, the post-peak behaviour of the specimen was still ductile.

With an elongated splice length, $l_s = 600$ mm, spalling of the edge concrete cover was prevented and a higher maximum load compared to a specimen with continuos reinforcement bars was reached. Splitting cracks at the straight part of the splice, though, occurred and caused a sudden load drop, before the load could increase again due to the influence of the bend part.

An increased width of the beam had a favourable influence on the load capacity. A higher load could be reached, since more remaining loops could carry the load after the loss of the outer bars. However, the stiffness in the cracked stage was similar to the one with a normal width. This indicates that the bond conditions of the inner loops were affected by splitting cracks due to the radial pressure, even though yielding was reached.

The stresses along the loop changed from compression to tension. With an elongated splice length as in specimen RV13 the major part of the initial anchorage was provided by the straight part of the splice.

The longitudinal splitting cracks, which led to spalling, started in the middle of the splice and were orientated parallel to the reinforcement loops.

# 4 Non-linear finite element analyses

The aim was to analyse aspects of loop splicing in beams by means of non-linear finite element analyses. It was intended to gain a deeper understanding of the behaviour of the loop splices. The specimens RV12, RV13 and RV15 were modelled by two-dimensional plane stress elements and the results were compared with experiments to control the reliability of the chosen models. The bond relation was varied using "good" and "other" bond conditions according to CEB-FIP Model Code, CEB (1993).

The calculation approach was divided into three main steps. In a pre-processing step the specimens were idealised and discretised by means of the pre-processor FEMGEN, Femsys (1998). In a second step the analysis was carried out by means of the finite element program DIANA, TNO (1998), and for the evaluation of the results the post-processing program FEMVIEW, Femsys (1998), was used.

## 4.1 Non-linear material models

The material behaviour of the concrete was modelled by a coaxial total stress-strain concept, also known as rotational crack model. The coaxial concept evaluates the stress-strain relationship in the principal directions of the strain vector. In Figure 4.1 a schematic stress strain relation for concrete under compression and tension is shown.

### 4.1.1 Concrete under tension

In the total stress-strain relation a crack is initiated, when the tensile strength is exceeded, see Figure 4.2. The following cracking is considered by a smeared crack model, in which the total strain is represented as the deformation of the uncracked material and the additional contribution of cracking. This strain is smeared over the area, which belongs to the integration points at which cracking occurred. In the present analyses a tension stress-strain relation according to Hordijk, TNO (1998) was chosen, in which the behaviour until the crack initiation is linear and then described by a non-linear softening relation, see Figure 4.5.

54
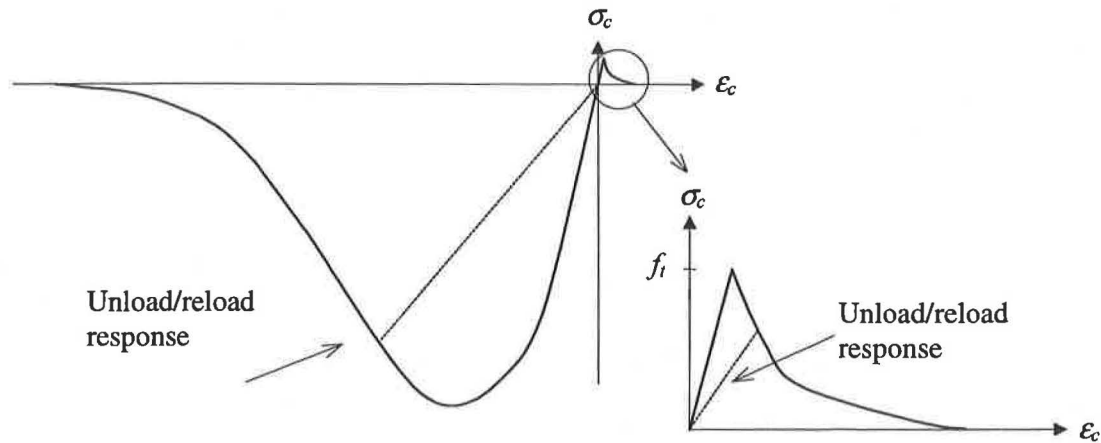
Figure 4.1    Schematic stress strain relation for concrete under compression and tension. The unloading behaviour is described by the secant stiffness. Modified from TNO (1998).

Since the total strain is smeared over one element or even only a part of the element, depending on the number of integration points, the tension softening behaviour depends on the element size.

To explain this dependence the cracking process is shown by use of a fracture mechanics model, see Figure 4.2. When a member is loaded under tension micro-cracks develop in the specimen at local stress concentration points, see Figure 4.2 b). With increasing load the cracks are connected and a fracture zone develops at the weakest point of the structure, as shown in Figure 4.2 c). At this point the material reaches its tensile strength $f_t$. Under further increasing external deformations the tensile stress in the fracture zone decreases, something that usually is referred to as tension softening. The material around the fracture zone unloads while the crack opens, see Figure 4.2 d). When the two parts are disconnected, the displacement is not longer depending on the tensile softening behaviour, see Figure 4.2 e).

This process can be described by a stress-displacement relation, which can be divided into a stress-strain relation depending on the length of the specimen and a stress opening relation as shown in Figure 4.3. Consequently, a total stress-strain relation considering the tension softening must be related to the size of the element, in which the fracture zone is developed. In DIANA, TNO (1998) the influence of the element size is introduced by dividing the area under the softening curve, defined as fracture energy, by

the crack-bandwidth $h$, see Figure 4.4. In the analyses the crack-bandwidth was chosen to the length of an element.

$$\sigma_c = 0 \qquad \sigma_c < f_t \qquad \begin{array}{c} \sigma_c = f_t \\ (w = 0) \end{array}$$

a)                b)                c)

$$\begin{array}{c} \sigma_c = f(w) \\ (0 < w < w_u) \end{array} \qquad \begin{array}{c} \sigma_c = 0 \\ (w \geq w_u) \end{array}$$

d)                e)
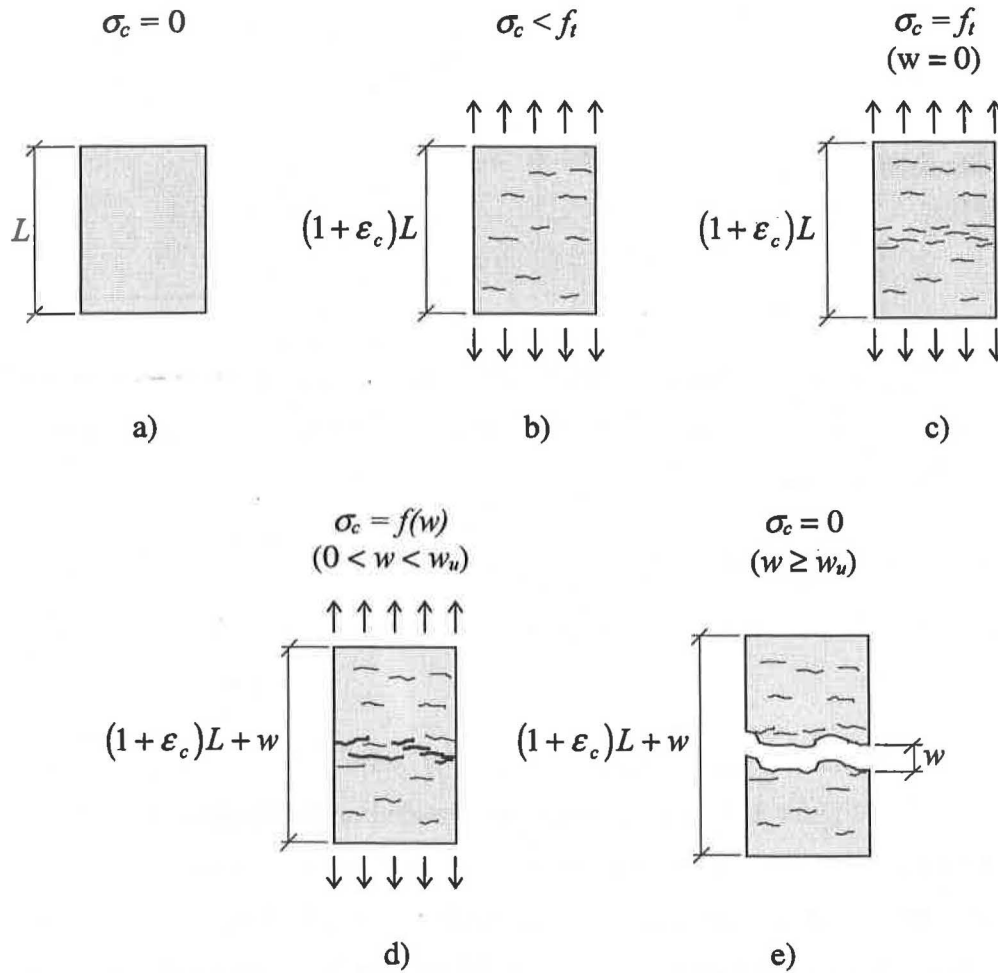
Figure 4.2    Stages in the formation of a crack in a concrete specimen subjected to increasing tensile deformation. From Johansson (1996).

In the coaxial crack model, the stresses are transferred only perpendicular to the crack. It is achieved by continuously updating the direction of the crack. Therefore, shear retention as in case of a fixed crack model does not have to be considered.
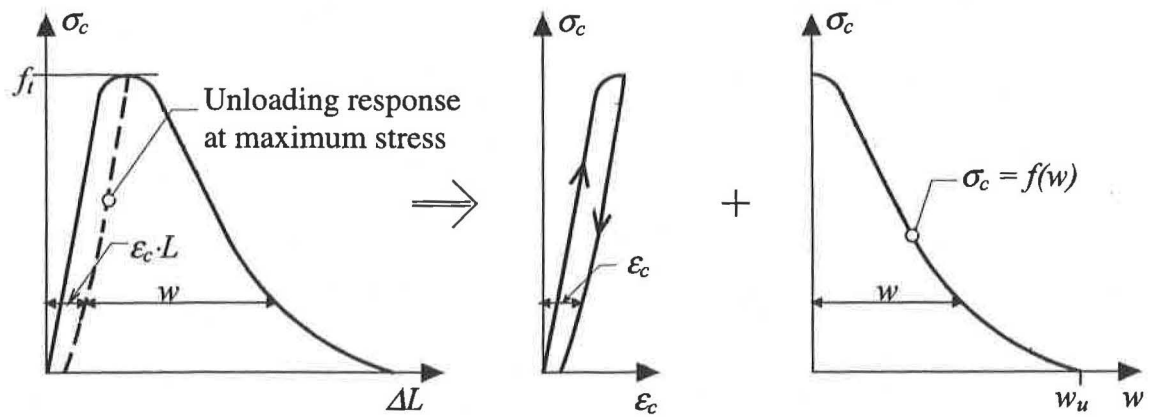
Figure 4.3    Mean stress-displacement relation for an uniaxial tensile test specimen. The displacement is divided into a stress-strain relation and a stress opening relation. From Johansson (1996).

The tensile strength of the concrete was determined according to MC90, CEB (1993) to

$$f_{ctm} = f_{ctko,m} \cdot \left( \frac{f_{ck}}{f_{cko}} \right)^{\frac{2}{3}}$$    (4.1)

with    $f_{ctko,m}$ = 1.40 MPa,
        $f_{cko}$ = 10 Mpa and
        $f_{ck}$ = $f_{cm}$ - 8 Mpa.

The fracture energy was set to $G_f$ = 113 N/m according to the material tests, presented in Section 3.1.1.
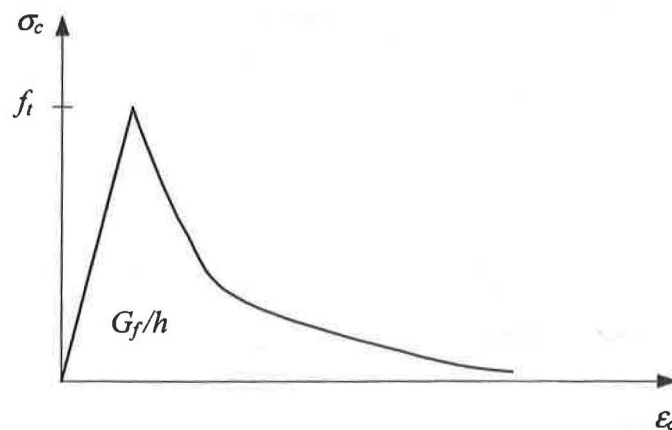


Figure 4.4    Stress-strain relation for concrete under tension according to Hordijk *et al*. Modified from TNO (1998).

## 4.1.2 Concrete under compression

The increasing part of the total stress strain constitutive relation for concrete under compression was obtained by the material tests, see Section 3.3.3. In the material tests the concrete cylinders were loaded by a load controlled device. Consequently, the tests were terminated at maximum load and the strain softening part could not be measured. Therefore, the descending branch was modelled according to CEB-FIP Model Code, CEB (1993). These expressions are based on compression tests of concrete cylinders of a height of $h_{cyl} = 300$ mm. However, the softening branch depends, similar to the tension softening relation, on the size of the specimen, see Lundgren (1999). To relate the softening branch to the element size used in the FE-model the plastic strains of the post-peak behaviour were increased by a factor of

$$\varepsilon_{2,\text{mod}} = \frac{h_{cyl}}{h} \cdot \varepsilon_2 \tag{4.2}$$

with $h$ equal to the crackbandwith used in the softening relation under tension and $\varepsilon_{2,\text{mod}}$ and $\varepsilon_2$ as defined in Figure 4.5.
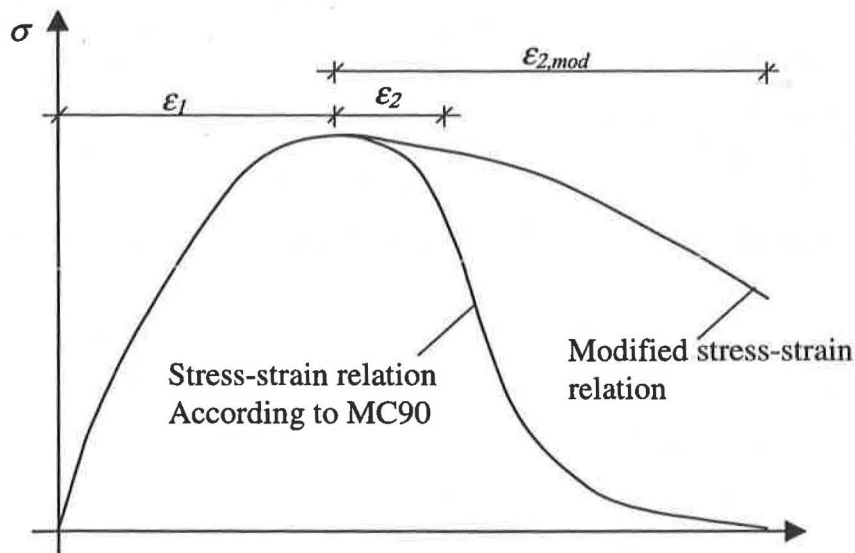


Figure 4.5     Determination of the modified stress-strain relation. The plastic strain of the descending branch is enlarged according to equation (4.2).

A drawback of the total stress-strain model is that the confinement effect due to lateral stresses cannot be considered in combination with a multi-linear compression model. However, it was preferred to use the results of the material test instead of a predefined

compression relation available in Diana, TNO (1998), hence the confinement effect was omitted. However, in an analysis based on two-dimensional models with plane stress elements, see Section 4.4, the confinement effect is small.
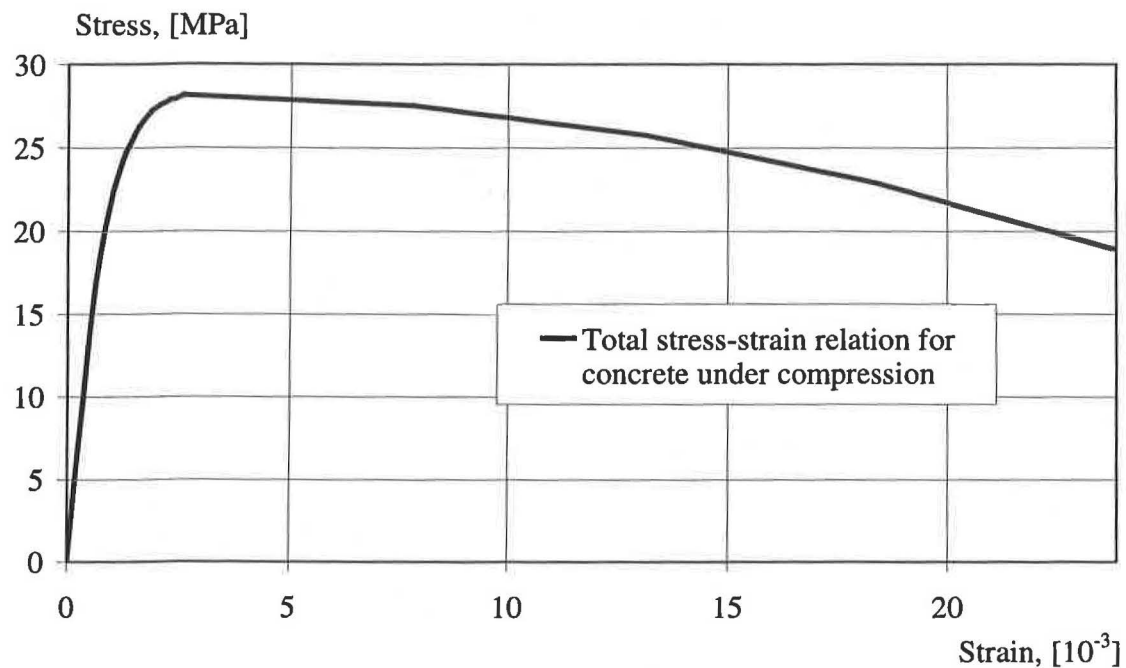


Figure 4.6    Total stress-strain relation for concrete under compression used in the finite element analyses.

## 4.1.3    Reinforcement

The constitutive relation for the reinforcement is modelled with the von Mises yield criterion with associated flow and isotropic hardening. The modulus of elasticity and the values for the strain hardening were determined by material tests, see Section 3.1.2 and Figure 4.7.
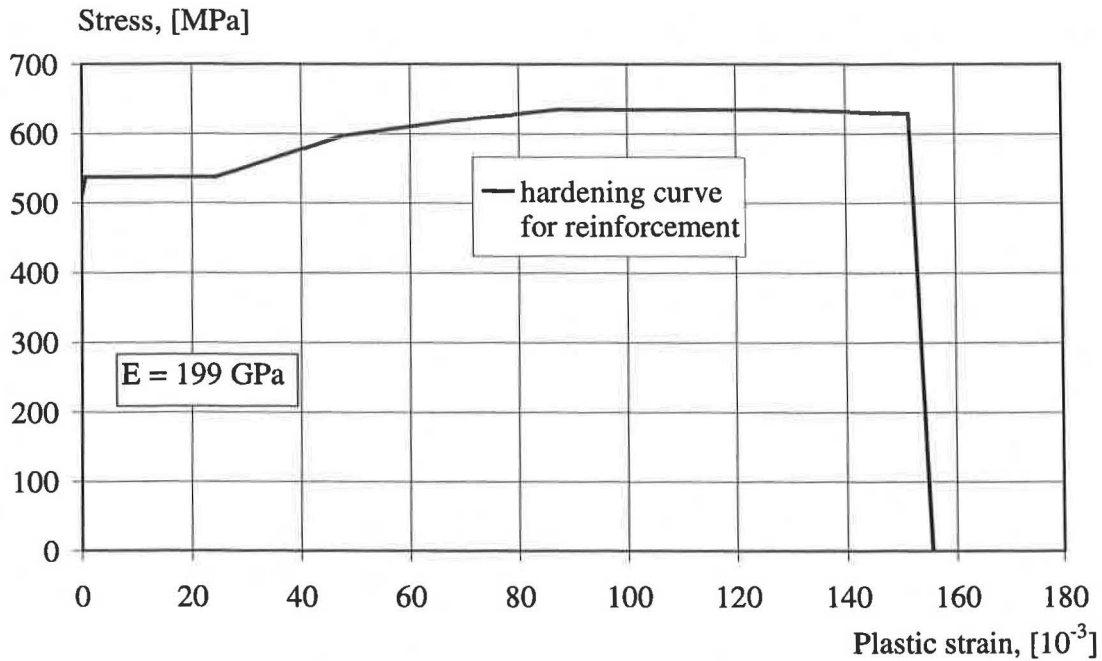
Figure 4.7    The constitutive relation for the reinforcement used in the FE-analyses.

## 4.1.4    Interaction between concrete and reinforcement

The interaction between concrete and reinforcement was modelled by tangential stresses along the reinforcement bar. Therefore, the inclined forces caused by the mechanical interaction of reinforcement ribs and the surrounding concrete were divided in components normal and parallel to the reinforcement axis, shown in Figure 4.8. The normal part was omitted. Consequently, a splitting failure could not occur. The effect of splitting had to be introduced in the constitutive relation of the bond behaviour. Several bond-slip relations can be found in CEB-FIP Model Code, CEB (1993). They are divided into relations for confined and unconfined concrete. Furthermore, the bond quality is divided into "good" bond conditions and "other" bond conditions and depends on the way of casting and the geometry of the member. In the present analyses the concrete in the splice zone was expected to be "unconfined" as splitting cracks could be observed in the analyses, see Figure 4.9.
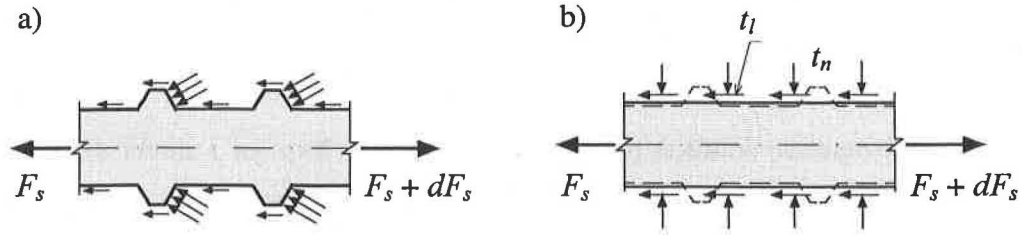
Figure 4.8    a) Contact stresses on a deformed bar embedded in concrete. b) Representation of these stresses by components on the mean surface. Modified from Plos (1996).
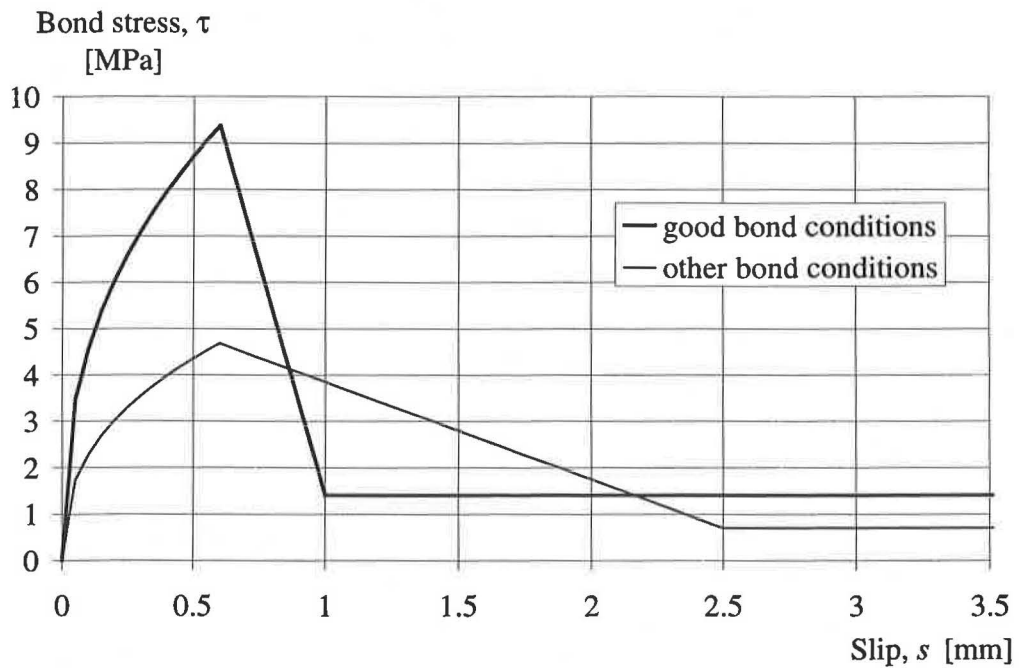


Figure 4.9    Bond-stress-slip relationship according to CEB-FIP Model Code, CEB (1993).

## 4.2    Non-linear numerical solution approach

The constitutive relations described in the previous section are non-linear and lead to a set of equilibrium equations of internal and external forces, which is non-linear depending on the previous deformation of the structure. An approach to solve this equation system is to divide the loading process in increments and to approximate the non-linear material behaviour in each increment by means of a linearization. To reduce

61

the deviation due to the simplification of the material behaviour an iterative loop is embedded in each increment.

An incremental-iterative solution procedure was used in form of a direct displacement control as incremental procedure combined with a Secant method, called BFGS (Broyden, Fletcher, Goldfarb and Shanno), as iterative procedure. In the following two sections the chosen models are further explained.

## 4.2.1   Incremental method

When using the displacement control as an incremental method in DIANA, displacements are prescribed at defined supports of the structure. The reacting force at the support is measured depending on the prescribed deformation. In this way, the post-peak behaviour of a specimen can be examined. The solution approach operates even when the load resistance of the structure decreases. The displacement control is an appropriate incremental solution method for the present analyses, since the post-peak behaviour may contain valuable information on the ductility of the structure. The graphical interpretation is shown in Figure 4.10 a) and compared to the in the present case less appropriate load controlled incremental method, shown in Figure 4.10 b).



a) displacement controlled   b) Load controlled
   incremental approach          incremental approach
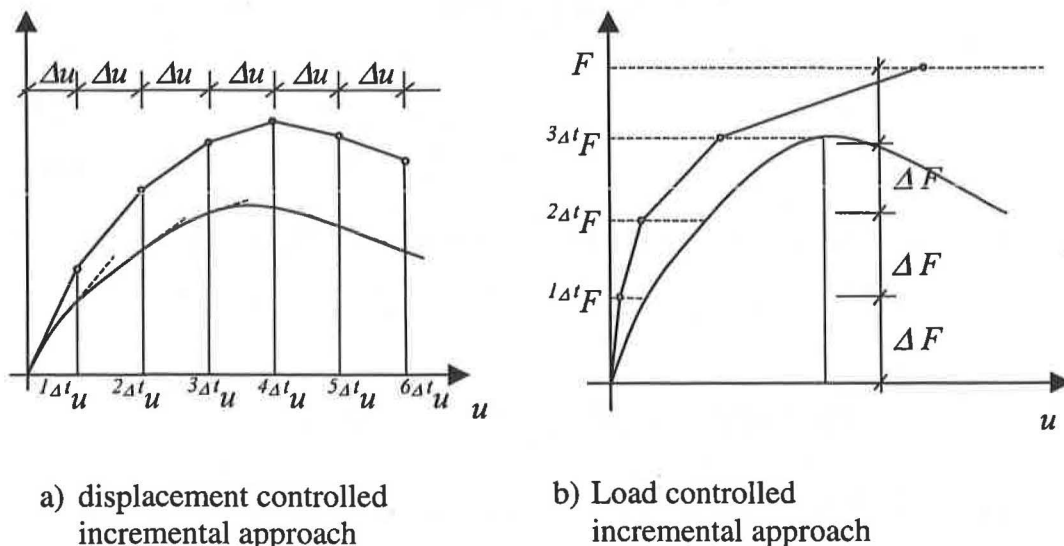
Figure 4.10   Comparison of load controlled and displacement controlled incremental method.

## 4.2.2   Iterative method

An iteration approach can be schematically divided into three steps:

1. Evaluation of the internal forces,

2. Evaluation of the global stiffness matrix and

3. Solution of a system of linear equations.

Three different groups are available in DIANA, see Figure 4.11:

- The Newton Raphson method (tangent stiffness method)

- The modified Newton –Raphson method (initial stiffness method)

- The quasi-Newton approach (secant stiffness method).

Although quite similar these methods differ mainly in the second step. The Newton–Raphson method evaluates a global tangent stiffness matrix at every iteration step. The expensive evaluation of the stiffness matrix then has to be performed for each iteration. To reduce the calculation effort the modified Newton-Raphson method uses the tangent stiffness matrix of the first iteration for all following. Consequently, the second step of the iteration approach has to be performed only at the start of the increment. However, more iterations are needed until the solution converges. A third group of incremental methods is the quasi-Newton approach, which uses instead of a tangent a secant stiffness matrix. The second step of the iteration approach is simplified. However, due to the rougher approximation of the stiffness more iterations are needed than in the Newton Raphson method. In analyses performed by Johansson (1996) the BFGS method resulted in satisfying results. Therefore the BFGS method was also chosen in the work presented here.

Tangent stiffness method



Initial stiffness method



Secant stiffness method
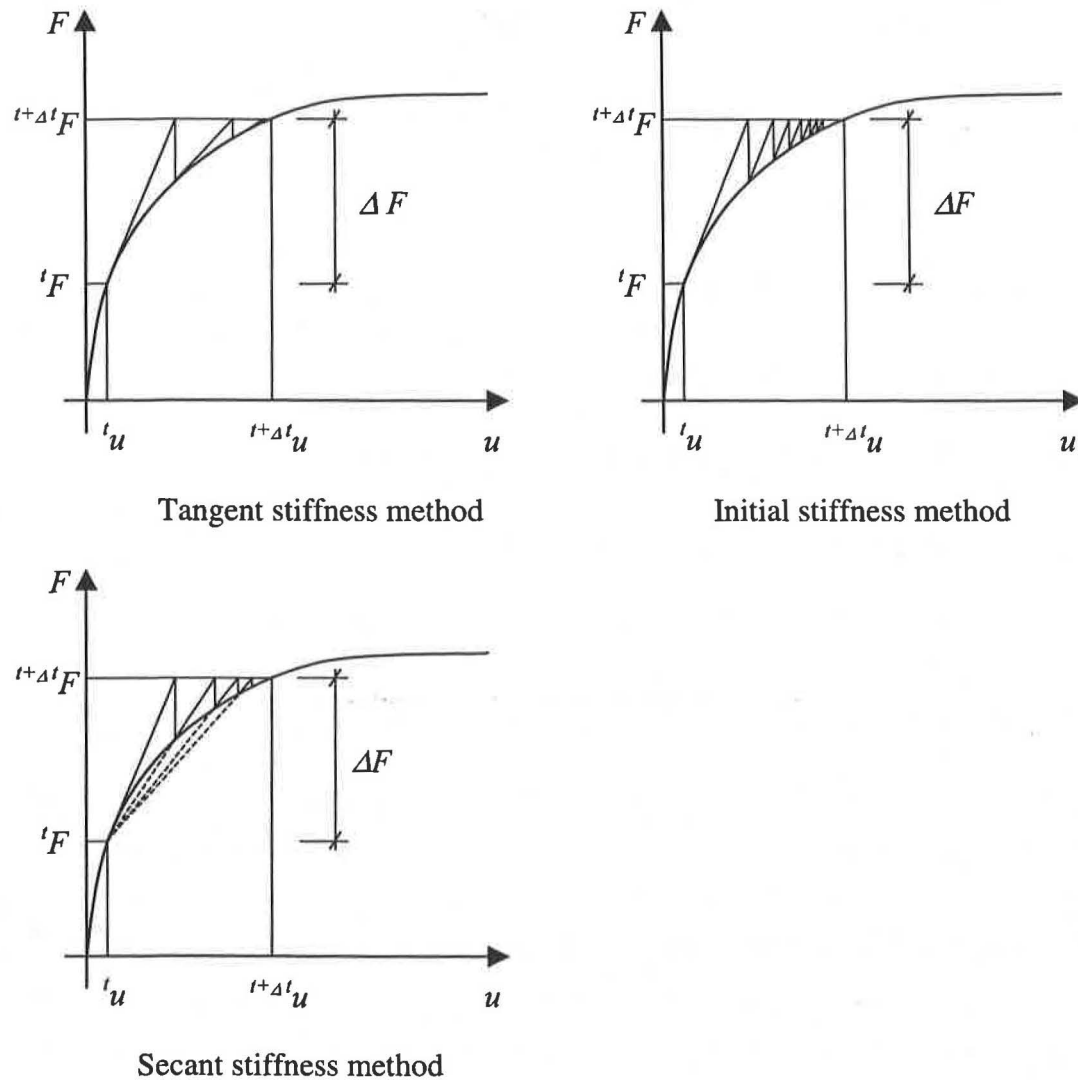
Figure 4.11    Different iteration methods for a one degree of freedom system.

## 4.3    Finite element model

The specimens RV12, RV13 and RV15 were idealised by means of two-dimensional finite element models, see Figure 4.12, Figure 4.13 and Figure 4.14. For the concrete plane-stress elements were used. Consequently, stresses out of the plane were not considered. Due to the irregular geometry of the loops rectangular 4-node and triangular 3-node elements were combined.

The reinforcement was considered by means of 2-node truss elements with one integration point. Hereby, only stresses in longitudinal direction are determined.

For the interaction between concrete and reinforcement interface elements were provided, which connect the nodes of reinforcement and the concrete. The interface elements modelled the bond behaviour along the reinforcement axis. Bond stresses perpendicular to the truss axis were not considered.
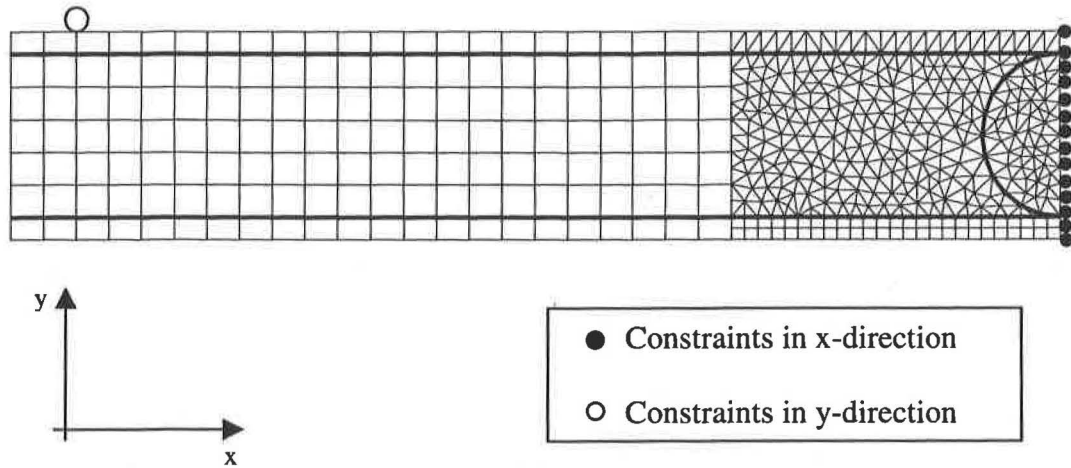


Figure 4.12    Finite element mesh for specimen RV12 using 103 truss, 204 rectangular plane stress, 539 triangular plane stress and 103 interface elements.
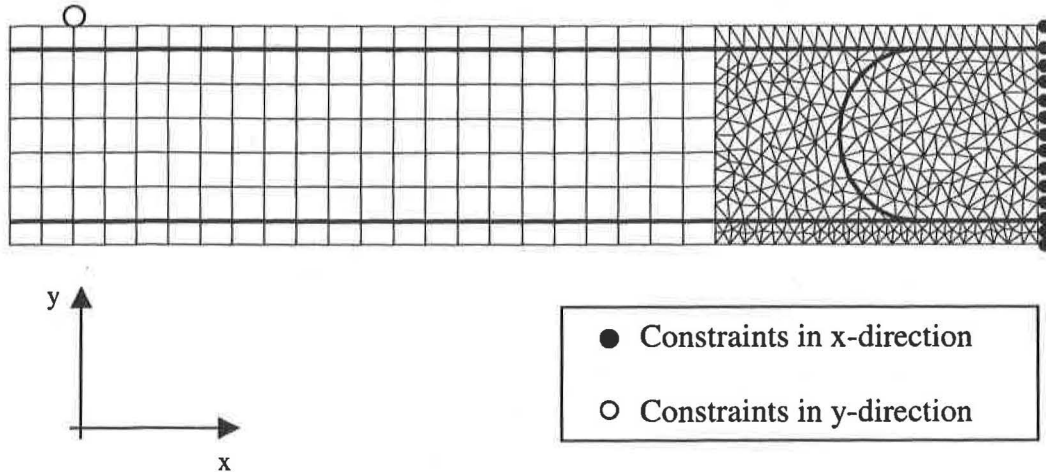


Figure 4.13    Finite element mesh for specimen RV13 using 116 truss, 146 rectangular plane stress, 648 triangular plane stress and 116 interface elements.
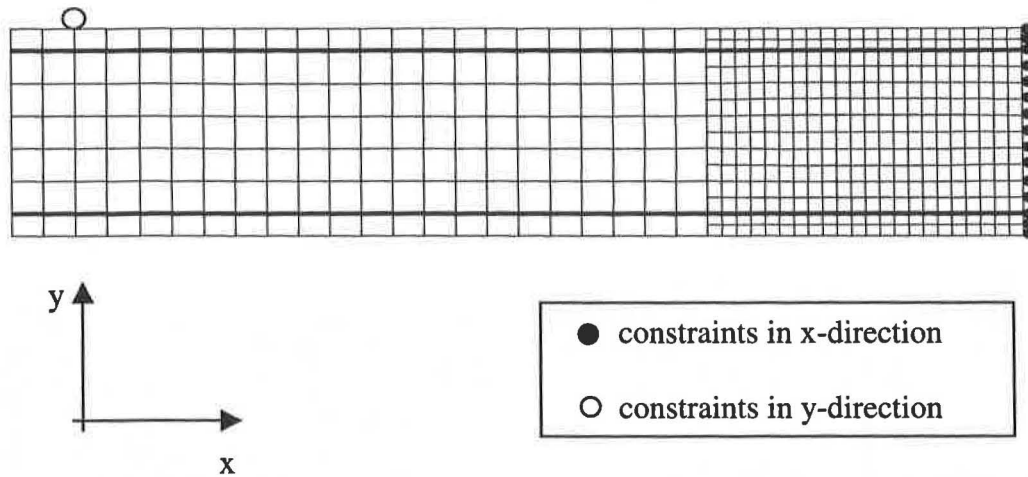
Figure 4.14    Finite element model of specimen RV15 using 88 truss, 550 rectangular plane stress and 88 interface elements.

To reduce the number of elements symmetry in the x-direction was used, so that only one half of the beam had to be modelled and the midsection correspondingly supported. Consequently, the reinforcement had to be treated in a separate way at the symmetry axis. For specimen RV15 with straight reinforcement it was sufficient to tie the reinforcement node to the constrained concrete node. However, for specimens RV12 and RV13 the interaction of the loop splices had to be considered. Therefore, the displacements of the reinforcement nodes in mid section were related to each other, see Figure 4.15.



x-direction:    $x_{n1} + x_{n2} = 0$
$x_{n3} + x_{n4} = 0$

y-direction:    $y_{n1} - y_{n2} = 0$
$y_{n3} - y_{n4} = 0$
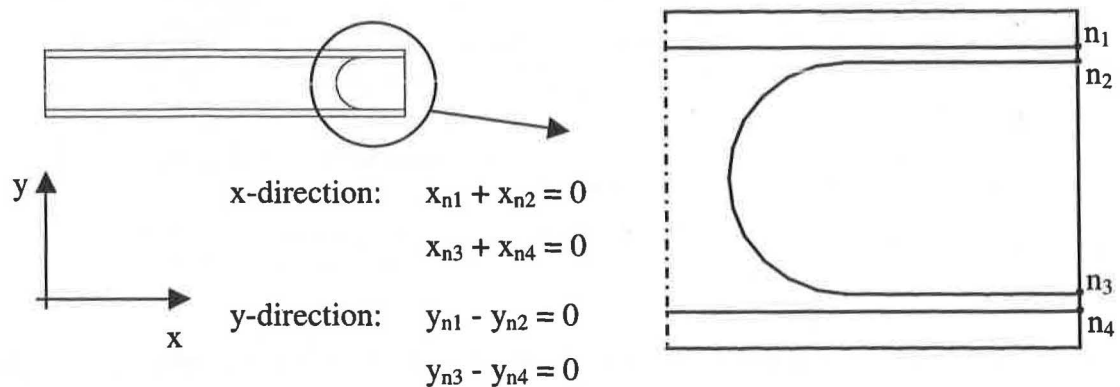
Figure 4.15    Consideration of the loop splices using symmetry. The displacements of the reinforcement nodes in mid-section were related to each other.

66

In the initial loading stage the support arrangement of the FE-model was different to the one of in the experiments. From beginning on the ends of the beams were supported. In a first load step the deformation due to the self-weight was determined. Then, the load was applied at the bottom of the specimen in mid-section; hence, the static system was determined. The loading and support plates used in the experiments were idealised by means of concentrated forces acting on single nodes.

Different mesh densities were used. In the middle of the beam, where the loop splice was located, the mesh was refined and an element edge size of about 20 mm was used. For the remaining part of the beam a coarser mesh with an element edge size of about 50 mm was used. To assure full functionality of the connection of the two parts the semi-discretised nodes of the fine mesh were tied to their neighboured nodes using a linear displacement relation, also known as interconnection.
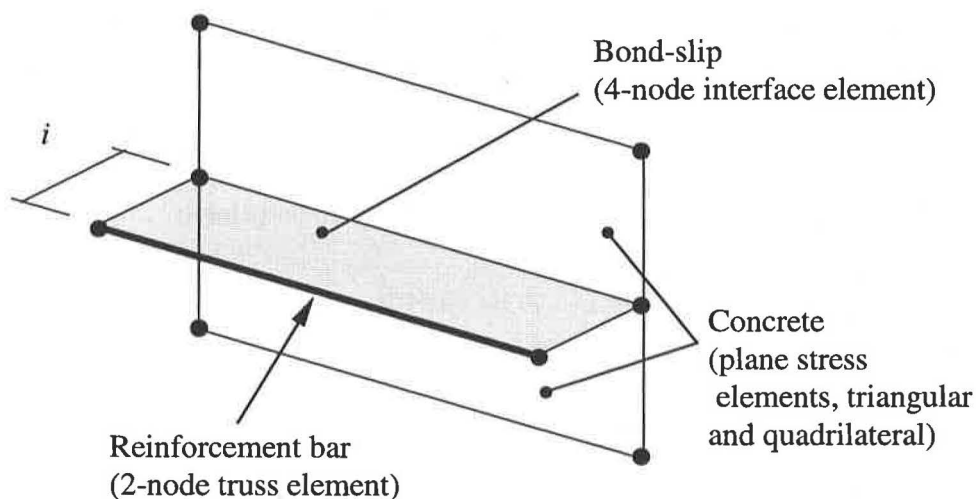


Figure 4.16    Finite element idealisation in DIANA of reinforced concrete elements using truss and interface elements. From Johansson (1996).

For the compression zone in the mid-section under the compressive reinforcement two element rows were used to consider the non-linear stress distribution. Due to stability problems at the edge element, where the concentrated force was introduced, the compression zone of specimen RV12 was modelled using rectangular elements. In specimen RV13, these problems did not occur, so that the complete mid zone could be modelled using triangular elements.

In the two-dimensional model neither spalling of the side concrete cover nor splitting along the straight part was considered. However, the model was developed to investigate the crack development in the splice zone and to analyse the dominating stress inside the loop splice for different splice lengths.

## 4.4    Results of the analysis

The influences of bond conditions and splice length were investigated. The results are presented and discussed separately for each specimen in the following sections.

The ultimate shear capacity was underestimated in all FE-analyses. With a tensile strength according to CEB-FIP Model Code, CEB (1993) and a fracture energy determined by material tests a premature shear failure prevented yielding of the reinforcement and hence a ductile behaviour. Therefore, the tensile strength and the fracture energy were increased by 25 %. It seemed reasonable to increase both since the former was determined according to CEB-FIP Model Code and the latter tested 28 days after casting, 7 days earlier than the performed experiments.

Unless stated the analyses were based on the following assumptions:

- fracture energy:    $G_f = 141$ N/m (25 % increased),
- tensile strength:    $f_t = 2.8$ N/m$^2$ (25 % increased) and
- bond conditions:    "good" bond conditions.

However, also analyses with the standard material properties and tensile strength and fracture energy varied were performed. These results are shown in Appendix C.

### 4.4.1    Specimen RV12

The test results of specimen RV12 were dominated by spalling of the edge concrete cover. In the FE-analysis spalling or splitting was omitted. Therefore, a large difference of stiffness and maximum load capacity was expected

The load-deformation relations of two FE-analyses with varied bond conditions are compared to the test results in Figure 4.17. The stiffness of the FE-analyses in the cracked state is significantly higher. Additionally, the maximum load capacity is higher than in the experiment. The results for "good" and "other" bond conditions are similar.

68

However, in case of "other" bond conditions yielding of the reinforcement was reached and a less stiff behaviour in the cracked state obtained. The stress distribution along the reinforcement for "good" and "other" bond conditions is shown in Figure 4.18 and Figure 4.19 for different load levels.
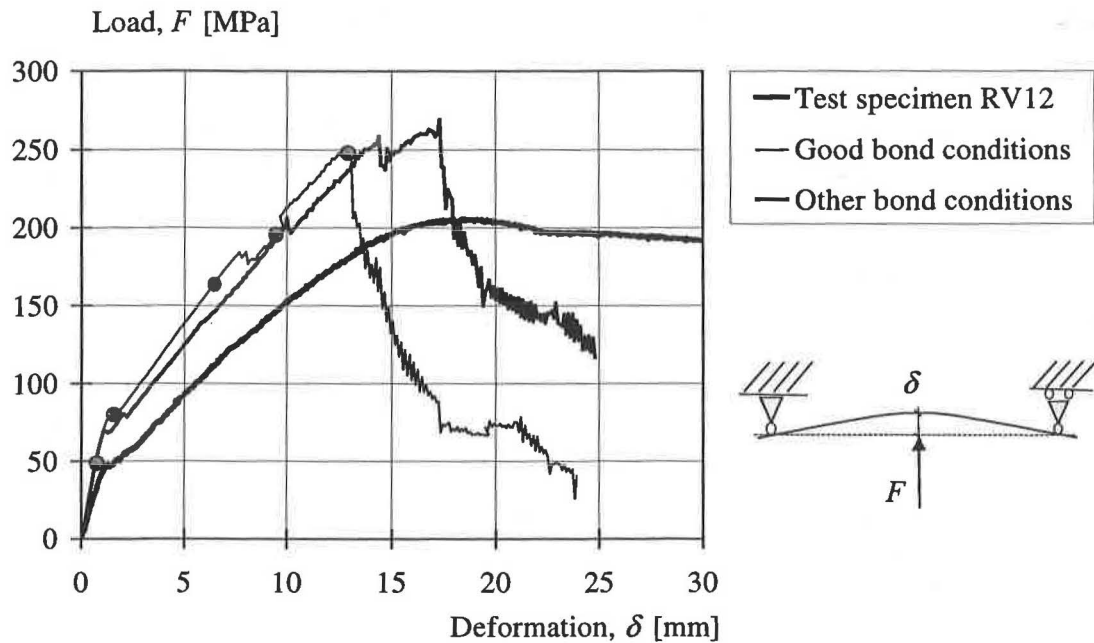


Figure 4.17    Comparison of the load deformation relation of test and FE-analyses using "good" and "other" bond conditions for specimen RV12.
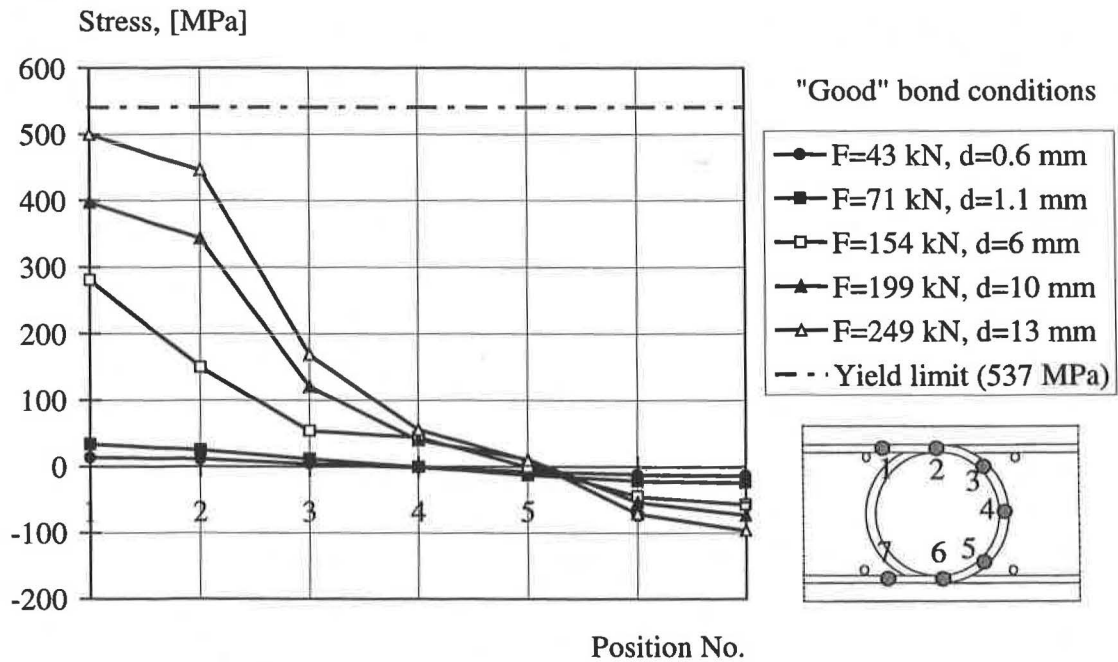
Figure 4.18    Distribution of the tensile stresses along the reinforcement loop using "good" bond conditions for specimen RV12.
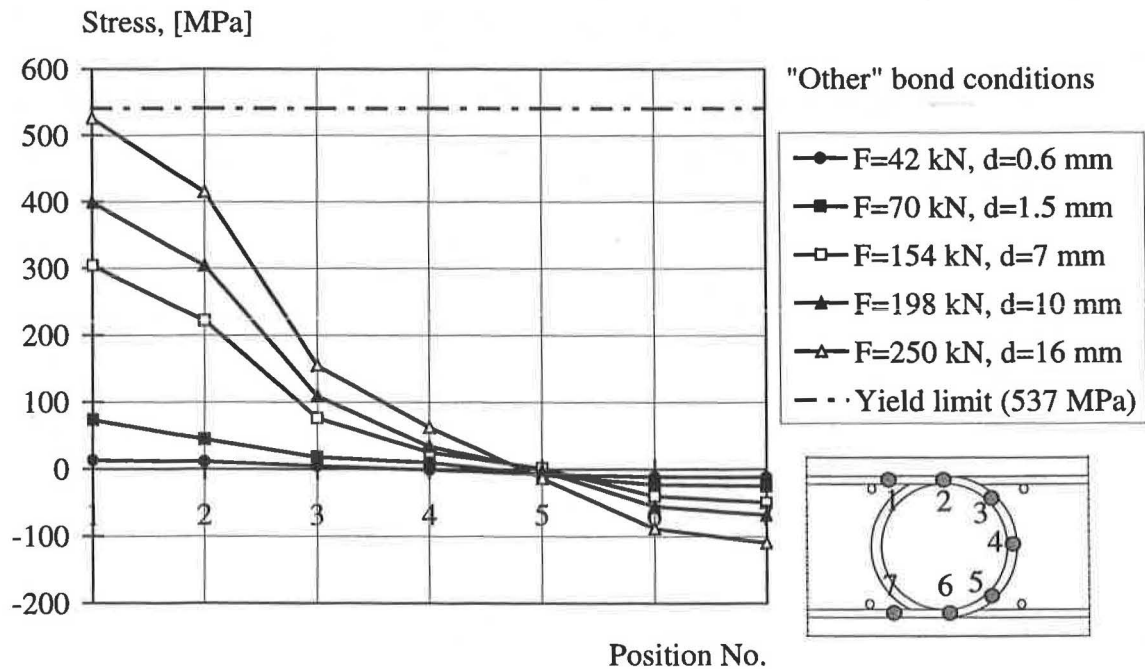


Figure 4.19    Distribution of the tensile stresses along the reinforcement loop using "other" bond conditions for specimen RV12.

A comparison of the stresses of FE-analyses and test is shown in Figure 4.20. Hereby, the stresses obtained in the test are higher than in the FE-analyses. However, the deformation of the test specimen at the same load level is as in the FE-analyses is considerably higher.

Stress, [MPa]
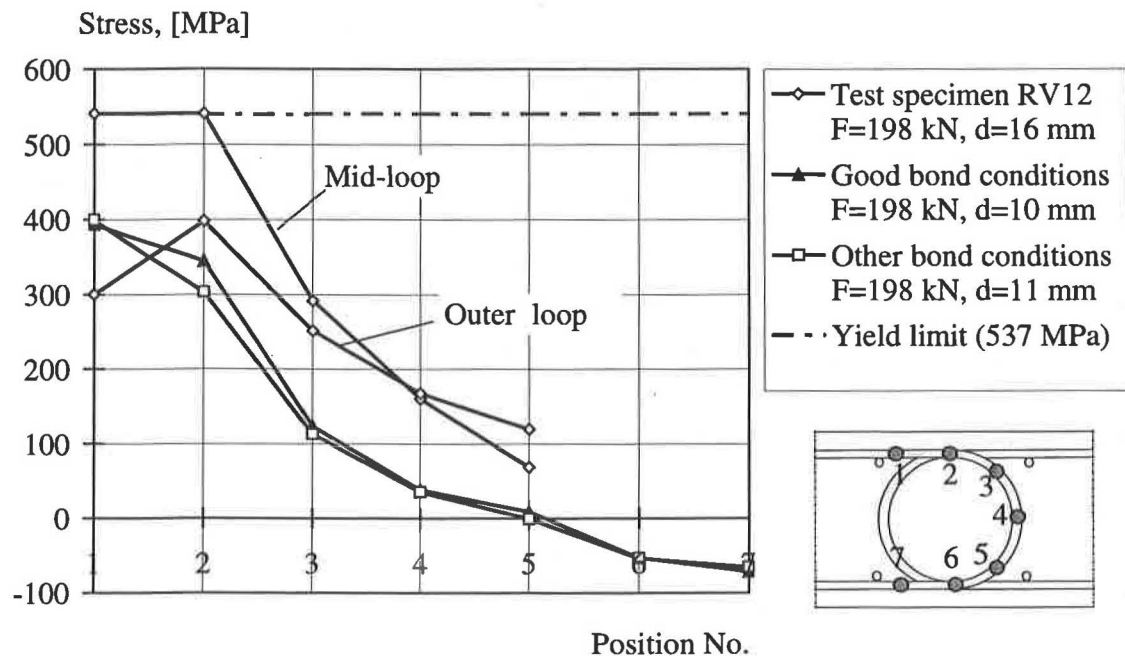


Figure 4.20    Distribution of the tensile stresses along the reinforcement loops for specimen RV12. The results of the test and FE-analyses are compared.

In Figure 4.21 the crack pattern of the test and a FE-analysis with "good" bond conditions are compared. A strain limit of 0.003 was chosen when showing the crack pattern; i.e. all elements in which the principal strain was larger than 0.003 are marked.



F = 249 kN, d = 13 mm                    At the end of testing
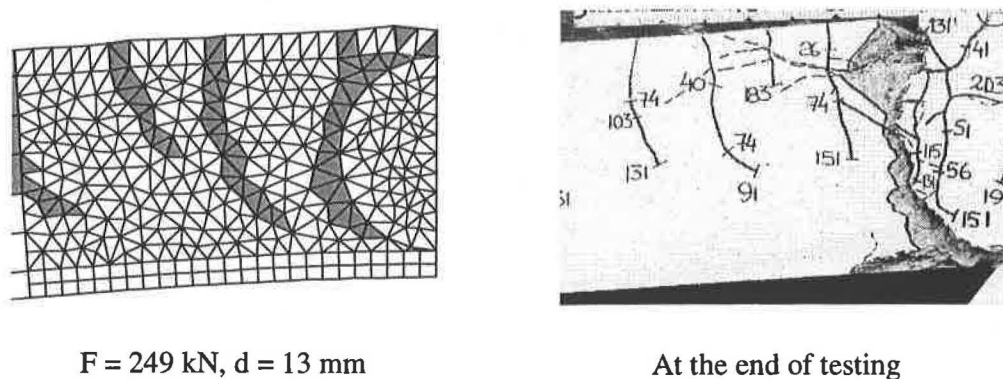
Figure 4.21    Comparison of crack pattern of FE-analyses and test of specimen RV12. The grey marked elements indicate a principal strain larger than 0.003.

71

## 4.4.2 Specimen RV13

The load-deformation relations for the FE-analyses using "good" and "other" bond conditions compared to the test results are shown in Figure 4.22. The results for "good" and "other" bond conditions are similar, even though a higher maximum resistance was reached using "other" bond conditions. The in the tests obtained load drop due to splitting, see Section 3.5.2, could not be modelled since the radial components of the bond stresses were omitted, see Section 4.4.3.
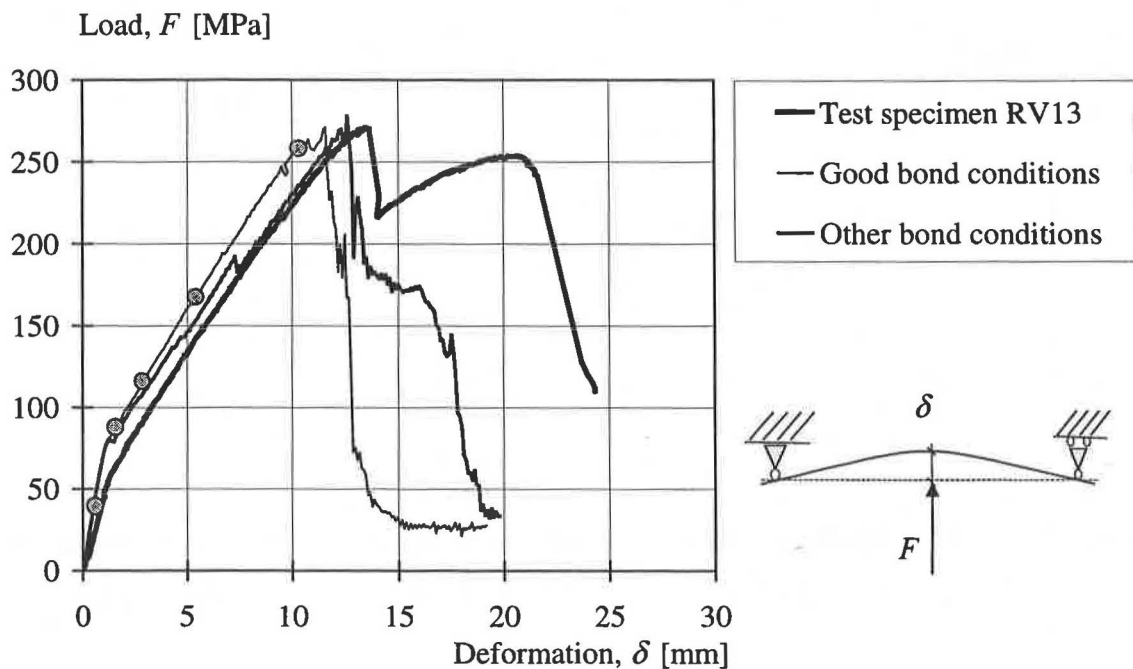


Figure 4.22  Comparison of the load-deformation relations of specimen RV13 for test and FE-analyses using "good" and "other" bond conditions.

The distribution of the stresses along the reinforcement loops for "good" and "other" bond conditions is shown in Figure 4.23 and Figure 4.24.
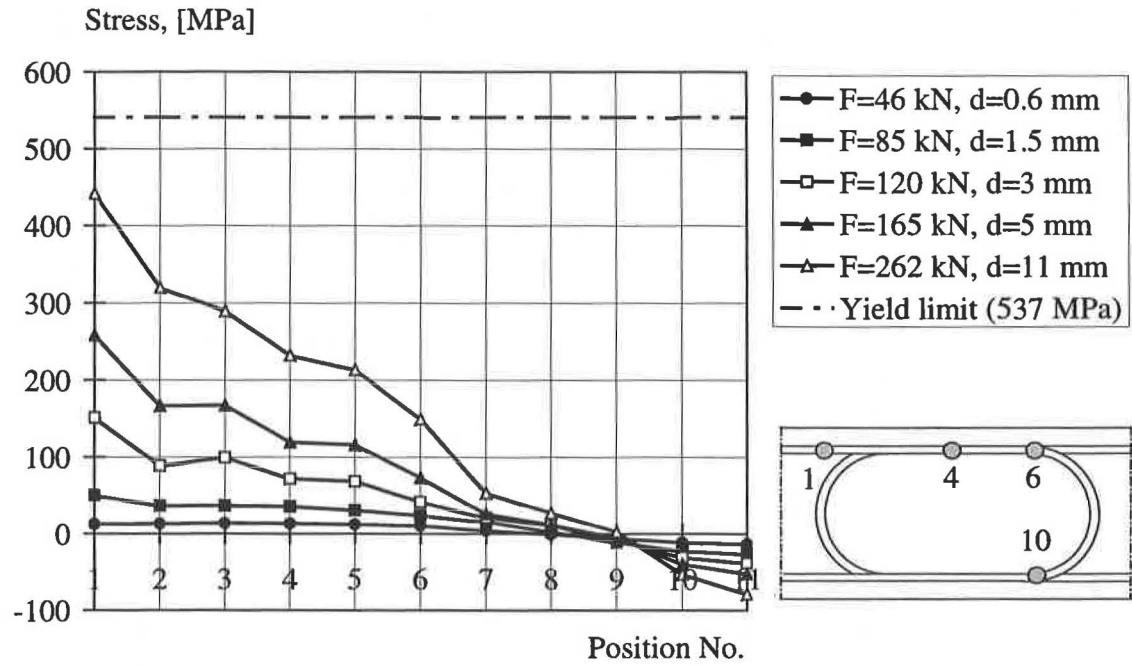
Figure 4.23 Distribution of the tensile stresses along the reinforcement loop using "good" bond conditions for specimen RV13.
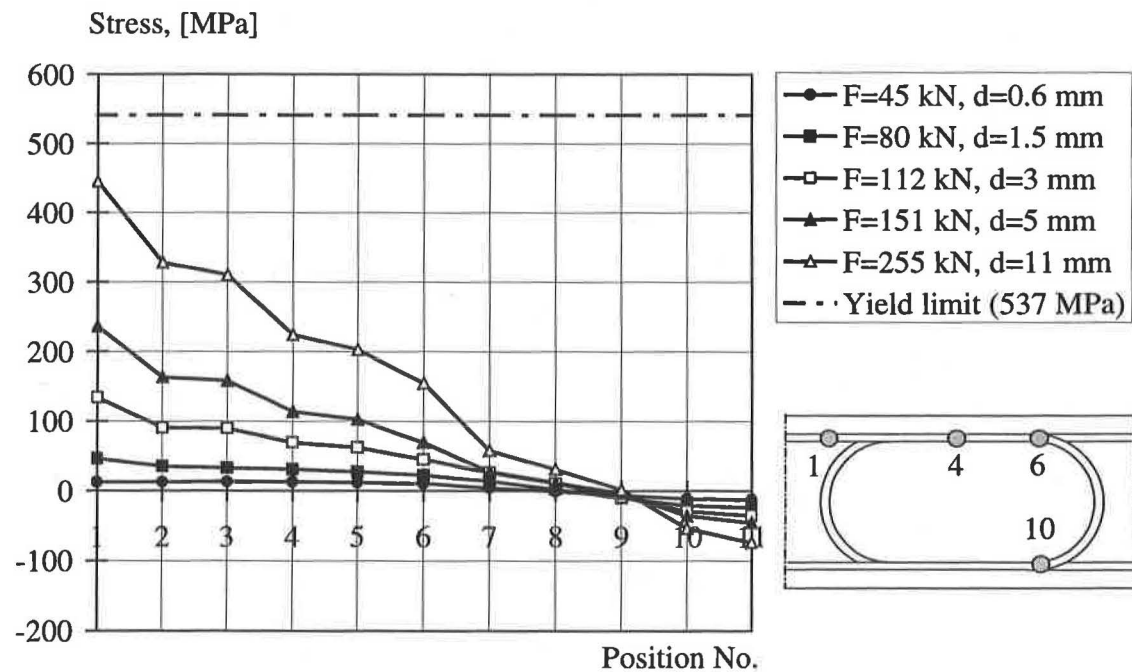


Figure 4.24 Distribution of tensile stresses along the reinforcement loop using "other" bond conditions for specimen RV13.

A comparison of the stresses of FE-analyses and test can be found in Figure 4.25. The stress distribution is very similar. In the FE-analyses as in the test the stresses are strongly reduced before the curved part. Almost no difference in the stresses in the reinforcement is obtained by varying the bond conditions.
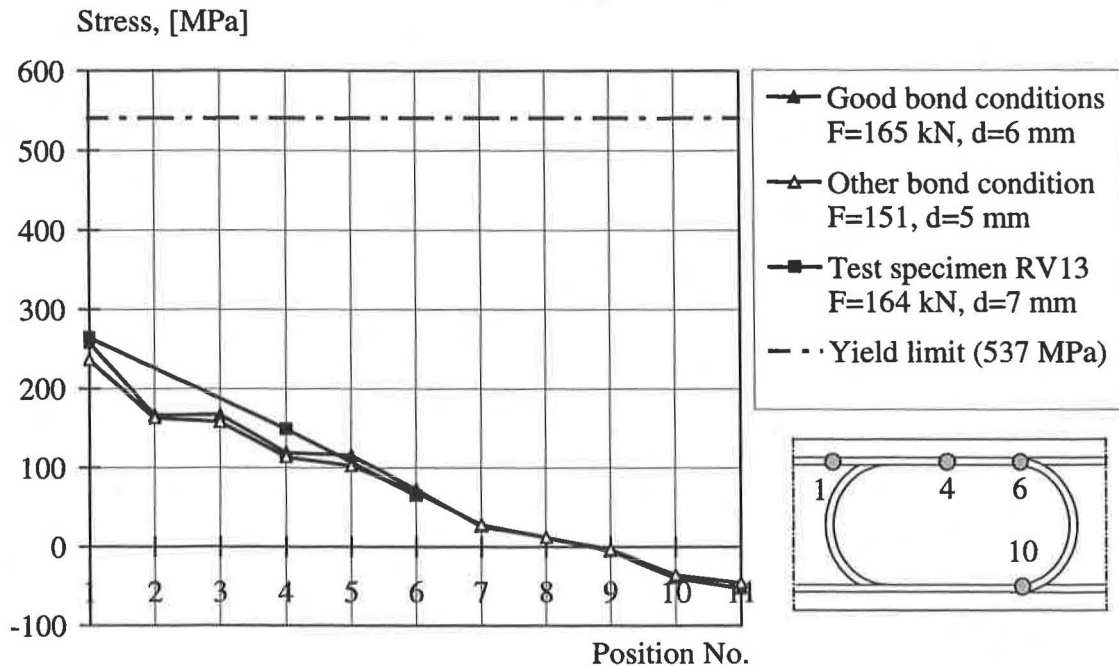


Figure 4.25    Comparison of tensile stresses of test and FE-analyses for specimen RV13.

The crack pattern of the analysis with "good" bond conditions and the test is compared in Figure 4.26. In both cases cracks are following the loop.
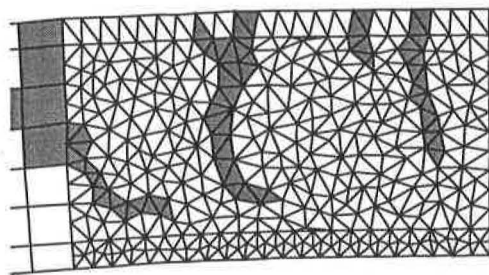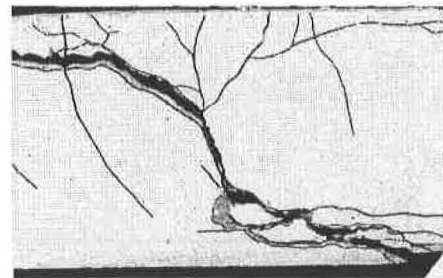


$F = 262$ kN, $\delta = 11$ mm                    At the end of testing

Figure 4.26    Comparison of crack pattern of the FE-analysis using "good" bond conditions and the test of specimen RV13. The grey marked elements indicate a principal strain larger than 0.003.

### 4.4.3 Specimen RV15

The comparison of the load-deformation relation for "good" and "other" bond conditions for specimen RV15 are shown in Figure 4.27. Hardening of the reinforcement was reached. However, a shear failure occurred before rupture of the reinforcement bars could take place. With "other" bond conditions a higher load capacity was reached.
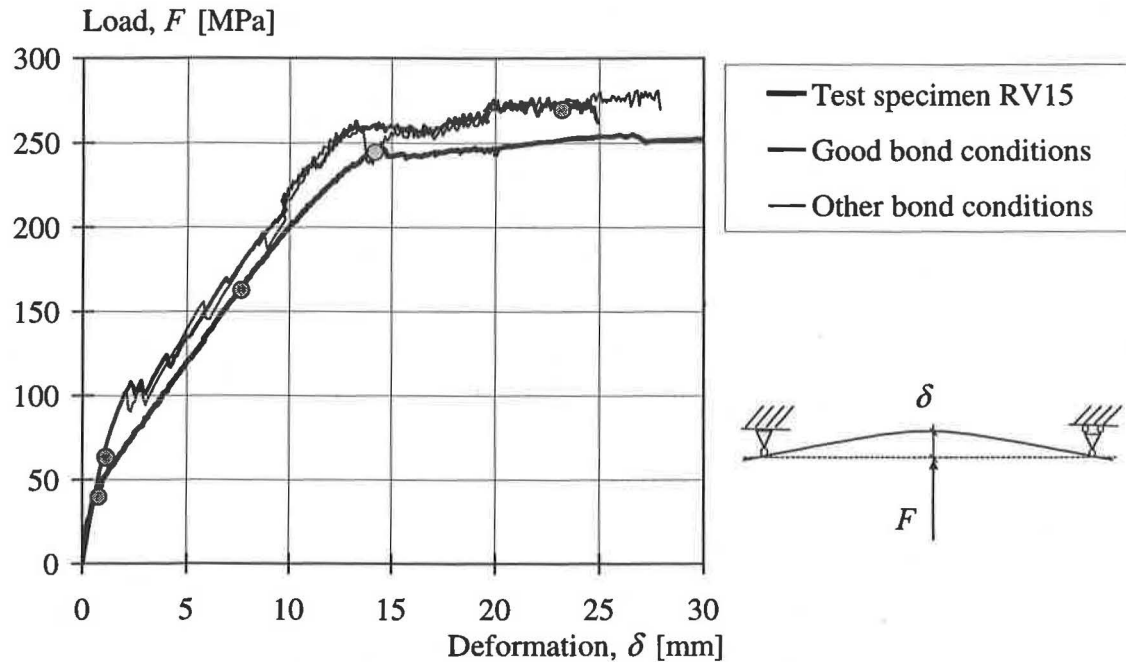


Figure 4.27    Comparison of the load-deformation relations of specimen RV15 for test and FE-analyses using "good" and "other" bond conditions.

The distributions of the tensile stresses along the reinforcement using "good" bond conditions are shown in Figure 4.28. A comparison with the stresses obtained in the test, see Figure 4.29, shows that in the test yielding of the reinforcement was reached earlier than in the FE-analyses, since the stiffness of the FE-model was higher than of the test specimen RV15.
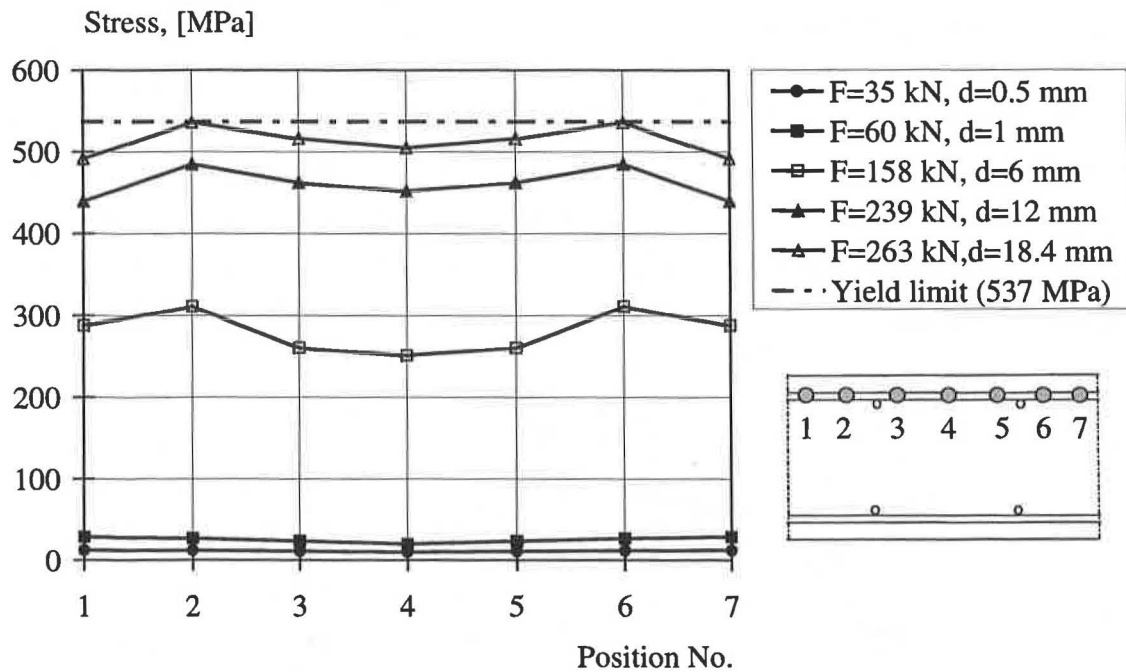
Figure 4.28    Tensile stresses in the reinforcement bars of the FE-analysis using "good" bond conditions for specimen RV15.
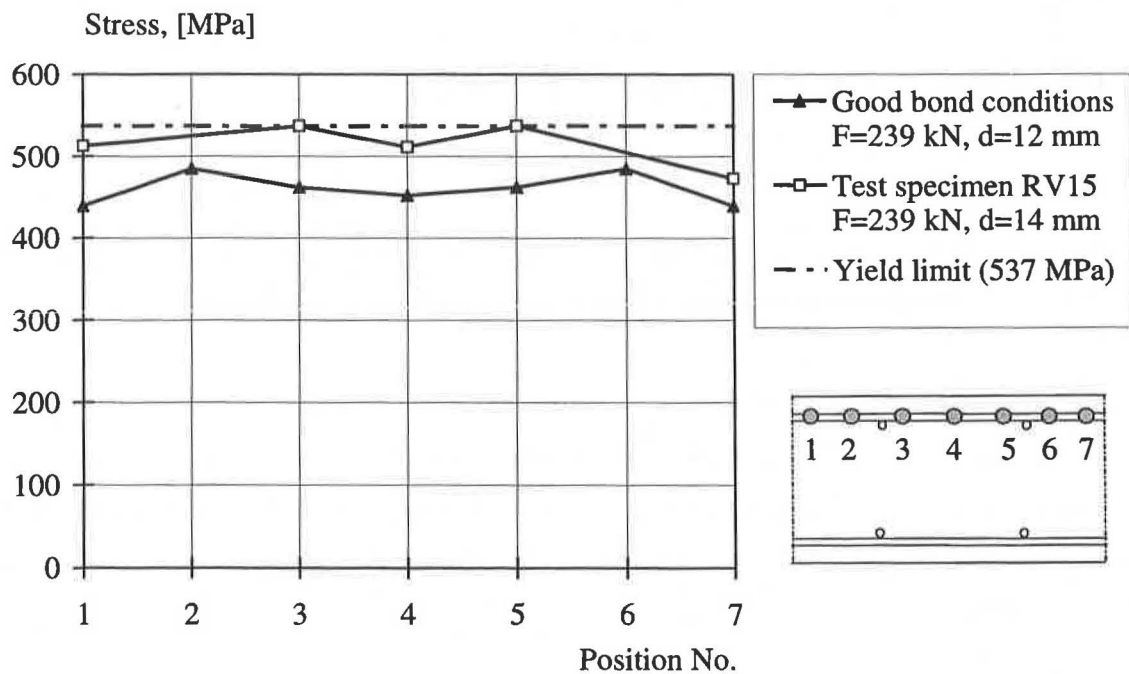


Figure 4.29    Comparison of the stresses in the reinforcement bars of test specimen and FE-analyses for specimen RV15.

The crack pattern of test and FE-analyses is compared in Figure 4.30. It can be seen that the propagation of the inclined cracks is influenced by the quadrilateral elements.



F = 258 kN, δ = 26.1 mm                              At the end of testing
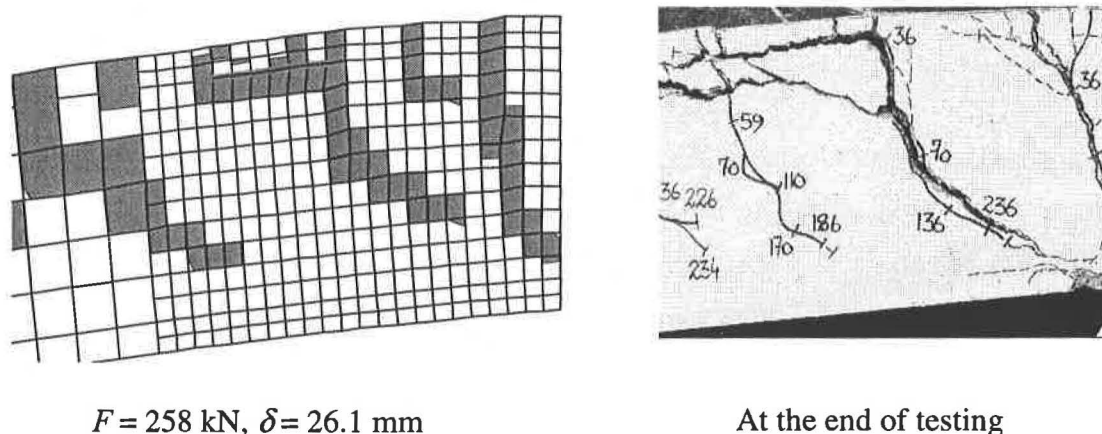
Figure 4.30    Comparison of the crack pattern of a FE-analysis using "good" bond conditions and the test of specimen RV15. The grey marked elements indicate a principal strain larger than 0.003.

## 4.5    Concluding comments concerning the non-linear FE-analyses

The results of the FE-analyses and experiments correspond well in case of an increased fracture energy and tensile strength. The load-deformation relations, the distribution of the stresses of the reinforcement and the crack pattern are similar. However, the shear capacity of the FE-models was underestimated. Even when yielding of the reinforcement was reached the ductile behaviour was relatively short. One reason for this behaviour is the overestimated stiffness of the specimens. Furthermore, the reinforcement was modelled using truss elements, so that the dowel action between reinforcement and concrete was not considered.

The results of the FE-analyses for specimen RV12 disagree with the results of the experiment, since spalling of the side concrete cover was not considered in the two-dimensional FE-model. Therefore, the maximum load of the experiment is smaller and the tensile stresses along the reinforcement loop correspondingly higher.

The different bond conditions examined here have a small influence on the stress distribution along the loop even though they influence the crack development and the

77

load-deformation. In contrary, the crack development and the load-deformation are influenced by the bond conditions. Using "good" bond conditions the reinforcement loops attract cracks, since the bond slip relation is stiffer. This higher stiffness due to "good" bond conditions also leads to a stiffer responds of the specimens as shown in Figure 4.17, Figure 4.22 and Figure 4.27.

Furthermore, the bond condition has a strong influence on the relation of the tensile stresses to the radial pressure, see Appendix D. The radial pressure $P$ is activated after a certain slip of the reinforcement. With "other" bond conditions this slip is earlier activated, hence the radial pressure, which may lead to spalling, acts earlier.

# 5 Conclusion

The minimum splice length for splicing of reinforcement loops outside frame corners without a transverse reinforcement is limited to 600 mm according to the Swedish Shelter regulation, Swedish Rescue Service Agencies (1998). In this way spalling of the edge concrete cover shall be avoided, so that a load capacity of a comparable specimen with continuous reinforcement bars can be obtained.

Experiments and non-linear finite element analyses were conducted to investigate the influence of varying splice length and beam width.

With an elongated splice length of 600 mm spalling of the edge concrete cover could be prevented. Most of the anchorage was provided by the straight part and the radial pressure due to the bend was therefore sufficiently small. However, a splitting failure along the straight bars occurred.

When the splice length was composed by two semi-circles without an additional straight part spalling of the edge concrete cover occurred. The maximum steel stress was acting at the beginning of the curved part. Consequently, the radial pressure caused spalling of the edge concrete cover. The maximum load was reduced by the capacity of the two outer bars. Nevertheless, the post-peak behaviour was still ductile.

An increased beam width had a favourable influence on the load capacity by constant reinforcement ratio. Again, the load capacity was reduced by the two outer loops. In relation more remaining loops could carry the load after the loss of the outer loop pairs.

The bond conditions have an important influence on the acting radial pressure. With increasing bond quality the slip, which is necessary to activate the radial pressure on the concrete is delayed. With delayed radial pressure the spalling of the edge concrete cover is also delayed.

# 6 Suggestions for further studies

In the present work the splicing of reinforcement loops were investigated by means of a three-point test set-up. Consequently, the loop splice was subjected by a bending moment and a shear force. To be able to investigate the influence of the shear force it is required to do similar experiments or non-linear finite element analyses based on a four-point test set-up.

In the non-linear finite element analyses the specimens were investigated based on a two-dimensional finite element model; thus the influence of the spalling of the side concrete cover was omitted. An investigation of loop splicing by means of a three-dimensional non-linear finite element model would be valuable, since the spalling effect could be considered.

The work carried out was limited on splicing of reinforcement loops without a transverse reinforcement in the splice zone. It might be valuable to study the influence of a transverse reinforcement under carefully consideration of its anchorage in the side concrete cover and a possibly unfavourable influence on the construction process.

# 7 References

Boverket (1994): Boverkets handbok för Betongkonstruktioner BBK 94, Band 1, Konstruktion (Boverket's Handbook for Concrete Structures, BBK 94, Vol. 1, Design. In Swedish). Boverket, Byggavdelningen, Karlskrona, Sweden.

BST Byggstandardisieringen (1987): Betongprovning med Svensk Standard, BST handbok 12, (Concrete testing according to Swedish Standard, BST Handbook 12. In Swedish).SIS-standardisieringskommisionen I Sverige och Svensk Byggtjänst.

CEB (1993): CEB-FIP Model Code 1990, Design Code. Thomas Telford, Lausanne, Switzerland.

Dragasović M., van den Beukel, A., Gijsbers F.B.J. (1975): Loop connections between precast concrete components loaded in bending. HERON vol. 20 1975 no. 3.

Eurocode 2 (1991): ENV1992-1-1, Eurocode 2: Design of Concrete Structures.

Femsys (1998): FEMGV User Manual,Version 5.2. Femsys Limited, 158 Upper New Walk, Leicester, LE1 7QA.

Franz G., Timm G. (1973): Versuche zur Haken-und Schlaufenverbindung bei biegebeanspruchten Platten. DafStb Heft 226. (Test of hook and loop connections for bending subjected plates. DafStb booklet 226. In German)

Imran I. and Pantazopoulou S.J. (1996): Experimental Study of Plain Concrete under Triaxial Stress. ACI Materials Journal 93-M67. Nov-Dec 1996.

Johansson M. (1997): New Reinforcement Detailing in Concrete Frame Corners of Civil Defence Shelters. Non-linear Finite Element Analyses and Experiments. Chalmers University of Technology, Division of Concrete Structures, Publication 96:1, Göteborg, Sweden.

Kordina K., Fuchs G. (1972): Untersuchungen an Übergreifungs-Vollstößen mit hakebförmig-gebogenen Rippenstählen, Universität Braunschweig (Studies of Splicing of hook-formed bars. University of Technology, Braunschweig. In German.).

Lundgren K. (1999): Three-Dimensional Modelling of Bond in Reinforced Concrete; Theoretical Model, Experiments and Applications. Chalmers University of Technology, Division of Concrete Structures, Publication 99:1. Göteborg, Sweden.

Magnusson J. (1997): Bond and Anchorage of Deformed Bars in High-Strength Concrete. Division of Concrete Structures, Chalmers University of Technology, Publication 97:1. Göteborg, Sweden.

Plos M. (1996): Finite Element Analyses of Reinforced Concrete Structures. Division of Concrete Structures. Chalmers University of Technology, Compendium 96:14, Göteborg, Sweden.

RILEM 50-FMC (1985): Determination of the fracture energy of mortar and concrete by means of three-point bend tests on notched beams. Materials and Structures, Vol.18, pp. 285-290.

Swedish Rescue Services Agency (1998): Skyddsrumsregler SR, Produktion och vidmakthållande Räddnings Verket. 1998 Rädningsverket, Karlsstad.

Tepfers R. (1973): A theory of Bond Applied to Overlapped Tensile Reinforcement Splices for Deformed bars. Division of Concrete Structures, Chalmers University of Technology, Publication 73:2, Göteborg, Sweden.

Timm G. (1969): Untersuchungen zur Verbindung von Stahlbetonplatten mit hakenförmig gebogenen Stäben. Fakultät für Bauingenieur- und Vermessungswesen der Universität Karlsruhe (TH). (Examination of connections of reinforced concrete plates using hook-formed bars. Department of Civil engineering. University of Technology Karlsruhe.).

TNO (1998): Diana-Finite Element Analysis. User's Manual release 7. TNO Building and Construction Research. Division of Engineering Mechanics and Information Technology, Delft, The Netherlands.

# Appendixes

# Appendix A

# A Drawings of test specimens and arrangement of strain gauges

## A.1 General dimensions
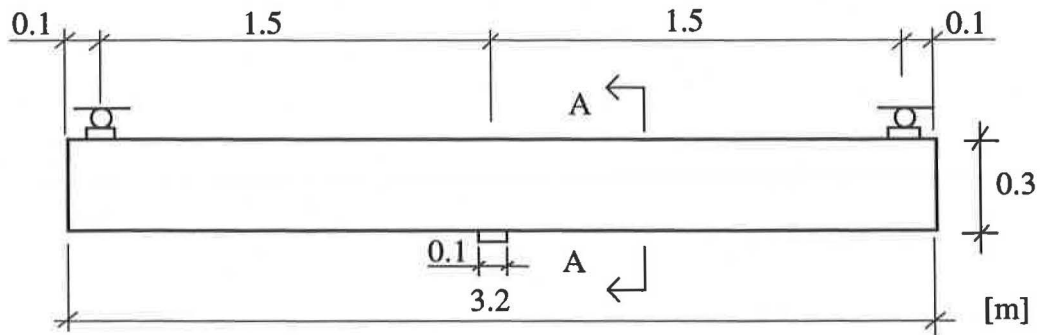


Figure A.1    Side elevation of specimen RV12, RV13, RV14, RV15.
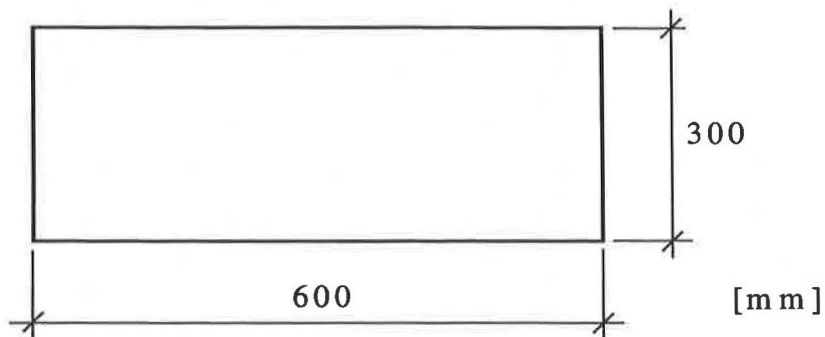


Figure A.2    Transverse section A-A of specimen RV12, RV13, RV15.
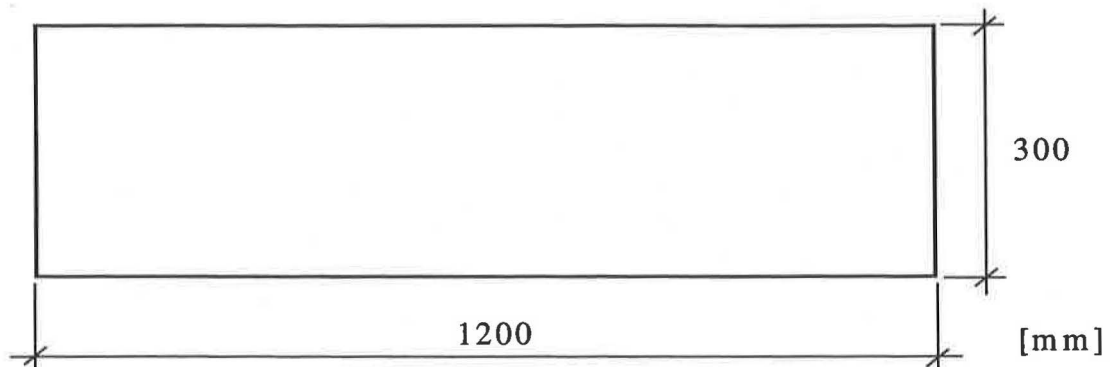


Figure A.3    Transverse section A-A of specimen RV14.

## A.2    Reinforcement detailing

### A.2.1  Specimen RV12
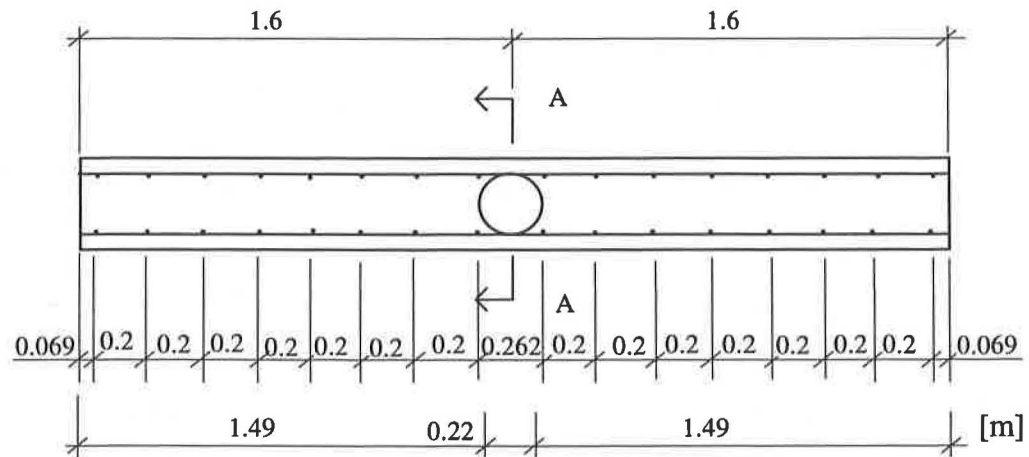


Figure A.4    Reinforcement detailing of specimen RV12 (side elevation).
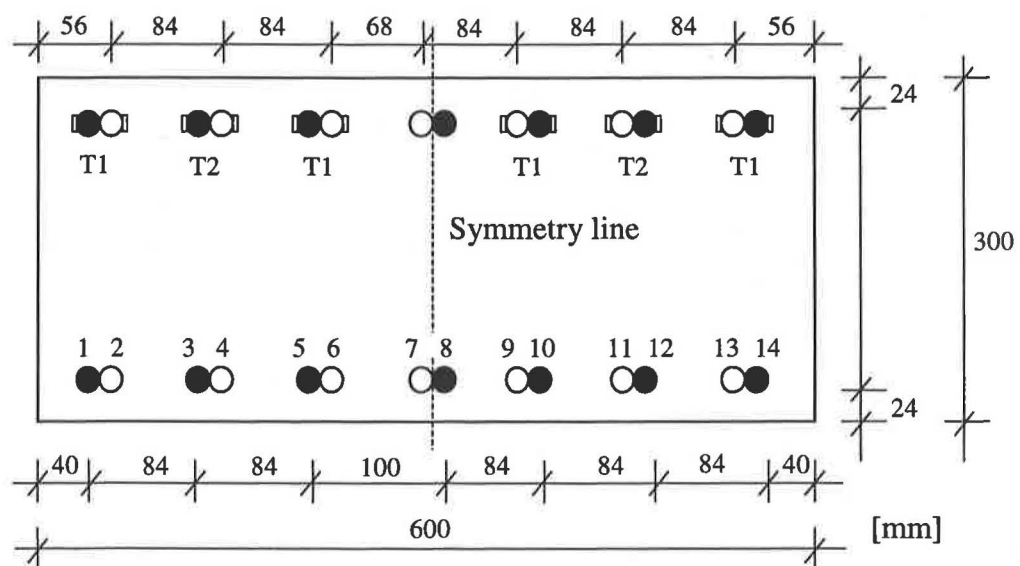


Figure A.5    Reinforcement detailing of specimen RV12 (transverse section A-A). T1 and T2 mark the type of strain gauge arrangement used, see Figure A.6 and A.7.
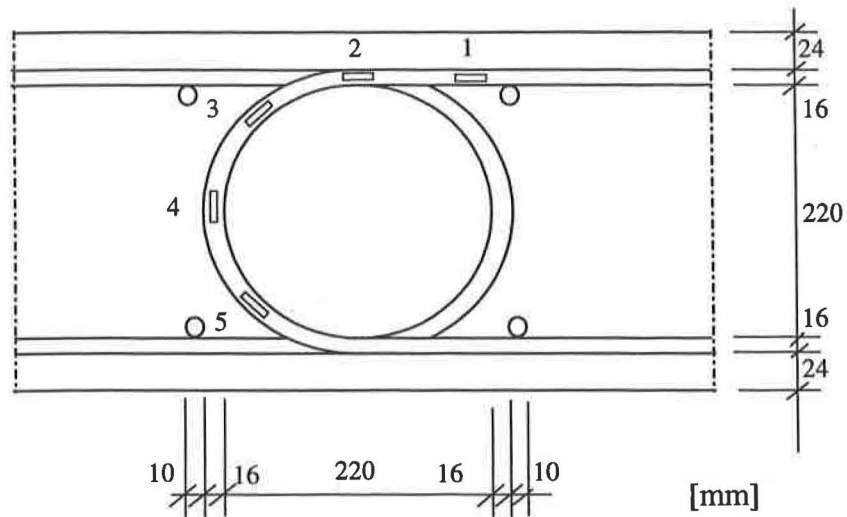
Figure A.6    Type 1 (T1) of strain gauge arrangement in specimen RV12.
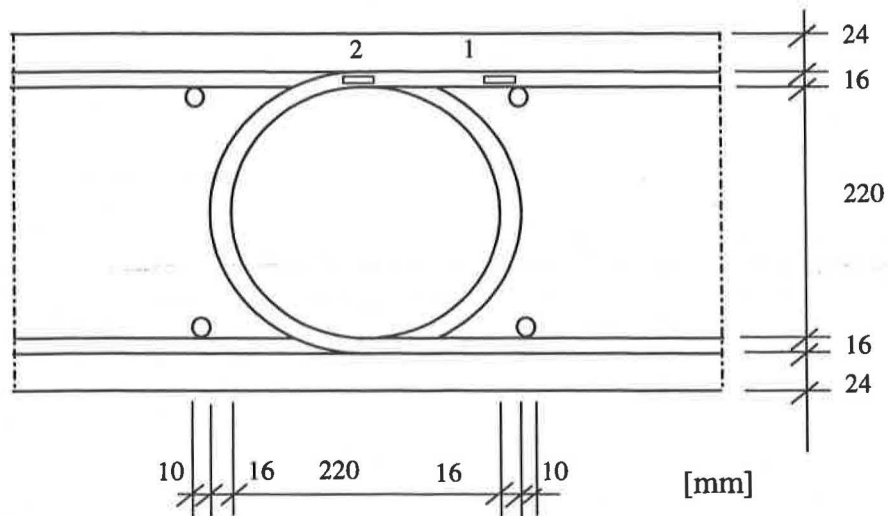


Figure A.7    Type 2 (T2) of strain gauge arrangement in specimen RV12.

14φ 16 (l=3.51 m)                                    32φ 10 (l=0.57 m)
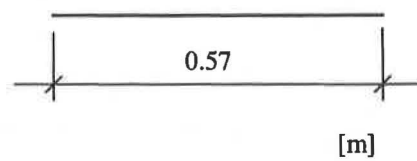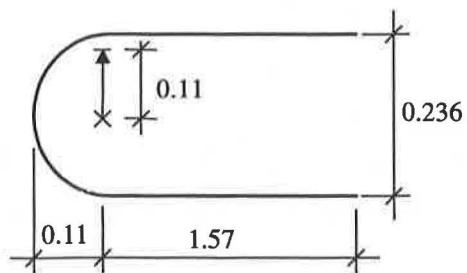


Figure A.8    Reinforcement in specimen RV12

A.3
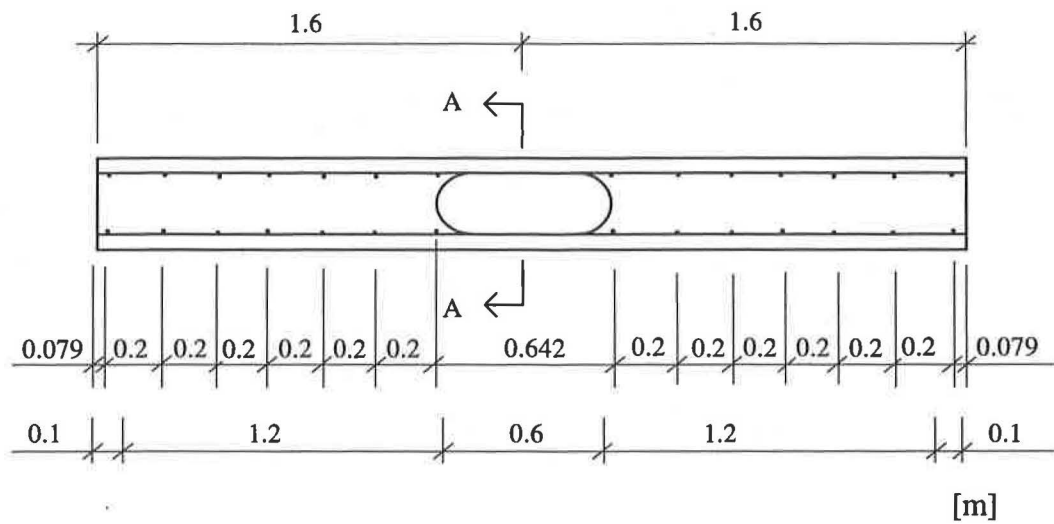
## A.2.2 Specimen RV13



Figure A.9    Reinforcement detailing of specimen RV13 (side elevation).
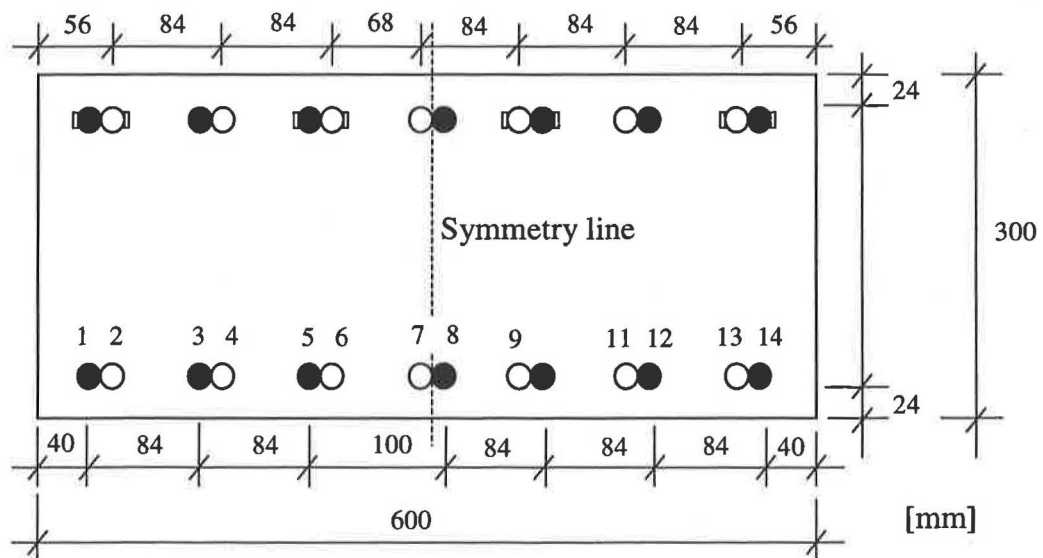


Figure A.10    Reinforcement detailing of specimen RV13 (transverse section A-A).
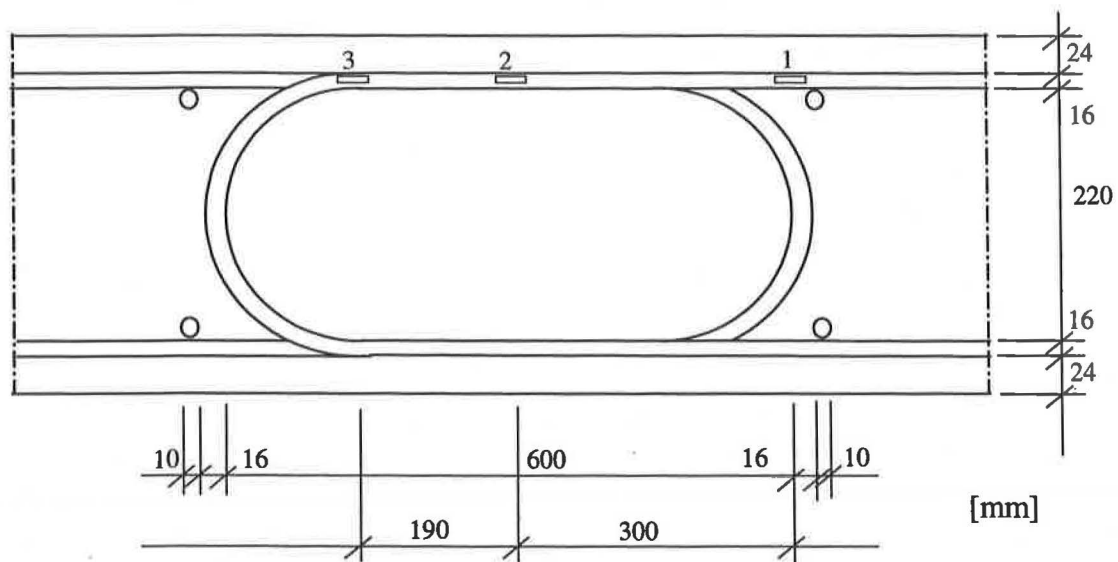
Figure A.11   Position of the strain gauges in specimen RV13.
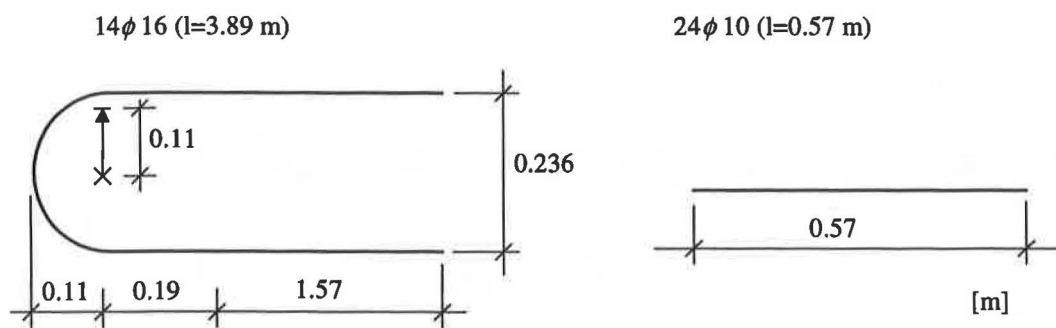


Figure A.12   Reinforcement in specimen RV13

## A.2.3 Specimen RV14
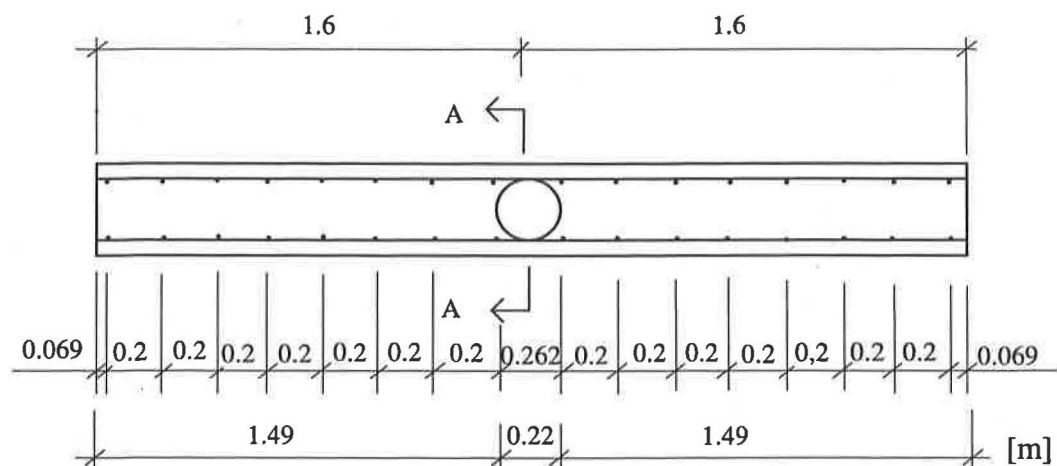


Figure A.13   Reinforcement detailing of specimen RV14 (side elevation).
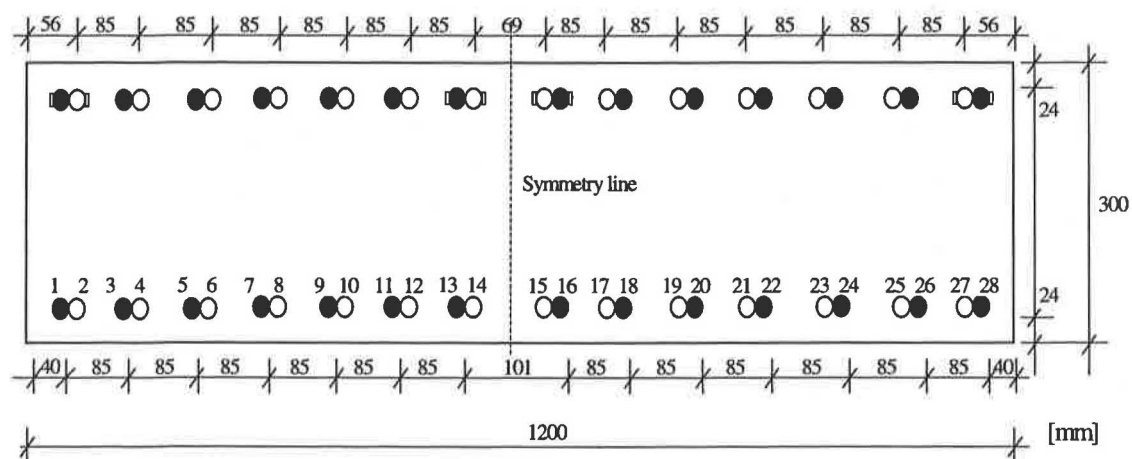


Figure A.14   Reinforcement detailing of specimen RV14 (transverse section A-A).

Figure A.15    Position of the strain gauges in specimen RV14.

28ϕ 16 (l=3.89 m)                    32ϕ 10 (l=0.57 m)



Figure A.16    Reinforcement in specimen RV14.
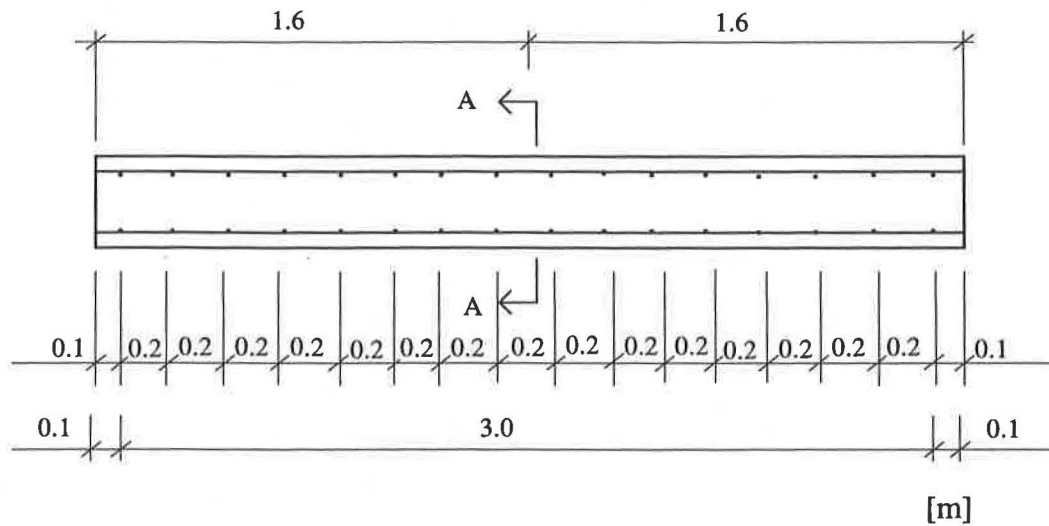
## A.2.4  Specimen RV15



Figure A.17   Reinforcement detailing of specimen RV15 (side elevation).
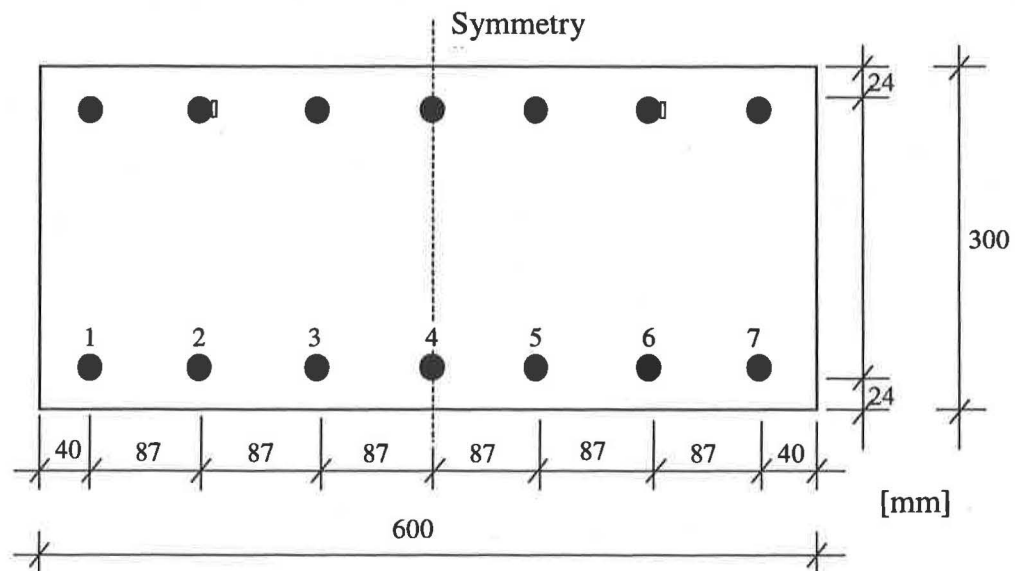


Figure A.18   Reinforcement detailing of specimen RV15 (transverse section A-A).

Figure A.19   Position of the strain gauges in specimen RV15.

14$\phi$16 (l=3,14 m)                     32$\phi$10 (l=3,14 m)



Figure A.20   Reinforcement in specimen RV15.

A.9

# Appendix B

# B Material tests

The material properties of concrete and steel in compression and tension are determined by material tests. These material tests are conducted by a standardised process depending on the regulation used. In this way, it is possible to compare different test-series, knowing the properties of the utilised materials. In the present study, the properties were tested according to Swedish standard, BST Byggstandardiseringen (1991).

## B.1 Concrete

For concrete the following properties were tested:

- compressive strength
- Young's modulus in compression
- fracture energy.

The test results for concrete depend mainly on the form and treatment of the test specimens. The main influences on the results are:

- test specimen's geometry and dimensions, the
- age of the specimen at testing, and the
- way of curing until the test date.

In the following sections the testing processes are mentioned and compared to the European code ENV 206 and the German code DIN 1048.

Additionally, the grading curves for the aggregates are shown on Page B.9 and B.10.

### B.1.1 Compressive strength and Modulus of Elasticity under compression

The compressive strength was tested on cubes and cylinders at an age of 28 days and additionally also at the first day of the full-scale tests. The dimensions were chosen according to Swedish standard and are shown in Figure B.1. In this standard, the curing process differs for cubes and cylinders. The cubes stay in the formwork for one day,

then they are stored four days under water with a temperature of around 20° Celsius. Afterwards, they are placed in air under normal conditions until the test age is reached. Whereas, the cylinders stay one day in the formwork and are then stored under water until their test age is reached. An overview of the regulation for the determination of the compressive strength according Swedish standard, ENV 206 and DIN 1048 are shown in Table B.1.



a) Cube

a) Cylinder
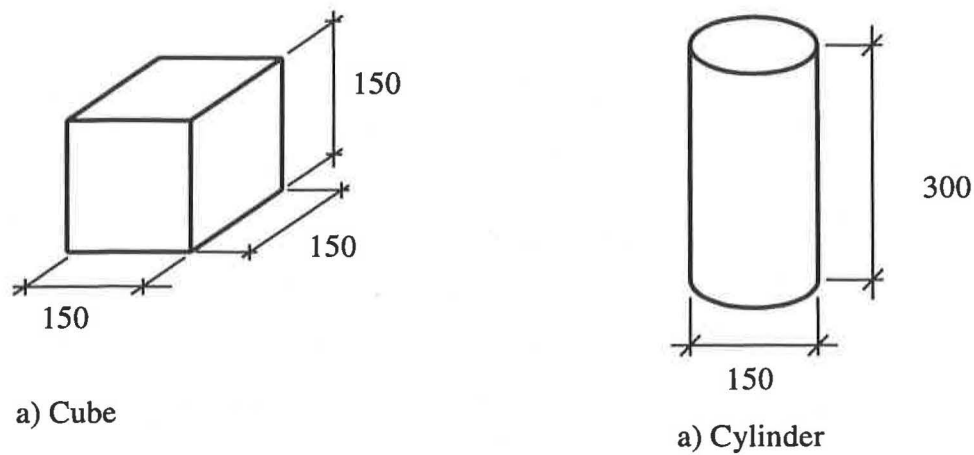
Figure B.1    Test specimen's dimensions according to Swedish standard.

Table B.1    Regulation for determination of compressive strength according to Swedish standard, ENV 206 and DIN 1048.

|  | Geometry | Dimension [mm] | Curing | Test date |
|---|---|---|---|---|
| **Swedish Standard** | **Cube** | **150** | **1 d formwork + 4 d under water + 23 d on air** | **28 d** |
|  | **Cylinder** | **$\phi\, 150 \times 300$** | **1 d formwork + 27 d under water** | **28 d** |
| ENV 206 | Cube | 150 | 1 d formwork + 27 d under water | 28 d |
|  | Cylinder | $\phi\, 150 \times 300$ | 1 d formwork + 27 d under water | 28 d |
| DIN 1048 | Cube | 200 | 1 d formwork+ 27 d on air | 28 d |

B.2
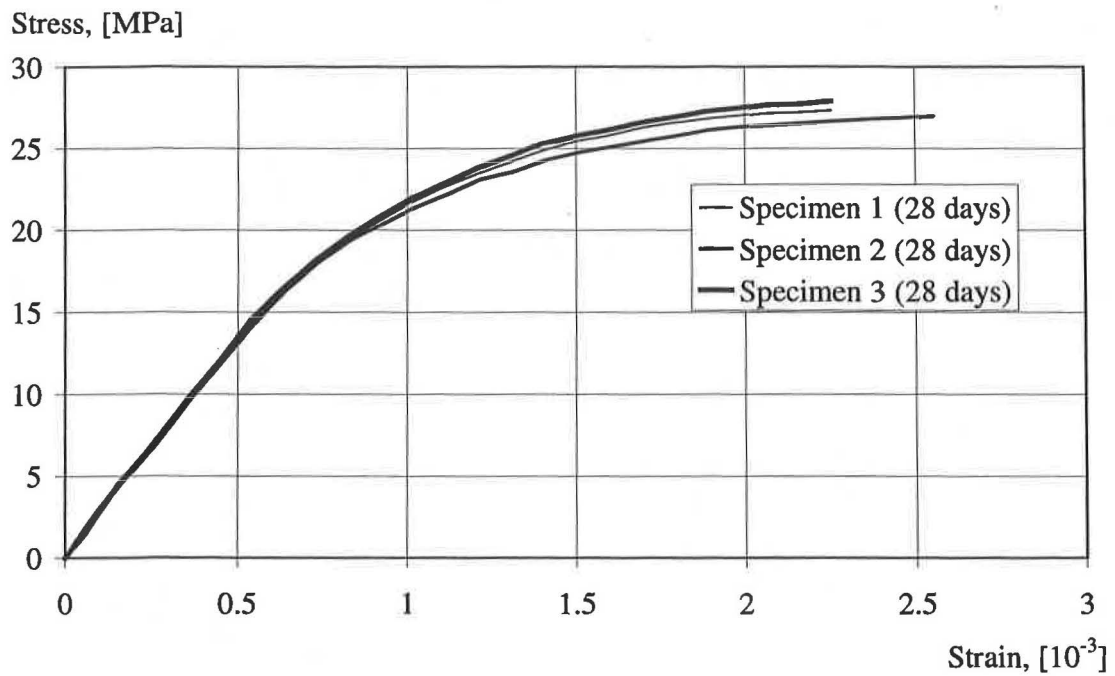
Figure B.2    Stress-strain relation in compression for the tests on Young's modulus after 28 days.
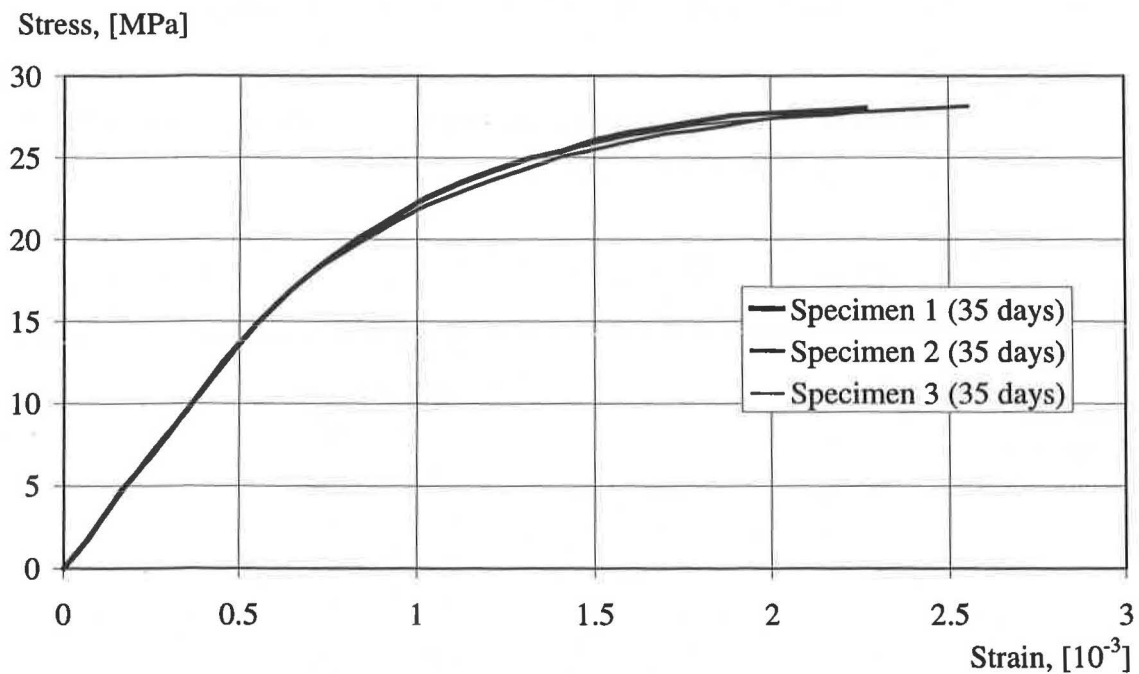


Figure B.3    Stress-strain relation in compression for the tests on Young's modulus after 35 days.

B.3

## B.1.2 Fracture energy

The fracture energy $G_f$ quantifies the toughness of the concrete. As the tensile strength this toughness is as an important factor concerning anchorage capacity of a bar. The fracture energy is defined as the amount of energy necessary to create one unit area of a crack. The test of the fracture energy is carried out for a standardised beam, with a notch in the middle with a depth of half of the beam height, see Figure B.4. In the deformation controlled test the load $F$ and the deformation $\delta$ at the middle of the beam are measured. The fracture energy is calculated from the equation

$$G_f = \frac{(W_o + m \cdot g \cdot \delta_o)}{A_{lig}} \qquad \text{[N/m]} \qquad (B.1)$$

with

$W_0$ = according to Figure B.5.

m = weight of the beam [kg],

g = acceleration due to gravity (9.81 m/s$^2$),

$\delta_0$ = deformation at the failure of the beam [m],

$A_{lig}$ = area of the ligament, defined as the projection of the fracture zone on a plane perpendicular to the beam axis [m$^2$].

A schematic load displacement curve is shown in Figure B.5.
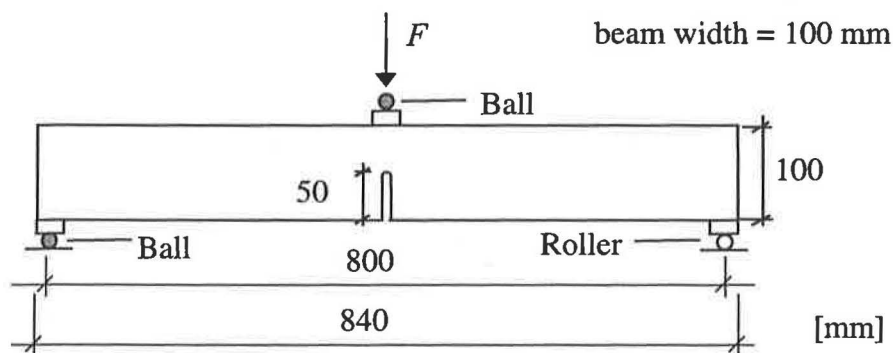


Figure B.4    Test specimen for the determination of the fracture energy, according to Rilem's recommendations, Hilleborg (1983).
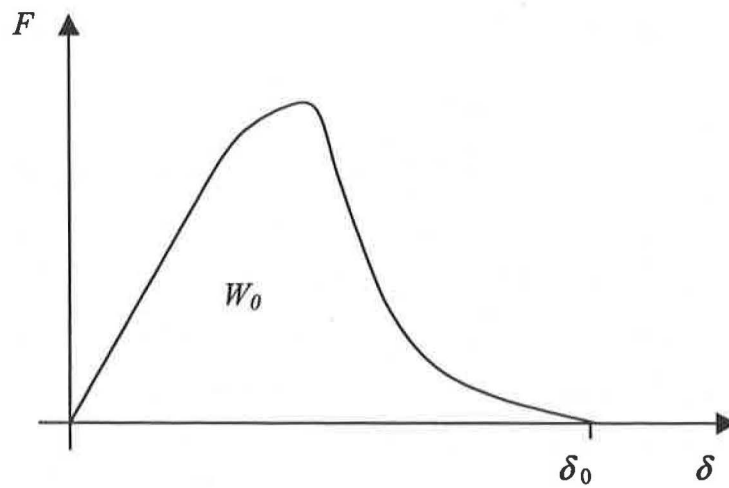
Figure B.5    Schematic load displacement curve for a fracture energy test according to
RILEM's recommendations, Hilleborg (1985).

The test results for the fracture energy used in the present test series are shown on the
following pages.

# RAPPORT

Chalmers Tekniska Högskola
Betongbyggnad
Att: Morgan Johansson
412 96 GÖTEBORG

| Handläggare, enhet/*Handled by, department* | Datum/*Date* | Beteckning/*Reference* | Sida/*Page* |
|---|---|---|---|
| Kent Malmström, Byggnadsteknik, ip<br>Tel +46 (0)33 16 51 20 | 1999-10-05 | 99B4,4817 | 1 (2) |

## Provning av betongbalkar

(2 bilagor)

### 1      Provföremål

Betongbalkar för brottmekanisk provning. En serie om 3 balkar distribuerades till SP genom Chalmers försorg. Balkarna var märkta 2/9 MJ och ankom 1999-09-28. Efter ankomsten försågs de därtill med nr 1-3. Omedelbart därefter sågades en ca 45 mm djup anvisning mitt på varje balk, varefter balkarna placerades i ett vattenlagringskärl.

### 2      Uppdrag

Brottmekanisk provning enligt RILEM "Determination of the fracture energy of mortar and conrete by means of three-point bend tests on notched beams".

### 3      Provningsmetod

Balkarna belastades i tre-punkts böjning helt enligt RILEMs rekommendationer. Spänn-vidden var i samtliga fall 800 mm. Balkarna förvarades i vatten med temperaturer (20 ± 2) °C fram till ca 30 min före provningen.

Belastningen var deformationsstyrd och påfördes med en nedböjningshastighet mätt på provkroppen av 0,25 mm/min. Belastning och nettonedböjning registrerades fortlöp-ande.

## 4　　　Resultat

Resultaten är sammanställda i tabell, som förutom mått- och viktsuppgifter även innehåller last vid första spricka och tillhörande nedböjning, deformation vid kollaps, uppgift om balkdelarnas vikt efter brott samt beräkning av brottenergin $G_F$ enligt RILEM.

**SP Sveriges Provnings- och Forskningsinstitut**
**Betongsektionen**

Kent Malmström
Tekniskt ansvarig

Rolf Lejestrand
Teknisk handläggare

**Bilagor**
1-2 Deformationskurvor

| Balk nr | 1 | 2 | 3 |
|---|---|---|---|
| Tillverkningsdatum | 1999-09-02 | 1999-09-02 | 1999-09-02 |
| Provningsdatum | 1999-09-30 | 1999-09-30 | 1999-09-30 |
| Dimension BxHxL (mm³) | 100,5x101,0x841 | 101,2x99,3x842 | 100,5x99,7x841 |
| Vikt (g) | 19980 | 19890 | 19810 |
| Densitet (kg/m³) | 2350 | 2360 | 2355 |
| Last vid första spricka (kN) | 1,190 | 0,830 | 1,030 |
| Tillhörande deformation (mm) | 0,123 | 0,076 | 0,120 |
| Ligament BxH₁ (mm²) | 100,5x56,0 | 101,2x55,3 | 100,5x55,2 |
| Deformation $\delta_0$ (mm) | 1,26 | 1,11 | 1,50 |
| Brottenergi $G_F$ (N/m) | 114 | 100 | 126 |
| Balkdelarnas vikt (g/g) | 9940/10030 | 9860/10020 | 9870/9940 |



**Balk 1**

**RAPPORT**

| Datum/*Date* | Beteckning/*Reference* | Sida/*Page* |
|---|---|---|
| 1999-10-05 | 99B4,4817 | 1 (1) |
| | | Bilaga 2 |
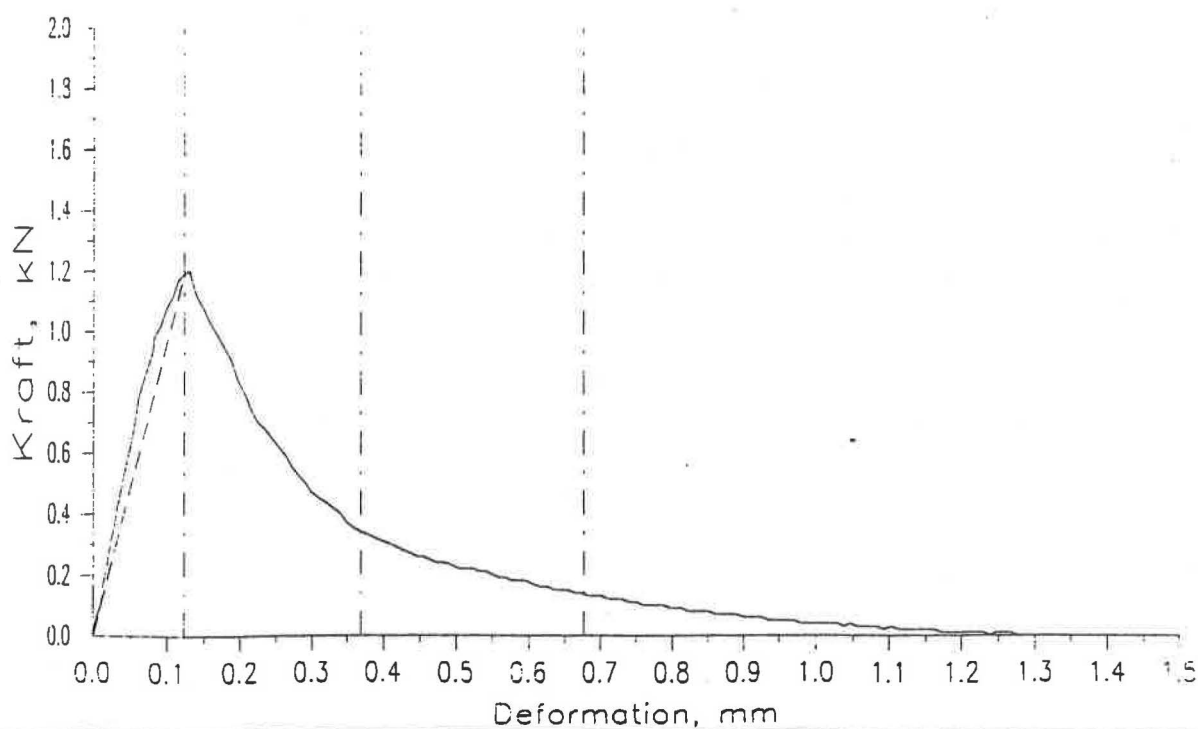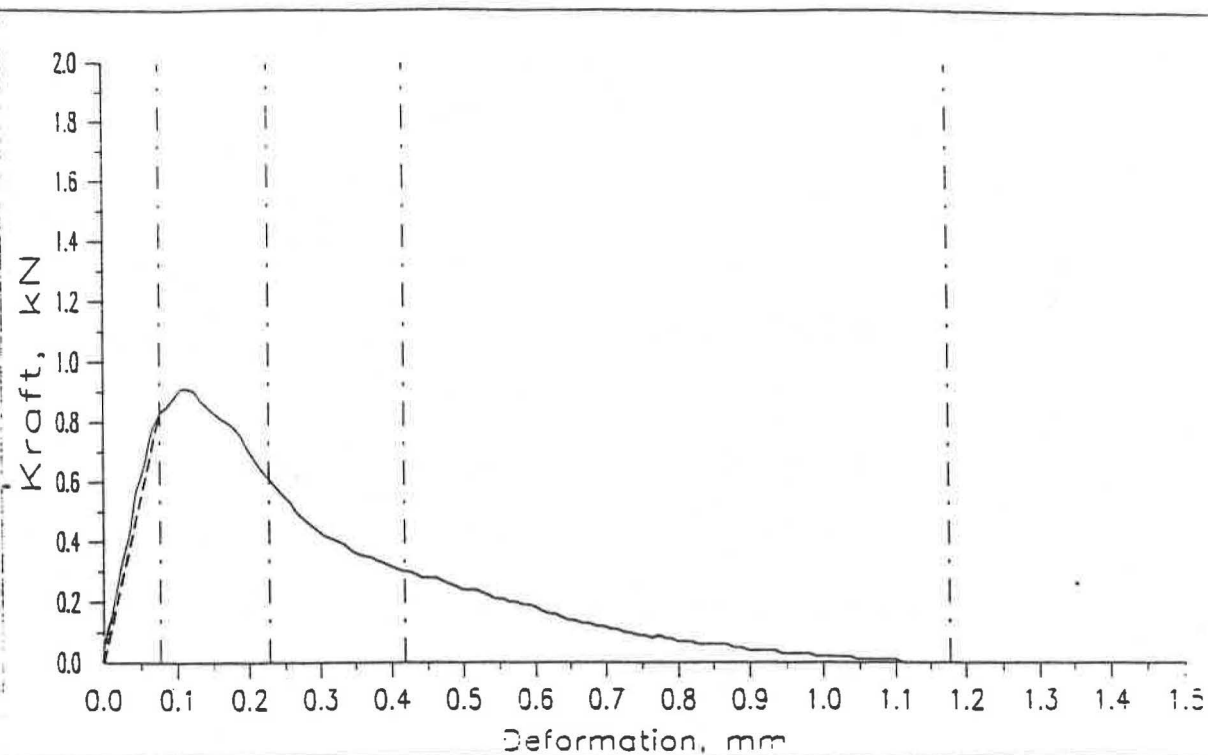
**Balk 2**
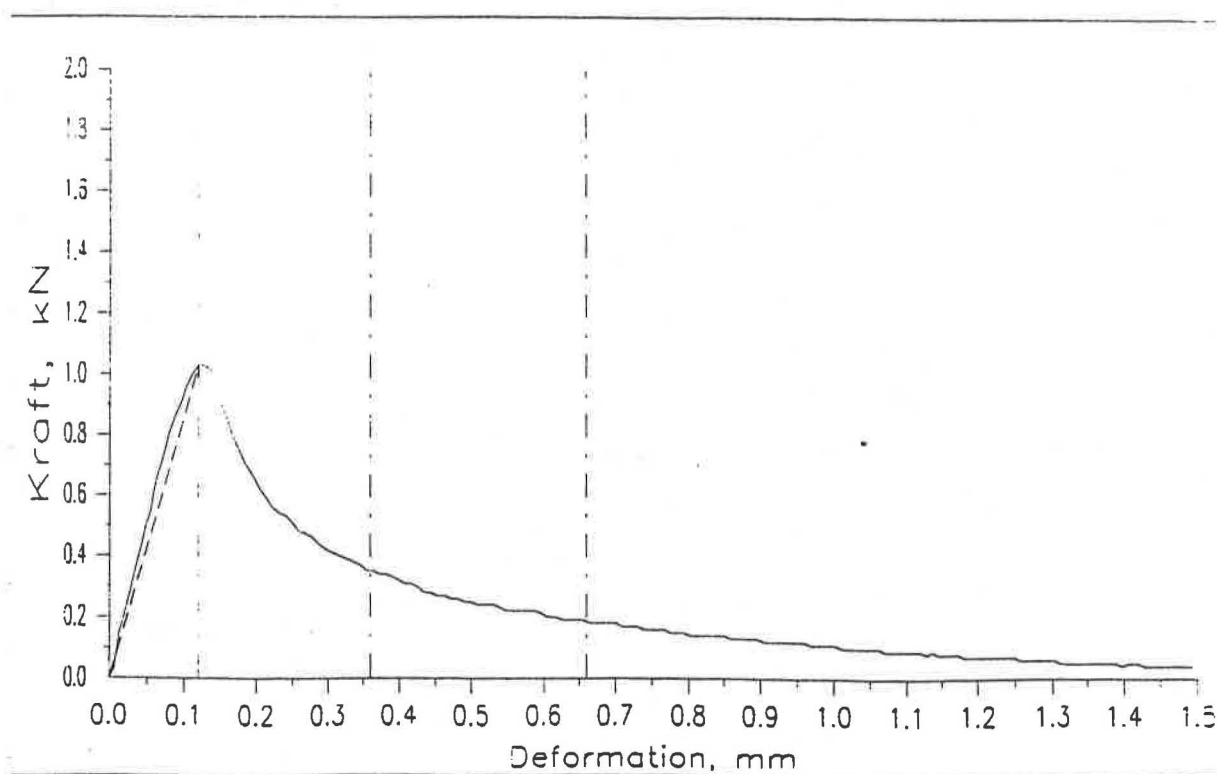


**Balk 3**

# PROTOKOLL FÖR BALLSTUNDERSÖKNIG

## MATERIALUPPGIFTER:

| Prov nr. | Materialbeteckning | Leverans från | Korn-form | Humus-grad | Slamhalt | Densitet | Fuktkvot % |
|---|---|---|---|---|---|---|---|
| 1. | STEN 8-16 | ÖSTAD | N K | | | | |
| 2. | | | | | | | |
| 3. | | | | | | | |

Vecka .... 35

Datum .... 1.9 .... 19 99

Arb.plats .... FB

.... 8

## SIKTANALYS:

| Sikt med fri mask-vidd mm | 1. Stannar gram | 1. % | 1. Passe-rar Σ% | 1. stann-ar Σ% | 2. Stannar gram | 2. % | 2. Passe-rar Σ% | 2. stann-ar Σ% | 3. Stannar gram | 3. % | 3. Passe-rar Σ% | 3. stann-ar Σ% |
|---|---|---|---|---|---|---|---|---|---|---|---|---|
| 31,5 | | | | | | | | | | | | |
| 22,4 | | | | | | | | | | | | |
| 16 | 168 | 4 | 96 | 4 | | | | | | | | |
| 11,2 | 2951 | 67 | 29 | — | | | | | | | | |
| 8 | 1172 | 27 | 2 | 98 | | | | | | | | |
| 4 | 95 | 2 | 0 | 100 | | | | | | | | |
| 2 | 1 | | | 100 | | | | | | | | |
| 1 | 2 | | | 100 | | | | | | | | |
| 0,5 | 8 | | | 100 | | | | | | | | |
| 0,25 | 12 | | | 100 | | | | | | | | |
| 0,125 | 12 | | | 50 | | | | | | | | |
| *) 0,063 | 13 | | | | | | | | | | | |
| < 0,063 | 4 | | | | | | | | | | | |
| Summa | 4436 | 100 | | 652 | | | | | | | | |
| Finh. modul | $M_1 =$ | | 6,52 | | $M_2 =$ | | | | $M_3 =$ | | | |

Beteckn. för kornform

N = Naturmaterial

K = Krossmaterial

NK = Natur+krossa

Beteckningar samt utför-andet av samtliga ballast-undersökningar, se Svensk standard

*) 0,075 kan användas enl. Svensk standard

## SIKTDIAGRAM:

U.S. standardsiktserie



Passerande mängd, procent

Svensk betongsiktserie, fri maskvidd mm

Anteckningar

# PROTOKOLL FÖR BALLASTUNDERSÖKNING

## MATERIALUPPGIFTER:

| Prov nr | Materialbeteckning | Leverans från | Korn-form | Humus-grad | Slamhalt | Densitet | Fuktkvot % |
|---|---|---|---|---|---|---|---|
| 1. | GRUS 0-8 | SJÖGÄRDE | N | | | | 6,0 |
| 2. | -"- | ÖSTAD | N | | | | 5,5 |
| 3. | | | | | | | |

Nr ...........
Datum 2 19 19 99
Arb.plats FB
RINGEN

## SIKTANALYS:

| Sikt med fri mask-vidd mm | 1 Stannar gram | 1 % | 1 Passe-rar Σ% | 1 Stan-nar Σ% | 2 Stannar gram | 2 % | 2 Passe-rar Σ% | 2 Stan-nar Σ% | 3 Stannar gram | 3 % | 3 Passe-rar Σ% | 3 Stan-nar Σ% |
|---|---|---|---|---|---|---|---|---|---|---|---|---|
| | | | | | | | | | | | 20/ | |
| | | | | | | | | | | | /80 | |
| 11,2 | | | | | 12 | 1 | 99 | 1 | | | 99 | 1 |
| 8 | 15 | 2 | 98 | 2 | 34 | 3 | 96 | 4 | | | 96 | 4 |
| 4 | 63 | 7 | 91 | 9 | 116 | 12 | 84 | 16 | | | 85 | 15 |
| 2 | 61 | 7 | 84 | 16 | 149 | 16 | 68 | 32 | | | 71 | 29 |
| 1 | 85 | 9 | 75 | 25 | 175 | 19 | 49 | 51 | | | 54 | 46 |
| 0,5 | 124 | 13 | 62 | 38 | 186 | 20 | 29 | 71 | | | 36 | 64 |
| 0,25 | 222 | 24 | 38 | 62 | 156 | 17 | 12 | 88 | | | 17 | 83 |
| 0,125 | 250 | 26 | 12 | 44 | 74 | 8 | 4 | 48 | | | 6 | 47 |
| *)0,063 | 95 | 10 | 2 | | 29 | 3 | 1 | | | | 1 | |
| <0,063 | 21 | 2 | | | 10 | 1 | | | | | | |
| Summa | 941 | 100 | | 196 | 939 | 100 | | 311 | | | | 289 |
| Finh. modul | $M_1 =$ | 1,96 | | | $M_2 =$ | 3,11 | | | $M_3 =$ | 2,89 | | |

Beteckn. för kornform:

N = naturmaterial
K = krossmaterial
NK = natur+kross

Beteckningar samt utföran-det av samtliga ballastun-dersökningar, se Svensk standard.

*) 0,075 kan användas enl. Svensk standard.

## SIKTDIAGRAM:

U.S. standardsiktserie



Passerande mängd, procent

Svensk betongsiktserie, fri maskvidd mm
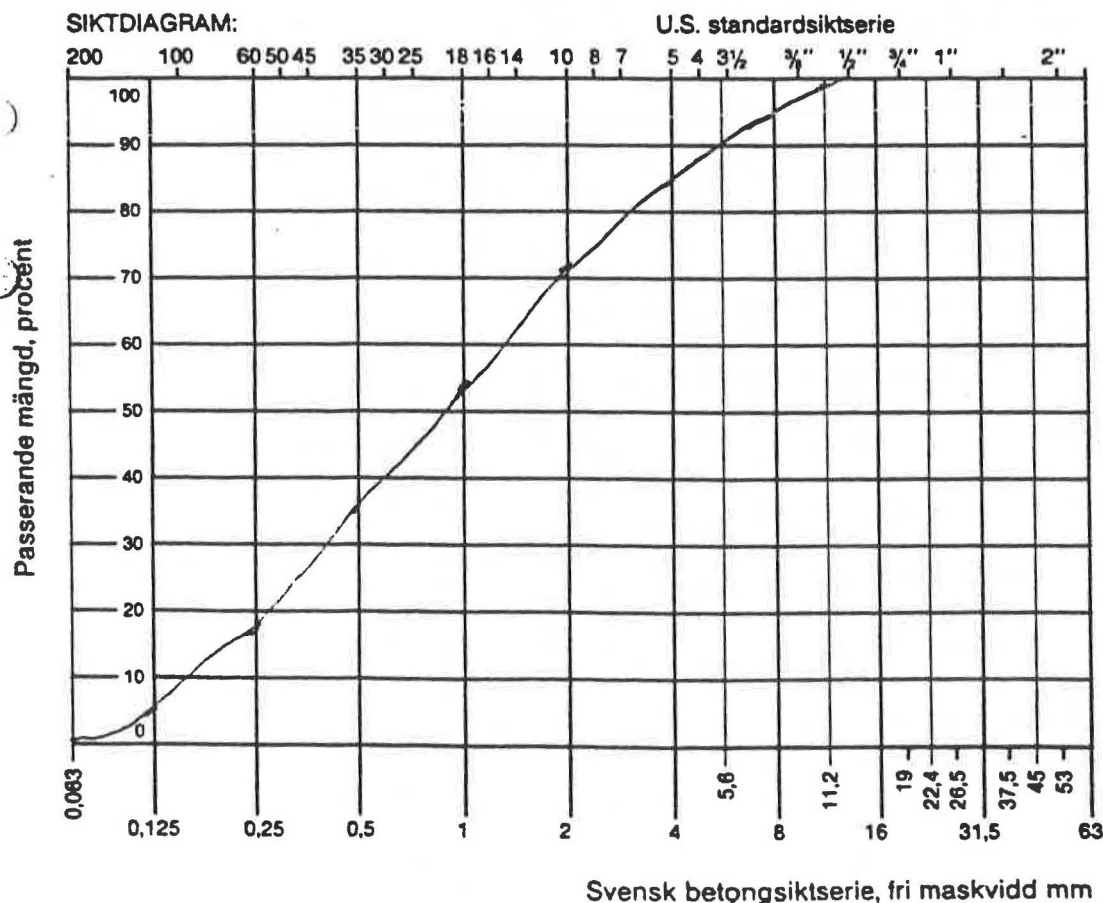
Anteckningar

## B.2    Reinforcement

Five reinforcement specimens of type B500BT were tested, each with a length of 1100 mm according to the standard procedure at the Chalmers Structural Engineering Laboratory. The load displacement curves are shown in Figure B.6.
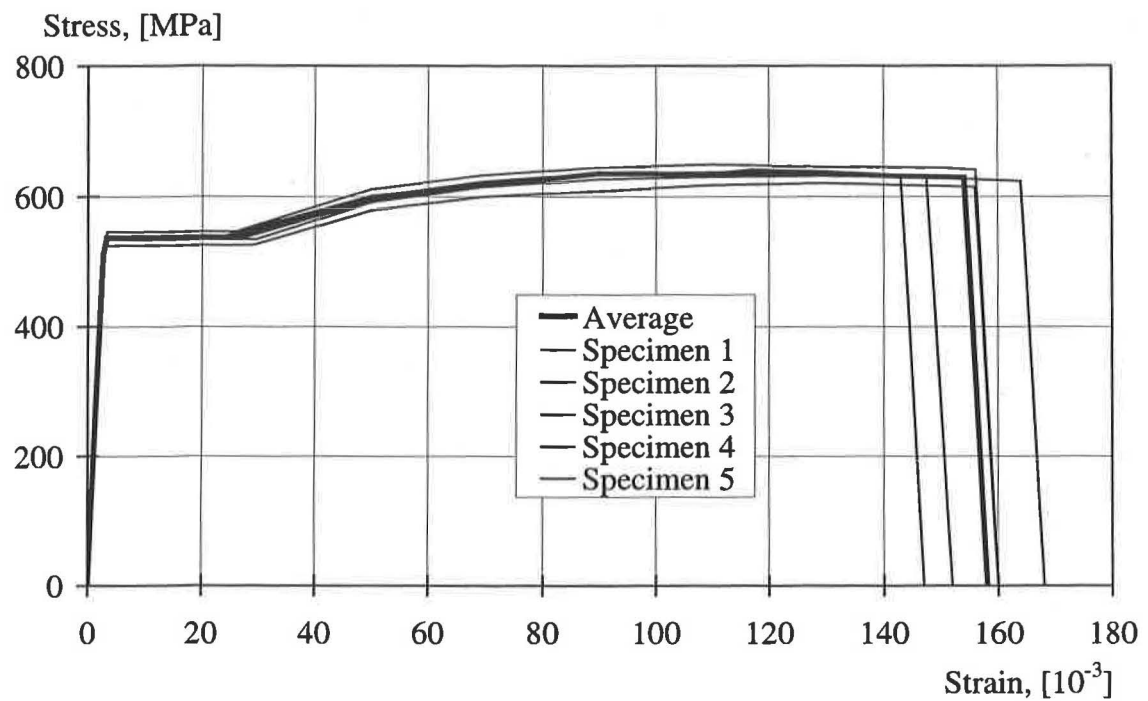


Figure B.6    Stress-strain relation for the reinforcement tests. The results of five specimens and their average are shown.

# Appendix C

# C Additional results of FE-analyses

## C.1 Results of FE-analyses with "normal" material properties

The results of the analyses described in Section 4.4 were based on modified material properties. The fracture energy and the tensile strength were increased by 25 %, called "increased" material properties. In this way it was possible to model the behaviour observed in the experiments. However, also analyses with "normal" material properties were carried out and their results presented in the following section. Hereby, the tensile strength, the fracture energy and the bond conditions were varied and the obtained load-deformation relations compared.

Unless stated following material properties were used:

fracture energy      $G_f$ = 113 N/m (according to the material test after 28 days)

tensile strength      $f_t$ = 2.22 MPa (according to CEB-FIP Model code, CEB (1993))

bond conditions      "good" bond conditions

### C.1.1 Specimen RV12

The load-deformation relations of two FE-analyses with varied bond conditions are compared to the test results in Figure C.1. With "other" bond conditions a slightly higher load capacity was reached. This coincides with the observations made in Section 4.4.

A comparison of the load-deformation relations of analyses with "normal" and "increased" material properties is shown in Figure C.2. Hereby, it can be seen that the tensile strength and the fracture energy have a strong influence on the load capacity. However, the tensile stresses in the reinforcement are not affected. A comparison of the tensile stresses for the analyses with "normal" and "increased" material properties is shown in Figure C.3. The stresses in the reinforcement loops are almost identical.
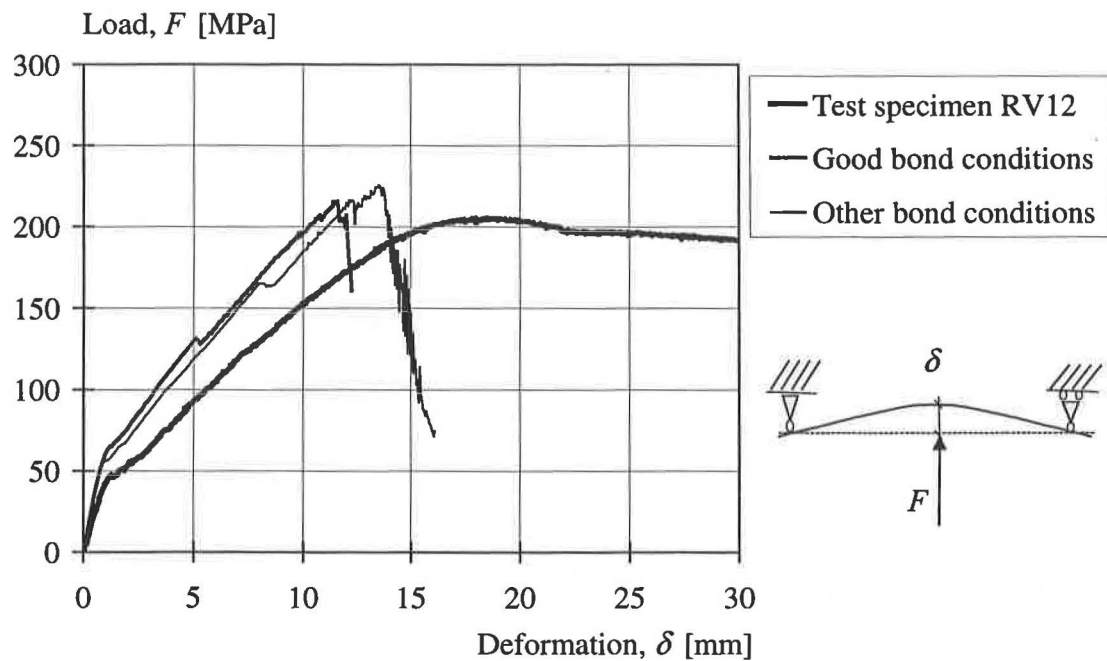
Figure C.1    Comparison of "good" and "other" bond conditions with "normal" material properties for specimen RV12.
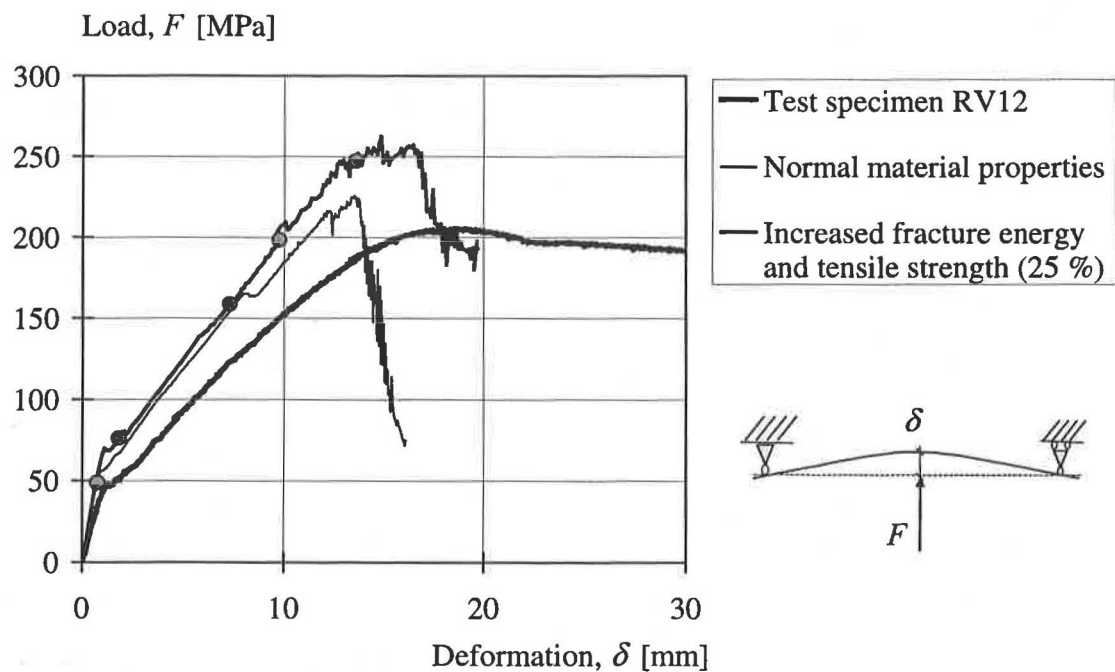


Figure C.2    Comparison of the load-deformation relations for "normal" and "increased" material properties using "other" bond conditions for specimen RV12

C.2
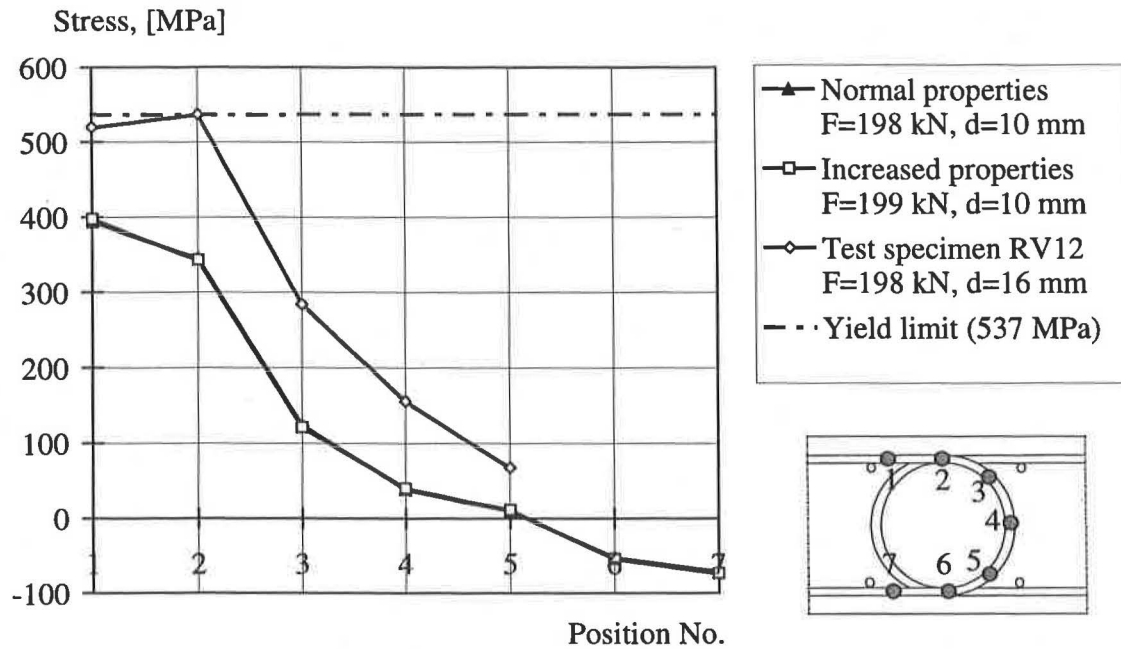
Figure C.3    Comparison of the tensile stresses for "normal" and "increased" material properties with "other" bond conditions for specimen RV12.

## C.1.2  Specimen RV13

For specimen RV13 the influences of fracture energy and tensile strength were investigated separately. Furthermore, the bond conditions were varied.

The load-deformation relations for "good" and "other" bond conditions using "normal" material properties are shown in Figure C.4. Contrary to former observations made in Section 4.4 the obtained load capacity was higher using "other" bond conditions.

Two analyses, in which the tensile strength and the fracture energy were varied respectively, were carried out, see Figure C.5 and Figure C.6. The tensile strength was increased by 25 % and the fracture energy doubled. Nevertheless, a simultaneously increase of both properties by 25 % resulted in a satisfying load prediction, see Figure C.7.

Load, $F$ [MPa]
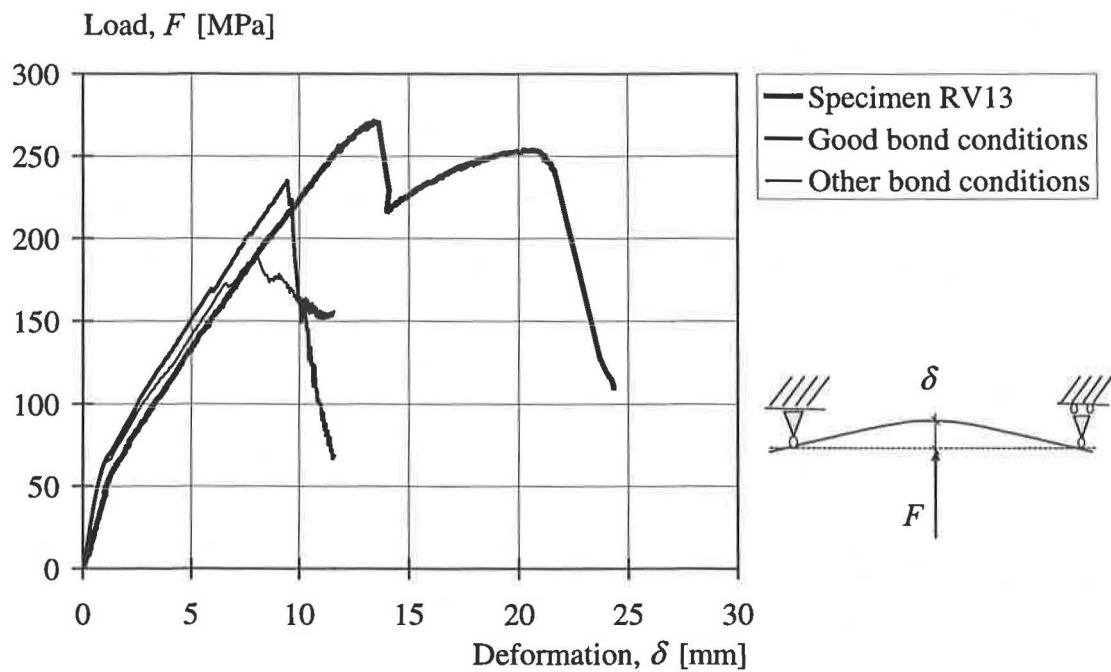


Figure C.4    Comparison of test and FE-analyses using different bond conditions and "normal" material properties for specimen RV13.

Load, $F$ [MPa]
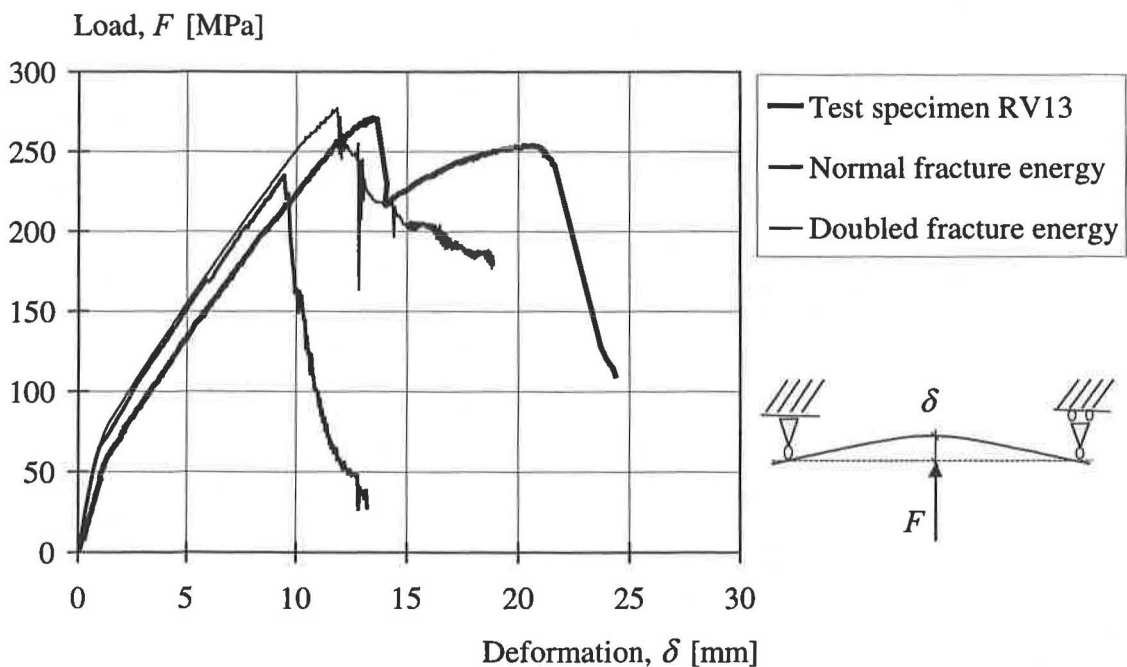


Figure C.5    Comparison of load-deformation relations using normal and doubled fracture energy for "good" bond conditions.
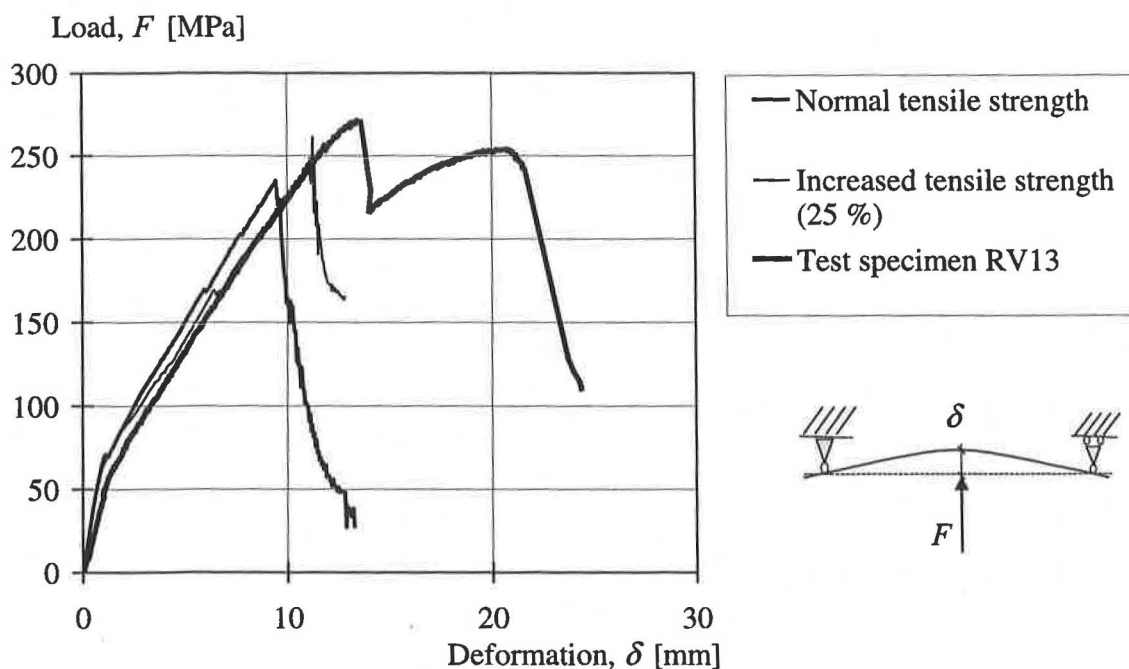
Figure C.6    Comparison load-deformation relations using normal tensile strength and high tensile strength for good bond conditions.
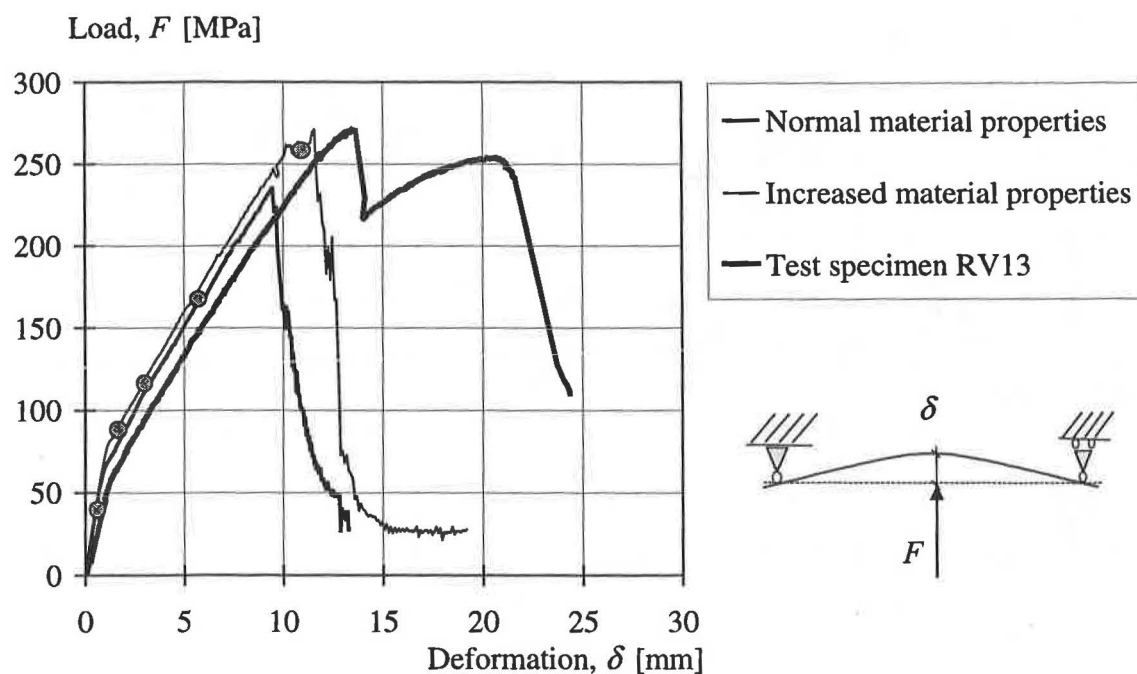


Figure C.7    Comparison of load-deformation relation using "normal" material properties and "increased" material properties for "good" bond conditions.

The comparison of the tensile stresses in the reinforcement for the analyses with "normal" and "increased" material properties is shown in Figure C.8. The tensile strength and the fracture energy of the concrete have a very small influence on the magnitude of the tensile stresses.
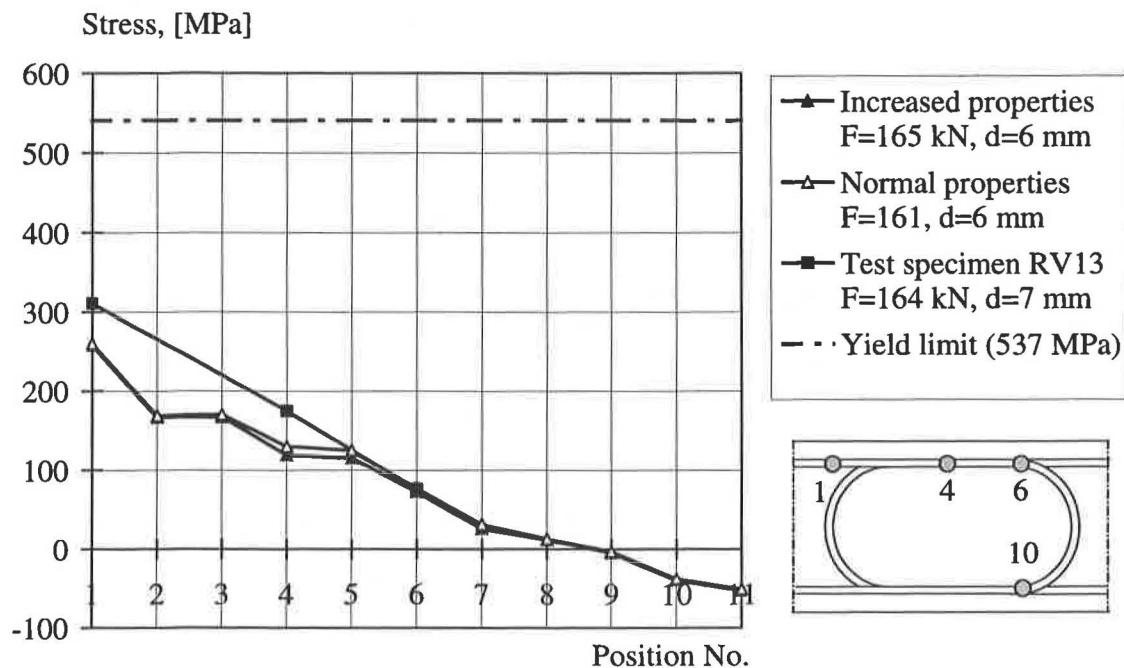


Figure C.8    Comparison of tensile stresses of test and FE-analyses using "normal" and "increased" material properties for "good" bond conditions.

## C.1.3  Specimen RV15

For specimen RV15 the bond conditions and the fracture energy were varied. The comparison of the load-deformation relation for "good" and "other" bond conditions are shown in Figure C.9. The fracture energy was doubled, see Figure C.10. Due to the higher fracture energy yielding of the reinforcement was obtained. However, the responds of the specimen became stiffer, since the change from uncracked to cracked state was delayed. Again, a simultaneous increase of fracture energy and tensile strength by 25 percent was used and compared to the test results and the analysis with normal material properties, see Figure C.11. Yielding of the reinforcement and a ductile post-peak behaviour was obtained.
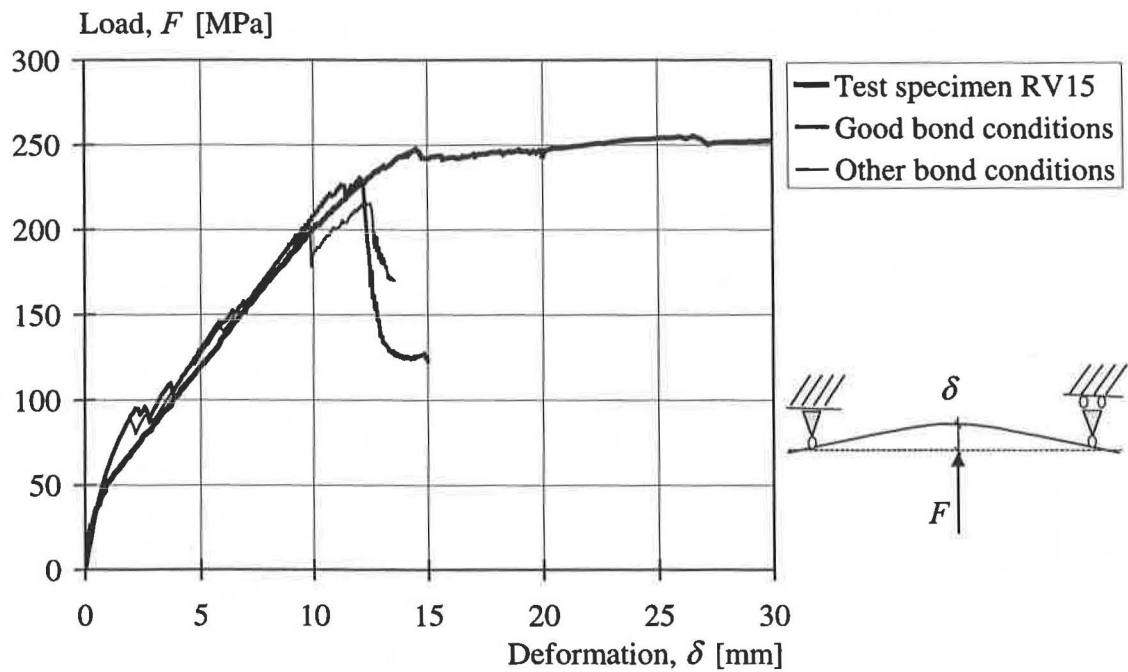
Figure C.9    Comparison of the load-deformation relations using "good" and "other" bond conditions for "normal" material properties.
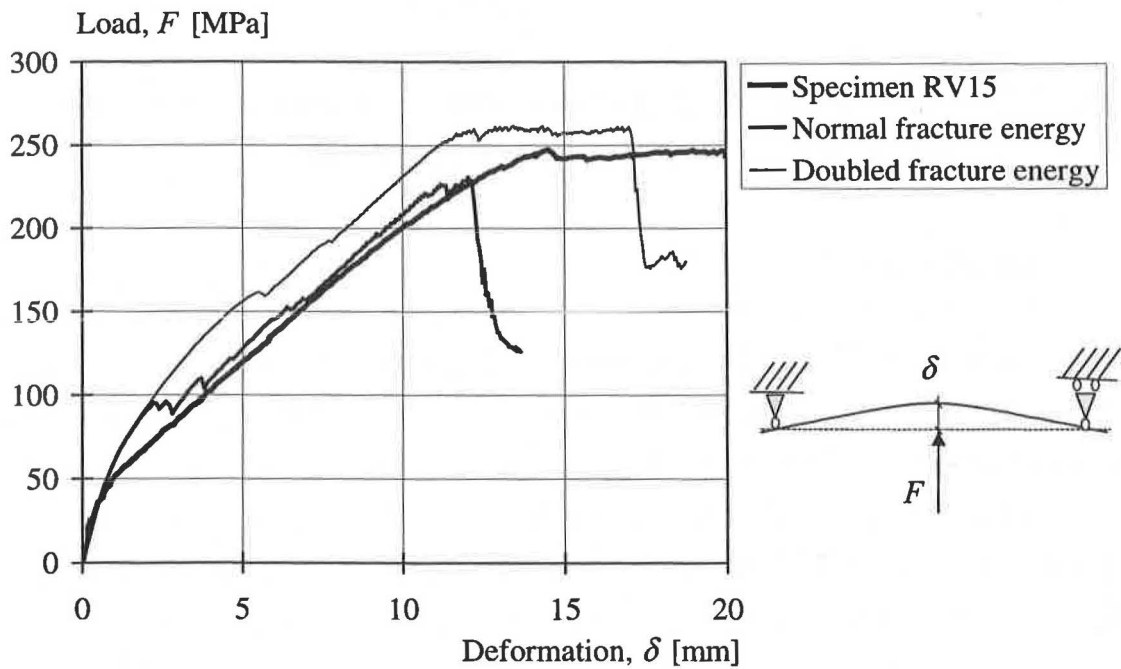


Figure C.10   Comparison of the load-deformation relations using "normal" and "doubled" fracture energy for "good" bond conditions.
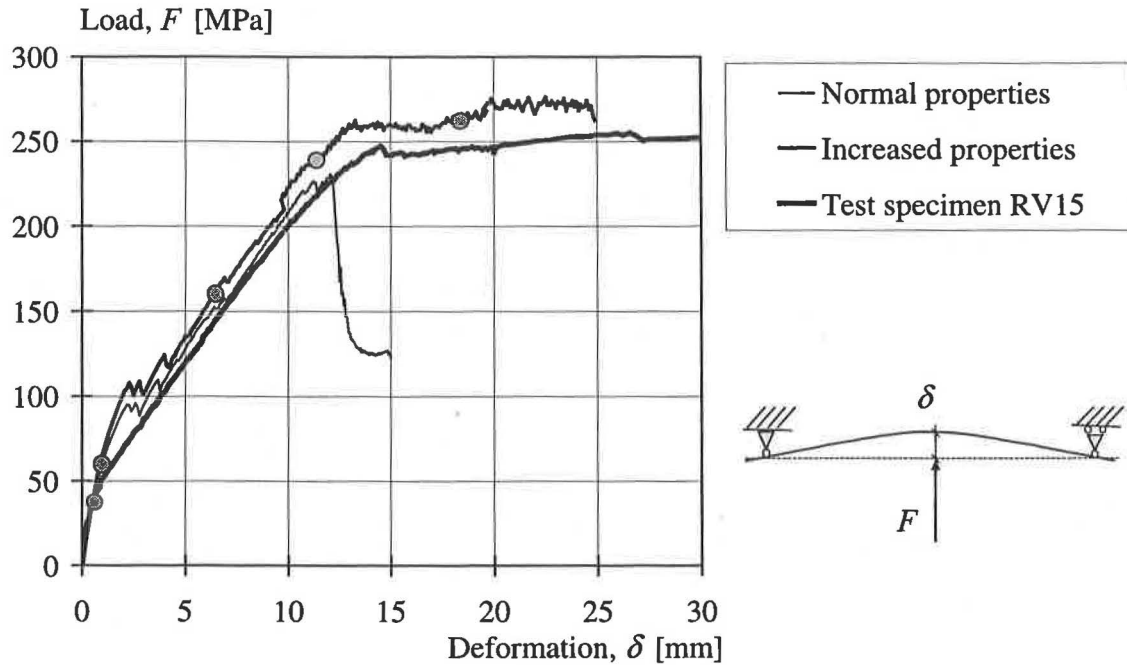
Figure C.11   Comparison of the load-deformation relations using "increased" and "normal" material properties for "good" bond conditions.

## C.2   Crack propagation in FE-analyses

In the following sections the crack propagation for FE-analyses with increased material properties of Section 4.4.2 are shown. The bond conditions were varied using "good" and "other" bond conditions. The grey marked elements indicate a strain larger than 0.003. The deformation of the specimens is magnified with a factor of 10.

### C.2.1   Crack propagation of specimen RV12 with "good" bond conditions
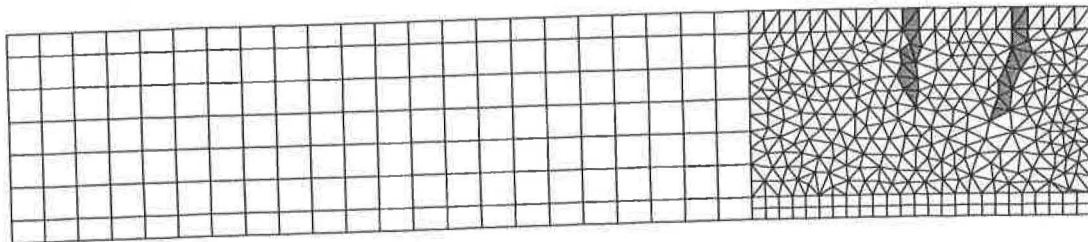


$F = 108$ kN, $\delta = 4$ mm
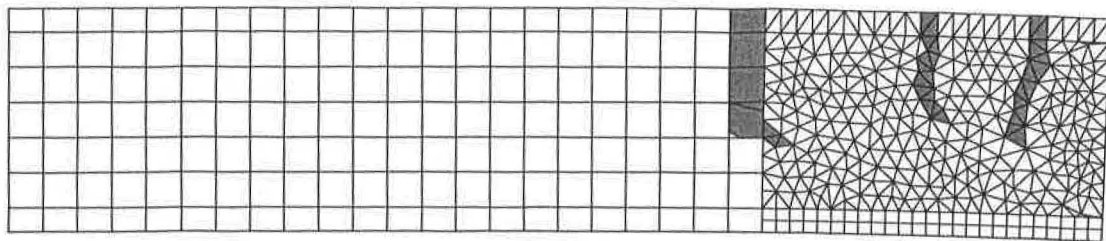
$F = 154 \text{ kN}, \delta = 6 \text{ mm}$
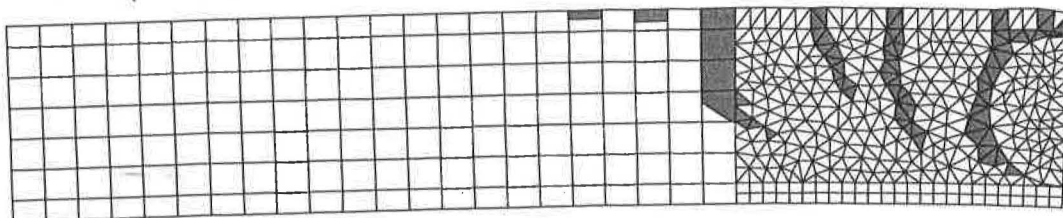


$F = 199 \text{ kN}, \delta = 10 \text{ mm}$
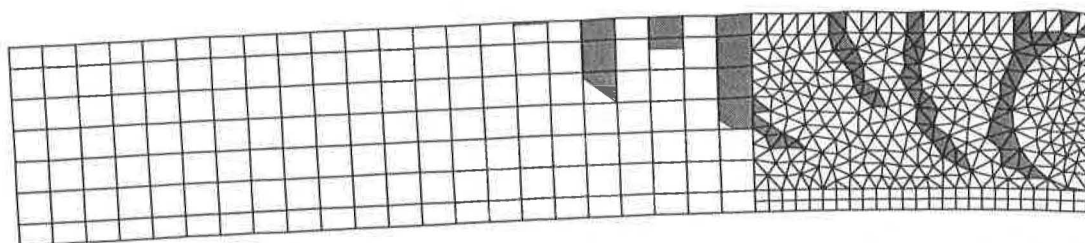


$F = 249 \text{ kN}, \delta = 13 \text{ mm}$

### C.2.2 Crack propagation of specimen RV12 with "other" bond conditions
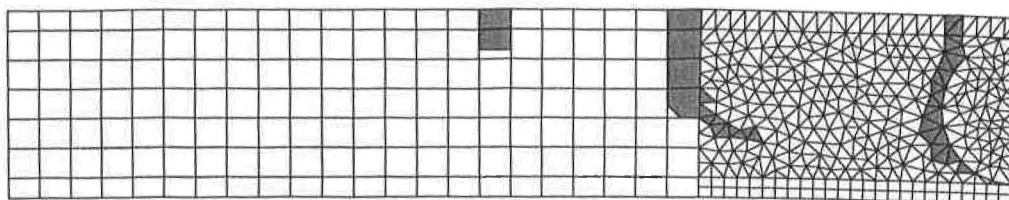


$F = 154 \text{ kN}, \delta = 7 \text{ mm}$
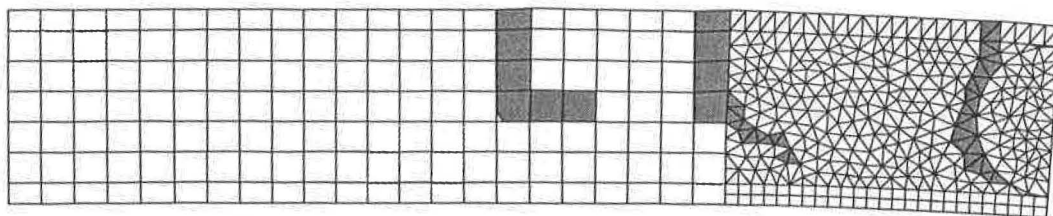
$F = 198, \delta = 10$ mm
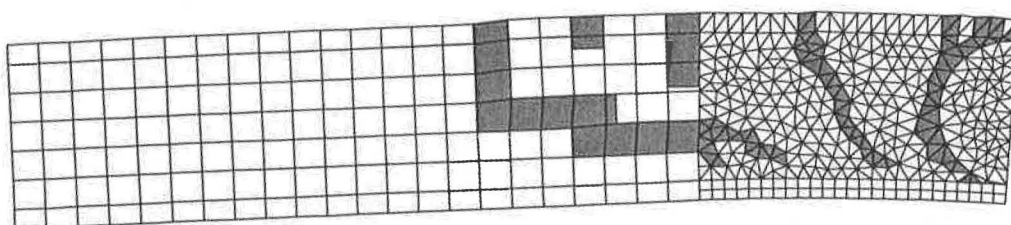


$F = 154$ kN, $\delta = 16$ mm

## C.2.3 Crack propagation of Specimen RV13 with "good" bond conditions
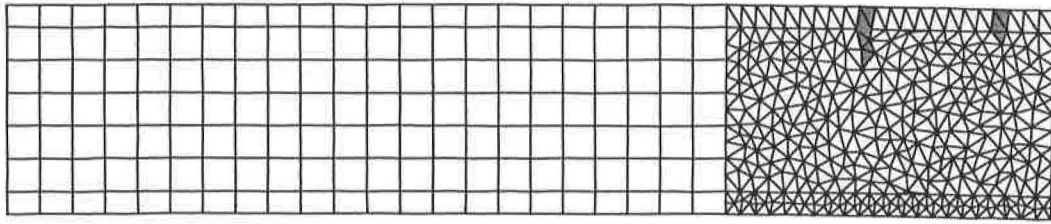


$F = 120$ kN, $\delta = 3$ mm
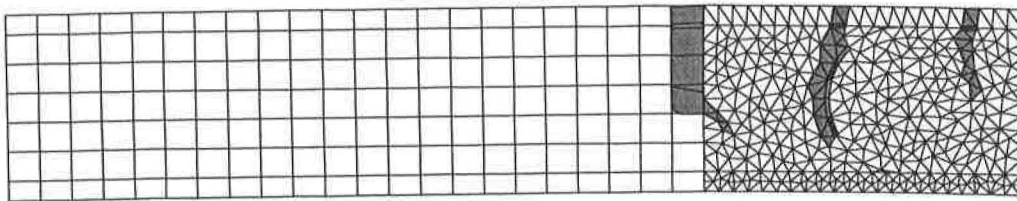


$F = 165$ kN, $\delta = 5$ mm
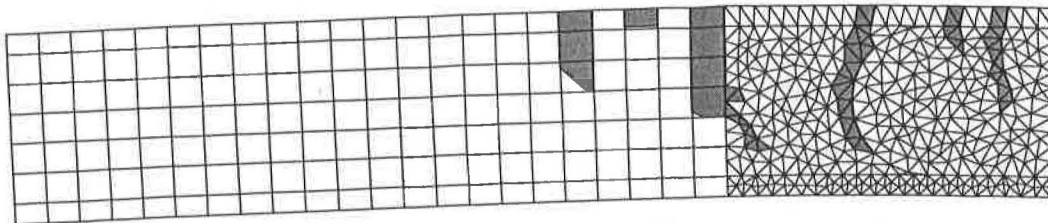


$F = 217$ kN, $\delta = 8$
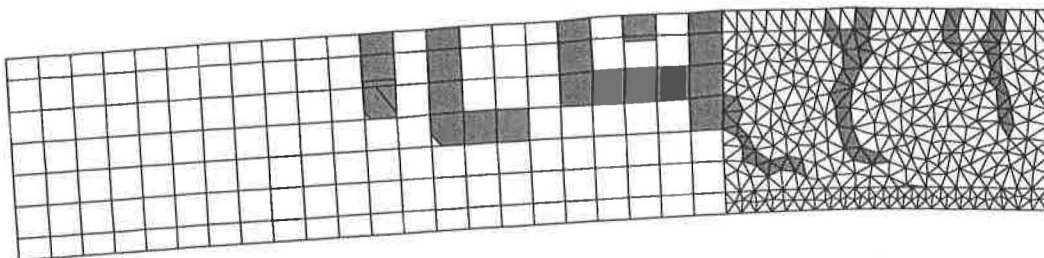


$F = 262$ kN, $\delta = 11$ mm

## C.2.4 Crack propagation of Specimen RV13 with "other" bond conditions
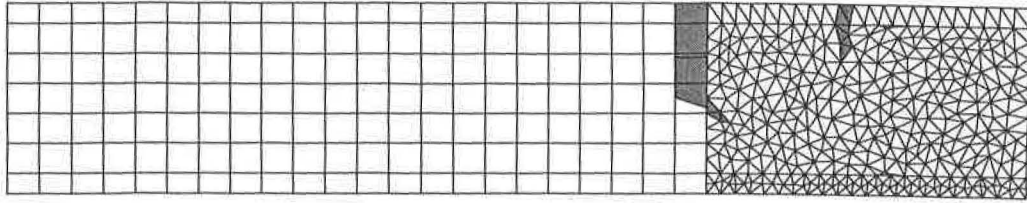


$F = 113$ kN, $\delta = 3$ mm
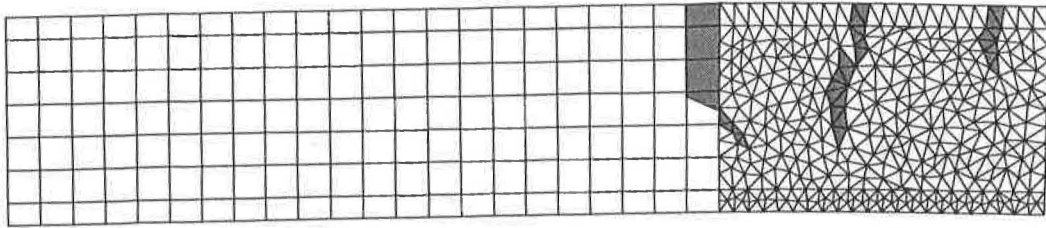


$F = 151$ kN, $\delta = 5$ mm
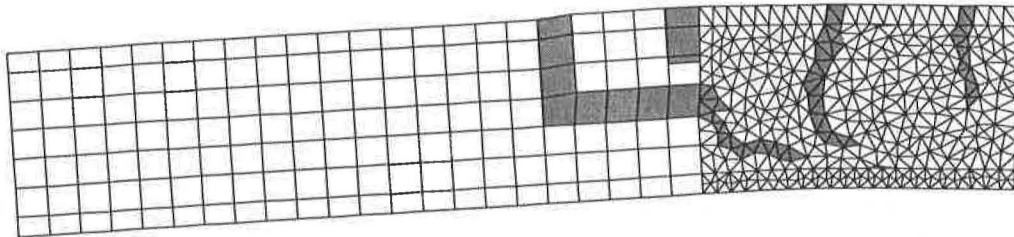


$F = 255$ kN, $\delta = 11$ mm

## C.2.5 Crack propagation of specimen RV15 with "good" bond conditions
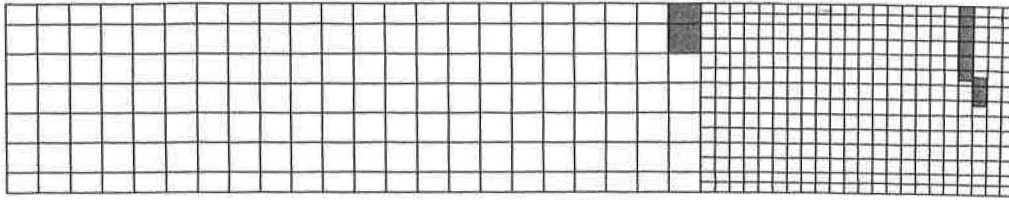


$F = 125$ kN, $\delta = 4$ mm
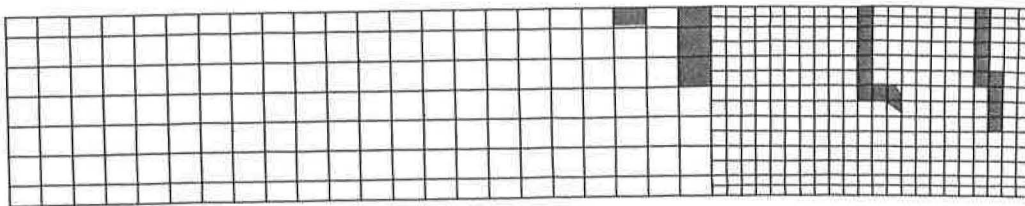


$F = 158$ kN, $\delta = 6$ mm
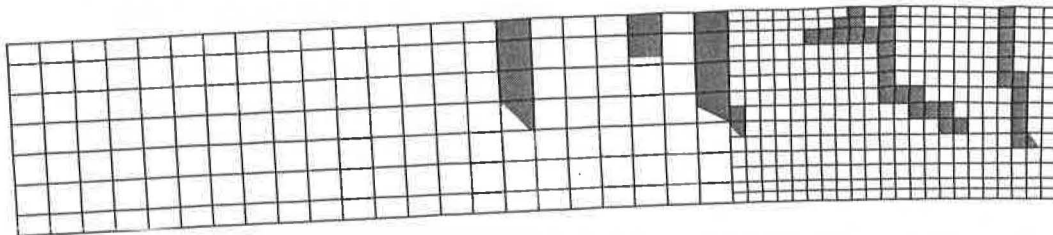


$F = 239$ kN, $\delta = 12$ mm



$F = 263$ kN, $\delta = 18.4$ mm

C.13
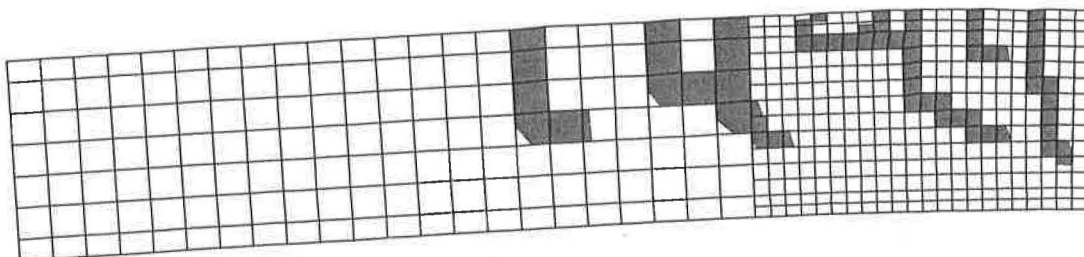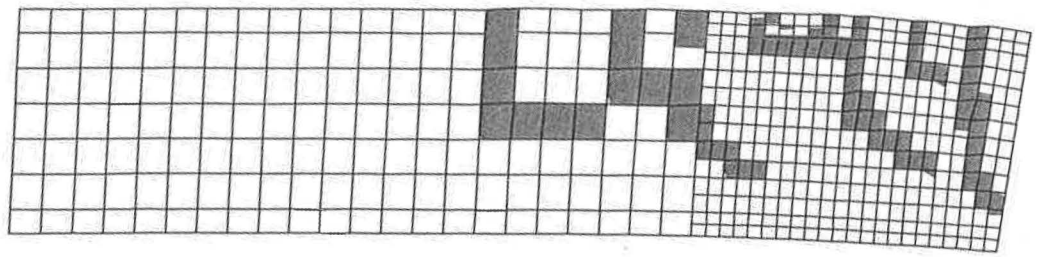
$F = 258$ kN, $\delta = 26.1$ mm

# C.3 Input files for DIANA

## C.3.1 Data file

In the data file the finite element mesh is defined. Furthermore, the material properties and the acting loads are introduced.

'COORDINATES'

In this section the position of the nodes is defined. The nodes of the truss elements have the same co-ordinates as nodes of the concrete elements at this position.

```
1    .00000E+00 3.20000E-02 .00000E+00
2    5.00000E-02 3.20000E-02 .00000E+00
3    1.00000E-01 3.20000E-02 .00000E+00
4    1.50000E-01 3.20000E-02 .00000E+00
5    2.00000E-01 3.20000E-02 .00000E+00

1103 1.54100E+00 4.78100E-02 .00000E+00
1104 1.56946E+00 3.60200E-02 .00000E+00
2048 1.60000E+00 3.20000E-02 .00000E+00
2093 1.60000E+00 2.68000E-01 .00000E+00
```

'DIRECTIONS'

General directions are specified. With the TR option for example (TR1, TR2, TR3) it is referred to the defined directions.

```
1    1.000000E+00 .000000E+00 .000000E+00
2    .000000E+00 1.000000E+00 .000000E+00
3    .000000E+00 .000000E+00 1.000000E+00
```

'ELEMENTS'
CONNECT

Four different element types were used in this example file. In the Section CONNECT the nodes of the elements are specified.

2-node truss elements (reinforcement):

```
1    L2TRU  1001 1002
2    L2TRU  1002 1003
3    L2TRU  1003 1004
4    L2TRU  1004 1005
5    L2TRU  1005 1006
...
```

4-node plane stress elements (concrete):

```
104  Q8MEM  2 106 107 3
105  Q8MEM  105 106 2 1
106  Q8MEM  119 118 113 112
```

```
107   Q8MEM   118 117 114 113
108   Q8MEM   117 116 115 114
...
```

3-node plane stress element (concrete in the refined mid-section)

```
308   T6MEM   439 332 384
309   T6MEM   390 377 338
310   T6MEM   440 327 378
311   T6MEM   459 144 378
312   T6MEM   451 95 90
...
```

2-node interface element (bond)

```
1001 L8IF    1001 1002 1 2
1002 L8IF    1002 1003 2 3
1003 L8IF    1003 1004 3 4
1004 L8IF    1004 1005 4 5
1005 L8IF    1005 1006 5 6
...
```

```
MATERI
```

Here, the different materials are allocated to the elements.

```
/ 104-846 / 1
/ 1-103 / 11
/ 1001-1103 / 101
:
GEOMET
```

Here, the cross-sectional geometry is allocated

```
/ 104-846 / 1
/ 1-103 / 11
/ 1001-1103 / 101
:
DATA
```

Two different crack-bandwidths were defined. One for the refined mesh in mid-section and one for the remaining part.

```
/ 104-257 / 1
/ 258-846 / 2
```

```
'MATERIAL'
```
In material 1 the properties of the concrete are defined. The tensile strength TENSTR and the fracture energy GF1 were increased by 25 %. A multi-linear compressive curve COMCRV MULTNL based on the results from the material tests was used.

```
1     DENSIT 2.4E+03
      TOTCRK ROTATE
      POISON 0.2
      YOUNG  2.55E+10
      TENSTR 2.86E+6
      GF1    146.9
      COMSTR 28.14E+6
```

C.16

```
COMCRV MULTLN
COMPAR 0.0            0.0
       -1.71E+6      -0.067E-3
       -7.18E+6      -0.258E-3
       -12.42E+6     -0.450E-3
       -16.90E+6     -0.641E-3
       -19.94E+6     -0.833E-3
       -22.37E+6     -1.024E-3
       -24.04E+6     -1.215E-3
       -25.29E+6     -1.407E-3
       -26.66E+6     -1.694E-3
       -27.26E+6     -1.885E-3
       -27.61E+6     -2.077E-3
       -27.91E+6     -2.268E-3
       -28.14E+6     -2.555E-3
       -27.53E+6     -7.845E-3
       -22.87E+6     -18.44E-3
       -14.07E+6     -29.03E-3
       -3.47E+6      -54.30E-3
       -0.93E+6      -114.3E-3
       -0.1E2        -5E+5
TENCRV HORDYK
```

The material properties and the constitutive relation of the reinforcement are defined as material number 11. The values were obtained from the material tests. Von Mises yield criterion YIELD VMISES was combined with a strain hardening law HARDEN STRAIN.

```
11   YOUNG  1.99E+11
     DENSIT 7.8E+3
     YIELD  VMISES
     YLDVAL 510E+6
     HARDEN STRAIN
     HARDIA 510E+6 0.0
            537E+6 0.00066
            537E+6 0.02419
            597E+6 0.04739
            619E+6 0.0674
            635E+6 0.0874
            635E+6 0.1073
            635E+6 0.127
            629E+6 0.152
            0.1E+6 0.155
            1      1E6
```

For the bond behaviour the relations according to CEB-FIP Model Code, CEB (1993) were used. In this analysis unconfined concrete and "other" bond conditions were assumed.

```
101  DSTIF  3.48E+12 3.48E+10
     BONDSL 3
     SLPVAL 0.0      0.0
            1.74E+6  0.05E-3
            2.29E+6  0.1E-3
            2.69E+6  0.15E-3
            3.02E+6  0.2E-3
            3.30E+6  0.25E-3
```

```
                      3.55E+6 0.3E-3
                      3.78E+6 0.35E-3
                      3.99E+6 0.4E-3
                      4.18E+6 0.45E-3
                      4.36E+6 0.5E-3
                      4.53E+6 0.55E-3
                      4.69E+6 0.6E-3
                      0.70E+6 2.5E-3
                      0.70E+6 100E+10
:
'GEOMETRY'

1       THICK  0.600
:
11      CROSSE 1.407E-3
:
101     CONFIG BONDSL
        THICK  0.352
:
'DATA'
1       CRACKB 0.05      (for coarse mesh)
2       CRACKB 0.02      (for refined mesh)
:
'SUPPORTS'
```

On node 267 the deformations were prescribed. The nodes in mid sections were constrained in x-direction. In this way the symmetry was considered.

```
120  TR 2
267  TR 2
/ 461 93 491 489 488 487 486 485 484 483 48 268 267 /
     TR 1
:
'TYINGS'
```

The semi-discretised nodes at the interface of the coarse and the refined mesh are tied to their neighboured nodes using a linear deformation relation.

```
BETWEE TR 1 2
298   71 146
297  146 145
296  145 144
295  144 143
294  143 23
269   23 142
```

Additionally, the interaction of the reinforcement nodes on the symmetry line was considered.

```
FIX  TR 1
2093 1093 TR 1 -1
2048 1048 TR 1 -1

'LOADS'
```

Here the self-weight and the size of one displacement step were defined.

The prescribed deformation starts at the initial deformation due to self-weight. In this way the system was statically determined

```
CASE 1
WEIGHT
2     -9.81
CASE 2
DEFORM
267    TR 2    -1.42E-4

CASE 3
DEFORM
267    TR 2     0.1E-3

COMBIN
1     1 1.0 2 1.0 3 0.0
2     1 0.0 2 0.0 3 1.0

'END'
```

## C.3.2  Command-file for linear analysis

With this file a preliminary linear analysis is performed. Furthermore, the FILOS-file is initiated and the data of the DATA-file processed. The MA=200000 specifies the maximum size of the FILOS-file.

```
*FILOS
INITIALIZE MA=200000
*INPUT
*LINSTA
*END
*END
```

## C.3.3  Command file for initiation of the non-linear analysis

Apart from other information the different material models are initiated (Plasticity PLASTI.N, Cracking TOTCRK.S, Interface INTERF). Furthermore, the load combinations are defined.

```
*NONLIN
 INITIA
  ANALYS PHYSIC
  USE
  PLASTI.N
  TOTCRK.S
  INTERF
 END USE
OPTION    TANGEN
END INITIA
LOADIN
 LOAD(1): (1) 1.0   (2) .0 /
 LOAD(2): (1) .0    (2) 1.0 /
END LOADIN
*END
```

## C.3.4 Command file for the non-linear analysis

*NONLIN

In the SELECT part the required output is specified. In this case the external post processor Femview, Femsys (1998), was used.

```
SELECT
 STEPS 1-300(10) /
NODES ALL /
ELEMEN ALL /
END ELEMEN
REINFO NONE /
END REINFO
END SELECT
OUTPUT FEMVIEW NONLIN BINARY FI="RV1212"
 STRAIN GLOBAL
 STRESS GLOBAL
 STRAIN PRINCI
 STRESS PRINCI
 DISPLA TOTAL GLOBAL
 FORCE RESIDU GLOBAL
END OUTPUT
```

In the "execute" command block the load steps carried out are defined. In this case first the responds of the specimen due to self-weight was determined LOAD(1) and then the responds due to the displacement prescribed LOAD(2).

```
EXECUT LOAD(1) STEPS
 SIZE.L 1(1) ND=6 GM=0 /
 PERFOR SECANS BFGS MI=20
 NORM ENERGY CONTINUE CO=0.000100
END EXECUT

EXECUT LOAD(2) STEPS
 SIZE.L 1.0(250) ND=6 GM=0 /
 PERFOR SECANS BFGS MI=30
 NORM ENERGY CONTINUE CO=0.000100
END EXECUT
```

*END

# Appendix D

# D Relation of steel stress and radial pressure acting on the concrete

The detailing in form of a reinforcement loop splice is influenced by several parameters, which complicate the analyses. To illustrate the main relation of steel stress to radial pressure a model with several simplifying assumptions is introduced.

The main assumptions are:

- The bond stress and the friction coefficient are constant along the loop.

- The relation $P = \dfrac{F_s}{r}$, as derived in Section E.2.1, is valid for varying steel force.

- The steel stress is not influenced by a torsional moment.

- The contact area is assumed to be plane, as shown in Figure D.4.

- The loop splice is subjected by pure bending.
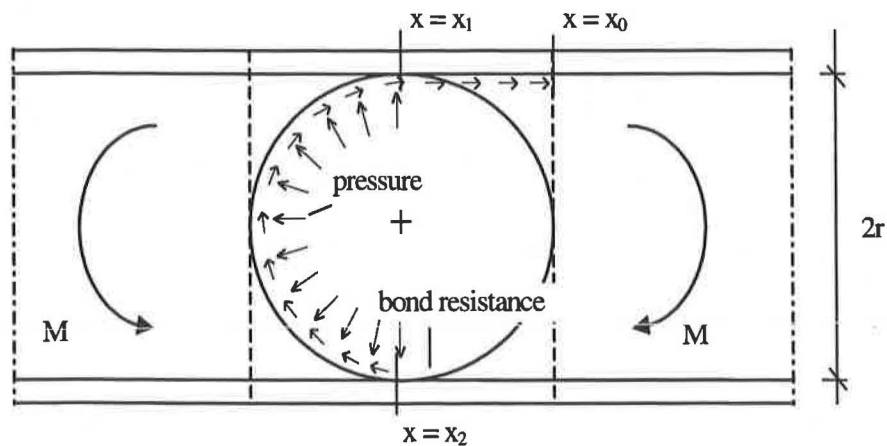


Figure D.1    Geometry and acting forces on the splice zone.

The loop can be divided into a straight part and a curved part. In the following sections the two parts are treated separately.

## D.1  Resistance along the straight part
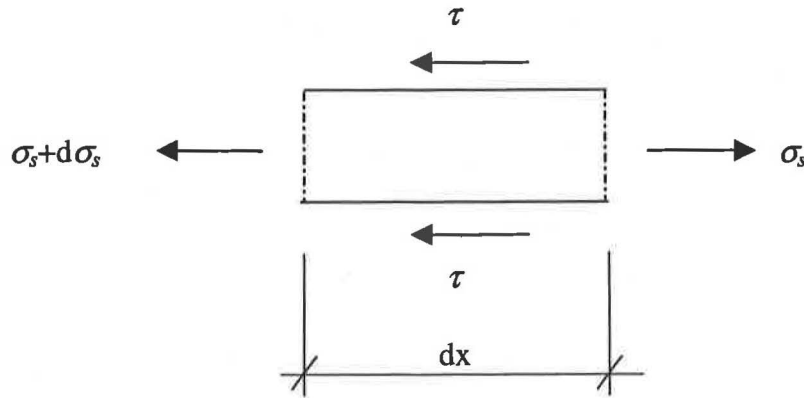


Figure D.2    Acting stresses in longitudinal direction at the straight part, with $\tau$ as the bond stress.

Equilibrium:

$$\left(\sigma_s + d\sigma_s\right)\cdot A_s + \tau\cdot U_s\cdot dx = \sigma_s\cdot A_s \tag{D.1}$$

with

$A_s$ = sectional area of the reinforcement bar,

$U_s$ = perimeter of the bar

$\tau$ = bond stress and

$\sigma_s$ = steel stress.

Differential equation:

$$\frac{d\sigma_s}{dx} = -\frac{\tau\cdot U_s}{A_s} \tag{D.2}$$

Solution for $\tau$ = constant on a length $x_1 - x_0$, see Figure D.1.

$$\sigma_{sx_1} = \sigma_{sx_0} - \frac{\tau\cdot U_s}{A_s}\cdot x_1 \tag{D.3}$$

with

$x_0 = 0$

## D.2 Resistance along the curved part

### D.2.1 Relation of steel stress to radial pressure
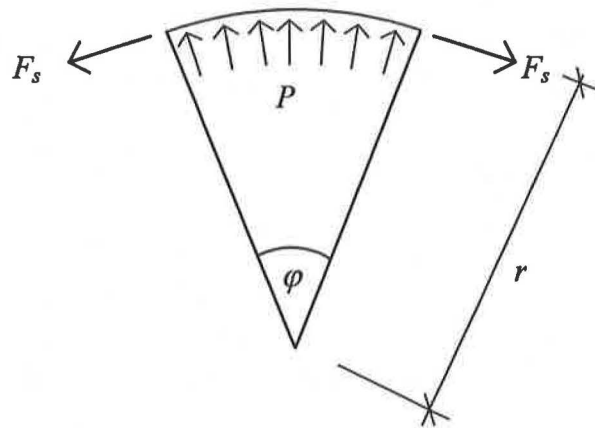


Figure D.3    Pressure along the curved part.

Equilibrium in vertical direction:

$$2 \cdot F_s \cdot \sin\left(\frac{\varphi}{2}\right) = \int_{-\frac{\varphi}{2}}^{\frac{\varphi}{2}} P \cdot \cos(\varphi) \cdot r \cdot d\varphi \tag{D.4}$$

$$2 \cdot F_s \cdot \sin\left(\frac{\varphi}{2}\right) = 2 \cdot P \cdot \sin\left(\frac{\varphi}{2}\right) \cdot r \tag{D.5}$$

$$P = \frac{F_s}{r} \tag{D.6}$$

with

$$F_s = \sigma_s \cdot A_s$$

and

$$P = P^* \cdot \phi$$

with $P^*$ as the simplified pressure distribution according to Figure D.4.

D.3
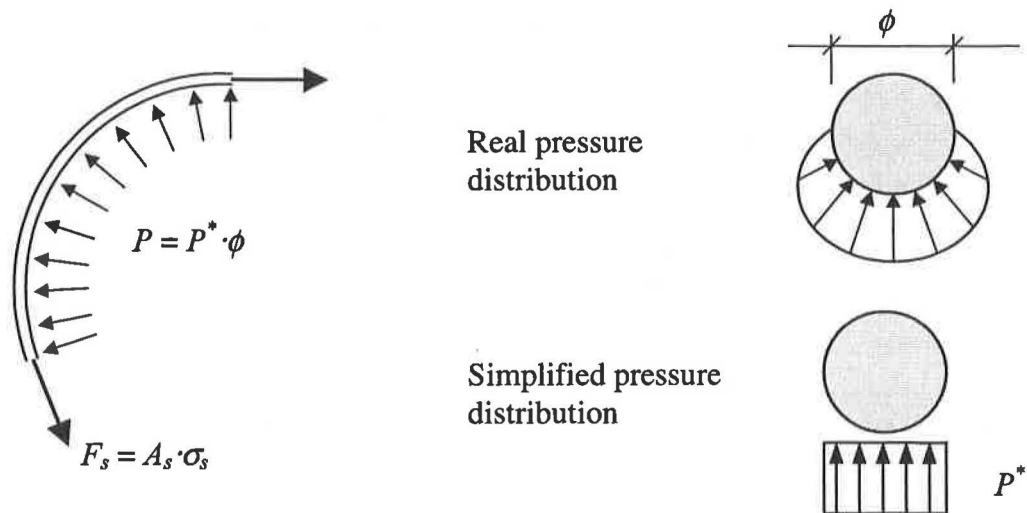
Figure D.4    Simplification of radial pressure distribution.

## D.2.2   Varying steel stress under consideration of bond and friction

The stress in the reinforcement is influenced by the bond stress along the loop and an additional friction resistance caused by the radial pressure. Both friction, with $\mu$ as friction coefficient, and bond $\tau$ are activated by a certain slip of the reinforcement bar.
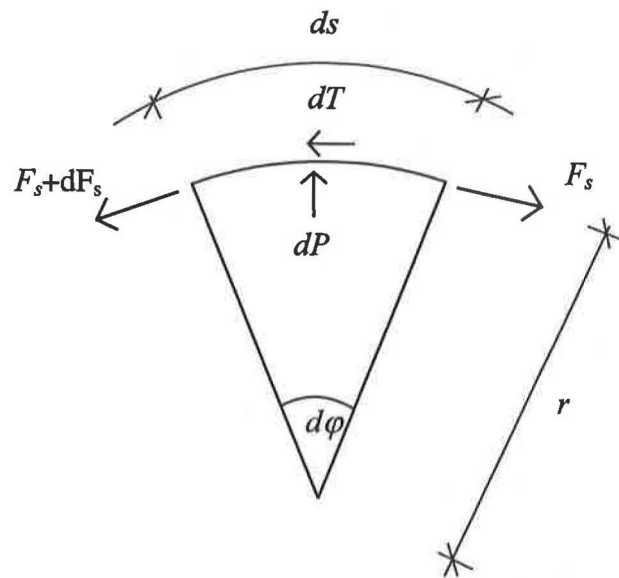


Figure D.5    Acting stresses along the curved part.

Geometry:

$$ds \approx r \cdot d\varphi \tag{D.7}$$

Equilibrium:

$$F_s + dF_s + dT = F_s \tag{D.8}$$

Friction and bond:

$$dT = \mu \cdot dP + \tau \cdot U_s \cdot ds \tag{D.9}$$

with

$\mu$ = friction coefficient

$$dP = r \cdot d\varphi \cdot P = r \cdot d\varphi \cdot \frac{F_s}{r} \tag{D.10}$$

$$dT = \mu \cdot r \cdot d\varphi \cdot \frac{F_s}{r} + \tau \cdot U_s \cdot r \cdot d\varphi \tag{D.11}$$

$$F_s + dF_s + \left(\mu \cdot F_s + \tau \cdot U_s \cdot r\right) \cdot d\varphi = F_s \tag{D.12}$$

**Differential equation:**

$$\frac{dF_s}{d\varphi} = -\left(\mu \cdot F_s + \tau \cdot U_s \cdot r\right) \tag{D.13}$$

Solution for a length $\pi \cdot r$:

$$\int_{F_{sx_1}}^{F_{sx_2}} \frac{1}{\mu \cdot F_s + \tau \cdot U_s \cdot r} dF_s = -\int_{\varphi_{x_1}=0}^{\varphi_{x_2}=\pi} d\varphi \tag{D.14}$$

$$\ln\left(\frac{\mu \cdot F_{sx_1} + \tau \cdot U_s \cdot r}{\mu \cdot F_{sx_2} + \tau \cdot U_s \cdot r}\right) = -\pi \cdot \mu \tag{D.15}$$

$$F_{sx_2} = \frac{1}{\mu} \cdot \left[e^{-\pi \cdot \mu} \cdot \left(\mu \cdot F_{sx_1} + \tau \cdot U_s \cdot r\right) - \tau \cdot U_s \cdot r\right] \tag{D.16}$$

# D.3 Results of the FE-analyses concerning the radial pressure

The theoretical considerations of the relation of steel stress to radial pressure are based on many simplifications. In earlier test series conducted by Timm G. (1969) it

was observed, that the anchorage along the curved part was less effective than expected. The additional part of the bond resistance was not activated. One of the conclusions was, that the radial pressure and therewith the friction is not activated until a certain slip of the reinforcement.

To investigate this phenomenon further the relation of steel stress to radial pressure versus the deformation of the specimen is shown for three finite elements at the beginning of the curvature, see Figure D.6 to Figure D.9. The expected value for the relation according to the theoretical model can be calculated by equation D.17 to

$$\frac{F_s}{P} = r \qquad \qquad (D.17)$$
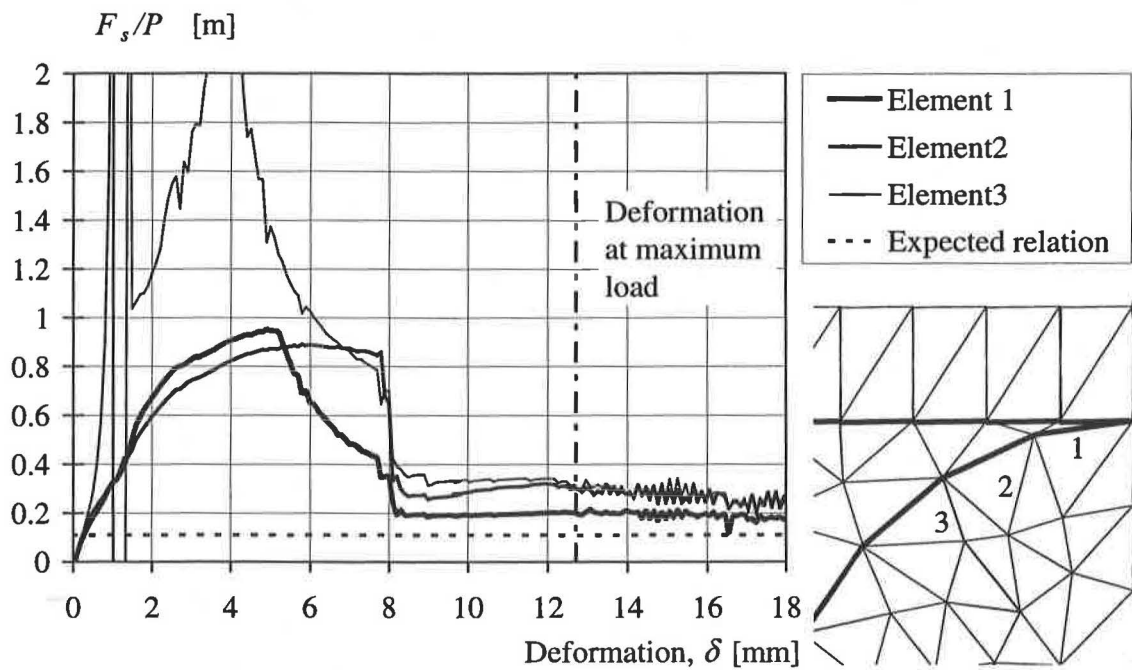


Figure D.6    Relation of steel stress to radial pressure versus deformation for specimen RV12 using "good" bond conditions.
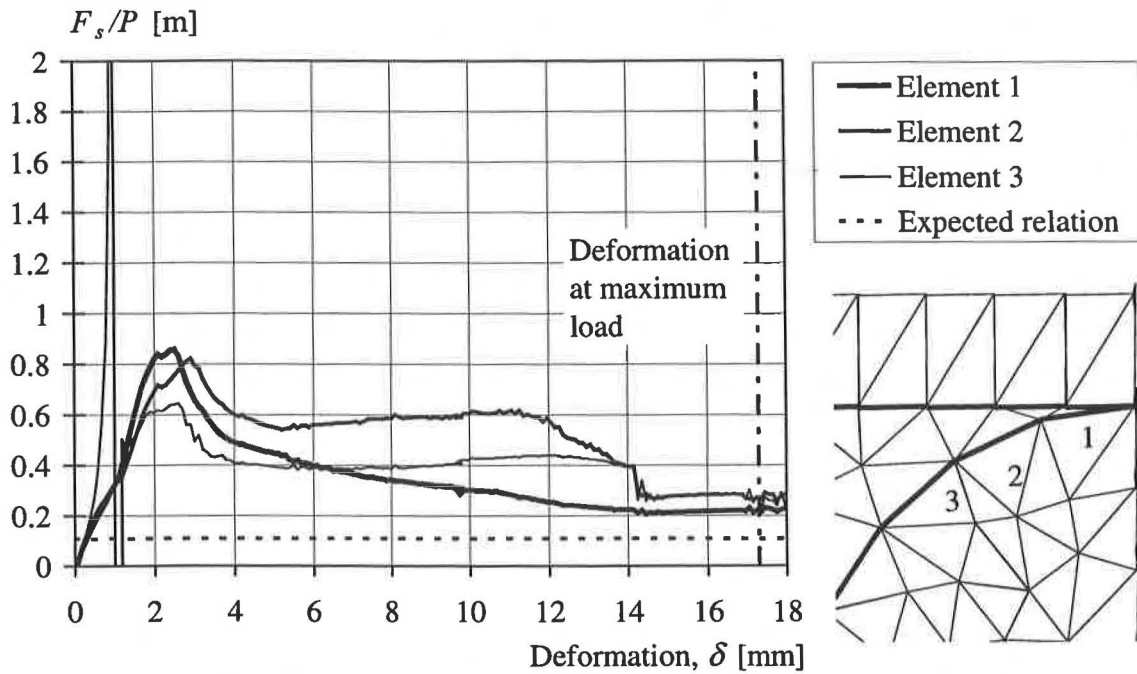
Figure D.7    Relation of steel stress to radial pressure versus deformation for specimen RV12 using "other" bond conditions.
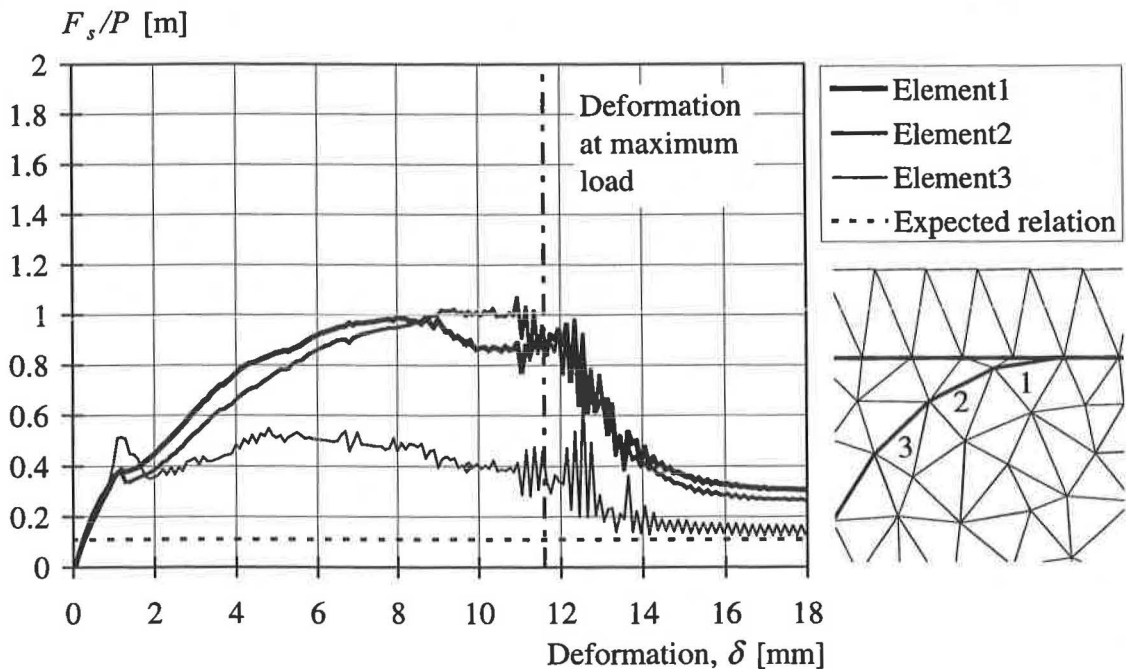


Figure D.8    Relation of steel stress to radial pressure versus deformation for specimen RV13 using "good" bond conditions.
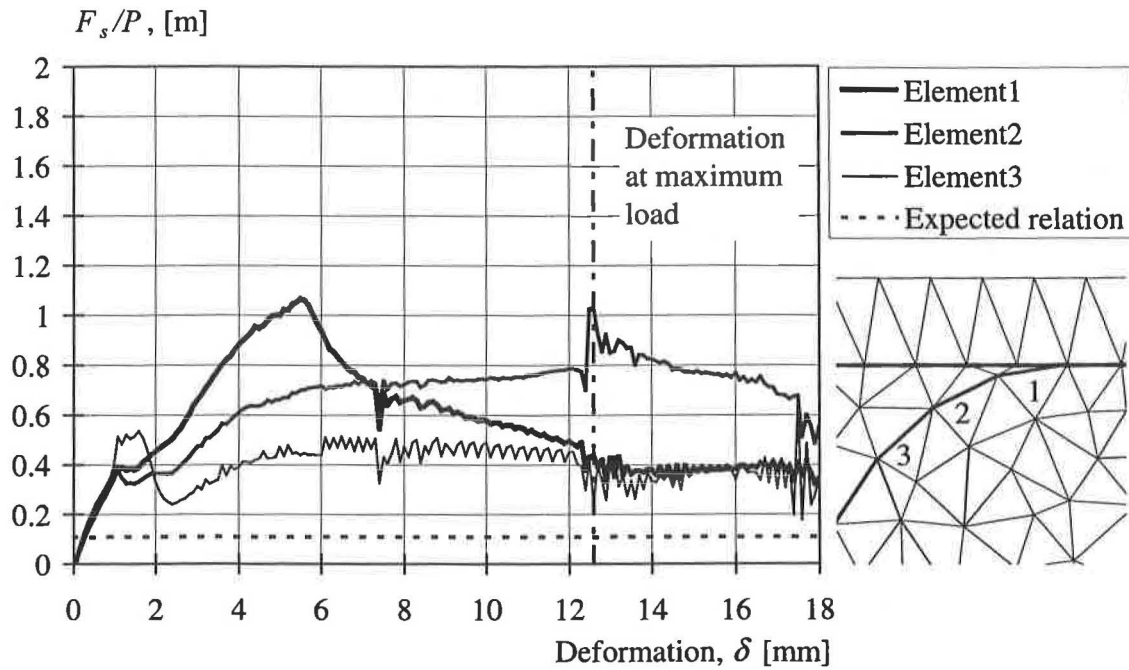
Figure D.9    Relation of steel stress to radial pressure versus deformation for specimen RV13 using "other" bond conditions.

The results in Figure D.6 to Figure D.9 show that the bond conditions influence the relation of steel stress to radial pressure. With good bond conditions the radial pressure starts to act later. Furthermore, in combination with a straight splice length the resulting radial pressure is considerably smaller than expected.

# Appendix E

# E Test results

## E.1 Results of the strain gauges

The results of the experiments are discussed in Section 3. There, some of the averages of the stresses in the reinforcement are shown, divided into outer and middle loops. Often, the results of the strain gauges differ even in the same part of the structure. Therefore, the strain-deformation relations of all strain gauges are shown in the following Figures F.1-F.28. The results of both sides of the section are compared, so that the significance of the average of the stresses used in Section 3 can be judged. The unloading beyond yielding is omitted, as the unloading behaviour of the strain gauges after a distinct yield phase does not seem to be reasonable.

The numbering of the strain gauges consist of the number of the loop and the number of the strain gauge of the loop. For instance, gauge number 141 refers to the gauge on position 1 of loop 14.
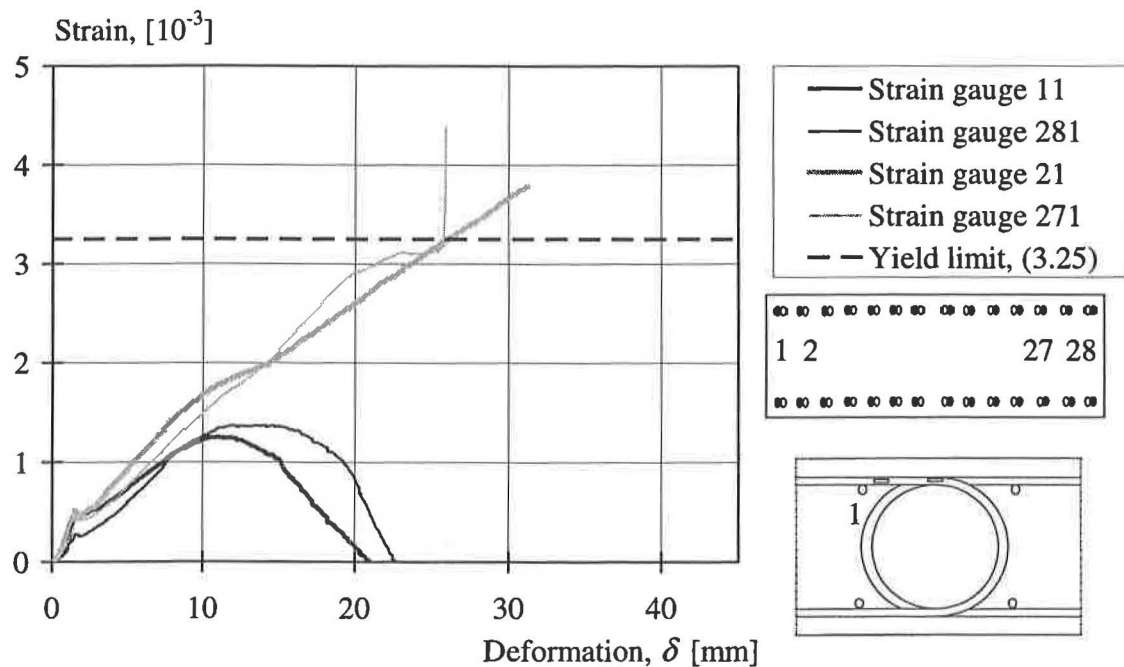
### E.1.1 Strain gauges of specimen RV12
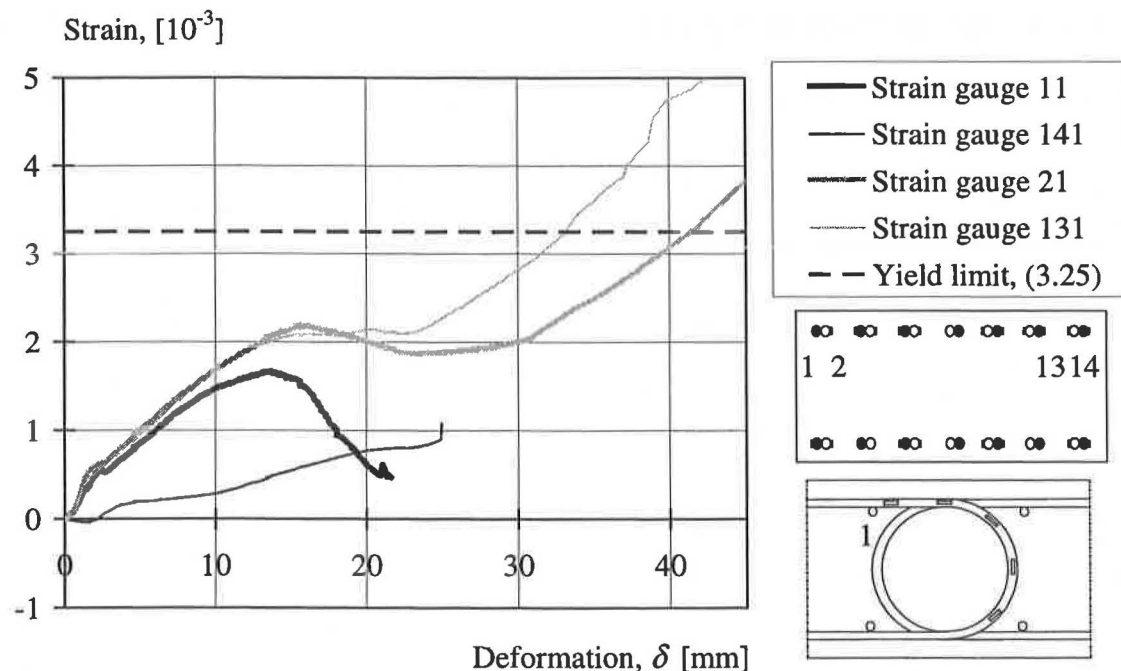


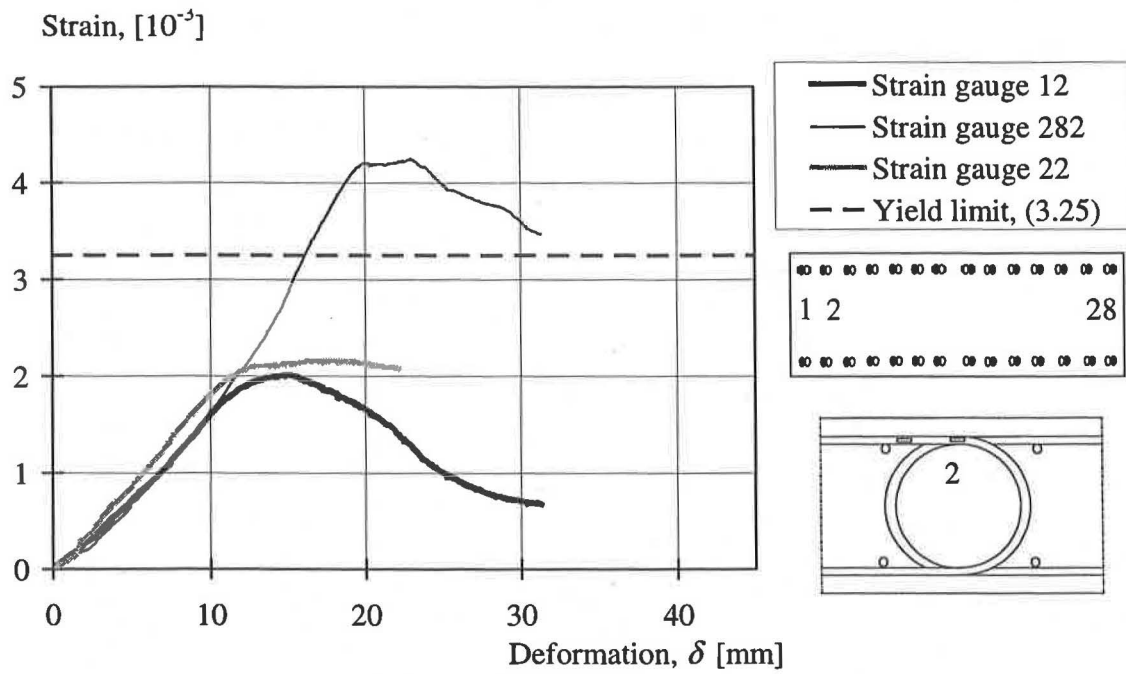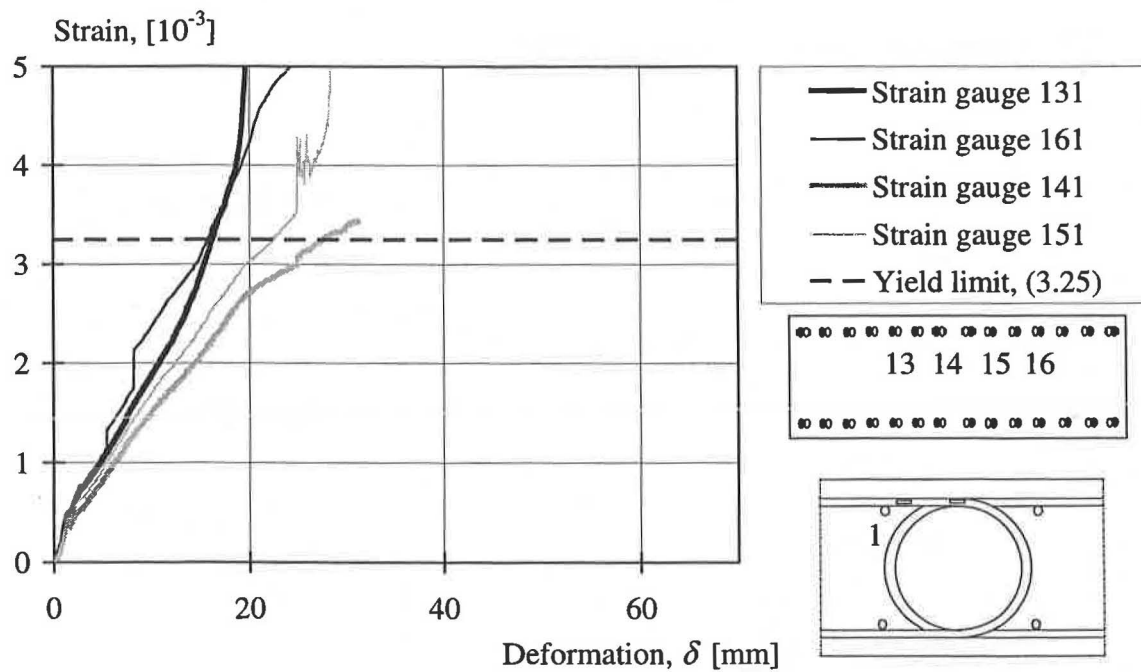Figure E.1    Strain-deformation relation of gauges 11, 141, 21 and 131 of specimen RV12.
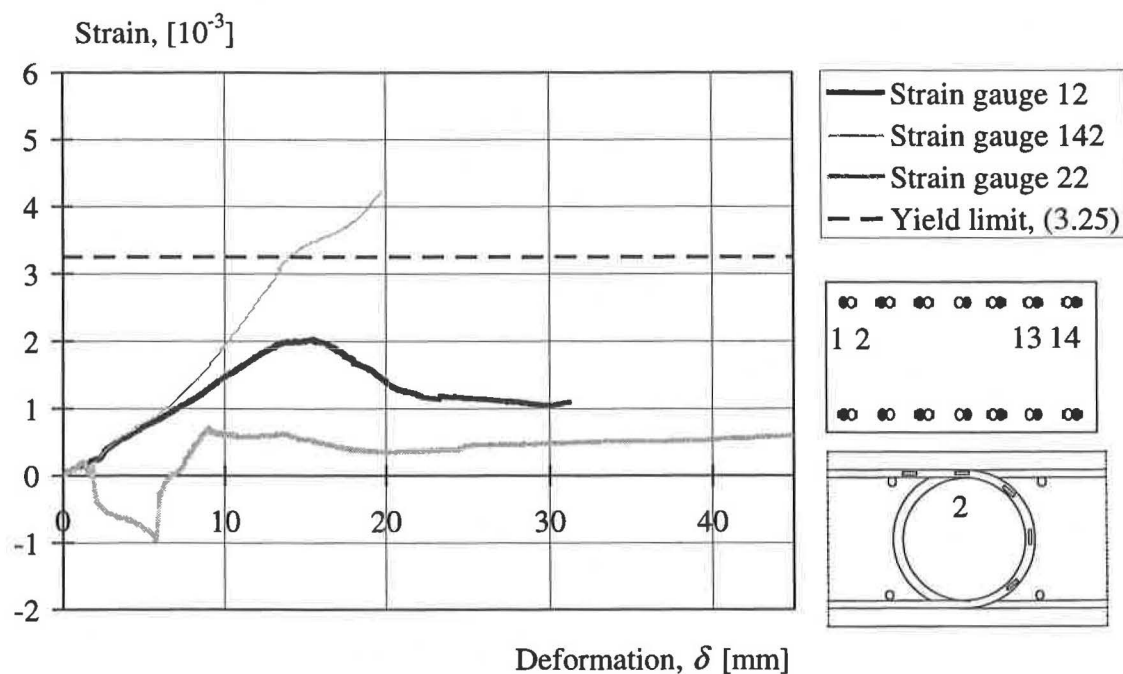
Figure E.2    Strain-deformation relation of gauges 12, 142 and 22 of specimen RV12.
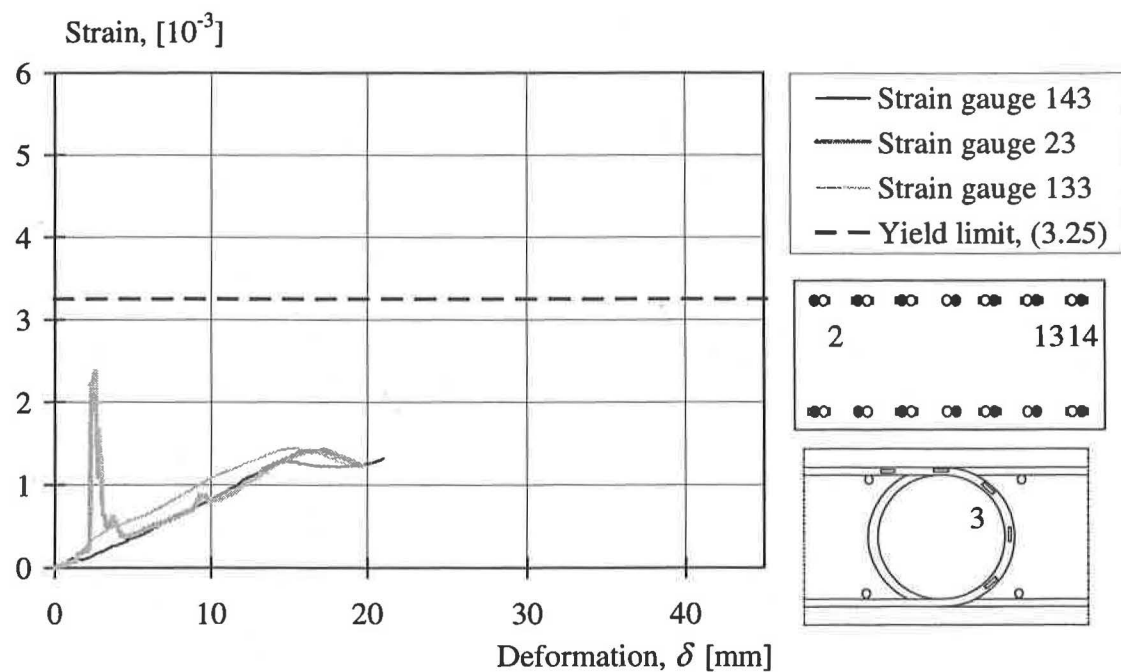


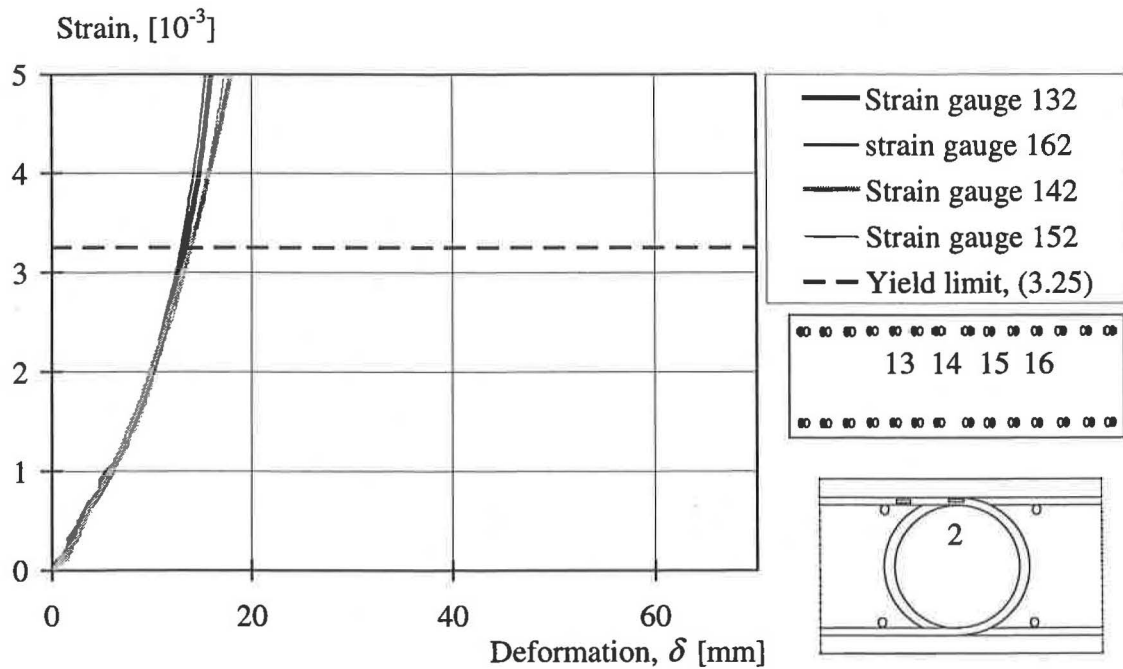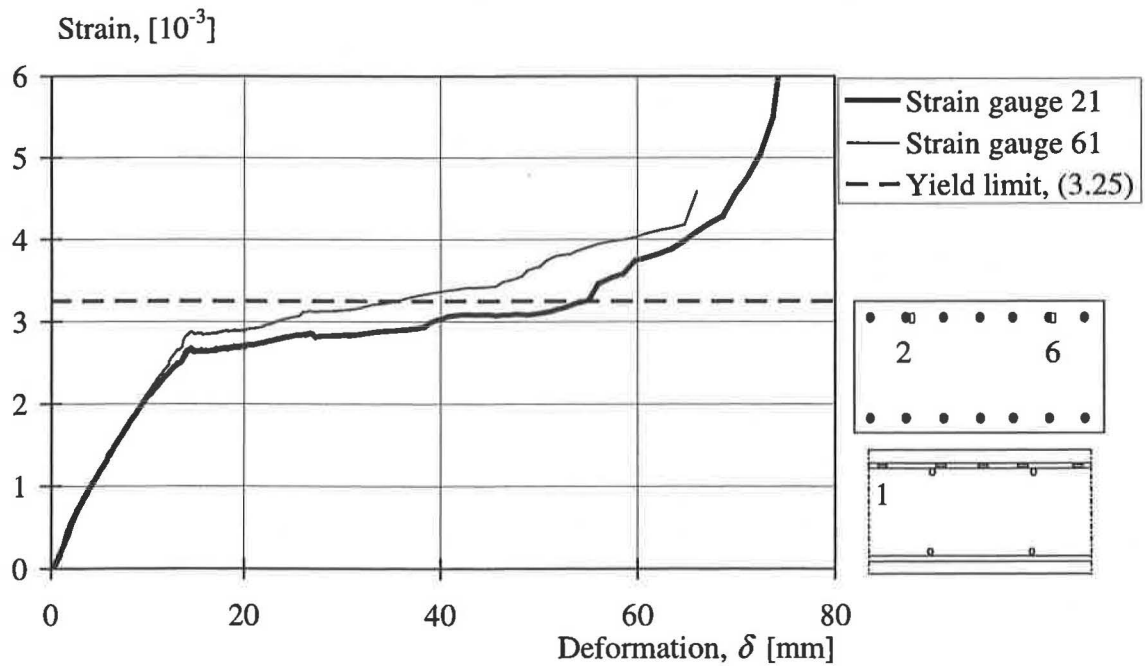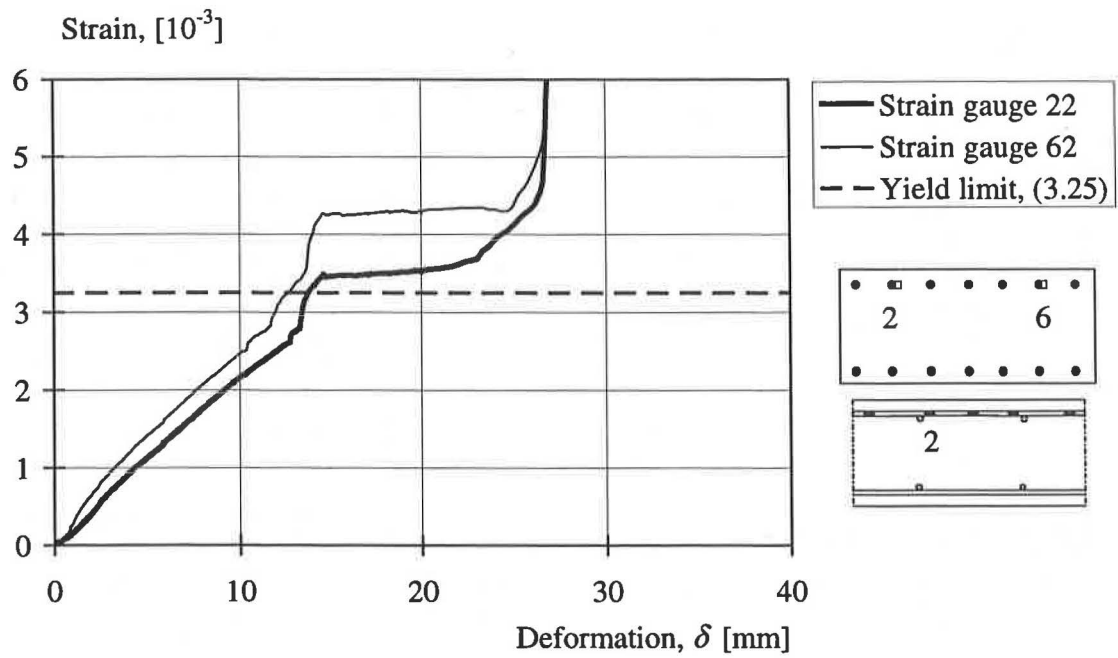Figure E.3    Strain-deformation relation of gauges 143, 23 and 133 of specimen RV12.
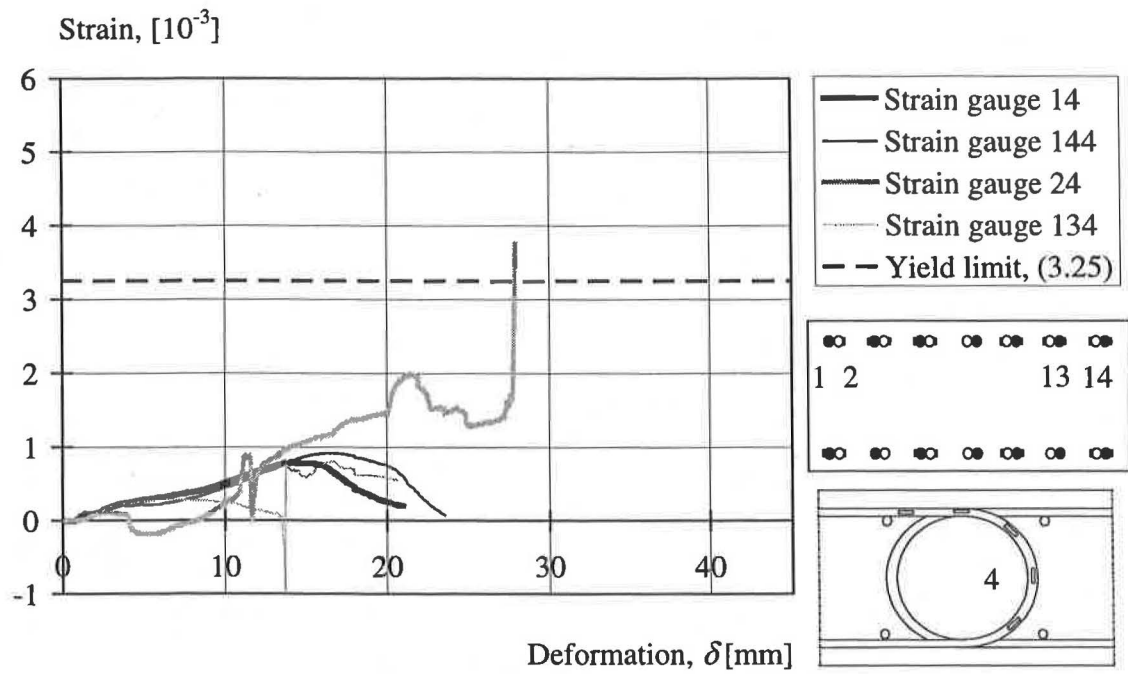
Figure E.4    Strain-deformation relation of gauges 14, 144, 24 and 134 of specimen RV12.
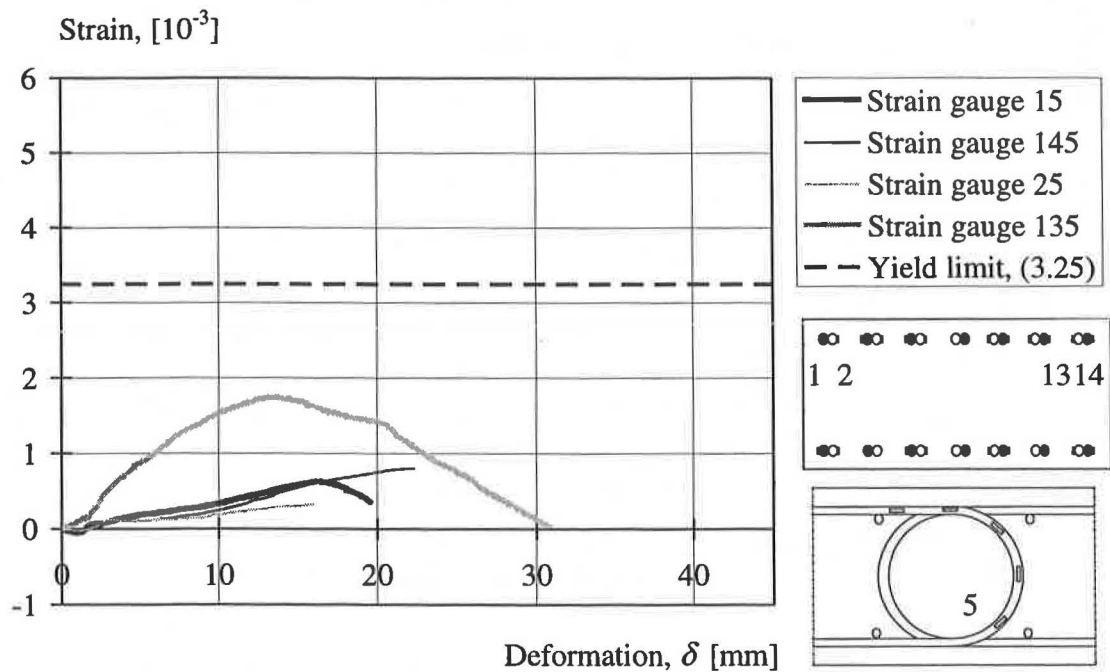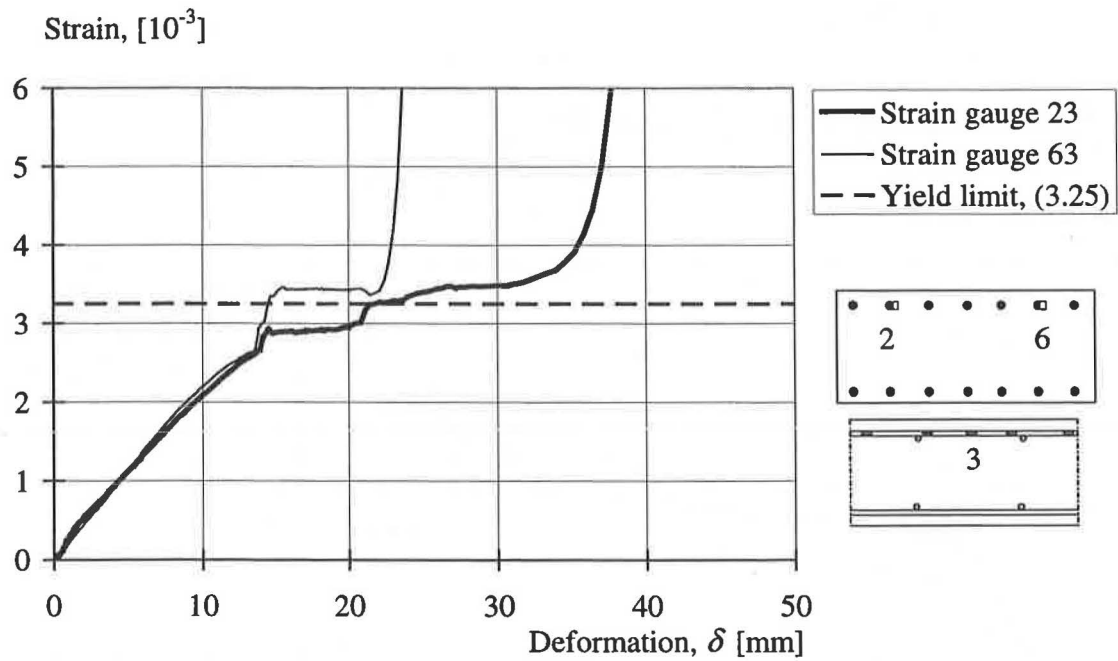


Figure E.5    Strain-deformation relation of gauges 15, 145, 25 and 135 of specimen RV12.
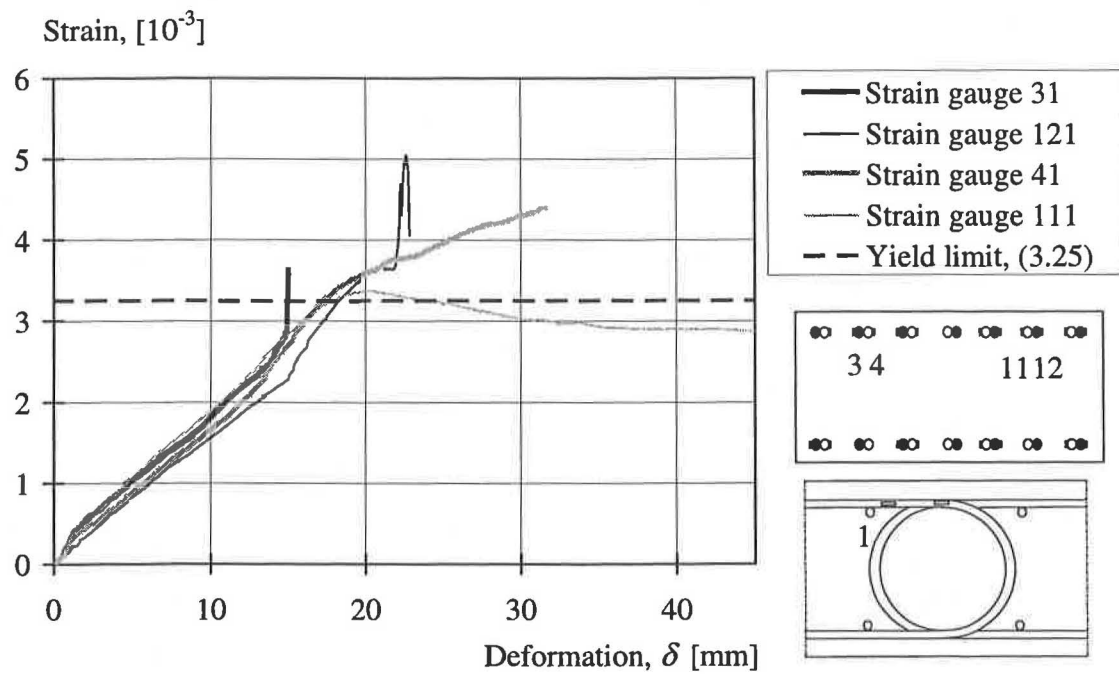
Figure E.6    Strain-deformation relation of strain gauges 31, 121, 41 and 111.
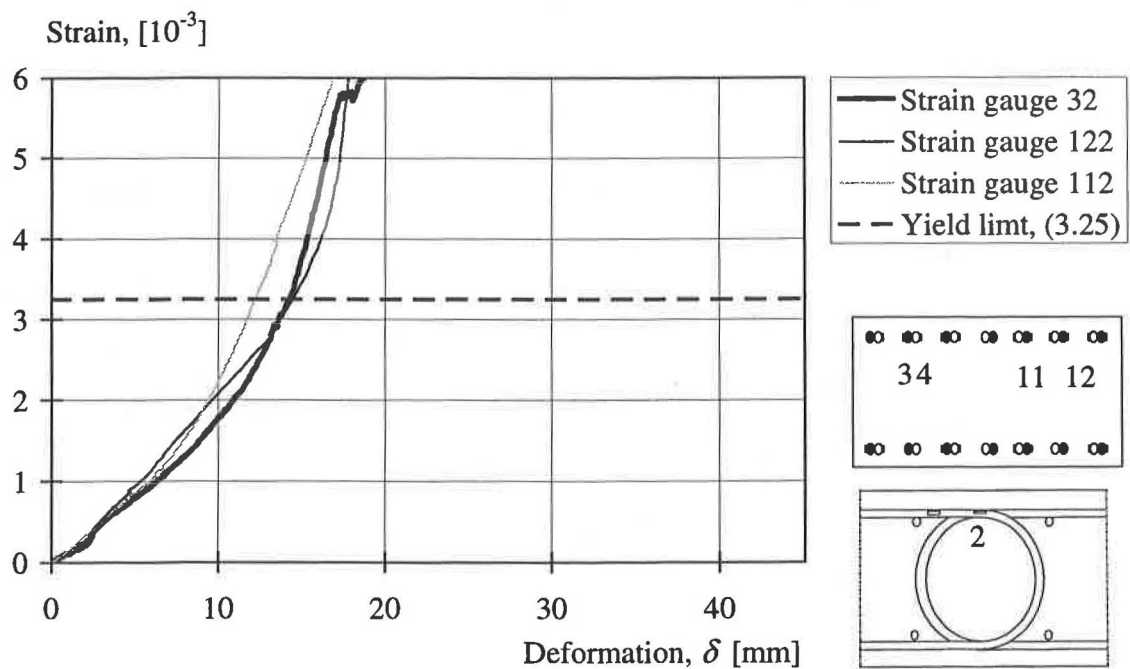


Figure E.7    Strain-deformation relation of gauges 32, 122 and 112 of specimen RV12.
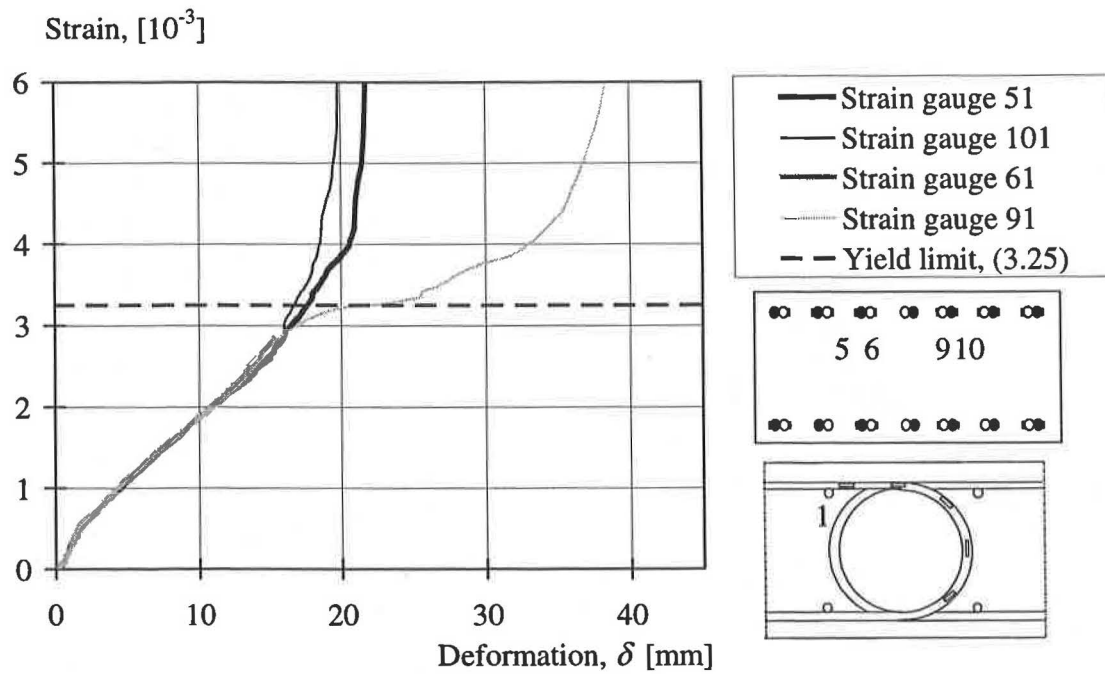
Figure E.8    Strain-deformation relation of strain gauges 51, 91, 61 and 101 of specimen RV12.
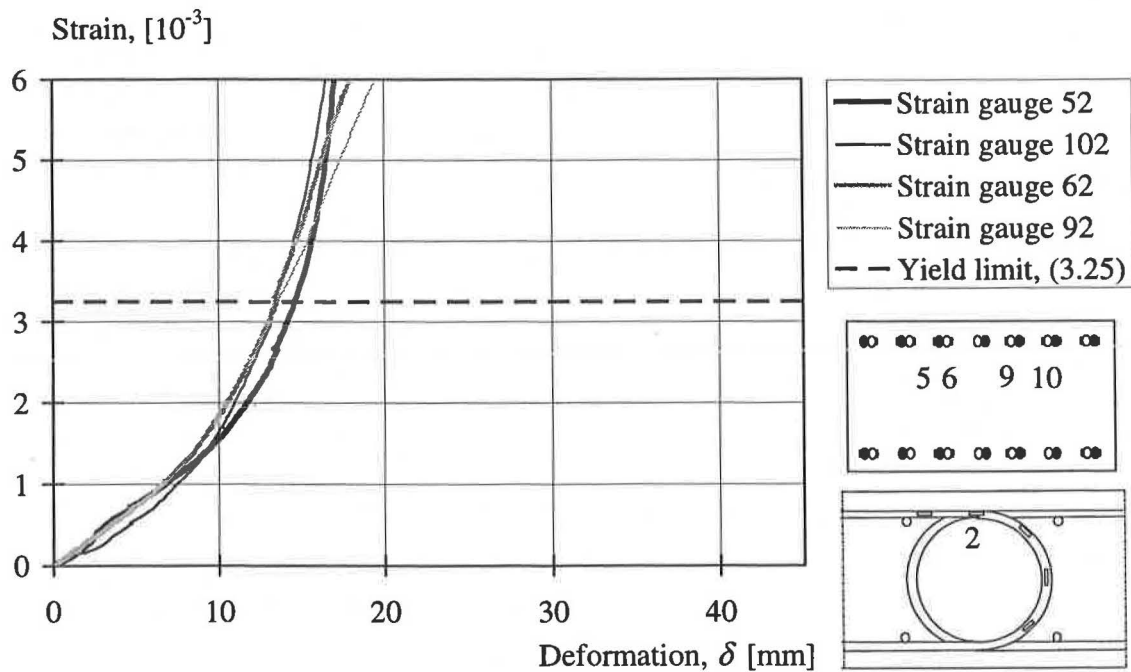


Figure E.9    Strain-deformation relation of gauges 52, 102, 62 and 92 of specimen RV12.
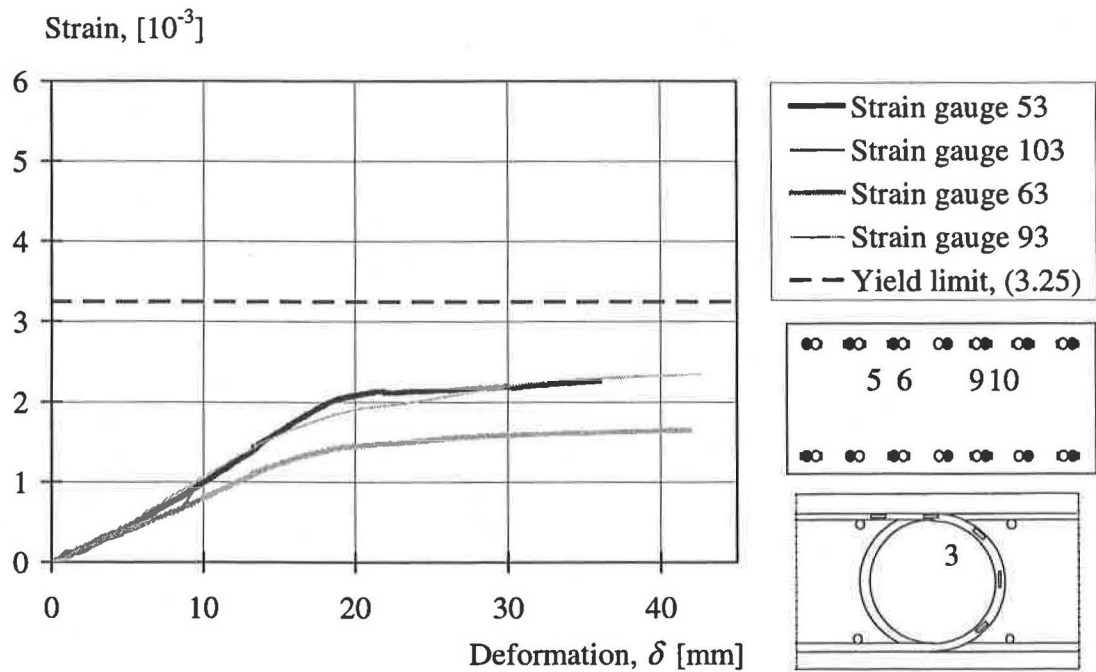
Figure E.10    Strain-deformation relation of gauges 53, 103, 63 and 93 of specimen RV12.
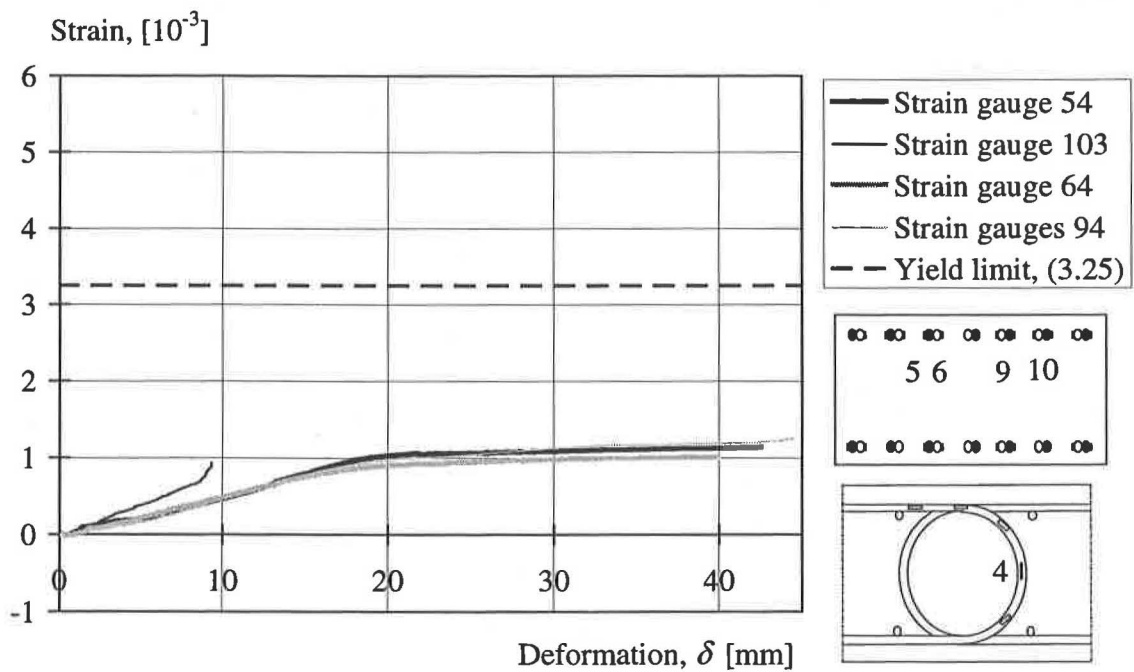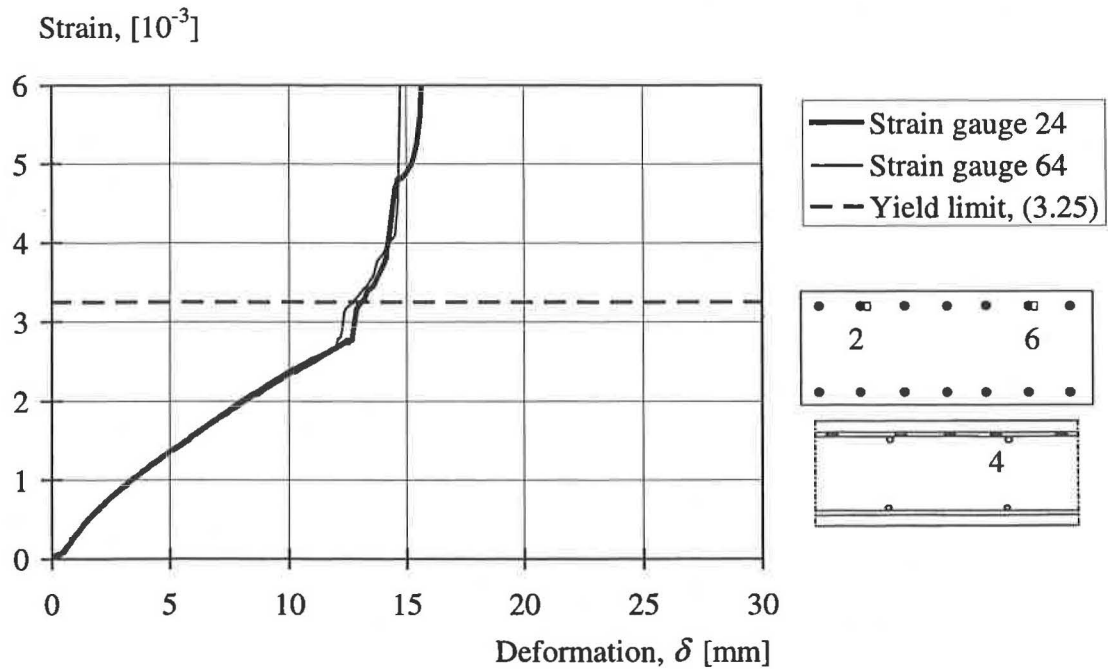


Figure E.11    Strain-deformation relation of gauges 54, 104, 64 and 94 of specimen RV12.
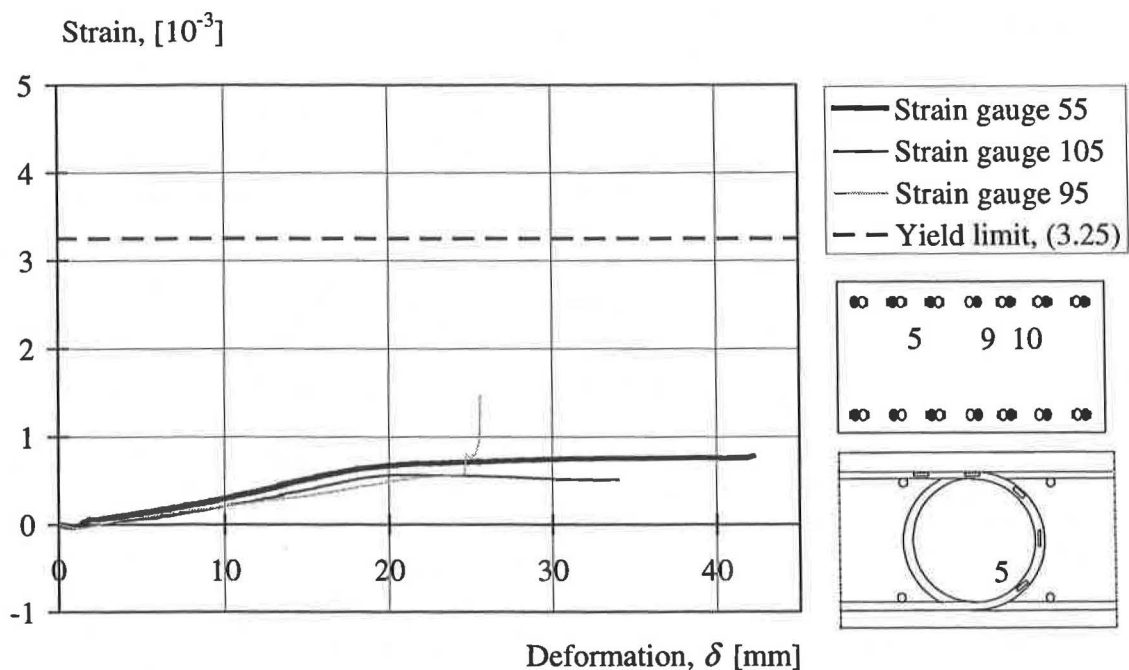
Figure E.12    Strain-deformation relation of gauges 55, 105 and 95 of specimen RV12.

## E.1.2    Strain gauges of specimen RV13
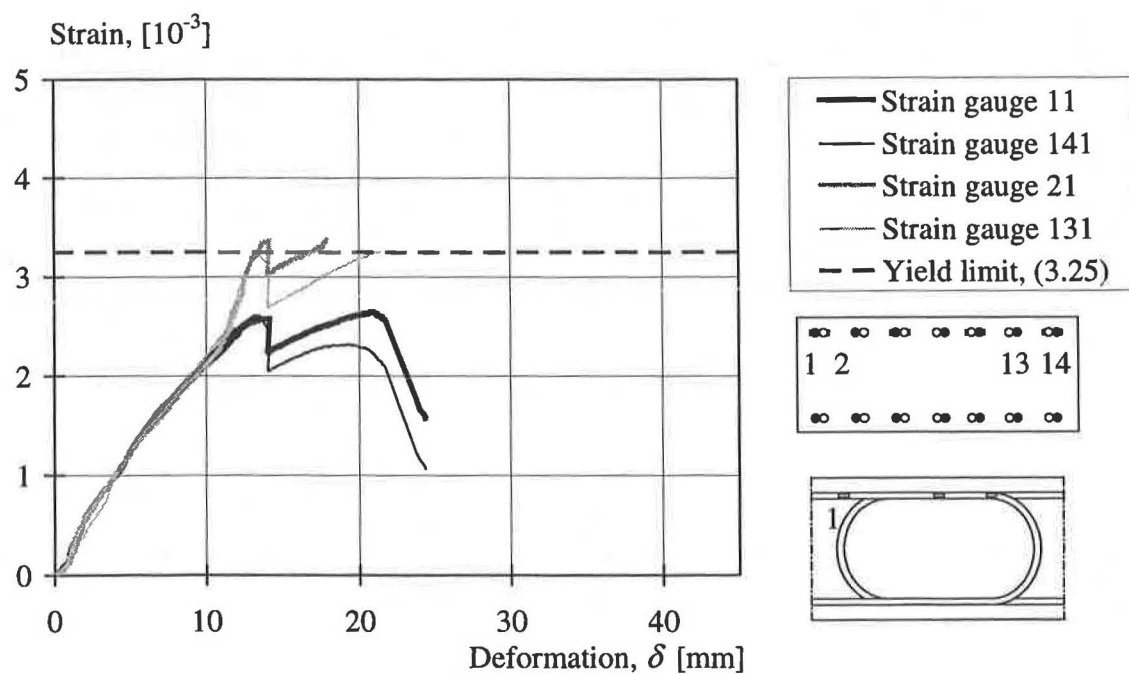


Figure E.13    Strain-deformation relation of gauges 11, 141, 21 and 131 of specimen RV13.
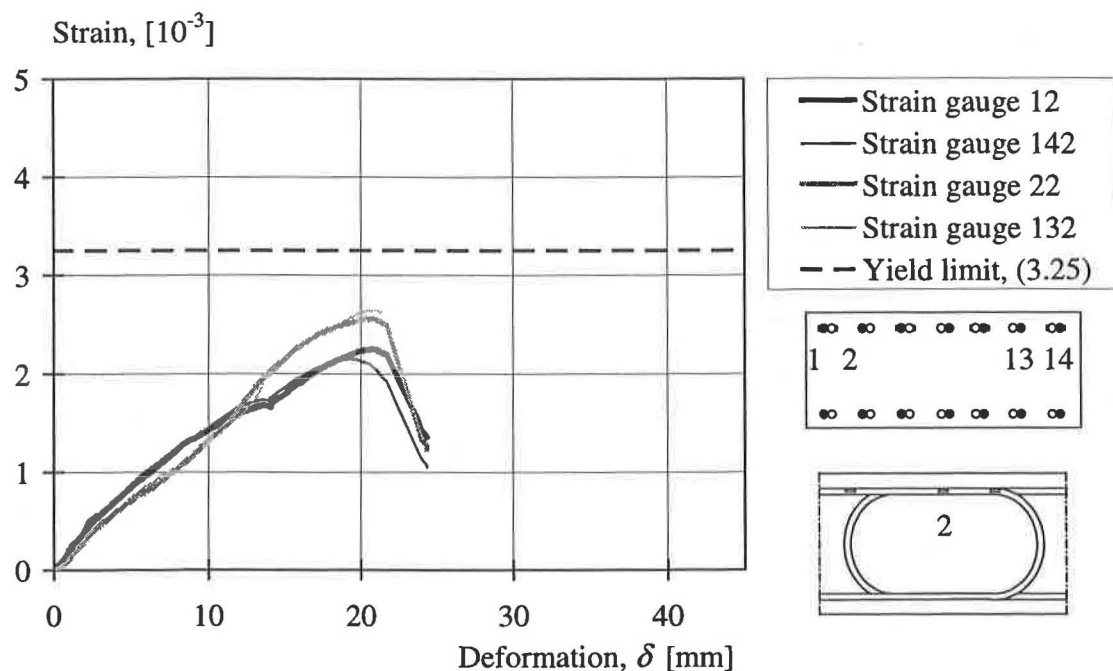
Figure E.14    Strain-deformation relation of gauges 12, 142, 22 and 132 of specimen RV13.
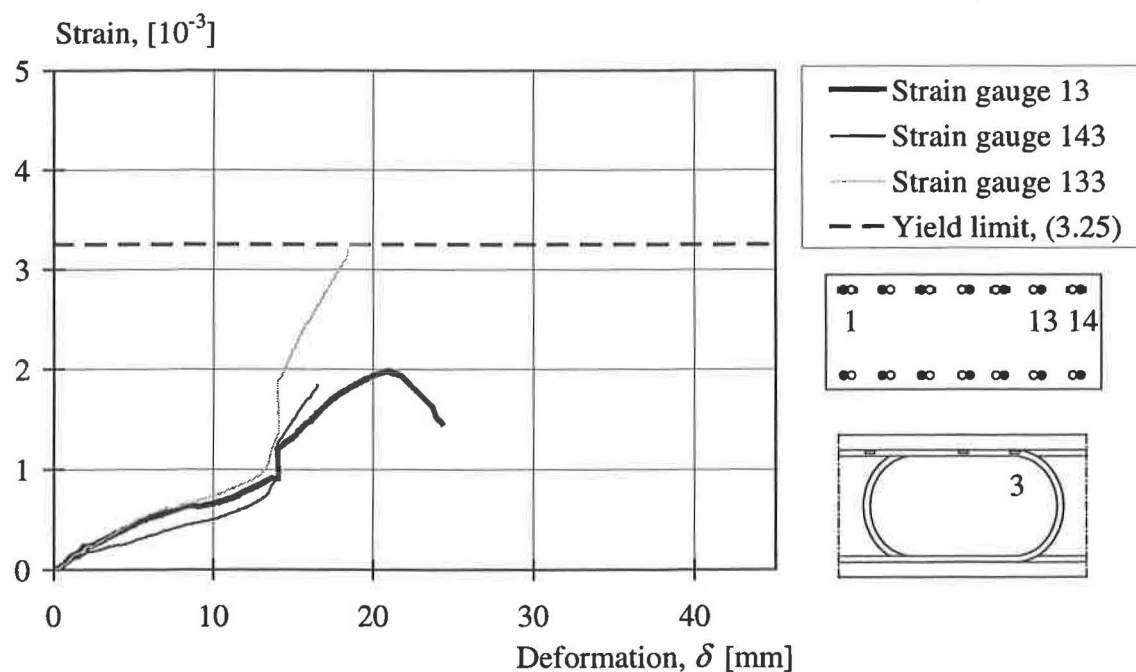


Figure E.15    Strain-deformation relation of gauges 13, 143 and 133 of specimen RV13.
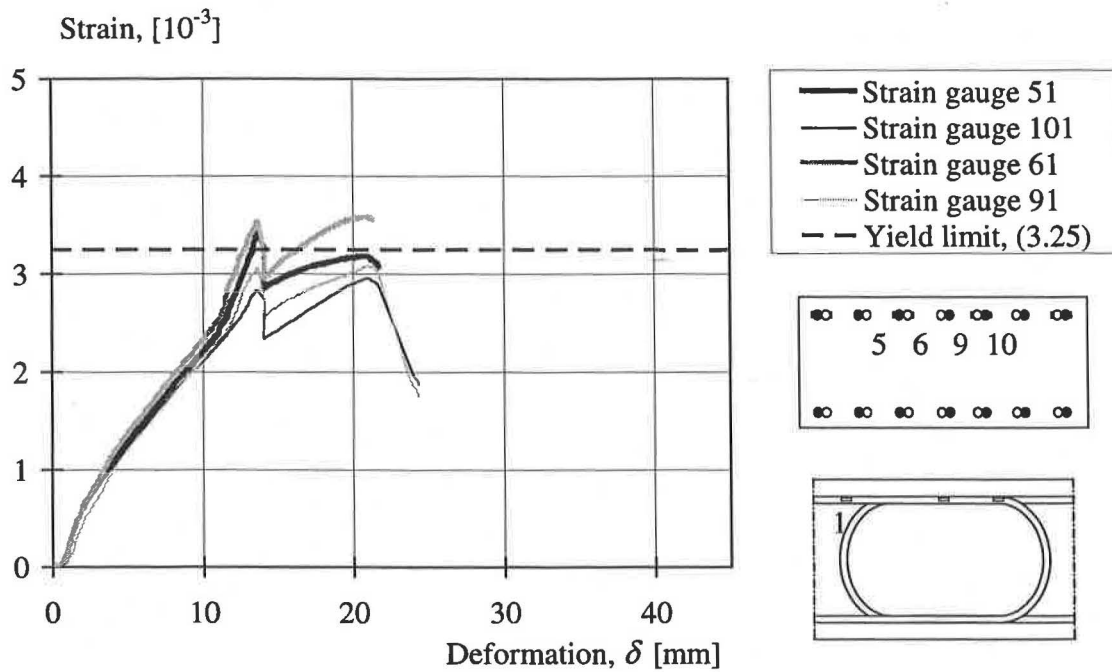
Figure E.16    Strain-deformation relation of gauges 51, 101, 61 and 91 of specimen RV13.
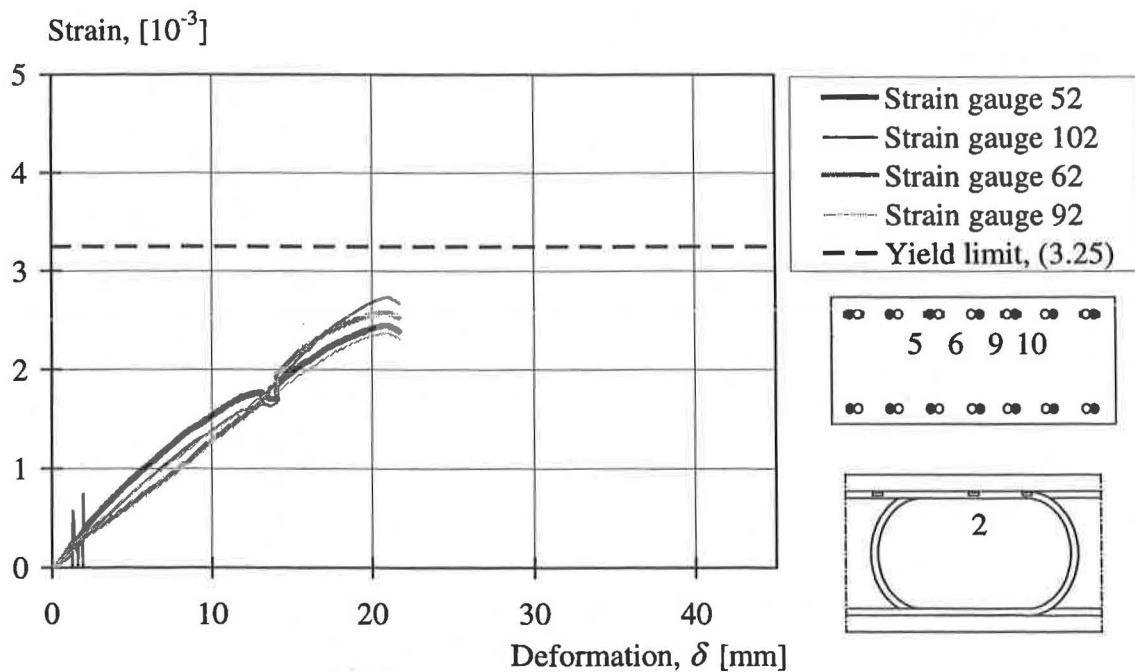


Figure E.17    Strain-deformation relation of gauges 52, 102, 62 and 92 of specimen RV13.
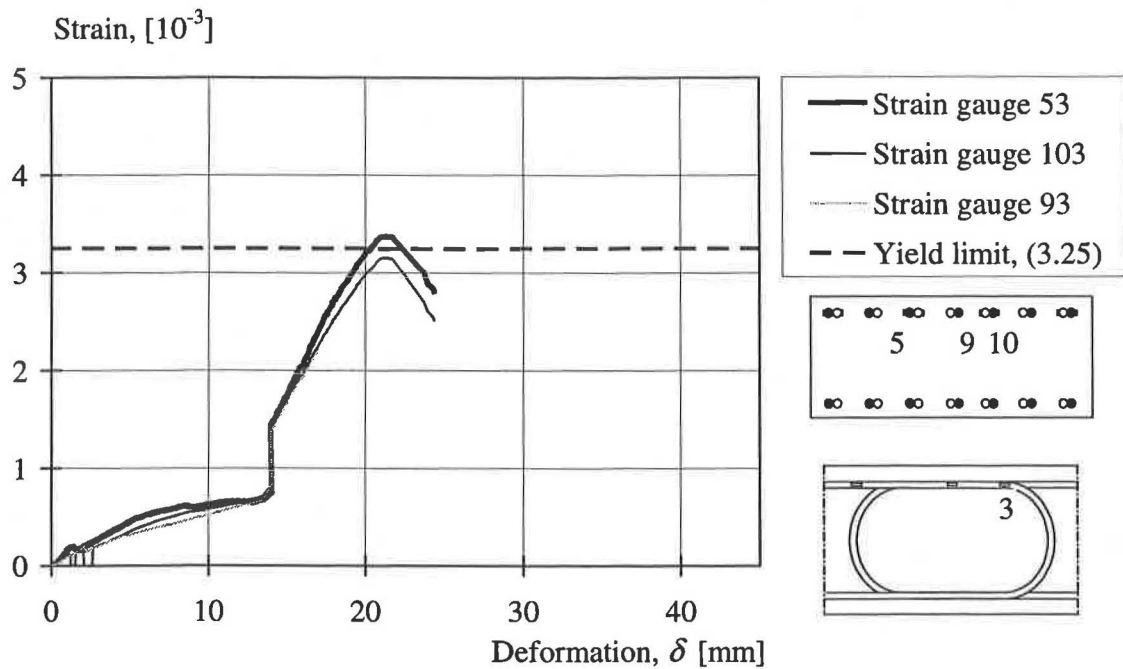
Figure E.18    Strain-deformation relation of gauges 53, 103 and 93 of specimen RV13.

## E.1.3    Strain gauges of specimen RV14



Figure E.19    Strain-deformation relation of gauges 11, 281, 21 and 271 of specimen RV14.

Figure E.20    Strain-deformation relation of gauges 12, 282 and 22 of specimen RV14.



Figure E.21    Strain-deformation relation of gauges 131, 161, 141 and 151 of specimen RV14.

Strain, [10$^{-3}$]



Figure E.22    Strain-deformation relation of gauges 132, 162, 142 and 152 of specimen RV14.

## E.1.4    Strain gauges of specimen RV15

Strain, [10$^{-3}$]



Figure E.23    Strain-deformation relation of gauges 21 and 61 of specimen RV15.

Figure E.24    Strain-deformation relation of gauges 22 and 62 of specimen RV15.



Figure E.25    Strain-deformation relation of gauges 23 and 63 of specimen RV15.

Figure E.26    Strain-deformation relation of gauges 24 and 64 of specimen RV15.
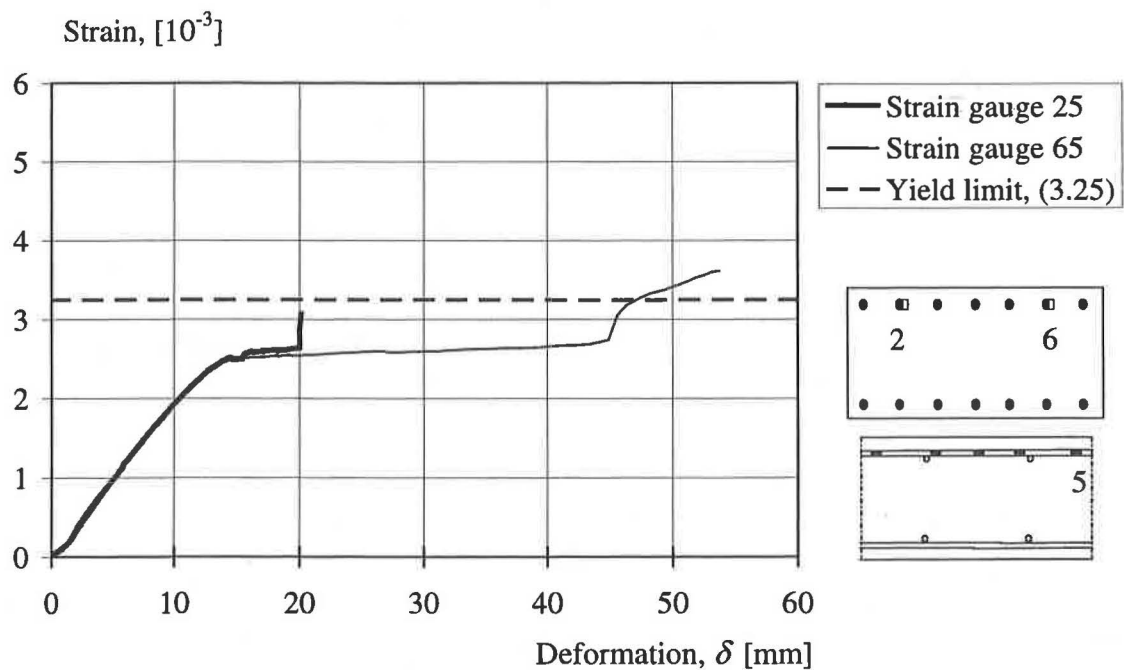


Figure E.27    Strain-deformation relation of gauges 25 and 65 of specimen RV15.

## E.2    Stresses at the position of the strain gauges

In Section 3 the stresses in some of the reinforcement loops are shown. The stress outputs of all reinforcement loops with strain gauges provided are shown in this section.

## E.2.1 Stresses of specimen RV12
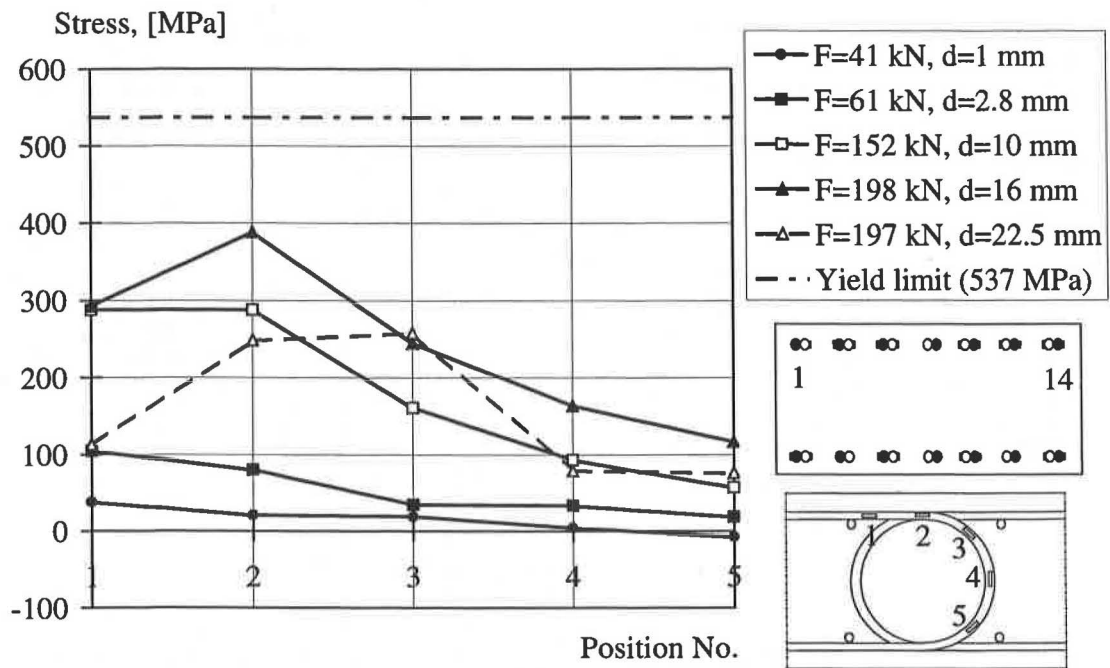


Figure E.28    Average stress of loops 1 and 14 of specimen RV12.
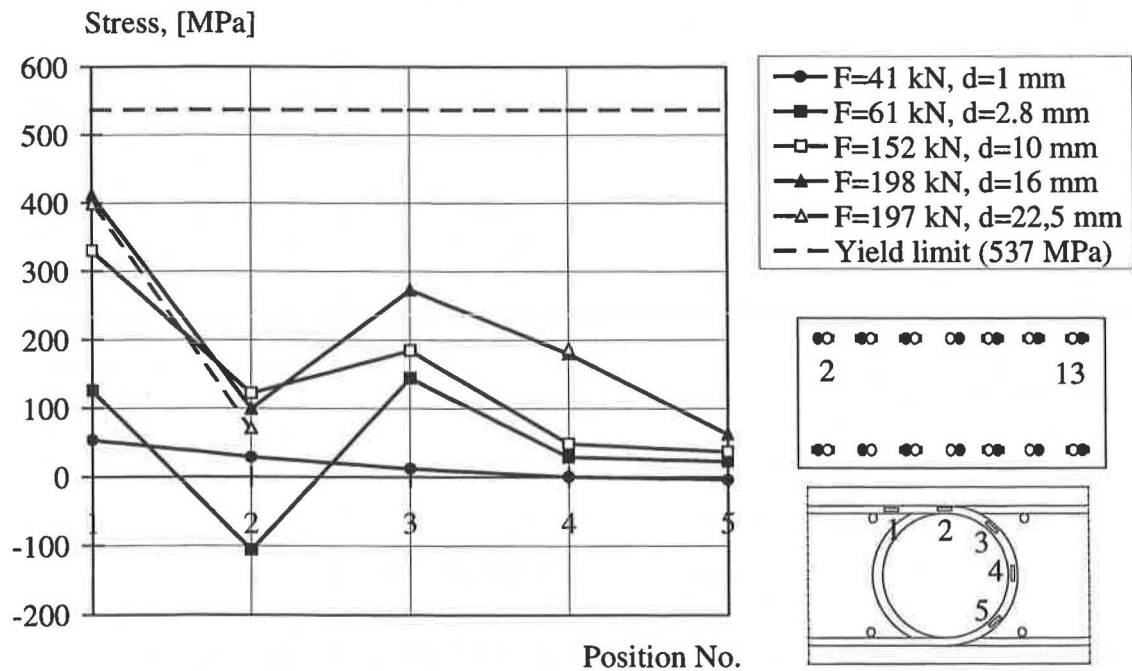


Figure E.29    Average stress of loops 2 and 13 of specimen RV12.
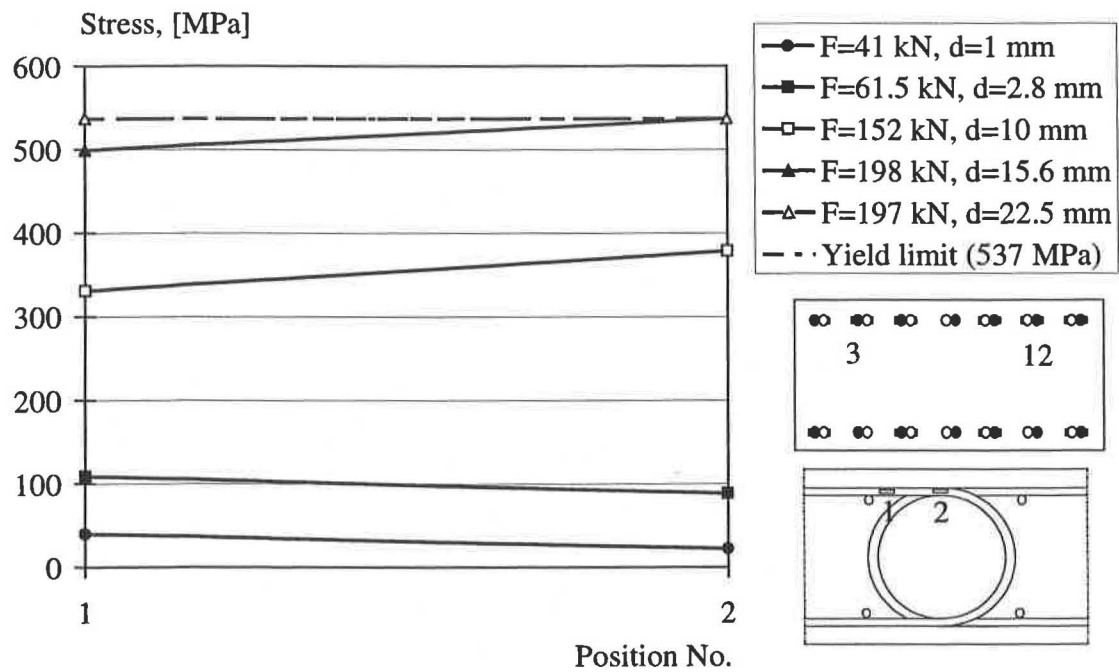
Figure E.30    Average stress of loops 3 and 12 of specimen RV12.
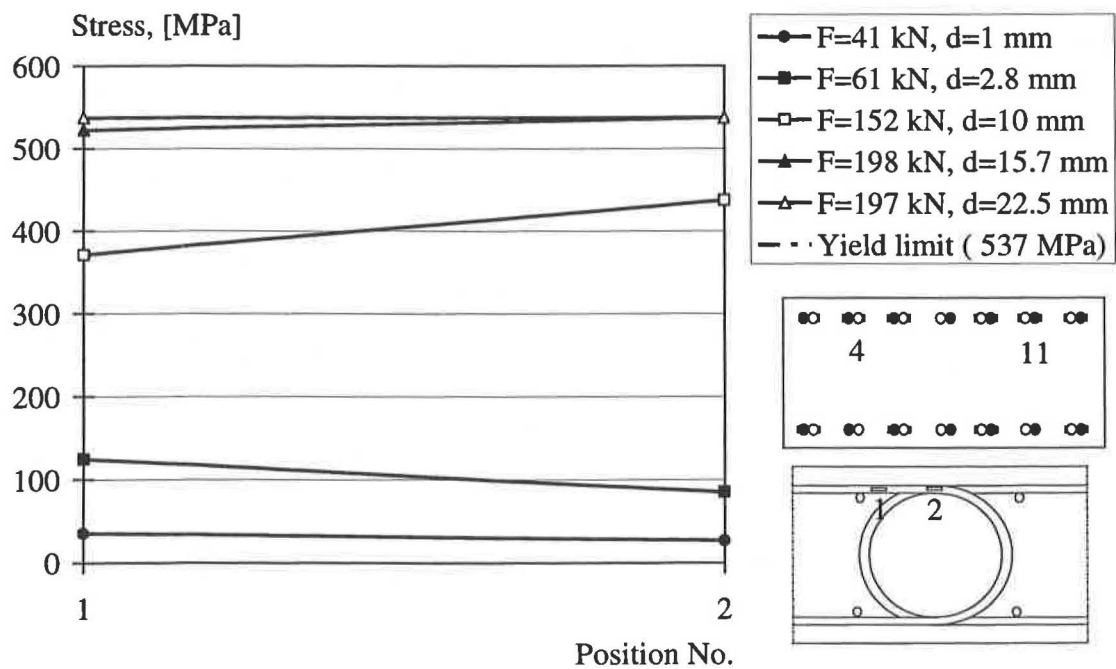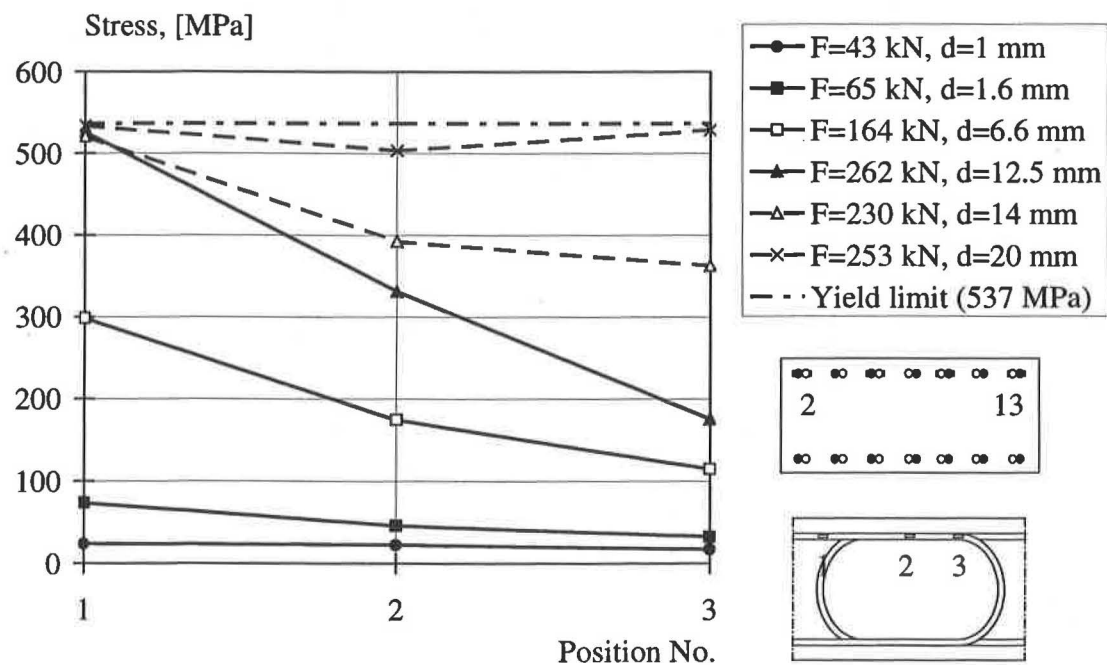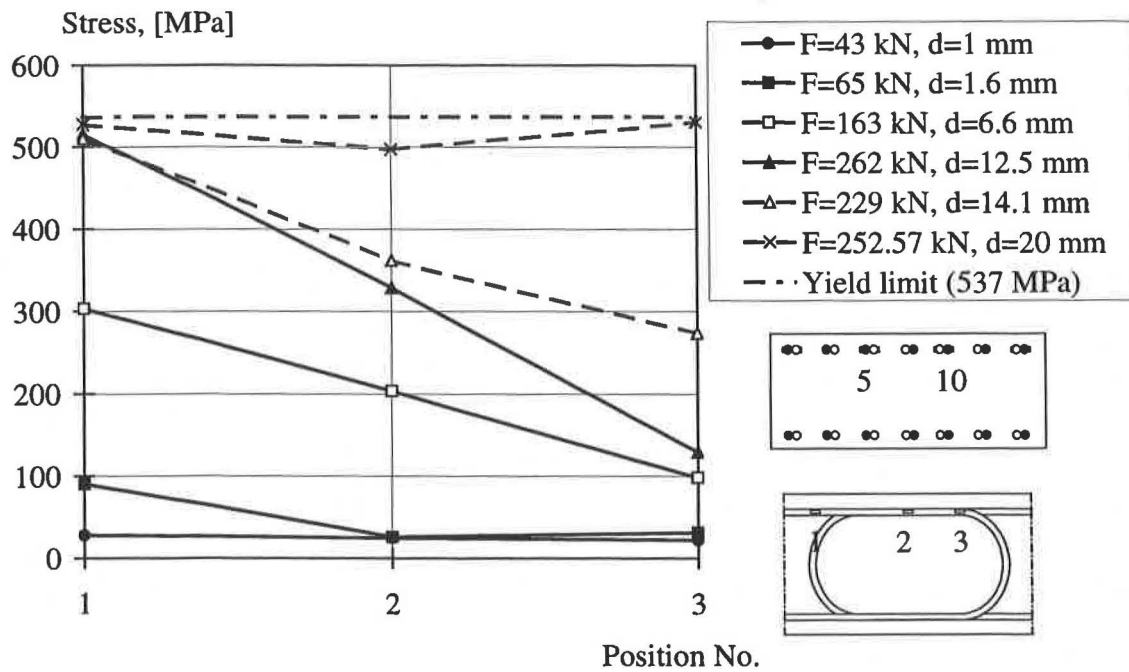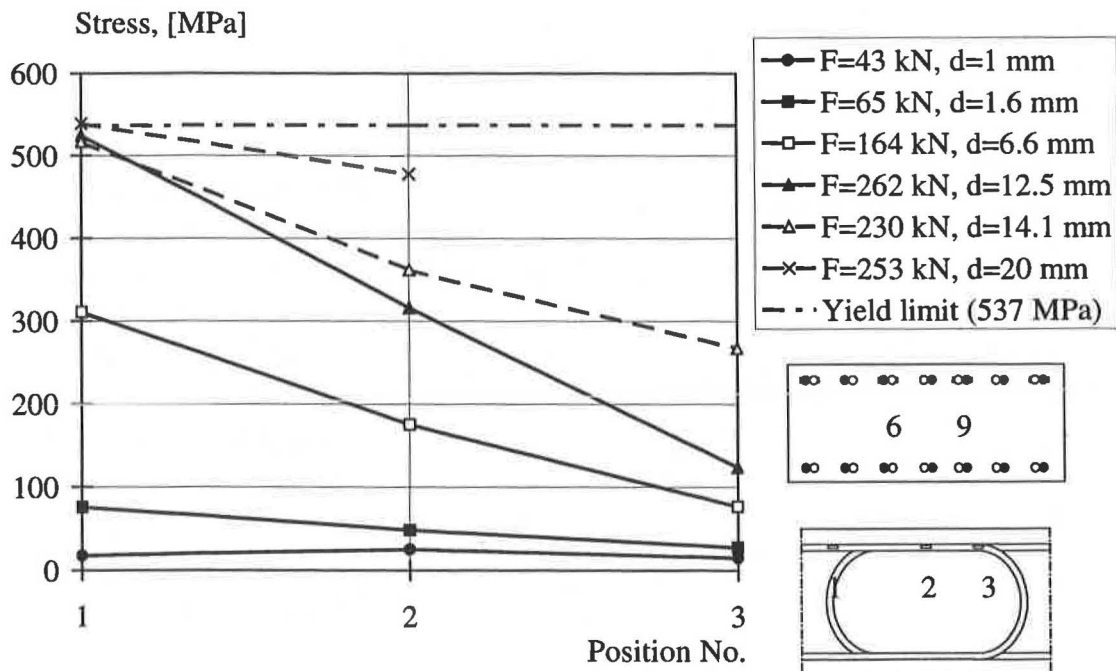


Figure E.31    Average stress of loops 4 and 11 of specimen RV12.
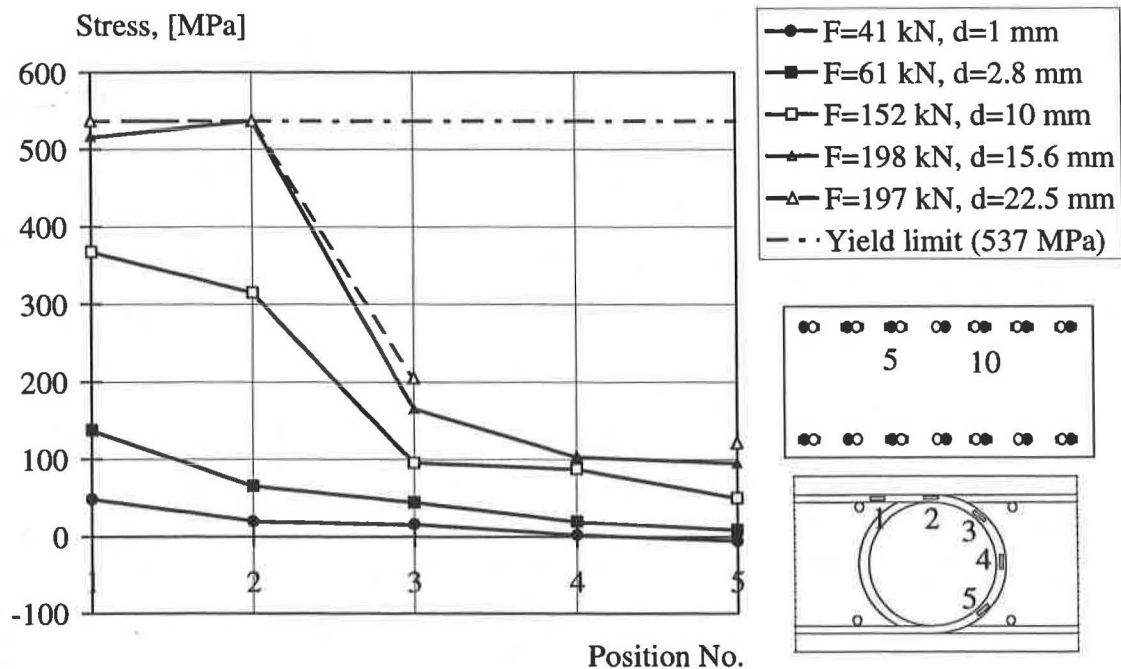
Figure E.32    Average stress of loops 5 and 10 of specimen RV12.
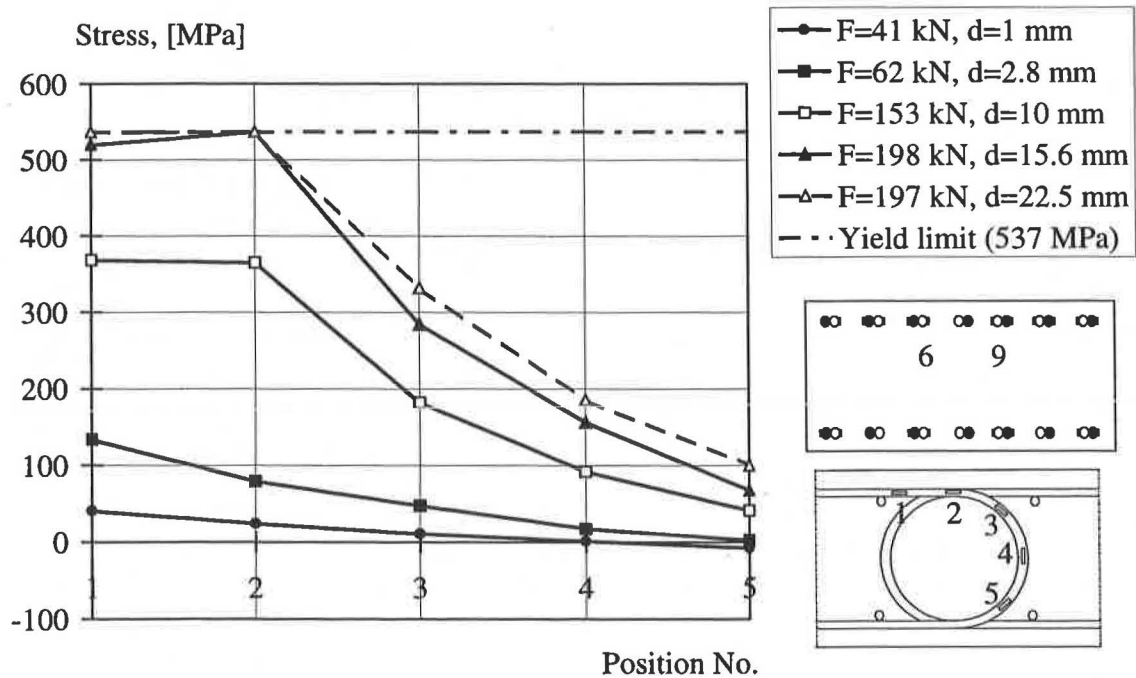


Figure E.33    Average stress of loops 6 and 9 of specimen RV12.
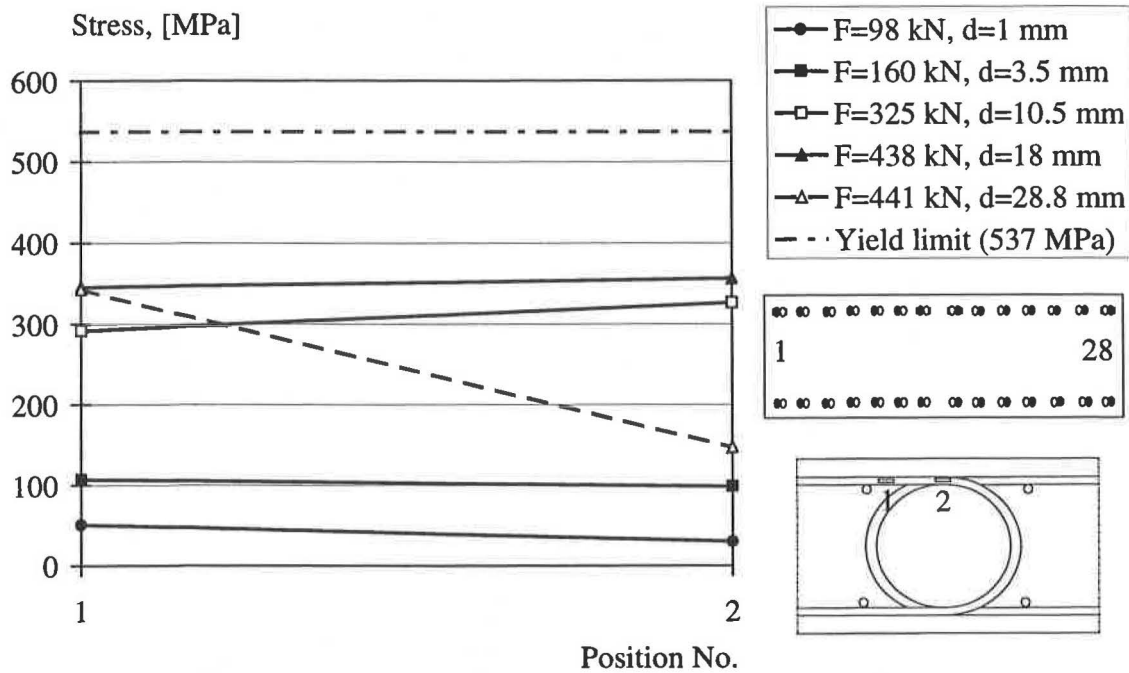
## E.2.2 Stresses of specimen RV13
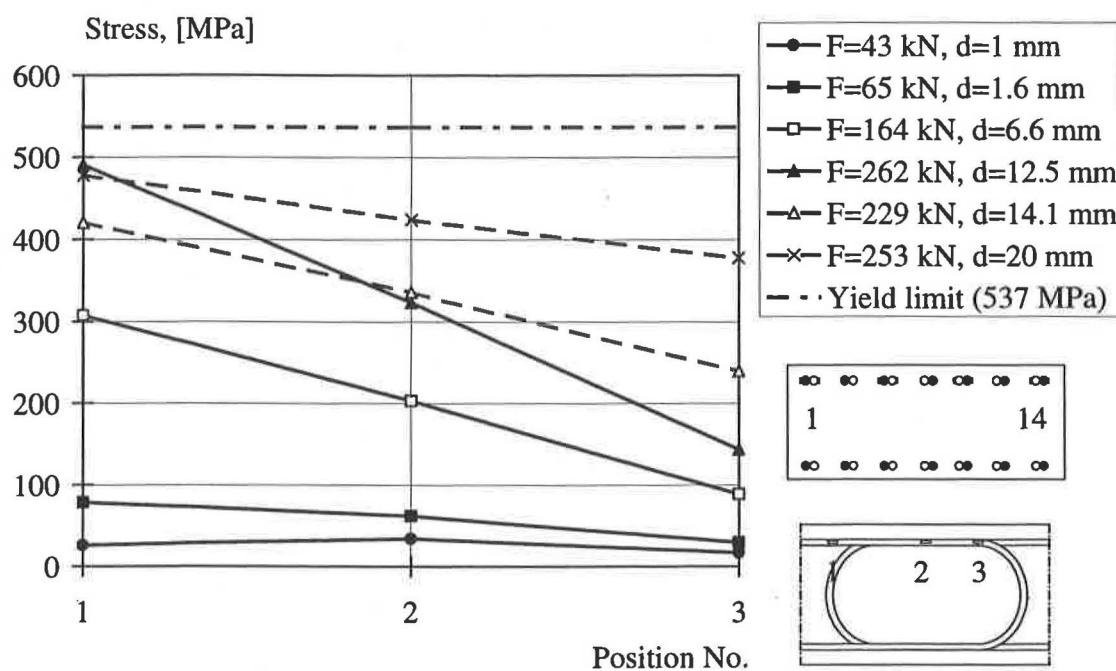


Figure E.34     Average stress of loops 1 and 14 of specimen RV13.



Figure E.35     Average stress of loops 2 and 13 of specimen RV13.

Figure E.36    Average stress of loops 5 and 10 of specimen RV13.



Figure E.37    Average stress of loops 6 and 9 of specimen RV13.

E.19

## E.2.3 Stresses of specimen RV14



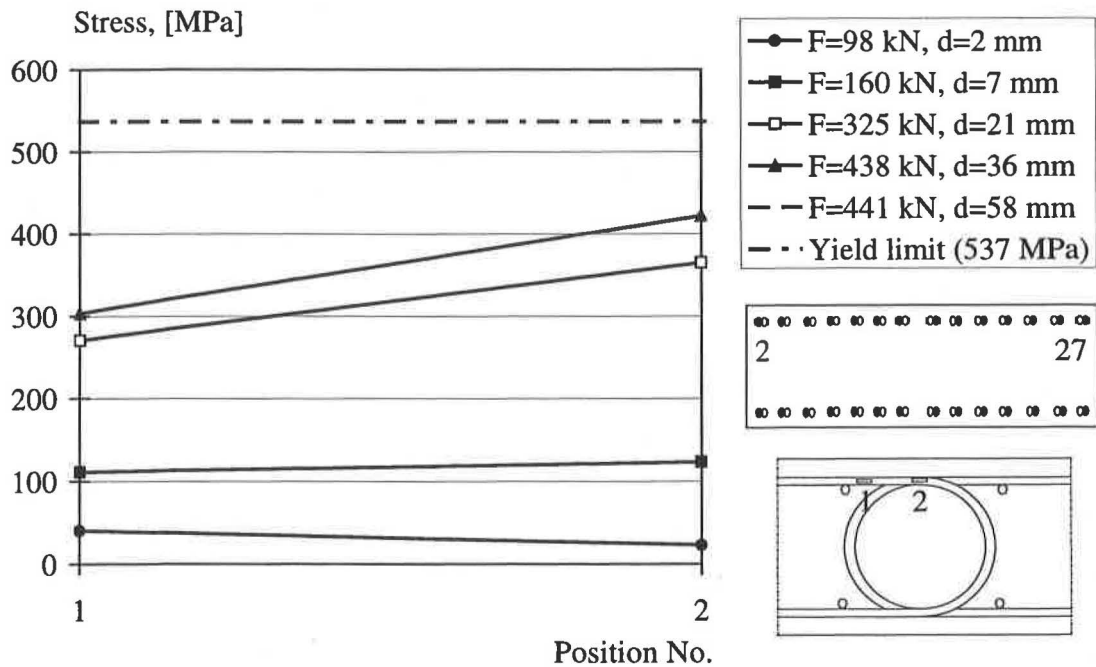Figure E.38    Average stress of loops 1 and 28 of specimen RV14.



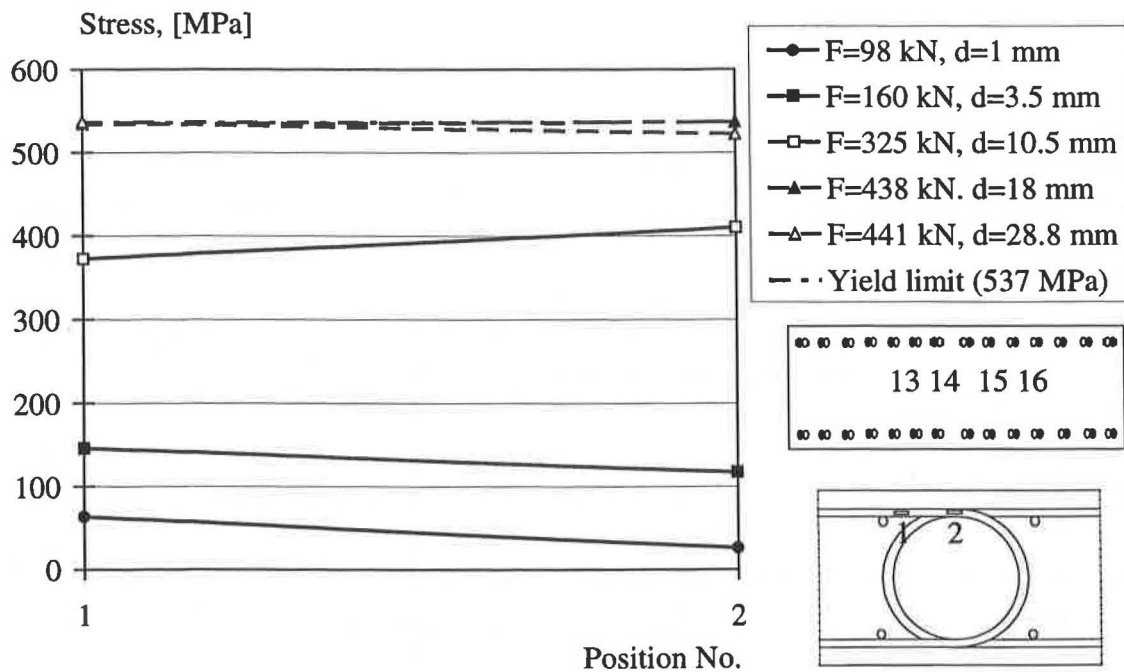Figure E.39    Average stress of loops 2 and 27 of specimen RV14.

Figure E.40    Average stress of loops 13, 14, 15 and 16 of specimen RV14.
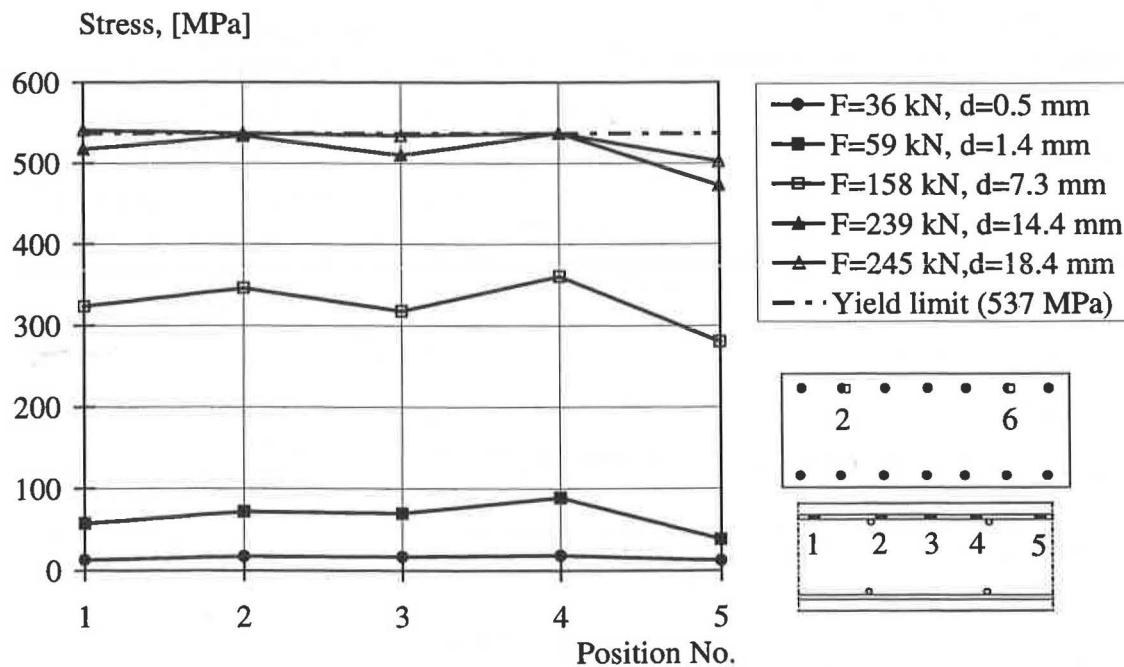
## E.2.4    Stresses of specimen RV15



Figure E.41    Average stress of loops 2 and 6 of specimen RV15.